Shark Biomimetics: The Role of Denticles and Riblets on the Turbulent Boundary Layer

Author:
Charlie James Lloyd

Supervisors:
Prof. Jeffrey Peakall
Dr. Alan Burns
Dr. Robert Dorrell
Dr. Gareth Keevil

A thesis submitted in accordance with the requirements
for the degree of Doctor of Philosophy

THE UNIVERSITY OF LEEDS

Centre for Doctoral Training in Fluid Dynamics

School of Computing

February, 2020

Declaration of Authorship

The candidate confirms that the work submitted is their own, except where work which has formed part of jointly authored publications has been included. The contribution of the candidate and the other authors to this work has been explicitly indicated below. The candidate confirms that appropriate credit has been given within the thesis where reference has been made to the work of others.

Chapter 3 contains material from a jointly authored paper currently under review:

C. J. Lloyd, J. Peakall, A. D. Burns, G. M. Keevil, R. M. Dorrell, P. B. Wignall, and T. Fletcher (under review).
"The influence of shark skin denticles, with and without riblets, on the turbulent boundary layer"

Chapter 4 contains material from a jointly authored paper accepted for publication in the International Journal of Computational Fluid Dynamics:

C. J. Lloyd, J. Peakall, A. D. Burns, G. M. Keevil, R. M. Dorrell (accepted, 2020).
"Numerical errors at the wall: On the sensitivity of RANS models to near wall cell size"

Both papers were primarily authored by C. J. Lloyd who was responsible for all data collection, processing, analysis, and writing. Contributions of all other authors were through advisory and editorial roles. The original fish scale CAD model was provided by T. Fletcher and P. B. Wignall for Chapter 3, and the experimental set up was carried out jointly by G. M. Keevil and C. J. Lloyd.

Abstract

Shark skin has fascinated biologists, engineers, and physicists for decades due to its highly intricate drag-reducing structure, which has motivated a plethora of research into bio-inspired hydrodynamically efficient surfaces. Throughout this thesis the effect of shark scales on the boundary layer is investigated, with a particular focus on the role of riblets in combination with denticles. In addition to examining flows over shark scales studies are also presented investigating the behaviour of Reynolds Averaged Navier-Stokes (RANS) models close to solid boundaries, and the scaling and driving mechanisms of secondary flows over ribletted surfaces.

Extensive numerical and analytical studies are carried out to determine the sensitivity of eleven turbulence closures to the near-wall grid resolution, and their consistency with asymptotic solutions. Results inform the choice of turbulence models adopted for simulations of wall bounded flows, particularly where numerical errors must be minimised.

Secondary flows over longitudinal riblets are found to be driven by Reynolds stress anisotropy, consistent with Prandtl's second type of secondary flow. The strength of the vorticity field is heavily dependent on the inner-scaled riblet spacing s^+ where two distinct regimes arise; a viscous regime where vorticity production is balanced by molecular viscous diffusion, and an inertial regime where an effective turbulent viscosity balances anisotropic production. The transition between these regimes occurs when riblet tips protrude into the buffer layer and cause increased turbulent mixing ($s^+ \approx 30$), such that vorticity reaches its maximum before reducing as s^+ increases further.

Riblets in combination with shark scales do not operate as they do when applied to smooth walls. Experimental and numerical studies reveal that riblets act to reduce pressure drag acting on roughness elements, rather than the viscous forces typically associated with longitudinal riblets. The mechanisms leading to this behaviour are driven by the ability of riblets to restrict spanwise motion and maintain streamwise-aligned near-wall flow. By doing so riblets protect downstream denticles from high momentum impinging fluid, and reduce high magnitude swirl generated at the exposed denticle edges, which can otherwise lead to increased turbulent production and enhanced momentum transfer through the roughness sub-layer. These mechanisms lead to a significantly more efficient rough surface than smooth denticles, although do not necessarily lead to an overall reduced drag compared to a flat plate. These studies conclude that riblets have evolved as a mechanism to reduce or eliminate the skin friction increase due to the presence of scales. The combination of scales and riblets appears to be relatively hydrodynamically efficient in terms of skin-friction drag, whilst also acting to maintain boundary layer attachment and providing the other advantages associated with scales such as anti-fouling, abrasion resistance, and defence against parasites.

Acknowledgements

I would like to thank my supervisors Jeff Peakall, Alan Burns, Gareth Keevil and Rob Dorrell for their guidance, insight, and enthusiasm for my work over the last four years. I would also like to thank my parents and family who have provided support and welcome distractions from my work, and my fiancée Ellie for all her love and encouragement. I am also very grateful to Lynn and Richard for their help, especially over the last year.

The experimental work would never have run so smoothly without help from the Sorby team, Gareth Keevil and Helena Brown - thank you for your technical support and direction. I am also grateful for the fish scale CAD model provided by Tom Fletcher and Henning Blom, the EPSRC Centre for Doctoral Training for funding my studies, and my colleagues for their valuable contributions and friendship.

I dedicate this work to my father.

Contents

List of Figures

List of Tables

List of Abbreviations

CAD	**C**omputer **A**ided **D**esign
CFD	**C**omputational **F**luid **D**ynamics
DNS	**D**irect **N**umerical **S**imulation
HMP	**H**igh **M**omentum **P**athway
LDA	**L**aser **D**oppler **A**nemometry
LMP	**L**ow **M**omentum **P**athway
PIV	**P**article **I**mage **V**elocimetry
RANS	**R**eynolds **A**veraged **N**avier-**S**tokes
RMS	**R**oot-**M**ean-**S**quare
RSM	**R**eynolds **S**tress **M**odel
SEM	**S**canning **E**lectron **M**icroscope
TKE	**T**urbulent **K**inetic **E**nergy

List of Symbols

Symbol	**Definition**
B	Additive log-law constant
$c_{f,x}$	Local streamwise viscous friction coefficient
$c_{p,x}$	Local streamwise pressure coefficient
C_f	Global streamwise friction coefficient
C_{fp}	Pressure contribution to C_f
C_{fv}	Viscous contribution to C_f
d	Wall distance
D_h	Denticle height
$D_t\phi$	Material derivative of a variable, ϕ
$\mathcal{D}_{ij}$	Total diffusion term in the transport of $\overline{u_i'u_j'}$
$\mathcal{D}_T$	Total diffusion term in the transport of k
$\hat{e}_x, \hat{e}_y, \hat{e}_z$	Unit vectors in the x, y, and z directions
F_D	Drag force in the streamwise direction
F_p	Pressure contribution to F_D
F_v	Viscous contribution to F_D
g	Square root of the turbulent timescale: $\sqrt{\tau}$
h	Riblet height
h_r	Grid refinement ratio
$\overline{h}$	Mean riblet height
k	Turbulent kinetic energy, $\frac{1}{2}\overline{u_i'u_i'}$
k_0	Roughness height
k_s	Sand-grain roughness height
n_i	Wall normal direction
p	Kinematic pressure
p'	Kinematic pressure fluctuation
$\overline{P}$	Ensemble averaged kinematic pressure
$\mathcal{P}$	Production of turbulent kinetic energy
$\mathcal{P}_{ij}$	Production tensor
Re_b	Bulk flow Reynolds number
Re_τ	Reynolds number based on the friction velocity
Re_θ	Reynolds number based on the momentum thickness
s	Riblet spacing

s^+	Inner-scaled riblet spacing
S_{ij}	Mean rate of strain tensor
t	Time
T_{xy}	Weighted shear stress, $\tau_{xy}(1-\eta)$
u_τ	Friction velocity, $\sqrt{\tau_w/\rho}$
u_i	Three component instantaneous velocity vector
u_i'	Three component velocity fluctuations
$-\overline{u_i'u_j'}$	Reynolds stress tensor
$u_{\mathrm{rms}}, v_{\mathrm{rms}}, w_{\mathrm{rms}}$	Root-mean-square of the velocity fluctuations
U, V, W	Three components of the ensemble averaged velocity vector, $\overline{U}_i$
$U_\infty, V_\infty, W_\infty$	Freestream velocities
U^+_{comp}	Composite velocity profile
U^+_{inner}	Inner component of U^+_{comp}
U^+_{outer}	Outer component of U^+_{comp}
$\overline{U}_i$	Ensemble averaged velocity vector
w	Denticle width
$\mathcal{W}(\eta)$	Wake function
x, y, z	Rectangular Cartesian coordinates
x^+, y^+, z^+	Inner-scaled Rectangular Cartesian coordinates
y_1	Wall distance for the wall-neighbouring cells
y_1^+	Inner-scaled wall distance
Γ	Recirculation frequency
δ	Boundary layer thickness; Channel half-height
δ_{ij}	Kronecker delta
δ_ν	Inner length scale, ν/u_τ
ΔU^+	Roughness function
Δ_y	Virtual origin offset
ε	Rate of turbulent dissipation
ε_{ij}	Dissipation rate tensor
η	Outer coordinate, y/δ
θ	Momentum thickness, $\int_0^\delta \frac{U}{U_\infty}\left(1-\frac{U}{U_\infty}\right)dy$
Θ	Denticle crown angle of attack
κ	Kármán constant
λ_{ci}^+	Inner-scaled swirl strength
ν	Kinematic molecular viscosity
ν_t	Kinematic turbulent viscosity
Π	Wake strength
Π_{ij}	Pressure-strain correlation tensor
ρ	Density
τ	Turbulent timescale, k/ε

τ_w	Streamwise mean wall shear stress
τ_{xy}	Sum of mean turbulent and viscous shear stresses, $\nu\frac{d\overline{U}}{dy} - \overline{u'v'}$
ω	Specific dissipation rate
ω'	Regularised specific dissipation rate, $\omega - \omega_w$
ω_w	Near wall specific dissipation rate, $\frac{6\nu}{\beta y_w^2}$
Ω_i	Mean vorticity vector
Ω_{ij}	Mean rotation tensor
Ω_x	Streamwise component of Ω_i
Ω_x^C	Convective term of the transport of Ω_x
Ω_x^{NS}	Normal stress term of the transport of Ω_x
Ω_x^{SS}	Shear stress term of the transport of Ω_x
Ω_x^V	Viscous dissipation term of the transport of Ω_x

Superscripts

$+$	Inner scaled variable, scaled by ν and u_τ

Chapter 1

Introduction

Sharks were once the dominant vertebrate group in the oceans, with fossils of modern sharks dating back to the Jurassic period (140 – 170 million years ago), and records of early ancestors dating back over 300 million years ago (Budker, 1971). The scales of sharks are among their most characteristic features, with a structure so similar to that of teeth that they are often termed dermal denticles (i.e 'skin-teeth'), where they erupt through the epidermis of the skin giving sharks a rough sand-paper like texture when handled. Dermal denticles vary considerably not only between shark species, but also depending on the location on the shark body. An example of this is provided by the Scanning Electron Microscope (SEM) images of Figure 1.1, adapted from Wen, Weaver, and Lauder (2014). Here the bonnethead shark (*Sphyrna tiburo*) denticles have a width of 100 – 200 µm and are reasonably tightly packed, with some regions of scales overlapping. Denticle shapes and sizes vary considerably between species; some are tightly packed and overlap like the bonnethead shark, while others are loosely arranged, some have sharp spine-like crowns while others appear smooth. A feature often present on fast-swimming sharks are the riblets observed in Figure 1.1, which typically align with the flow direction, although even these can vary between species (Bechert, Hoppe, and Reif, 1985). For example, the riblets on the bonnethead shark samples of Figure 1.1 are

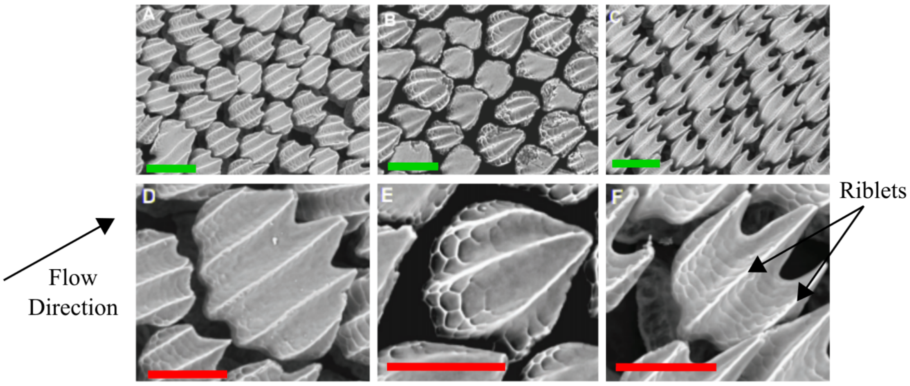

FIGURE 1.1: Scanning Electron Microscope (SEM) images of bonnethead shark (*Sphyrna tiburo*) skin at three locations: The head (left), the dorsal fin (centre), and the anal fin (right). Green scale bar are 200 µm, red scale bars are 100 µm. Image adapted from Wen, Weaver, and Lauder (2014).

different at each sample location, varying from 5 parallel riblets at the shark head, to 3 converging riblets on the pectoral fin, to 3 parallel riblets on the anal fin. Despite the long evolutionary time scales, fossil denticles have been found to consist of many of the same features that modern denticles possess. For example, riblets have been observed on some of the earliest records of fossil scales (Sansom et al., 2012).

There are three theorised functions of shark skin denticles; defence against parasites, resistance against abrasion, and hydrodynamic efficiency (Reif, 1985). It is this last function that is the focus of this thesis. In particular seeking to utilise bioinspiration and biomimicry of these complex rough surfaces for the purpose of improved hydrodynamic efficiency for engineering applications subject to high fluid drag. There has been extensive research on the topic of shark skin inspired surfaces for the purpose of reduced viscous drag, i.e the drag force imposed by the molecular viscosity of a fluid as it passes over a solid surface. But despite such variability in denticle shape, research has primarily focused on the riblet features present on the crown of some shark scales. Bioinspired longitudinal riblets have successfully reduced drag by up to 10% in laboratory experiments (Bechert et al., 1997), and the fluid dynamic mechanisms that lead to such efficiency are reasonably well understood. However, literature concerning hydrodynamic experiments on complex three dimensional shark skin denticles is scarce, and studies vary considerably regarding techniques and flow conditions, making comparisons between data sets extremely difficult (see e.g. Bechert, Hoppe, and Reif, 1985; Bechert et al., 2000; Zhao et al., 2012; Wen, Weaver, and Lauder, 2014). Concerning the simplest of flow conditions, canonical flows over flat plates and through channels, some authors report drag reduction of a greater magnitude than ribletted plates (e.g. Zhao et al., 2012; Chen et al., 2014; Domel et al., 2018), while others report significant increases to drag (e.g. Bechert, Hoppe, and Reif, 1985; Boomsma and Sotiropoulos, 2016). Through a review of these studies in Chapter 2 this lack of agreement is identified as a poor understanding of the relationship between denticle geometry and hydrodynamic performance. Only a few have reported drag measurements of more than one denticle geometry (e.g. Bechert, Hoppe, and Reif, 1985; Fletcher, 2015), or adopted techniques that can obtain flow field data close to the denticles (e.g. Boomsma and Sotiropoulos, 2016), both of which are key to understanding the morphological evolution of denticles and identifying potential biomimetic engineering applications.

These deficiencies necessitate the use and development of techniques that can quantify effects of denticle geometry on the boundary layer, motivating the use of Reynolds Averaged Navier-Stokes (RANS) closures. While Direct Numerical Simulation (DNS) has been successfully adopted for modelling shark skin flows it is extremely costly; the large difference in length scale between the shark skin denticles and the boundary layer height necessitates considerably finer grids than smooth wall flows (see e.g. Boomsma and Sotiropoulos, 2016). In contrast RANS closures are significantly cheaper but require validation, especially given that simpler flows, such as those over ribletted plates, have yet to be accurately predicted (e.g. Launder and Li, 1993; Djenidi and Antonia, 1995). This thesis therefore comprises of several RANS studies, aimed at developing and validating RANS models for smooth and ribletted channel flows before carrying out numerical simulations of the flow over shark scales. These additional studies also allow investigation into the limiting behaviour and numerical properties of RANS models near solid boundaries, and the identification of mechanisms driving and sustaining secondary flows above streamwise-aligned parallel riblets. Finally RANS closures are adopted to model the boundary layer flow over shark scales, validated against Laser Doppler Anemometry (LDA) experiments. These LDA experiments obtain boundary layer measurements above 3D printed smooth and ribletted denticles, assessing their influence on the boundary layer and effects on skin friction. Experimental and numerical data are subsequently employed to identify the role of riblets in combination with denticles.

1.1 Aim and objectives

The aim of this thesis is to develop experimental and numerical techniques capable of carrying out parametric studies on denticle geometry, and using these to identify the role of riblets in combination with denticles to establish whether riblets are solely responsible for drag reduction. This will be realised through the following objectives:

1. Carry out a review of previous work on the hydrodynamics of riblets and shark scales and identify knowledge gaps and appropriate experimental and numerical methodologies.

2. Carry out laboratory experiments to obtain flow field measurements of a turbulent boundary layer flow over smooth and ribletted denticles.

3. Establish the near-wall behaviour and numerical properties of Reynolds Averaged Navier-Stokes (RANS) closures for a fully developed smooth channel flow, and identify models appropriate for modelling rough-wall flows.

4. Validate RANS closures by simulating a fully developed channel flow over two-dimensional sawtooth riblets and comparing solutions to experimental and numerical literature data. Use these results to identify the mechanisms driving and sustaining secondary flows at the riblet tips, and how secondary flows scale with the riblet size.

5. Extend numerical models to shark skin denticles and validate solutions against experimental data. Use solutions to investigate near-denticle flow structures and identify the role of riblets in combination with shark skin denticles.

1.2 Thesis organisation

Each of the five objectives is presented as a separate Chapter in this thesis. Chapter 2 presents an introduction to boundary layer flows and the quantification and effects of surface roughness. The literature regarding flows over riblets is then detailed in Section 2.3, with a particular focus on the secondary flows that develop near the riblet surface. Finally the fluid dynamic experiments on shark skin denticles are reviewed in Section 2.4, with a focus on their application to canonical boundary layer flows. Application of denticles to more complex flow conditions such as boundary layer separation are briefly reviewed for completeness.

Chapter 3 presents an experimental study on 3D printed smooth and ribletted shark skin denticles, using 2D Laser Doppler Anemometry (LDA) to measure the turbulent boundary layer flow. Turbulent statistics and drag coefficients are compared at several Reynolds numbers in order to identify the role of riblets in combination with denticles.

Chapter 4 presents analytical and numerical solutions for a fully developed turbulent channel flow approximated using RANS closures. The motivation of this work is to determine appropriateness of turbulence models for the simulation of rough-wall flows, where near-wall grid resolutions will vary significantly. There is a particular emphasis on the choice of scale-determining variable used to close RANS models, which is found to have a significant influence on discretisation error. The RANS models deemed appropriate through smooth channel flow simulations are extended to ribletted channels and validated against experimental and numerical literature data in Chapter 5. Furthermore, an extensive analysis on the mechanisms driving and sustaining secondary flows is carried out, using both numerical and analytical techniques. Finally, the flow over shark scales is simulated using RANS models in Chapter 6, and validated against the experimental data of Chapter 3. New insights regarding the influence of riblets on near-denticle flow are identified, and with the support of experimental data the implications on the hydrodynamic function of shark skin are discussed. The thesis is concluded in Chapter 7, summarising all present work and detailing key areas that require further research.

Chapter 2

Boundary layers, surface roughness, and the hydrodynamics of shark skin denticles

Shark skin is a highly intricate rough surface comprised of tooth-like denticles embedded into the dermis. Denticles are thought to have evolved to the benefit of hydrodynamic efficiency, defence against abrasion, and protection against parasites (Reif, 1985). The drag forces acting on a shark body can be split into several different components (Fletcher et al., 2014): Form drag due to the displacement of fluid around the shark body, induced drag due to the lift forces created by the foil-like fins, and skin friction drag arising from the no-slip condition and subsequent large velocity gradients at the shark surface. Hydrodynamically shark skin denticles are extremely small with respect to the length scales associated with the flow around a shark, and are located within the turbulent boundary layer, such that their primary influence is on skin friction drag. Before discussing the fluid dynamics of denticles the turbulent boundary layer is introduced, as is the influence of a typical rough surface. Longitudinal surface riblets are then discussed, a particular type of shark-skin inspired surface roughness that has been shown to reduce drag by up to 10 % (Bechert et al., 1997). Unlike denticles, riblets have seen an extensive amount of research over the last few decades, and their drag reducing mechanisms are reasonably well understood (e.g. Luchini, Manzo, and Pozzi, 1991; Bechert et al., 1997; García-Mayoral and Jiménez, 2011a). Finally the hydrodynamics of shark skin denticles are discussed, in the context of both separating flows and attached turbulent boundary layer flows.

2.1 The turbulent boundary layer

The turbulent boundary layer, arising from the no-slip condition, is governed by two sets of scales whose influence is stratified in terms of wall distance (Jiménez, 2004). Near the wall molecular viscosity (ν) is dominant and the appropriate velocity scaling is the friction velocity, $u_\tau = \sqrt{\tau_w/\rho}$, where τ_w is the wall shear stress and ρ is the fluid density.

The wall shear stress is given by

$$\frac{\tau_w}{\rho} = \nu \frac{\partial U}{\partial y}\bigg|_{y=0} \tag{2.1}$$

where U is the mean streamwise velocity and y is the wall-normal coordinate. The inner length scale is consequently given by $\delta_\nu = \nu/u_\tau$, which governs the fluid flow in the boundary layer close to the wall. Variables scaled by u_τ and ν are identified with the superscript $+$; i.e near the wall the appropriate scaling for the mean streamwise velocity U is $U^+ = U/u_\tau$ and the wall-normal coordinate y is scaled such that $y^+ = yu_\tau/\nu$. Below a wall-normal distance of $y^+ \approx 5$ the mean streamwise fluid velocity scales linearly with the wall-normal distance: $U^+ = y^+$. Further from the wall is the buffer layer, which exists between $5 \lesssim y^+ \lesssim 30$. This is the most active region of the boundary layer where the production of turbulent kinetic energy reaches its maximum.

As the distance to the wall increases further the dependence on molecular viscosity vanishes and the governing length and velocity scales are the freestream velocity U_∞ and the boundary layer thickness δ, which are known as outer scales. This leads to a Reynolds number $\delta^+ = Re_\tau = \delta u_\tau/\nu$, which quantifies the scale separation between δ and δ_ν. At high δ^+ the situation can arise where neither scaling is appropriate; y^+ is too large for viscosity to play a dominant role, and the outer coordinate $\eta = y/\delta$ is too small for δ to be relevant. This leads to the well known log-law or overlap region, where the mean streamwise fluid velocity is governed by a logarithmic profile based on the wall distance:

$$U^+ = \frac{1}{\kappa} \ln y^+ + B, \tag{2.2}$$

where the Kármán constant, κ, and B are log-law constants. This law is extremely robust for wall bounded flows and typically exists for $y^+ \gtrsim 30$ and $\eta \lesssim 0.15$, given δ^+ is large. The log-law constants κ and B tend to fixed values at high Reynolds numbers (Nagib and Chauhan, 2008), their values dependent on the properties of the wall bounded flow. The parameter κ depends only on the properties of the overlap region.

The full velocity profile can be observed in Figure 2.1. The overlap region exists for a significant part of the flow and grows with increasing δ^+. It can account for upwards of 70 % of the total growth of streamwise mean velocity, and half of the overall production of turbulent kinetic energy (Jiménez, 2004).

The wake region exists for a significant portion of the boundary layer, $\eta \gtrsim 0.15$, where the fluid variables tend to their freestream values. The composite profile of Coles (1956) is often used to describe the velocity profile for a boundary layer:

$$U^+ = U^+_{\text{inner}} + U^+_{\text{outer}}. \tag{2.3}$$

Generally U^+_{inner} is quantified by the log-law (2.2), which is valid for $y^+ \gtrsim 30$ (Pope, 2001), although other forms have been developed that are valid for the full inner region (e.g Musker, 1979). U^+_{outer} typically takes the form

$$U^+_{\text{outer}} = \frac{2\Pi}{\kappa}\mathcal{W}(\eta) \tag{2.4}$$

where Π is the wake strength constant (typically order unity) and $\mathcal{W}(\eta)$ is a wake function that is assumed universal with the normalisation conditions $\mathcal{W}(0) = 0$ and $\mathcal{W}(1) = 1$. Chauhan, Nagib, and Monkewitz (2007) review several formulations of $\mathcal{W}(\eta)$, successfully finding that exponential forms of $\mathcal{W}(\eta)$ approximate the wake region well.

Π is generally regarded as a constant with a value ≈ 0.4, although Nagib and Chauhan (2008) have shown that this can vary at low Reynolds numbers. In addition to this the effect of freestream turbulence can also weaken the wake strength, even causing it to be negative when turbulence levels are high (Thole and Bogard, 1996). Generally the effects of freestream turbulence are limited to the outer regions of the boundary layer, although Thole and Bogard (1996) have shown that in the inner region fluctuating root-mean-square (RMS) velocities can be affected if the freestream turbulence levels exceeds those of the boundary layer generated turbulent fluctuations.

The presence of a wall is strongly felt by turbulent fluctuations, where the fluid velocity vector is decomposed into a mean component U_i and a fluctuating component u'_i. The influence of turbulent fluctuations on the mean velocity is felt through the Reynolds stresses, $\overline{u'_i u'_j}$ where the overbar represents Reynolds ensemble averaging. The tensor $\overline{u'_i u'_j}$ is symmetric; diagonal terms are normal stresses and contribute to turbulent kinetic energy (k) by $k = \frac{1}{2}\overline{u'_i u'_i}$, and off-diagonal terms are shear stresses. For a boundary layer flow with no spanwise spatial dependence the only non-zero off-diagonal Reynolds stress is $\overline{u'v'}$. The non-zero Reynolds stresses for a fully developed channel flow at

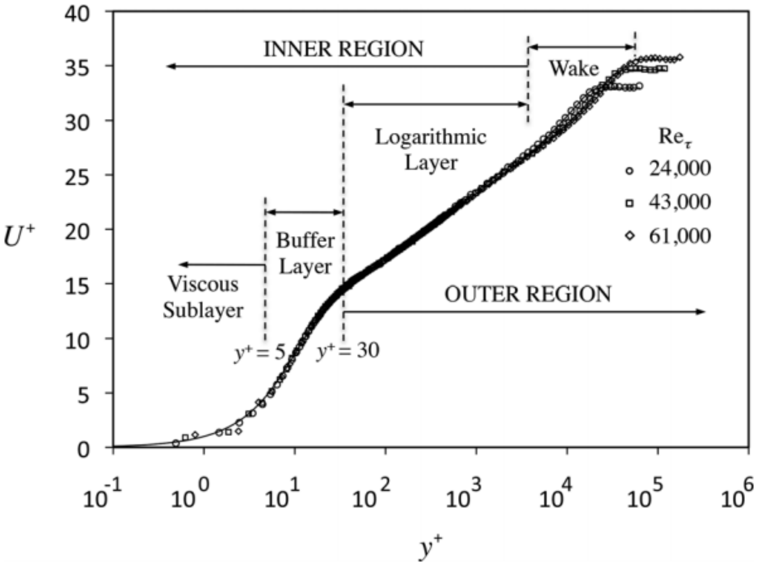

FIGURE 2.1: Typical boundary layer profile for three Reynolds numbers. Image taken from Perlin, Dowling, and Ceccio (2016).

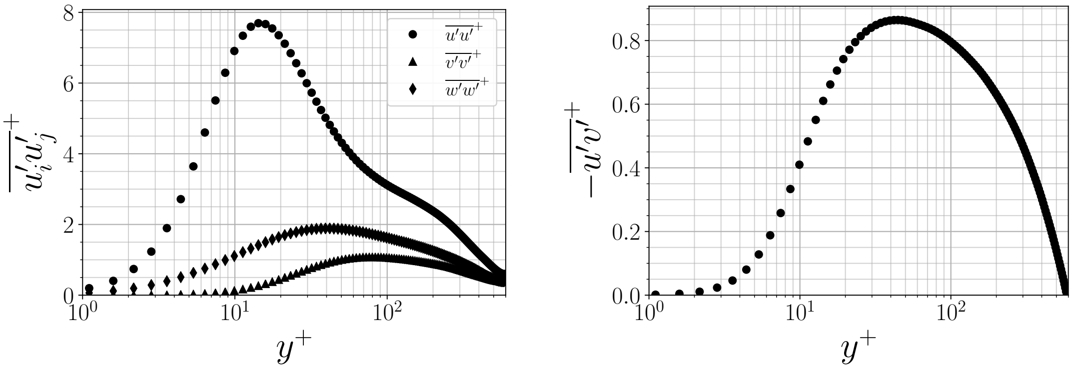

FIGURE 2.2: Diagonal (left) and shear (right) Reynolds stresses for a fully developed channel flow at $Re_\tau = 587$. Data from DNS of Moser, Kim, and Mansour (1999).

$Re_\tau = 587$ can be observed in Figure 2.2, using data from the Direct Numerical Simulation (DNS) of Moser, Kim, and Mansour (1999). A particularly interesting feature of the near-wall Reynolds stresses is the distribution of turbulent kinetic energy over the diagonal stresses. The streamwise component has a significantly larger peak in the buffer layer and contributes most to the overall turbulent kinetic energy. The large differences in the diagonal Reynolds stresses indicate that near-wall turbulence is highly anisotropic, and only tends to isotropy far from the wall; for the channel flow of Moser, Kim, and Mansour (1999) one finds that only at the channel centre ($y^+ = 587$) do the Reynolds stresses converge to a near-isotropic state. Very near the wall ($y^+ \lesssim 10$) the wall-normal stresses $\overline{v'v'}^+$ are near negligible compared to the tangential stresses. This arises from kinematic conditions and leads to a two-component limit near both free-slip and no-slip walls (Yokojima and Shima, 2010), a phenomenon known as kinematic blocking. As a result of kinematic blocking turbulent kinetic energy is re-distributed from wall-normal stresses to tangential components in a thin-layer near the wall (Mansour, Kim, and Moin, 1988). Interestingly energy is redistributed in an opposing manner further from the wall, such that tangential components of the Reynolds stresses transfer turbulent kinetic energy back to the wall-normal component due to the effects of pressure fluctuations (Manceau, Wang, and Laurence, 2001). Kinematic blocking and pressure-echo effects present complications to turbulence modellers attempting to parameterise near-wall turbulence (Manceau, 2015).

2.2 Surface roughness

The majority of real engineering problems are subject to surface roughness which generally increases skin friction. The first quantitative study on the effect of surface roughness was carried out by Nikuradse (1933) who applied different grain sizes of sand to a pipe flow and measured the resulting friction factor (equivalent to the coefficient of friction, C_f). Nikuradse (1933) quantified the effect of surface roughness using the scaling

$k_s^+ = k_s u_\tau / \nu$ where k_s is the sand-grain roughness height. Three regimes were identified based on the value of k_s^+:

$$k_s^+ < 5 : \text{Hydraulically smooth},$$

$$5 \le k_s^+ \le 70 : \text{Transitionally rough},$$

$$70 < k_s^+ : \text{Fully rough}.$$

The hydraulically smooth regime occurs when the roughness elements do not protrude above the viscous sub-layer; in this case roughness has no effect on the flow. During the transitional stage roughness elements begin to protrude beyond the viscous sub-layer, creating additional turbulent mixing and pressure drag on individual elements; both of these effects increase the friction factor relative to a smooth surface. As the roughness height increases it protrudes further into the inner region, reducing the near-wall peak of turbulent kinetic energy and destroying the buffer region of the flow. In the fully-rough regime the buffer region is completely broken down and the friction factor is no longer a function of the Reynolds number.

Outside the 'roughness sub-layer' turbulent motions are independent of surface conditions (Raupach, Antonia, and Rajagopalan, 1991), although there has been evidence that roughness can affect the wake strength Π (Flack, Schultz, and Shapiro, 2005). It has been generally accepted that the roughness sub-layer extends $\approx 3k_s - 5k_s$ (Jiménez, 2004). Quantifying the flow in this region is of course dependent on the geometry of the rough surface. Outside the roughness sub-layer the mean streamwise velocity maintains its composite form (2.3) with an additive constant to the inner profile:

$$U^+_{\text{inner}} = \frac{1}{\kappa} \ln y^+ + B - \Delta U^+, \tag{2.5}$$

where ΔU^+ is usually known as the roughness function, and acts as an offset to the smooth-wall velocity profile. There is some complication in defining a wall-normal coordinate y over a rough surface. In order to account for the offset of the flow a virtual origin Δ_y must be defined, such that $y = \widetilde{y} - \Delta_y$, where $\widetilde{y}$ is the original wall-normal coordinate. Theoretically this virtual origin arises from the momentum loss of the surface, and is equal to the mean height of momentum absorption of the surface (Thom, 1971; Jackson, 1981). Experimentally this is generally estimated by maximising the best-of-fit of the logarithmic velocity profile above the rough surface (Raupach, Antonia, and Rajagopalan, 1991; Jiménez, 2004).

In the fully rough regime ($k_s^+ \gtrsim 70$) the roughness function is related to k_s^+ by (Nikuradse, 1933)

$$\Delta U^+ = \frac{1}{\kappa} \ln k_s^+ - 3.4. \tag{2.6}$$

This provides a particularly useful relationship between the observed offset to the inner velocity profile ΔU^+ and the inner scaled effective sand-grain roughness height k_s^+, such that any typical rough surface quantified by a roughness height k_0 can be transformed to an equivalent sand-grain roughness height by establishing the offset ΔU^+ and using the relationship (2.6). Dimensional analysis suggests that for $k_0^+ \gg 1$ a rough surface should have a sand-grain roughness height k_s proportional to the dimensions of the roughness elements, where pressure-drag over individual elements dominates over viscous drag (Jiménez, 2004). Roughness that follows this behaviour is known as $K-$ type, and is the most common form of roughness (Jiménez, 2004). $D-$type roughness, a term first established by Perry, Schofield, and Joubert (1969), does not behave in this manner, and instead has a sand-grain roughness height independent of the dimensions of the roughness elements. This seemingly contradictory behaviour occurs when roughness elements are tightly packed and shield each other from high speed fluid, as depicted in Figure 2.3. Here it can be observed that $D-$type roughness is characterised by confined regions of recirculating flow inbetween roughness elements, leading to a partial-slip surface at the roughness crest. In contrast, fluid penetrates inbetween $K-$type roughness elements, leading to large pressure forces acting on individual elements. This behaviour is well quantified by Leonardi, Orlandi, and Antonia (2007) who simulate the flow over spanwise-homogeneous square roughness elements of different spacings. They observed a strong dependence on the contributions of viscous and pressure drag acting on the roughness elements; when viscous drag is dominant the effective sand-grain roughness height k_s^+ does not scale with the size of the roughness elements i.e $D-$type. When pressure-drag dominates over viscous drag the flow can penetrate inbetween roughness elements and the $K-$type roughness regime is recovered.

As discussed, typical $K-$type roughness obtains a roughness sub-layer typically in the range $3k_s - 5k_s$; beyond this limit the flow is independent of the surface roughness. According to the Townsend (1976) hypothesis the effect of roughness on the boundary layer is limited to the inner region, as long as the ratio δ/k_0 is large. Jiménez (2004) and Flack, Schultz, and Shapiro (2005) provide support for this theory and set the lower limit at $\delta/k_0 \geq 40$. Below this value it's possible that the impact of roughness can be felt over the entire boundary layer, a phenomena known as 'blocking'. This behaviour arises from the influence of roughness on the log-layer (Jiménez, 2004). As discussed in Section 2.1

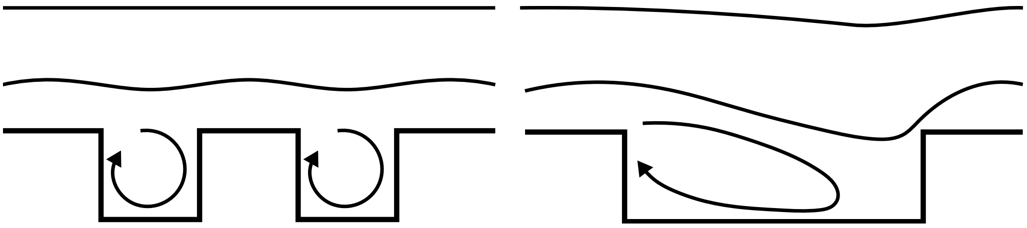

FIGURE 2.3: $D-$ (left) and $K-$ (right) type roughness. Flow from left to right.

the log-layer can account for upwards of 70 % of the total growth of streamwise mean velocity, and half of the overall production of turbulent kinetic energy (Jiménez, 2004). The blockage ratio δ/k_0 is a measure of how much the roughness influences this log-layer; if the roughness height is too large, or conversely the boundary layer too thin, then the roughness can break down a large proportion of the inner region leading to a global effect felt over the full boundary layer height. Examples of flows that operate in the high blockage ratio regime are flows through heat exchangers (Jiménez, 2004) and flows over urban canopies (Cheng and Castro, 2002). Crucially it is not enough to quantify the influence of a rough surface on the turbulent boundary layer by just a roughness Reynolds number k_0^+. Unless the boundary layer is very thick compared to the roughness height, blockage effects may also affect the flow, making it vital to report the ratio δ/k_0.

2.3 Longitudinal riblets

Surface roughness is generally detrimental to skin friction due to contributions of pressure drag on roughness elements (Leonardi, Orlandi, and Antonia, 2007) and large increases in turbulent mixing in the inner layer (Jiménez, 2004), as discussed in Section 2.2. However, this is not true of all rough surfaces. An extensive amount of work has been carried out on simplified, sharkskin-inspired, surface riblets which have been successful in reducing drag for open channel flows, closed channel flows, and when applied to aerofoils (Bixler and Bhushan, 2013). Surface riblets are generally two-dimensional, with no variation in cross section in the streamwise direction. The most popular cross sectional shapes are blade-like, sawtooth, and scalloped, although they are theorised to reduce drag in the same way. An example of blade-like riblets is presented in Figure 2.4, and when compared to the denticle samples of Figure 1.1 it is clear that the intricate details present on real shark scales are lost. Riblets are typically characterised by their spacing in wall units, $s^+ = u_{\tau 0} s/\nu$ (Dean and Bhushan, 2010), where s is the spacing between riblet tips and $u_{\tau 0}$ is a reference flat plate friction velocity, although other characteristic scalings

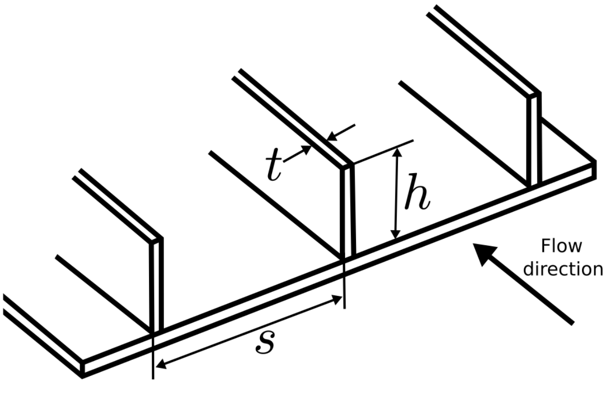

FIGURE 2.4: An example of blade-like riblets where s is the riblet spacing, h is the riblet height, and t is the width of the riblet tip.

have been suggested. For example, García-Mayoral and Jiménez (2011b) proposed a scaling based on the cross-sectional groove area, $(A_g^+)^{1/2}$ where for the blade like riblets in Figure 2.4 $A_g = sh$ where h is the riblet height. These scalings are clearly analogous to the sand-grain roughness height k_s^+, essentially a measure of how large the riblet geometry is compared to the viscous length scale. The performance of a typical ribletted surface is presented in Figure 2.5, where the difference in wall shear stress, $(\tau_w - \tau_0)/\tau_0 = \Delta\tau/\tau_0$, is plotted against the dimensionless riblet spacing, s^+, where τ_w is the wall friction for the riblets, and τ_0 is the friction for a reference smooth surface. The viscous regime exists for riblets with a spacing of $s^+ \lesssim 10 - 15$ where the drag reduction scales linearly with spacing, depending on the particular riblet geometry. For $s^+ \to 0$ one should obtain $\Delta\tau \to 0$; i.e for vanishingly small riblets τ_w should tend to the flat plate shear stress τ_0. The gradient of the linear viscous regime is given by m_s and is often used to quantify the performance of a particular type of riblet (Bechert et al., 1997).

A more robust quantification of the viscous region is provided by García-Mayoral and Jiménez (2011b): $(A_g^+)^{1/2} \lesssim 11$. For small s^+ the riblets are submerged in the viscous sub-layer. Realising this, Luchini, Manzo, and Pozzi (1991) used the two-dimensional linear Stokes equations to investigate the flow field. The performance of a particular riblet geometry was found to be related to its virtual origin, whereby the riblet surface can be represented by a flat plate whose origin lies somewhere below the riblet tips. Luchini, Manzo, and Pozzi (1991) determined that the virtual origin of spanwise flow lies deeper in the riblet than for streamwise flow. The difference between these two origins is termed the protrusion height, Δ_h. Luchini, Manzo, and Pozzi (1991) argued that the larger the protrusion height, the larger the restriction on spanwise flow that could otherwise lead to turbulent mixing above the riblets. Further to this, Luchini, Manzo, and Pozzi (1991) calculated theoretical protrusion heights for various riblet geometries, clearly linking the

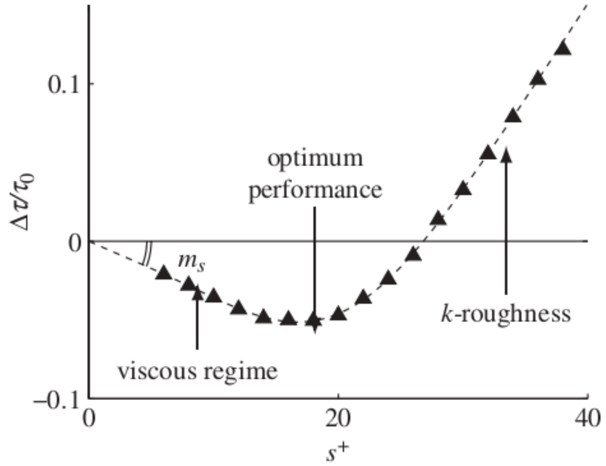

FIGURE 2.5: General structure of a drag reduction profile for a typical ribletted surface. m_s is the slope of the viscous regime. Image taken from García-Mayoral and Jiménez (2011a), originally adapted from Bechert et al. (1997).

drag reduction of the viscous region to the riblet cross section. This theory is supported by the inhibition of near-wall low speed streaks observed by Chu and Karniadakis (1993), and the study of Yang et al. (2016) who observed a reduced number of sweep and ejection events over a ribletted surface which are known to be large contributors to turbulent mixing (Pope, 2001). The Stokes flow approximation is further supported by García-Mayoral and Jiménez (2011b); through Direct Numerical Simulation (DNS) of a channel flow García-Mayoral and Jiménez (2011b) identified a stable spanwise recirculation pattern inside the riblet spacing that mimicked those of a two-dimensional linear Stokes solution.

An empirical model predicting the drag reduction of a ribletted surface in the viscous regime was derived by Bechert et al. (1997):

$$\frac{\Delta\tau}{\tau_0} = m_s s^+ = -\frac{\mu_0(\Delta_h/s)}{(2C_f)^{-1/2} + (2\kappa)^{-1}} s^+, \tag{2.7}$$

where m_s is the gradient indicated by Figure 2.5, $\mu_0 = 0.785$ is an empirical constant, $C_f = \tau_w/\frac{1}{2}\rho U_\infty^2$ is the friction coefficient, and U_∞ is the freestream velocity. The roughness function of (2.5) is related to the protrusion height by $\Delta U^+ = -\mu_0 \Delta_h^+$, such that the mean velocity profile is shifted upwards, contrary to typical rough surfaces.

The breakdown or optimum regime is obtained when the riblet spacing s^+ increases beyond $s^+ \approx 10$, where the recirculating flow identified by García-Mayoral and Jiménez (2011b) becomes increasingly unstable and asymmetric. At the breakdown region, García-Mayoral and Jiménez (2011b) identified the formation of large spanwise vortices, above the riblet tips, due to a Kelvin-Helmholtz type instability. The same vortices were identified in further simulations at a Reynolds number of $Re_\tau = \delta^+ \approx 550$ (García-Mayoral and Jiménez, 2012), and drag reduction profiles of a similar magnitude to the $Re_\tau \approx 180$ case were obtained. While not explicitly discussed, the agreement between these simulations could be partly due to the blockage ratios. The riblet geometry investigated by García-Mayoral and Jiménez (2012) was blade-like, as per Figure 2.4, with the dimensions $s = 2h$, and $s = 4t$. If it is assumed that the riblet height is an appropriate roughness length scale then the blockage ratio at $s^+ = 16$ is $\delta/h = 22.5$ at $Re_\tau = 180$. However, the blade-like riblets are only present on 25 % of the wall surface, such that their average height, $\overline{h}$, over the whole plate leads to a blockage ratio of $\delta/\overline{h} = 90$. The true roughness height will likely lie between these two values, but it seems reasonable that the blockage ratio is close to the regime $\delta/k_0 \approx 40$ such that blockage effects are minimal (Jiménez, 2004). Any increase to Re_τ will increase the separation between h and δ, thus increasing the blockage ratio further. Perhaps this partly explains why solutions at $Re_\tau \approx 180$ are so similar to $Re_\tau \approx 550$, since even at the lowest Reynolds number blockage effects are weak.

As the dimensionless riblet spacing increases beyond the optimum regime, $s^+ \gtrsim 30$, the riblets begin to interact with layers above the viscous sub-layer leading to increased turbulent mixing. Here the riblets behave like typical K-type roughness. As the riblet spacing increases, they lose their ability to constrict spanwise flow and fast moving fluid can penetrate to the base of the grooves, as observed by Lee and Lee (2001).

The riblet drag reduction profiles obtained by Bechert et al. (1997) and García-Mayoral and Jiménez (2011b) can be observed in Figure 2.6. Here the drag reduction, $DR = -\Delta\tau/\tau_0$ is normalised against the viscous slope m_s. Blade-like, scalloped and sawtooth riblets of varying dimensions are plotted in the experimental ensemble, leading to convergence to a common curve in the viscous region, with deviations occurring for $s^+ \gtrsim 15$. The DNS data of García-Mayoral and Jiménez (2011b) lies in the centre of the experimental scatter. Better collapse of the data can be obtained when normalising by $(A_g^+)^{1/2}$ as per García-Mayoral and Jiménez (2011a) (Figure 2.6. Despite some scatter due to differences in riblet geometry, Figure 2.6 demonstrates excellent agreement between the different investigative techniques; the viscous regime predicted by linear stability analysis (Luchini, Manzo, and Pozzi, 1991) is obtained for small s^+, while the experiments and DNS lead to consistent predictions of the breakdown and $K-$type roughness regimes.

In contrast, Reynolds Averaged Navier-Stokes (RANS) type methodology has seen little use for the prediction of these flows. The earliest reports of RANS simulations over riblets were from Launder and Li (1993) and Djenidi and Antonia (1993), who both adopted Low Reynolds number $k-\varepsilon$ turbulence closures. Launder and Li (1993) investigated the flow over several riblet configurations; idealised (zero-thickness) L-shaped (blade-like) riblets, V-grooved (sawtooth) and a U-type riblet. The predicted behaviour of the zero-thickness riblets were similar to the drag reduction regimes described previously; a linear region was obtained for small inner scaled riblet heights h^+ (an equivalent

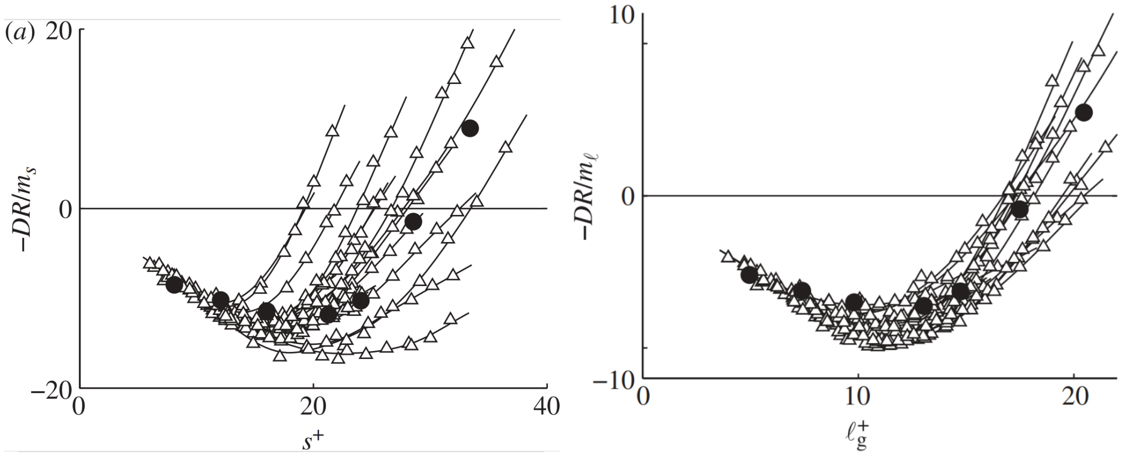

FIGURE 2.6: Drag reduction of different riblet geometries as a function of the inner-scaled riblet spacing s^+ (left) and inner-scaled square-root of the cross-sectional groove area $l_g^+ = (A_g^+)^{1/2}$ (right). Drag reduction is normalised by respective viscous slopes, m_s and m_l. Data are (△) experimental data of Bechert et al. (1997), and (●) DNS data for blade-like riblets from García-Mayoral and Jiménez (2011b). Image taken from García-Mayoral and Jiménez (2011a).

.

scale to s^+), where the drag reduction behaves like equation (2.7), a break-down regime follows where an inflection point is reached, and then drag slowly increased like $K-$type roughness. While the trends are consistent with experiments and DNS the values of the optimum h^+ were four times larger than those observed in experiments, and the drag reduction was overpredicted by greater than 20 % for a channel bulk Reynolds number of $Re_b = U_b\delta/\nu = 50000$ and $s/h = 1$, where U_b is the channel bulk velocity. When extending the problem to finite-thickness riblets different behaviour emerged; while levels of drag reduction were similar to those of experiments, the critical values of h^+ were always over predicted. In addition to this the RANS model predicted *increased* drag for $s^+ \lesssim 10$, rather than a linear decrease as per equation (2.7). This lack of a linear regime was also predicted by the RANS predictions of Djenidi and Antonia (1993). This is a particularly concerning solution, given that one would expect to converge to a flat plate solution, i.e $\Delta\tau/\tau_0 = 1$, for vanishingly small riblets: $h^+ \to 0$.

These result are perhaps unsurprising; both Launder and Li (1993) and Djenidi and Antonia (1993) adopted Low Reynolds number $k - \varepsilon$ turbulence closures that could not account for near-wall anisotropy. They assumed the Reynolds stresses could be adequately represented by a scalar eddy viscosity, ν_t, which was damped towards its near-wall asymptotic solution using functions based on the local turbulent Reynolds number, and in the case of the model of Chien (1982) adopted by Djenidi and Antonia (1993) also wall distance and friction velocity, which are difficult to calculate for ribletted geometries.

In contrast, the simulations of Benhalilou and Kasagi (1999) were more successful. In particular, when accounting for anisotropy of ν_t through the algebraic closure of Myong and Kasagi (1990) secondary flows near the riblet tips were revealed, which have been identified through DNS (Choi, Moin, and Kim, 1993) and Particle Image Velocimetry (PIV) (Suzuki and Kasagi, 1994). This additional algebraic closure led to similar levels of drag reduction as Walsh (1982) for sawtooth riblets, and good agreement with experimental data concerning the optimum s^+. However, the simulations of Benhalilou and Kasagi (1999) did not obtain convincing behaviour concerning the viscous regime of the riblets. For the case where $s = h$ the anisotropic $k - \varepsilon$ model obtained no difference in C_f until $s^+ \approx 8$, after which drag decreased. This is in contrast to the viscous behaviour identified by Bechert et al. (1997) and later García-Mayoral and Jiménez (2011a), where drag reduction should scale linearly with the protrusion height as per (2.7), asymptotically reducing to zero as s^+ decreases. While Benhalilou and Kasagi (1999) obtained much better predictions than other attempts using two-equation models there is still some non-physical behaviour that has yet to be properly predicted by these simple RANS models.

Djenidi and Antonia (1995) took a different approach by adopting the Reynolds stress closure with Low Reynolds number approximations developed by Launder and Shima (1989). This model provides a fuller description of the effect of turbulence by solving transport equations for individual components of the Reynolds stress tensor, rather than through some algebraic closure. Naturally these models can resolve anisotropic flows,

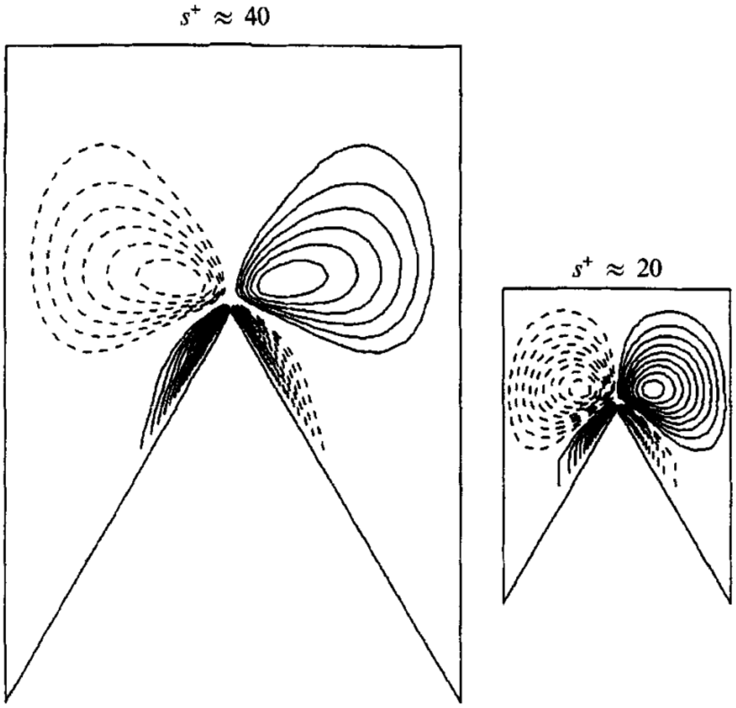

FIGURE 2.7: The secondary flow of Choi, Moin, and Kim (1993), obtained through DNS of the flow over triangular riblets with a 60° ridge angle. Contours are vorticity $\Omega_x \delta / U_c$. Contour lines represent increments of 0.04 for $s^+ = 40$ and 0.02 for $s^+ = 20$. Values of $\Omega_x \delta / U_c$ at the vortex centres are 0.36 for $s^+ \approx 40$ and 0.19 for $s^+ \approx 20$. Negative contours are dashed.

with a trade off of increased computing costs and numerical stiffness. Djenidi and Antonia (1995) solved for a developing flow over sawtooth riblets and obtained a maximum drag reduction of approximately 1 %, as opposed to ≈3.5 % obtained by the experiments of Bechert et al. (1997) for the same riblets. Unfortunately only four data points were provided for comparisons against literature drag reduction, and so conclusions concerning the success of the model are limited. What is clear from the most successful attempts at modelling riblet flows using RANS methodology is that accounting for anisotropy is essential if reasonable predictions are to be obtained.

Secondary flows over longitudinal roughness

An interesting feature of the flow over riblets is the generation of a secondary flow close to the riblet tips, whereby streamwise-aligned vortices are generated with upward flow at the riblet tips and downward flow at the riblet valley. This can be observed in Figure 2.7, which shows the streamwise vorticity Ω_x scaled by outer variables, δ and the channel centreline mean velocity U_c (Note that the DNS of Choi, Moin, and Kim (1993) was carried out on an asymmetric channel flow with riblets on one wall). These secondary flows have mainly been observed using DNS (e.g. Choi, Moin, and Kim, 1993; Chu and Karniadakis, 1993; Goldstein and Tuan, 1998), but there have been reports of these flows in experiments (e.g. Suzuki and Kasagi, 1994). It should be noted that these streamwise-aligned secondary flow structures are a time-averaged phenomenon, as opposed to the instantaneous Kelvin-Helmholtz spanwise vortices observed by García-Mayoral and Jiménez (2011b) that appear in the breakdown regime. The mechanisms that generate and sustain streamwise secondary flows have seen little investigation. Goldstein and Tuan (1998) carried out the first and only study to attempt to quantify how secondary flows are generated at the riblet tips and how they influence the drag acting on the wall surface. Goldstein and Tuan (1998) found that secondary flows are near negligible for closely spaced riblets (small s^+) in the drag reducing regime, and only appear when the riblet spacing is large, i.e in the breakdown and drag-increasing regimes (Figure 2.5). It was hypothesised that the generation of secondary flows was linked to the poor performance of riblets at large s^+, by enhancing turbulent mixing near the wall. Goldstein and Tuan (1998) argued that instantaneous spanwise fluctuations were responsible for the generation of secondary flows, whereby the riblet tips act to deflect spanwise flow upwards, leading to the formation of vortices shed on the leeward side of the riblet tips (Goldstein and Tuan, 1998). These vortices lead to a time-averaged vortex pattern with upward flow at the riblet tips and downward flow at the valleys. It was further hypothesised that when riblets are small with respect to the viscous length scale (small s^+) the spanwise flow is constricted by the riblets and vorticity generation is suppressed. Only when the riblet spacing increases do the secondary flows emerge, acting to break down the drag reducing regime. This theory was tested by subjecting an isolated riblet to a spanwise-oscillating flow, with no streamwise forcing (Goldstein and Tuan, 1998). The resulting time-averaged flow pattern was indeed similar to the secondary flows observed in turbulent boundary layer flows over riblets.

However, the secondary flow pattern of Figure 2.7 has also been observed in RANS predictions (Benhalilou and Kasagi, 1999); it is not entirely obvious how a steady-state RANS simulation is capable of capturing this secondary flow mechanism if it is reliant on instantaneous flow deflections. Perhaps an explanation can be provided by investigating the classifications of secondary flows defined by Prandtl (1953). There are two common types of secondary flow - skew induced and turbulent-stress induced; these form secondary flows of the first and second kind, respectively (Prandtl, 1953). Skew induced vorticity typically requires streamwise curvature. Goldstein and Tuan (1998) provided strong evidence that skew-induced vorticity is either negligible or identically zero for fully developed flow over streamwise-aligned riblets. Goldstein and Tuan (1998) also argued that there was not sufficient evidence that the second kind of secondary flows were responsible for the observed vorticity, although budgets of the transport of turbulent kinetic energy and streamwise vorticity were not presented, which have often been instrumental in quantifying this type of secondary flow (e.g. Huser and Biringen, 1993; Anderson et al., 2015; Hwang and Lee, 2018). Perhaps then a dismissal of the second type of secondary flow was premature. Goldstein and Tuan (1998) attribute secondary flow to spanwise-blocking of the instantaneous velocity fluctuations at the riblet tip, a mechanism that could be thought of as analogous to the kinematic blocking that occurs in the presence of no-slip and free-slip surfaces (Yokojima and Shima, 2010), as discussed in Section 2.1. Local to the riblet surface kinematic blocking will effect both spanwise and vertical directions, due to the two-dimensionality of the riblet cross section. Perhaps then this change in distribution of the Reynolds stresses could lead to the stress-induced vorticity observed by Goldstein and Tuan (1998). It therefore seems plausible that the instantaneous flow mechanism hypothesised by Goldstein and Tuan (1998) may be equivalently explained by the second law of secondary flows (Prandtl, 1953). This may explain why Benhalilou and Kasagi (1999) observed the same vorticity field using RANS simulations with anisotropic eddy-viscosity closures.

There are still open questions regarding the presence of the vorticity field. Goldstein and Tuan (1998) suggest that the secondary flow is negligible for small s^+, but what quantifies how small s^+ must be for vorticity to play no role? And what happens as the riblet spacing continues to grow? The hypothesis of Goldstein and Tuan (1998) suggests that vorticity may continue to grow indefinitely since the riblet tips become more exposed to high speed spanwise flow, but this behaviour has not yet been investigated. In addition, the vorticity contours of Figure 2.7 indicate that the size of the secondary flow relative to the riblet tip is near identical for $s^+ = 20$ and $s^+ = 40$, while the strength of the vorticity is approximately halved for $s^+ = 20$. It seems then that while the strength of the vorticity field may decrease with s^+ as implied by Goldstein and Tuan (1998), the secondary flow may still be present, even for very small s^+.

Some insight could be gained by investigating other types of roughness-induced secondary flow. Recently, significant research has been carried out in order to quantify the large-scale secondary flows induced by spanwise-heterogeneous roughness (Willingham et al., 2014; Anderson et al., 2015; Vanderwel and Ganapathisubramani, 2015; Hwang and Lee, 2018; Medjnoun, Vanderwel, and Ganapathisubramani, 2018; Vanderwel et al., 2019). While similar to the riblets discussed so far, the spanwise-heterogeneous roughness discussed here is significantly larger, operating in the fully rough regime ($k_0^+ \gtrsim 70$) and with spacings between roughness elements of the same order as the boundary layer thickness. An example of the secondary flows introduced by large-scale spanwise-heterogeneous roughness is presented in Figure 2.8. Here large secondary structures can be observed that lead to spanwise inhomogeneities in the streamwise velocity field far from the riblet surface. Vanderwel and Ganapathisubramani (2015) found that the size of these structures increases as the spacing between elements, S, increases, until $S \approx \delta$. for $S \gtrsim \delta$ the secondary flows stop growing and tertiary flows form inbetween roughness elements. The upper bound for the size of these secondary flows is therefore determined by the boundary layer height (Vanderwel and Ganapathisubramani, 2015). While the size of the secondary flow region scales with S, the strength of the secondary flow is dependent on the aspect ratio of the roughness element (Hwang and Lee, 2018). Wide

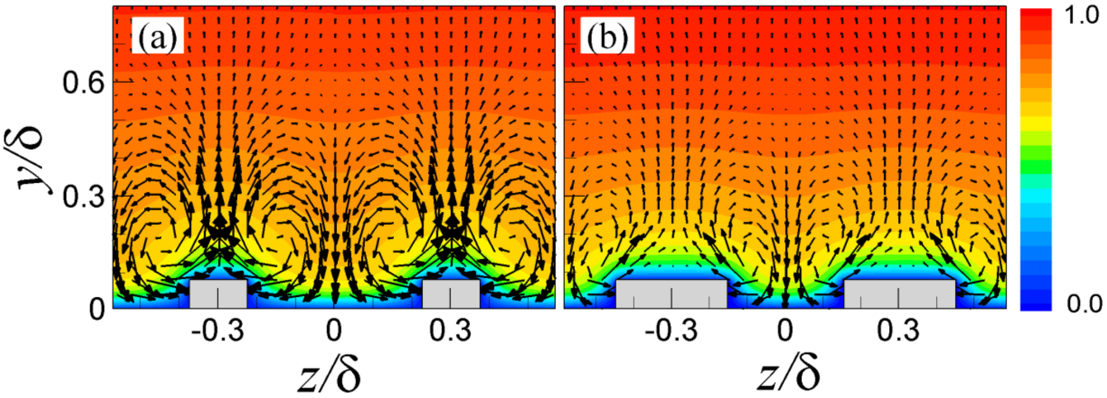

FIGURE 2.8: Secondary flows induced by large scale spanwise-heterogeneous roughness of different aspect ratios. Contours are mean streamwise velocity normalised by freestream velocity. Figure adapted from Hwang and Lee (2018).

roughness elements lead to stronger secondary flows at the element edges with tertiary flows present above the centre of the roughness element.

The form of the secondary flows induced by large-scale heterogeneous roughness appears consistent with those that form over riblets (Figure 2.7). Flow is deflected upwards at the element edges, and downwards at the valley between elements. The main difference between the two cases is the size of the secondary flow, which is confined to the roughness sub-layer for riblets.

The $\delta-$scale secondary flows have a substantial effect on the outer flow, whereby fluid is channelled through high and low momentum pathways; HMP and LMP, respectively (Mejia-Alvarez and Christensen, 2013). These exist at the regions between counter-rotating vortices, where HMPs occur in regions of downward secondary flow, acting to transport high momentum fluid towards the wall, and LMPs occur in regions of upward flow, transporting near-wall low momentum fluid into the outer regions of the boundary layer (Willingham et al., 2014; Anderson et al., 2015; Vanderwel and Ganapathisubramani, 2015; Hwang and Lee, 2018; Medjnoun, Vanderwel, and Ganapathisubramani, 2018; Vanderwel et al., 2019). These have also been observed for complex multi-scale roughness (Mejia-Alvarez and Christensen, 2013; Barros and Christensen, 2014).

Some recent insight into the mechanisms that drive these secondary flows has been gained through investigations of the turbulent kinetic energy and streamwise vorticity budgets (Anderson et al., 2015; Hwang and Lee, 2018). Anderson et al. (2015) adopted Large Eddy Simulation (LES) to investigate the flow over a strip-type roughness, whereby the effects of a physical rough surface were inferred through the boundary conditions of a flat surface. Anderson et al. (2015) recognised that the vertical flow must be driven by an imbalance in the transport of turbulent kinetic energy, such that vertical and spanwise velocities are generated to convect k in regions of local imbalance. It was hypothesised that the dominant balance required for this to hold was between production and destruction of turbulent kinetic energy, since viscous and turbulent transport terms are negligible far from the wall. The regions where production exceeded destruction the greatest, i.e regions of higher shear stress associated with larger roughness heights, necessitated negative convective vertical velocities in order for the transport of k to balance. This was supported by numerical data which showed that the regions where production of k was greatest corresponded to the spanwise locations of HMPs. Note that these simulations led to HMPs (*downward* convective flow) above the regions of high roughness, in contrast to that in Figure 2.8. Anderson et al. (2015) also investigated budgets of streamwise vorticity, showing that the secondary flows are generated through gradients of the Reynolds stresses, which were balanced by convection. This suggests the secondary flow is driven and sustained by turbulence and is therefore of the second kind (Prandtl, 1953). However, while the analysis provided reasonable explanations as to how secondary flows arise and how they interact with the HMPs and LMPs, accurate calculation of the budgets of k and Ω_x transport equations were not presented.

In contrast, Hwang and Lee (2018) adopted DNS to simulate the flow over resolved spanwise-heterogeneous rough surfaces. The resulting secondary flows can be observed in Figure 2.8, with LMPs (upward flow) above the roughness elements. This is in agreement with riblet-induced secondary flows (e.g. Choi, Moin, and Kim, 1993; Goldstein and Tuan, 1998) and experiments on $\delta-$scale heterogeneous roughness Vanderwel and Ganapathisubramani (2015) and Vanderwel et al. (2019), but not with the LES of Anderson et al. (2015). Hwang and Lee (2018) calculated all budgets of the transport of turbulent kinetic energy and showed that the balance between production and destruction of k could not explain the mechanisms driving the secondary flow. In order to balance the transport of k, the transport terms neglected by Anderson et al. (2015) were also required, and found to be large in the vicinity of the roughness, due to high spatial gradients. Differences between the LES of Anderson et al. (2015) and the DNS of Hwang and Lee (2018) were attributed to the different techniques of modelling the rough boundary; the strip-type roughness patches of Anderson et al. (2015), treated through the boundary conditions of a flat surface, could not produce the strong near-wall gradients that emerged from the sharp corners of the resolved rough surfaces of Hwang and Lee (2018). Not only did the resolved rough surfaces influence the budgets of k, but it also led to a reversal of the secondary flow direction, such that upward flow was associated with the location of the roughness elements. The driving mechanisms that led to the secondary flow were still hypothesised to be of the second kind (Hwang and Lee, 2018), but the reversal of the flow direction could not be explained without the theory of Goldstein and Tuan (1998), where it was thought that blockage of the instantaneous spanwise flow led to the time-averaged secondary flow structures. Unfortunately budgets of streamwise vorticity were omitted from the analysis of Hwang and Lee (2018), which may have provided further insight into the generation of secondary flows.

Summary

The drag reducing behaviour of riblets has been investigated considerably over the last few decades. Riblets have been reported to reduce skin friction by up to 10 % (Bechert et al., 1997), mechanisms of which have been readily explained by linear stability analysis (Luchini, Manzo, and Pozzi, 1991), experiments (Bechert et al., 1997) and DNS (García-Mayoral and Jiménez, 2011b). However, RANS models have seen little use for these flows and their predictions for these flows have led to poor agreement with experiments and DNS. Isotropic eddy-viscosity models lead to especially poor predictions of the viscous regime where riblets are small, often leading to non-physical solutions (Launder and Li, 1993). Better predictions can be obtained when adopting anisotropic models, such as the algebraic closure used by Benhalilou and Kasagi (1999), but these have been used little for the study of boundary layers over ribletted surfaces.

A topic that has seen little investigation is the secondary flow features close to the riblet tips, where upward flow is found at the riblet tips and downward flow above the riblet valleys. Goldstein and Tuan (1998) hypothesised that the riblet tips act to block spanwise instantaneous fluctuations which are subsequently deflected upwards, leading to the formation of time-averaged secondary flows. However, these features have also been observed in steady-state RANS predictions (Benhalilou and Kasagi, 1999) which do not resolve instantaneous flows. It is also unclear how these structures scale with the riblet dimensions; Goldstein and Tuan (1998) suggested that secondary flows are negligible for small s^+ but Choi, Moin, and Kim (1993) showed that they are present and of the same size for $s^+ \approx 20$ as for $s^+ \approx 40$, albeit with a smaller vorticity magnitude. It is unclear how small must riblets be for vorticity to vanish. It is also unclear how secondary flows scale at large s^+; do they continue to grow in strength as s^+ increases?

Further investigation of roughness-induced secondary flows have provided some insight into how they may be generated. Large scale spanwise-heterogeneous roughness has seen significant interest in recent years, differing from riblets primarily by their differences in length scale. While riblets are more similar in size to viscous length scales δ_ν, large scale spanwise-heterogeneous roughness have spacings similar to that of the boundary layer thickness. For these large scale roughnesses the secondary flows are thought to be of the second kind (Prandtl, 1953); i.e generated through gradients of the Reynolds stresses. This has been shown through calculation of the budgets of turbulent kinetic energy and streamwise vorticity by Anderson et al. (2015) and Hwang and Lee (2018). Perhaps then these mechanisms are consistent for riblets, despite the large differences in length scale. If RANS models can be validated for flows over riblets, they could prove a useful technique for analysing the generation of secondary flows, and how they scale with riblet dimensions.

2.4 The hydrodynamics of shark skin denticles

Shark skin is comprised of small tooth-like dermal denticles which protrude from a flexible epidermis. There are three theorised functions that denticles provide; hydrodynamic, resistance to abrasion, and defence against parasites (Reif, 1985; Fletcher et al., 2014). An extensive range of denticles were documented by Reif (1985), highlighting the differences between shark species and the location of scales on the fishes. The study also indicates the complex features of real shark scales such as three dimensionality beneath the exposed scale, overlapping, diverging and converging riblets, variable angles of incidence, and the aerofoil-like shape of each scale with a smooth leading edge and a sharp trailing edge. These features can be observed in Figure 2.9; even when considering just one species the scales can vary significantly when moving from the head to the tail. Despite such variability, all previous studies investigating the drag reduction of shark scales have used $s^+ = u_\tau s/\nu$ as an appropriate roughness Reynolds number, if one has been given. This one parameter is of course not enough to capture variability between different denticles, especially since some denticles do not possess riblets on their crowns. A feature of denticles not shown in Figure 2.9 is the flexible epidermis in which they are embedded; it has been shown experimentally that mako shark denticles are capable of bristling under the influence of local back-flow, whereby their angle of attack is increased and their trailing edge lifts further into the boundary layer enhancing turbulent mixing and providing

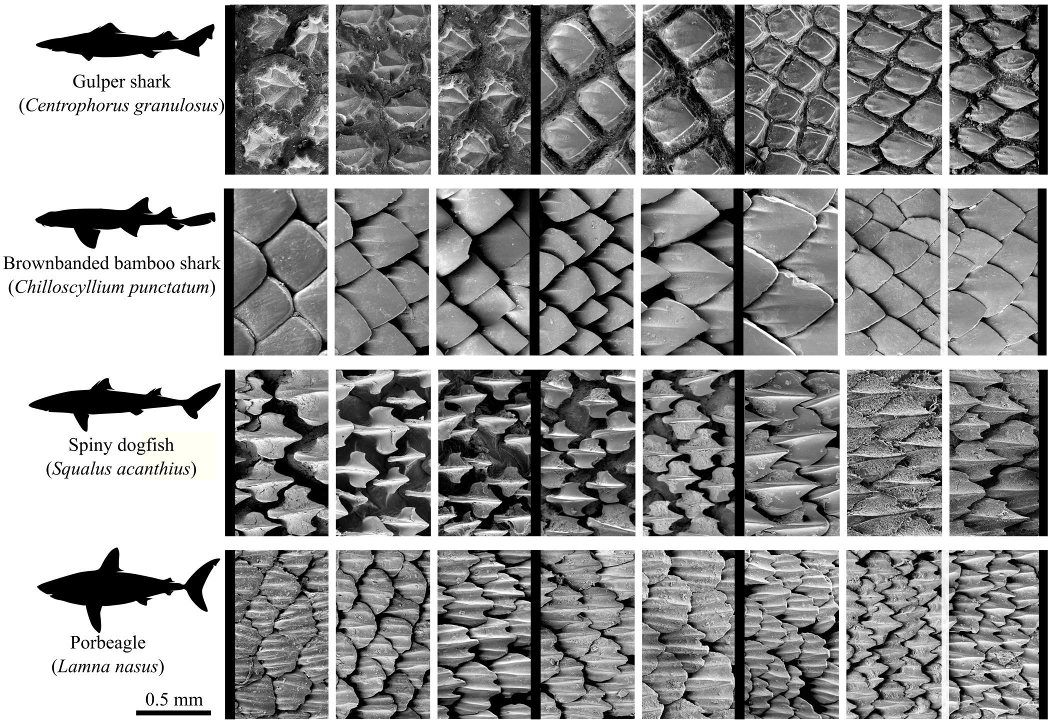

FIGURE 2.9: Scanning Electron Microscope (SEM) images of shark skin denticles taken from the flank along a central line from head to tail (left to right). Image adapted from Fletcher (2015).

resistance to flow separation (Lang et al., 2014). The vast range of these features, and the variability between species, results in little understanding as to why many of these features exist.

2.4.1 Shark skin subject to the canonical boundary layer

This section investigates the numerical and experimental studies on the fluid dynamics of shark skin surfaces when subject to flat plate boundary layers and channel flows. As discussed in Section 2.3 comparable studies on riblets lead to robust results, with drag reduction profiles agreeing for all typical families of longitudinal riblets (sawtooth, blade-like, etc.) when scaled by an appropriate roughness Reynolds number (See Figure 2.6). The same cannot be said for experimental and numerical data on shark skin denticles, despite the techniques adopted being reasonably similar.

Experimental studies

Alongside work on longitudinal riblets, Bechert, Hoppe, and Reif (1985) also investigated the drag reduction of plastic shark skin denticle replicas, manufactured using a combined printing/casting technique. Denticles were enlarged by a factor of 5, equating to a denticle length of 1.3 mm. The drag force acting on a large array of replicated mako denticles was measured in a wind tunnel using a force balance at two bristling angles; 5 % and 10 %, along with an array of silky shark denticles. None of the three configurations reduced drag, despite s^+ values falling in the expected drag reducing regime of longitudinal riblets. A significant increase to the drag force was observed when the angle of attack was increased from 5 % to 10 %. However, the authors noted that their replication process was unable to capture some of the intricate details that exist on real denticles, such as features beneath the denticle crowns.

The same group carried out further investigations on shark skin denticle surfaces using an oil channel (Bechert et al., 2000). In this case the manufacturing technique was improved and replica hammerhead denticles were fabricated at a length of 19 mm, 100 times larger than those found in nature. The oil viscosity was 100 times larger than that of water, leading to a similar possible range in s^+ as equivalent longitudinal riblet experiments. Denticles were mounted to thin anchors which could control the angle of attack of the denticles. The stiffness of the anchors could be adjusted; at high stiffness the denticles were essentially fixed in place at a given angle of attack. When soft, the denticles angles were allowed to adjust depending on local flow conditions. The difference in wall shear stress obtained by Bechert et al. (2000) using a force balance is presented in Figure 2.10. When the denticles were flat (scales aligned in Figure 2.10) they were tightly packed, essentially mimicking a ribletted surface. A modest 3 % reduction in drag was measured, and the dependence on s^+ was similar to that of riblets (Figure 2.5). While not fully captured the region $s^+ \rightarrow 0$ seems to reduce to the linear viscous regime as per longitudinal riblets. However, when the denticles were set to a larger angle of attack using the adjustable-stiffness anchors drag increased significantly, for both soft and hard spring regimes.

The experiments of Bechert, Hoppe, and Reif (1985) and Bechert et al. (2000) suggest that the three-dimensionality of denticles is detrimental to flat plate drag; drag is only reduced when denticles are tightly packed and essentially resemble a ribletted plate. Bechert, Hoppe, and Reif (1985) and Bechert et al. (2000) concluded that hydrodynamic advantages of denticles are reserved for more complex flow conditions, such as boundary layer separation. However, there have also been experiments with contrary results. Comparable studies by Wen, Weaver, and Lauder (2014), Wen et al. (2015) and Domel et al. (2018) were carried out in a water flume, using mako scales 3D printed at a width of 1.6 mm, 12.4 times the size of the original mako scales. Drag was directly measured using a force balance and the profiles of Figure 2.11 were obtained. In this case, the difference in drag was quantified by D_s/D_m rather than $\Delta\tau/\tau_0$, where D_s and D_m are the drag forces acting on the scales and the reference flat plate respectively. There are significant differences between the results of Wen, Weaver, and Lauder (2014) and Bechert et al. (2000). Firstly, the viscous regime, if present, is difficult to distinguish. If it exists then it has been shifted to significantly lower values of s^+ than the data of Bechert et al. (2000), in Figure 2.10. In addition to this, the entire drag reduction regime of the denticles has been shifted to much lower values of s^+ than those of Bechert et al. (2000) and comparable longitudinal riblet studies. It should be noted that the 3D printed denticles of Wen, Weaver, and Lauder (2014) were not closely packed like those of Bechert et al. (2000), and yet reduced drag more so, which is in contrast to the conclusions of Bechert et al. (2000) who suggested that shark skin denticles only reduce drag when they resemble a ribletted

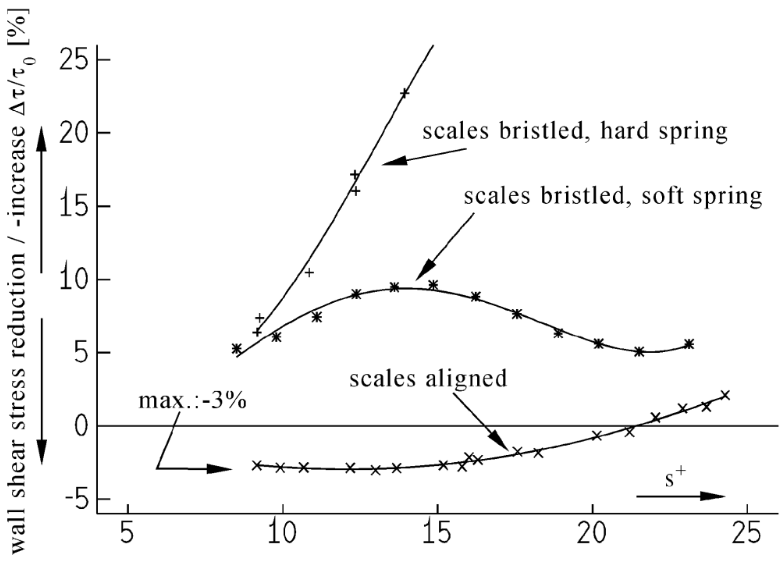

FIGURE 2.10: Drag reduction of hammerhead denticles at three bristling angles. Image taken from Bechert et al. (2000).

surface.

The original experiments of Wen, Weaver, and Lauder (2014) were extended by Wen et al. (2015) who investigated the effects of different denticle arrangements. Aligned and overlapping denticles were compared against staggered and overlapping and aligned non-overlapping regimes. A drag reduction of approximately 3 % for $s^+ \lesssim 8$ was observed for the staggered-overlapping case, while drag was increased for the other two arrangements, consistent with previous arguments that tightly packed denticles reduce drag more than loosely packed. More recently Domel et al. (2018) used the same facilities to investigate the effects of mako shark denticle size; the smallest denticles, printed at a 2.1 mm length (approximately 10 times magnified), reduced drag by up to 30 %, while the larger denticles printed at lengths of 3.15 mm and 4.2 mm increased drag relative to the flat plate.

Differences between the experiments of Bechert et al. (2000) and Wen, Weaver, and Lauder (2014), Wen et al. (2015) and Domel et al. (2018), could be attributed to the choice of length scale. While s^+ is a reasonable choice for quantifying 2D riblets there are many possible length scales that could better represent an array of sharkskin denticles. s^+ cannot provide information regarding the spacing between individual denticles, their staggered/aligned formation, their width, length, or height. Interestingly there has been no attempt to determine a more appropriate length scale, and many studies do not even quantify a roughness Reynolds number (e.g. Zhang et al., 2011b; Chen et al., 2014; Fletcher, 2015; Domel et al., 2018). This makes comparisons between the different data sets difficult.

3D printing was also adopted by Fletcher (2015) who fabricated arrays of shark skin denticles from several species of sharks. Unlike any other previous work Fletcher et al. (2014) included smooth denticles as well as ribletted. The denticle arrays were mounted to a flat plate and fixed in a water flume. Laser Doppler Anemometry (LDA) was adopted

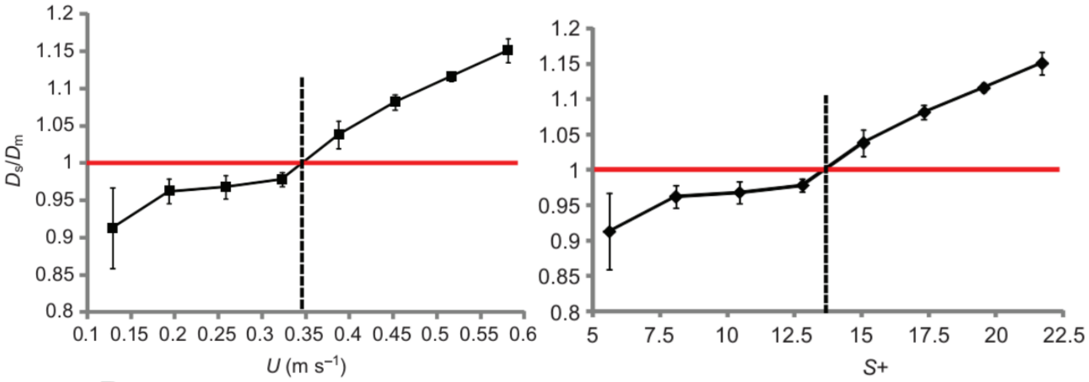

FIGURE 2.11: The drag reduction of 3D printed mako denticles as a function of bulk velocity (left) and dimensionless riblet spacing (right). Image taken from Wen, Weaver, and Lauder (2014).

to measure the fluid velocity in the developing boundary layer over the denticles, and compared against a reference flat plate. The method of Clauser (1956) was adopted in order to determine the coefficient of friction, an indirect technique that estimates the friction velocity based on a best-of-fit to the log-law (2.5). Variations of this technique have been successfully adopted by many experimentalists (e.g. Perry and Li, 1990; Schultz and Flack, 2003; Squire et al., 2016). However, Fletcher (2015) provided little detail on the accuracy of the technique; details such as precision/repeatability errors were not reported, Reynolds numbers were not calculated (which are vital for assessing the extent of the log-law region), and the method of estimating the wall-position was based on identifying the LDA measurement volume position at which the mean velocity dropped below an arbitrarily small value. The wall-position is known to have substantial influence on the scaling of the boundary layer and therefore the friction velocity if using indirect techniques for its measurement (Örlü, Fransson, and Alfredsson, 2010). Fletcher (2015) obtained substantial drag reduction of over 50 % for an array of replica *Lophosteus* denticles. However, no comparisons were made against other literature data, even for the reference flat plate.

Chen et al. (2014) investigated the effects of ribletted shark skin on skin friction by creating precise moulds from large samples of a fast-swimming *Carcharhinus brachyurous* (copper) shark. Replication errors were less than 2.6 % when comparing the surface of the replica compared to the original sample, but dimensions were only taken on the exposed shark skin surface. This moulding technique is unlikely to capture geometrical features below the crown-surface, making it only suitable for tightly packed and overlapping denticle arrays, a disadvantage not mentioned by the authors. This fabrication technique also captures imperfections, asymmetries, and changes in denticle geometry that exist on real shark scale arrays. Clearly this model is more physical, but isolating the effects of slight geometric changes between the different denticles is impossible without flow measurements local to individual denticles. With a global force balance Chen et al. (2014) observed consistently lower drag for their shark skin surface when compared to longitudinal riblets. At a maximum the longitudinal riblets reduced drag by 8 %, in agreement with the data of Bechert et al. (1997), while the replica shark skin reduced drag by a maximum of 12 %, although no attempt was made to quantify dimensionless parameters such as bulk flow Reynolds numbers or s^+. Despite this, the drag reduction behaviour appears reasonable, whereby the drag reduction increased to a maximum as the flow velocity increased which then decreased as the flow velocity increased further, indicative of passing through the breakdown regime that is observed for riblets (Bechert et al., 1997).

A similar experimental technique was adopted by Zhao et al. (2012), although the results differed significantly. Their replica shark skin, based on an unspecified shark species skin sample, reduced drag by a maximum of 18.6 % which occurred at the lowest flow rate tested. This then decreased to a minimum of 9.7 % at the highest flow rate tested, but like Chen et al. (2014) no attempt was made to quantify dimensionless parameters that could allow comparisons to other literature data.

Zhang et al. (2011b) adopted the same experimental techniques on a *Isurus oxyrinchus* (shortfin mako) sample. Drag reduction was compared to a ribletted surface, a shark skin replica, and a shark skin replica with non-long polymer chains attached to the surface. The polymer surface was introduced as a method to mimic the mucus excretion of sharks. Small fishes are known to rely on mucus excretion to increase burst swimming speeds; when added to a fluid this mucus can reduce drag by up to 66 % (Rosen and Cornford, 1971). However, unlike most fishes, sharks mucus production is restricted to small areas beneath the denticle crowns. It is therefore often assumed that mucus excretion has a lesser effect for sharks, although the topic is still poorly understood (Bechert, Hoppe, and Reif, 1985; Fletcher, 2015). Zhang et al. (2011b) measured a maximum drag reduction of 8 % for the sharkskin replica which increased to 24 % when the polymer was added. In addition to this, the drag reduction effect increased with increasing flow rate, contrary to the sharkskin without polymer added to its surface. However, Zhang et al. (2011b) applied the polymer coating to the whole surface, which was perhaps not a physical representation of mucus excretion. In addition, no comparisons were made to other data sets, and flow conditions such as the bulk flow Reynolds numbers and s^+ were not presented.

Zhang et al. (2011a) adopted the same experimental techniques as Zhang et al. (2011b) and obtained a maximum drag reduction of 12.8 % at the slowest flow rate, which reduced to a value of $\sim$9 % at the highest flow rate. This behaviour is similar to that of the non-polymer covered sharkskin of Zhang et al. (2011b), although the magnitude of drag reduction is consistently $\sim$3 % higher. Like Zhang et al. (2011b) appropriate Reynolds numbers and s^+ are not reported.

A consistent theme of all previous fluid dynamic experiments on shark skin is the sole use of force balances to quantify global effects of shark scales, with the exception of Fletcher (2015). Perhaps differences between these experiments could be explained if flow field data were available, but as of yet the influence of shark scale geometry on boundary layer dynamics has not been experimentally measured.

Numerical studies

The denticles of Wen, Weaver, and Lauder (2014) have also been used by Boomsma and Sotiropoulos (2016), who performed Direct Numerical Simulation (DNS) to investigate the flow near staggered and aligned denticles. The complexities associated with creating boundary-fitted meshes over the shark skin surface were avoided by adopting an immersed boundary method, where the effect of the denticle surface was treated as a body force in the Navier-Stokes equations which were discretised over a uniform background grid. Periodic boundary conditions were adopted to simulate a fully developed channel flow at a Reynolds number of $Re_\tau = 180$ and a riblet spacing of $s^+ = 16$. A longitudinal riblet case was also simulated for comparison. The riblet surface behaved as expected; a drag reduction of approximately 5 % was obtained, arising from a reduction of the Reynolds stresses when normalised against the reference flat plate friction velocity. In contrast, the denticles were found to induce separation and large vortices near the scale surface, leading to pressure drag and increased turbulent mixing. The results were validated against those of Bechert, Hoppe, and Reif (1985) but significantly overpredicted the drag compared to Wen, Weaver, and Lauder (2014), despite the shark scales being identical. Boomsma and Sotiropoulos (2016) argued that this was due to the different experimental conditions of Wen, Weaver, and Lauder (2014) and Bechert, Hoppe, and Reif (1985). The denticles of Wen, Weaver, and Lauder (2014) were exposed to a developing boundary layer flow rather than a fully developed channel flow, and the laboratory Reynolds number was much greater than that of the simulations (although Re_τ is not explicitly given by Wen, Weaver, and Lauder (2014), given that the boundary layer thickness is not measured). However, it was readily admitted that the replication process of the denticles adopted by Bechert, Hoppe, and Reif (1985) led to a poor capture of the denticle geometry and subsequently there were no gaps inbetween the denticles of Bechert, Hoppe, and Reif (1985), unlike the arrays of Wen, Weaver, and Lauder (2014) and Boomsma and Sotiropoulos (2016).

Perhaps differences can be explained by the blockage ratio δ/k_0 of the simulations. While García-Mayoral and Jiménez (2012) concluded that simulations of ribletted channels at $Re_\tau \approx 180$ were similar to those at $Re_\tau \approx 550$, the blockage ratios were either close to or greater than the limit $\delta/k_0 = 40$ as specified by Jiménez (2004) and discussed in Section 2.3. However, if it is assumed that the roughness height k_0 is similar to the denticle height then the simulations of Boomsma and Sotiropoulos (2016) lead to a ratio of $\delta/D_h \approx 8.2$, assuming $\delta^+ = 180$ and the denticle height is $D_h^+ = 1.37s^+$ as specified by Boomsma and Sotiropoulos (2016). The roughness height k_0 would have to be significantly smaller than denticle height to get close to the limit $\delta/k_0 > 40$, as required to ensure blocking effects are negligible (Jiménez, 2004). The large denticle height compared to the channel half-height could influence the drag force due to blocking, and ultimately increase drag relative to the flat plate. However, increasing Re_τ, and therefore δ/D_h is no trivial task. The simulations of Boomsma and Sotiropoulos (2016) required over 100 M computational points in order to adequately resolve the denticle geometry. In order to increase the Reynolds number the relative size of the denticles would have to reduce significantly in order to maintain a width of $s^+ \approx 16$, subsequently requiring many more denticles in order to cover the same channel domain size, which would of course require much finer grids. The advantage of immersed boundary methods is that uniform grids can be adopted, but these uniform grids are unable to locally refine around small geometries, perhaps limiting their use to these low Reynolds number flows. It should be noted that while the low blockage ratio may clearly have an effect on the simulations of Boomsma and Sotiropoulos (2016) its impact on experimental studies is unknown due to the lack of boundary layer thickness measurements. This is a further limitation of the sole use of force balances in previous experiments.

RANS methods have also seen little use for the prediction of shark skin flows. Zhang et al. (2011a) carried out the only study using RANS methodology, alongside experiments on shark skin (discussed in the previous section). Zhang et al. (2011a) adopted a finite volume method with the Renormalization Group (RNG) $k - \varepsilon$ turbulence closure (Yakhot et al., 1992) with enhanced wall functions at the wall boundary, to solve the fully developed flow field over an array of approximately 30 shark scales. The shark scales were micro-CT scans of those that were replicated using the moulding technique. While the RANS simulations predicted a drag reduction of the same order as the experiments, they increased from 7 % to 14 % as the flow rate increased; i.e a trend opposite to the experiments. However, the methodology is poorly documented and parameters such as bulk flow Reynolds numbers are not presented, and cannot be obtained from the parameters that were reported. Assuming the fluid was water the bulk Reynolds number was $Re_b \approx 720$, which is small, especially given that a high Reynolds number RNG $k - \varepsilon$ turbulence closure is adopted. Even at $Re_b \approx 2800$, typical of Low Reynolds number DNS, the log-law is difficult to distinguish, if it is even present (see e.g. Moser, Kim, and Mansour, 1999). In addition to this, solution convergence is not achieved and no comments are made regarding grid independence or the inner-scaled near-wall cell sizes, y_1^+, which are vital for assessing applicability of wall function approximations (Wilcox, 2006). Despite these issues the results of Zhang et al. (2011a) have often been used to justify the drag reduction observed in experiments (Chen et al., 2014; Luo et al., 2015).

Summary

When compared to the wealth of literature on longitudinal riblets it is clear that the behaviour of shark skin denticles on the turbulent boundary layer is poorly understood. The few studies that have been carried out are strongly conflicting, with some claiming that denticles are detrimental to skin friction (e.g. Boomsma and Sotiropoulos, 2016) and some claiming they can be significantly more efficient than longitudinal riblets (e.g. Domel et al., 2018). There are two key factors that could explain this poor agreement between literature data: Differences in the denticle geometry between experiments, and limitations of the measurement techniques adopted.

The denticle geometry is of course important to control; experiments on longitudinal riblets have shown that small deviation in riblet geometry can lead to large deviations in their efficiency to reduce drag (Bechert et al., 1997). Regarding shark skin there are significant deviations in denticle geometry, not only between different species but also depending on their location on the shark body. Often the denticle geometry is poorly reported, and sometimes even the particular species is omitted. In addition to this, comparisons between the different data sets are made even more difficult due to the lack of adequate scaling of results; drag reduction is often reported as a function of bulk flow velocity, rather than a more useful quantification of the denticle size, such as s^+ (although even s^+ is questionable, given how many other length scales could quantify a denticle surface). Despite such variation only Bechert, Hoppe, and Reif (1985) and Fletcher (2015) have attempted to quantify differences in drag reducing behaviour of different types of denticle.

Denticle geometries also differ significantly due to replication processes; recent moulding techniques seem capable of replicating denticle surfaces to a high degree of accuracy, but are limited to tightly packed denticles and are unlikely to be able to resolve cavities beneath the crown surface. In addition to this, studies have been carried out on moulds taken from real shark skin surfaces, which are difficult to control in regard to spatial variations and imperfections. Another approach is to adopt 3D printing, although this technique requires scaling of the denticle surface by at least an order of magnitude. However, this method is able to capture the three-dimensionality of denticles much better than moulding techniques.

In addition to denticle geometry there are also limitations in the present literature regarding experimental and numerical techniques. Most experimental work on shark skin surfaces subject to canonical boundary layers are limited by their use of force balances, but as studies on longitudinal riblets have shown, some of the most informative studies have analysed flow field data in order to understand drag reducing mechanisms (e.g. Lee and Lee, 2001; García-Mayoral and Jiménez, 2011b), and yet these have only been obtained using numerical techniques for shark skin subject to canonical boundary layer flows (Boomsma and Sotiropoulos, 2016). In addition to this, many studies do not report important quantifications of the flow such as the Reynolds numbers and the length scales of their denticles in inner-units. Numerical methods can also be used to investigate the flow fields, but only one DNS study has been carried out on these complex surfaces, and this was performed at a single denticle size of $s^+ = 16$, with a single type of denticle arranged in two ways: staggered and aligned (Boomsma and Sotiropoulos, 2016). Computational costs make this technique unsuitable for large parameter studies on denticle geometry. Perhaps a more promising technique is RANS modelling, although at present only a single case study has been attempted for the flow over sharks, which suffers from poor documentation. RANS methods are certainly more attractive than DNS if large parameter studies on denticle geometry are desired, but at present they have yet to be properly validated.

2.4.2 Shark skin applications to complex flows

This section has so far only discussed the literature associated with shark skin applied to flat plates and channel flows. These simple flow configurations are commonly adopted due to their applicability to a wide range of engineering flows, and the repeatability of

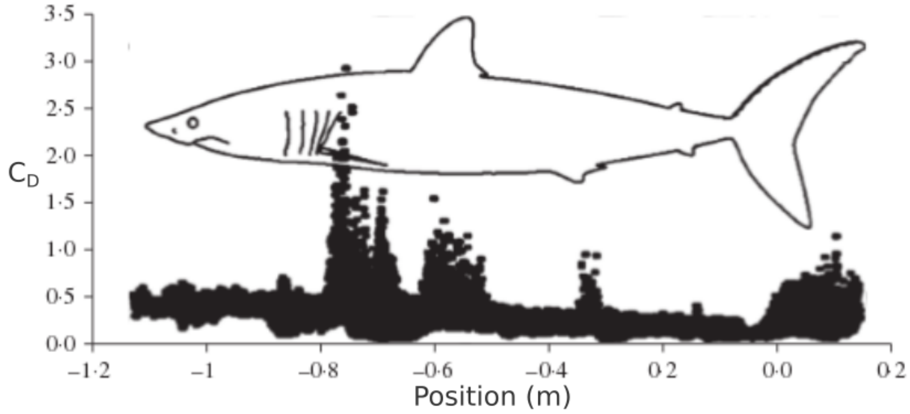

FIGURE 2.12: The distribution of the coefficient of drag over a mako shark. Image taken from Díez, Soto, and Blanco (2015).

experiments. However, the flow field around a shark is far from these idealised canonical flows.

The distribution of drag over a shortfin mako shark is presented in Figure 2.12, taken from the RANS simulation of Díez, Soto, and Blanco (2015). Here the coefficient of drag C_D consists of all drag forces, rather than just skin friction. Díez, Soto, and Blanco (2015) adopted the realizable $k - \varepsilon$ turbulence closure (Shih et al., 1995) with wall functions which accounted for roughness through a modification to the log-law. Treating roughness through boundary conditions is clearly a large simplification to the shark scale geometry, but resolving denticles over a full shark would require an infeasible number of elements. Díez, Soto, and Blanco (2015) stated that the shark body had a wetted-area of approximately 0.58 m^2, and with average denticle dimensions of 100 – 200 µm in width and length the shark has of the order 10 – 100 M individual denticles on its surface. Clearly fully resolving the flow over such a large separation in length scales is not feasible. The drag coefficient results of Díez, Soto, and Blanco (2015), presented in Figure 2.12, indicate an increased coefficient of drag near each of the fins and a slowly decreasing coefficient of drag along the main body. The authors also investigated scale morphology, where 24 Scanning Electron Microscope (SEM) images were taken at various locations on the shark body, although little analysis was provided linking the morphology to the flow field. The authors did note that smooth scales typically exist on the leading edge of the fins and the nose of the shark. Riblets were found to develop further downstream. One could postulate that since a boundary layer develops from laminar to turbulent, and knowing that surface roughness has little effect in laminar flows (Nikuradse, 1933), the transition from smooth scales to ribletted scales reflects the transition from a laminar to a turbulent boundary layer. However, the same conclusion cannot be drawn when considering the morphological study of Fletcher (2015). Figure 2.13 displays the contour maps of two denticle geometries over the body of a *Lamna nasus* (porbeagle). Strongly converging riblets can be observed on the nose and pectoral fin of the fish and slightly converging

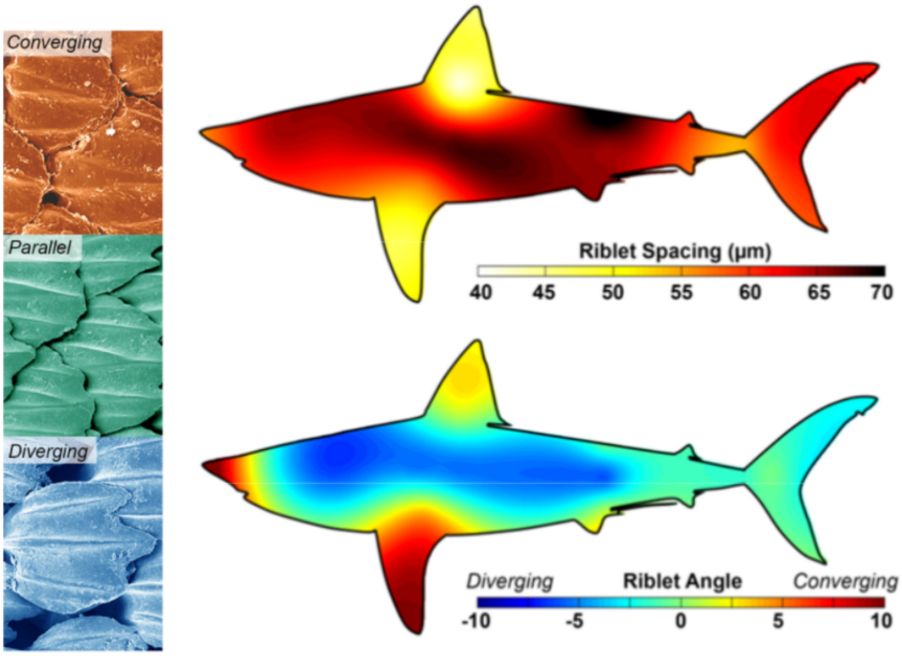

FIGURE 2.13: Distributions of riblet spacing and riblet angle over a *Lamna nasus* (porbeagle). Image taken from Fletcher (2015).

scales are found on the dorsal fin. Fletcher (2015) hypothesised that converging riblets could act as a turbulent trip, similar to those observed on aerofoils. This is further supported by the conclusions of Bechert, Hoppe, and Reif (1985) who argued that denticles could increase turbulent mixing and result in a reduced susceptibility to flow separation. If this is the case then why does the mako shark analysed by Díez, Soto, and Blanco (2015) possess smooth scales on the nose? Figure 2.13 also indicates a reduced riblet spacing on the fins. Referring to Section 2.3 small riblet spacings are associated with higher flow rates; i.e an increase to the friction velocity, u_τ will require a reduction in riblet spacing, s, if the s^+ value is to be maintained. The findings of Díez, Soto, and Blanco (2015) reinforce this by determining increased flow velocities near the fins of the shark.

An aspect of some shark skin that has not yet been discussed is the effect of passive bristling as a mechanism for maintaining attached boundary layers. This effect can be observed in Figure 2.14; while shark scales are rigid, they are embedded into a flexible epidermis which allows the denticle angle of attack to be altered (Lang et al., 2014). The precise mechanism that leads to this bristling is still unknown. Bechert, Hoppe, and Reif (1985) suggested that the variation in mechanical tension of the epidermis could control the bristling mechanism. At high speeds the epidermis is under larger tension than lower speeds; Bechert, Hoppe, and Reif (1985) argued that perhaps it is this mechanism that drives scale bristling. However, Lang et al. (2014) concluded that the presence of recirculating flow could be enough to bristle scales alone. This was determined by imaging the effect of a small pulsating jet which created a backflow over a shark skin sample. However, the authors noted that since experiments were carried out on a small section of shark skin the mechanical tension was unlikely to be matched for a real shark. Lang et al. (2014) applied these sharkskin sections to a NACA 4412 aerofoil and measured the resulting flow field using Digital Particle Image Velocimetry (DPIV). They compared the resulting backflow for a sharkskin surface with bristling scales, and a smooth surface. They found that at low angles of attack the sharkskin surface produced more backflow than the smooth surface. However, backflow was substantially reduced for large angles of attack; at a foil angle of 18° there was a large amount of separation for the smooth surface but very little for the sharkskin. The authors hypothesised that at low angles of attack the backflow was too weak to induce bristling, and as a result the performance of the foil was hindered by its increased thickness. However, DPIV is unable to capture the bristling behaviour directly since the scales are so small. There are also other issues with this technique; since sharkskin was directly applied to the foil there is much uncertainty concerning the mechanical properties of the epidermis and the variability between individual scales. These issues were eliminated by the experimental technique of Wen, Weaver, and Lauder (2014) and Wen et al. (2015) who 3D printed arrays of mako scales onto a flexible membrane, mimicking that of a shark epidermis. The membranes were subsequently applied to the surface of a self-propelling (flapping) foil, where it was hypothesised that the flexibility of the epidermis could have implications on thrust generation. Both studies concluded that the swimming speed of the flapping foil was increased when denticles were present, but both the cost of transport (energy required per unit distance) and power required increased. The authors suggested that this is likely due to the poor representation of the flexible membrane to real shark skin, where scales are more flexibly embedded into the dermis. It was suggested that dynamic experiments are more representative of shark skin and should be further investigated.

Summary

Numerous studies have been carried out in the last decade concerning application of shark skin to complex flows, which are generally more applicable to the flow over a real

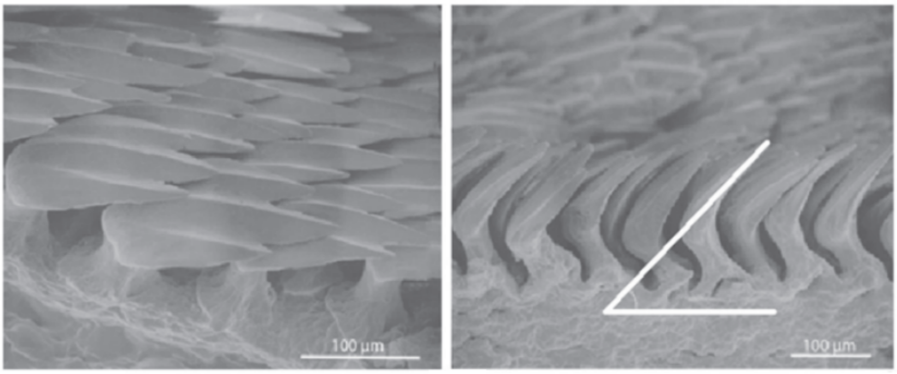

FIGURE 2.14: Bristling scales of a shortfin mako shark. The scales are bristled to an angle of 45°. Image taken from Lang et al. (2014).

shark skin body than the canonical boundary layers discussed in Section 2.4.1. Discussion has focused on two main categories; morphological studies on the distribution of denticle geometry in relation to the fluid flow over a shark body (e.g. Díez, Soto, and Blanco, 2015), and the bristling of mako shark denticles in response to separating flows (e.g. Lang et al., 2014). There are interesting and open questions regarding both of these areas. Quantifying the morphology of shark scales in response to the fluid flows over the shark body is one of the primary motivations for the hydrodynamic study of shark scales, but there are limitations to present techniques. RANS methods have been successful in quantifying the global flow around a shark body (Díez, Soto, and Blanco, 2015), but these can only give approximations for the drag distributions due to the lack of resolution at the shark skin surface. One cannot hope to resolve the flow around both individual denticles and the full shark body in a single simulation due to the vast separation in length scales. However, these simulations may be useful in providing information regarding how denticle geometry is distributed in response to large-scale flow structures, for example in regions of high curvature and possible boundary layer separation. Despite this, only Díez, Soto, and Blanco (2015) have attempted such quantification.

The bristling of mako shark denticles in response to separating flows has been shown to substantially reduce backflow when applied to aerofoils (Lang et al., 2014). However, the precise mechanisms that lead to this behaviour are not yet fully understood, in part due to experimental limitations. Shark scales printed at large length scales suffer from being unable to replicate the tensile properties of a sharks epidermis (Wen et al., 2015), while experiments on real bristling shark skin surfaces have not yet obtained flow field measurements local to individual denticles; PIV has only been adopted to capture the large scale separating flow, rather than the local flow around moving denticles. It is vital to obtain these measurements in order to understand the precise mechanisms that lead to bristling, and the influence of bristling on the local flow field.

2.5 Conclusions

Substantial work has been carried out on understanding the influence of longitudinal riblets on the canonical boundary layer. The drag reducing behaviour of riblets is well understood, with significant contributions from experimental, numerical, and theoretical frameworks. However, there is still a significant lack of support from RANS type methodology; the few studies published suggest that accounting for anisotropy of the Reynolds stresses is essential for properly modelling ribletted channels, although it is still unclear how well RANS methodology can capture these flows. In addition to this the generation of the secondary flows at the riblet tips have been investigated little. Goldstein and Tuan (1998) carried out the only study that has investigated the mechanisms that lead to secondary flows, attributing upward flow to the blocking of spanwise instantaneous velocity fluctuations at the riblet tips. However, this mechanism seems inconsistent with other roughness-induced secondary flows such as over large-scale spanwise-heterogeneous roughness, where the recent work of Anderson et al. (2015) attributed secondary flow generation to the second kind proposed by Prandtl (1953). In addition to this, the steady-state RANS predictions of Benhalilou and Kasagi (1999) obtained the same secondary flow features of Goldstein and Tuan (1998), indicating that perhaps instantaneous blocking of fluctuations is not entirely responsible for the generation of secondary flows. Furthermore, it is unclear how these secondary flows scale with the riblet size, at either low or high s^+. RANS models may prove useful for investigating this scaling, but require significant validation before parameter studies are carried out, given that previous studies have not yet obtained consistent predictions with experiments (e.g. Djenidi and Antonia, 1993; Launder and Li, 1993).

The flow over shark skin surfaces is poorly understood, even for the simplest of flows. Regarding the canonical boundary layer some authors claim that denticles can decrease skin friction drag more-so than riblets, while others suggest denticles substantially increases it. Two key factors that could explain this poor agreement have been identified: Differences in denticle geometry between experiments, and differences in the measurement techniques adopted. As comparable studies on riblets have shown, small differences in roughness geometry can have large implications on performance, which could explain the vast deviations in results for the flows over denticles. Despite this, only Bechert, Hoppe, and Reif (1985) and Fletcher (2015) have attempted to determine the effects of different denticle geometry on fluid dynamic performance. Not only is this vital to understanding why different geometric features exist on individual denticles, it may also explain why there are such vast differences in previous experimental results. Due to their small length scales denticle geometry is difficult to control experimentally. Various techniques have been adopted when fabricating these surfaces, the most promising of which is 3D printing, as adopted by Wen, Weaver, and Lauder (2014), Wen et al. (2015), Fletcher (2015), and Domel et al. (2018). This technique has the advantage of a uniform and controlled surface with the ability of capturing the geometric features beneath the denticle crown, although requires scaling of the denticle geometry by at least an order of magnitude.

Furthermore, previous experiments have been limited by their use of force balances which cannot obtain flow field data over the shark skin surface. Some of the most informative studies on the flow over riblets have analysed flow field data in order to understand drag reducing mechanisms (e.g. Lee and Lee, 2001; García-Mayoral and Jiménez, 2011b), and yet these have only been obtained using numerical techniques for shark skin subject to canonical boundary layer flows (Boomsma and Sotiropoulos, 2016).

There are also many investigations carried out on the behaviour of shark skin in complex flows, such as the dynamic flapping of foils covered in replicated denticles, the bristling effects of denticles exposed to separating flows, and the influence of mucus-like polymers applied to the denticle surface. The application of denticles to more complex flows is certainly an active area of research, but has only been briefly discussed in this review. However, since there is such a lack of agreement in the literature concerning even the simplest of flows, it is this area that will be the focus of this Thesis.

Chapter 3

Experiments on shark skin denticles: The influence of shark skin denticles, with and without riblets, on the turbulent boundary layer

3.1 Introduction

Shark skin has fascinated biologists, engineers, and physicists for decades due to its highly intricate drag-reducing structure. Shark skin is comprised of small tooth-like dermal denticles which protrude from a flexible epidermis and are typically 0.1 – 1 mm in width. Considerable variety in denticle shape can be observed (e.g. Figure 2.9), not only between different species, but also depending on the location on the body (Reif, 1985; Díez, Soto, and Blanco, 2015; Feld et al., 2019). They are strongly three dimensional, some overlap while others have large gaps, and many are smooth, while some have small riblet features protruding from their crown. Shark skin denticles are thought to have evolved for the benefit of hydrodynamic efficiency, resistance against abrasion, and defence against parasites (Reif, 1985), although hydrodynamic experiments have been largely limited to the riblets present on the denticle crown of some fast-swimming sharks. Shark skin-inspired streamwise surface riblets have seen significant development over the last few decades, and have been shown to reduce skin friction drag by up to 10 % (Bechert et al., 1997), depending on the shape of the riblets and their dimensionless length scale $s^+ = u_\tau s/\nu$, where s is the spacing between riblets, $u_\tau = \sqrt{\tau_w/\rho}$ is the friction velocity, τ_w is the wall shear stress, ρ is the fluid density, and ν is the fluid kinematic viscosity. The drag reducing behaviour of riblets over a flat plate or channel flow boundary layer has been thoroughly investigated using experimental modelling (e.g. Walsh, 1982; Walsh, 1990; Bechert et al., 1997; Lee and Lee, 2001), Direct Numerical Simulation (DNS) (e.g. Choi, Moin, and Kim, 1993; García-Mayoral and Jiménez, 2011b), and linear stability analysis (e.g. Luchini, Manzo, and Pozzi, 1991). However, there are many sharks that have not evolved riblet-like features on their denticle crowns (Reif, 1985). It is not yet known whether denticles are hydrodynamically beneficial without riblets, or indeed how riblets may influence the boundary layer in combination with shark skin denticles.

Bechert, Hoppe, and Reif (1985) were the first to quantify the drag force obtained when the denticles of fast swimming sharks are exposed to a boundary layer flow. Mako and silky shark skin denticles, both with riblets on the crown, were replicated and fixed to a plate section in a wind tunnel. Force balance data were recorded and an increased drag force was obtained for all the flow regimes tested when compared to a smooth surface. Further investigations were carried out using an oil channel (Bechert et al., 2000). In this case the reduced viscosity of the fluid allowed ribletted hammerhead denticles to be fabricated at a larger length scale which led to better capture of the three dimensional shapes while maintaining similar values of s^{+}. A 3 % reduction in drag was observed when the denticles were tightly packed and resembled a ribletted surface. When the denticle angle of attack was increased, drag increased substantially with respect to the reference flat plate. This led to similar conclusions as their previous study (Bechert, Hoppe, and Reif, 1985); three dimensionality of shark skin denticles is detrimental to skin friction, and drag is only reduced when denticles are tightly packed and resemble a ribletted surface. Similar conclusions were drawn by Boomsma and Sotiropoulos (2016) who adopted DNS to simulate a channel flow with mako shark denticles on the wall surface. For a riblet spacing of $s^{+} = 16$ Boomsma and Sotiropoulos (2016) obtained a drag increase of over 50 % compared to the smooth channel.

Shark skin denticle surfaces have also been reported to reduce drag as much as, if not more-so, than longitudinal riblets (e.g. Chen et al., 2014; Wen, Weaver, and Lauder, 2014; Domel et al., 2018). Wen, Weaver, and Lauder (2014) 3D printed an array of mako shark skin denticles and directly measured the drag forces when subject to a developing boundary layer in a water flume. They obtained similar levels of drag reduction as ribletted plates, despite a relatively loosely packed denticle arrangement when compared to those of Bechert et al. (2000). Drag was reduced by a maximum of 9 % at $s^{+} \approx 5.6$, with a critical s^{+} of 14, above which drag increased. This is approximately half the expected critical s^{+} for longitudinal riblets (Bechert et al., 1997). More recently Domel et al. (2018) made use of the same experimental facilities to measure the forces acting on arrays of 3D printed mako denticles at different sizes. They observed significant decreases in drag in excess of 30 % for their smallest denticles, printed at a length of 2.05 mm. Moulding techniques have also seen recent success for the fabrication of shark skin surfaces; Tightly packed and overlapping denticles have been moulded and cast by Zhang et al. (2011a), Zhang et al. (2011b), and Chen et al. (2014), leading to a maximum drag reduction of 8 – 12 %.

Despite large differences in results, all the highlighted studies have investigated ribletted denticles of fast swimming sharks. An open question is whether the riblets are solely responsible for the drag reducing effect of shark skin, or whether smooth denticles may also reduce skin friction. The combined interaction of riblets and denticles is still unknown. In addition to this, there have been few reports of flow field measurements for attached boundary layer flows over shark skin surfaces. Some of the most informative studies on streamwise aligned riblets have taken flow field measurements or adopted numerical techniques in order to establish which fluid dynamic mechanisms lead to increased/decreased drag (e.g. Lee and Lee, 2001; García-Mayoral and Jiménez, 2011b).

To address these issues this chapter presents the first flow field measurements of a boundary layer flow over arrays of replica shark skin denticles, using two-component Laser Doppler Anemometry (LDA). Two types of denticles are fabricated; a smooth *Poracanthodes sp.* (extinct shark relative) scale, and a ribletted denticle similar to the mako denticles of Wen, Weaver, and Lauder (2014) but with comparable proportions to the smooth denticle. This work is the first to investigate the influence of smooth shark skin denticles on an attached turbulent boundary layer, and quantify differences between the more typical ribletted denticles that are comparable with those common in previous work.

3.2 Methodology

Two types of sharkskin denticle were created using Blender (2017) CAD software; one based on *Poracanthodes sp.* an early fossil ancestor of sharks (Brazeau, 2009), and another based on the same denticle but with mako-inspired riblets added to its crown. These can be observed in Figure 3.1. *Poracanthodes sp.* denticles were chosen due to their similarities with modern fast swimming shark denticles, while maintaining a smooth denticle crown without riblets. Like modern sharks, the *Poracanthodes sp.* denticle has an overhanging crown, a sharp trailing edge, and a slightly thinner neck region below which the denticle embeds into the dermis (Reif, 1985). Using Blender (2017) CAD software the fossil sample was made symmetrical and smoothed along the trailing edge in order to remove imperfections. The model was also clipped at the base of the neck region such that only material exposed to water is replicated. The mako-based denticle is built upon the smooth denticle, but with three riblets added to the denticle crown, consistent with the denticle of Wen, Weaver, and Lauder (2014). While the riblets have been added to the

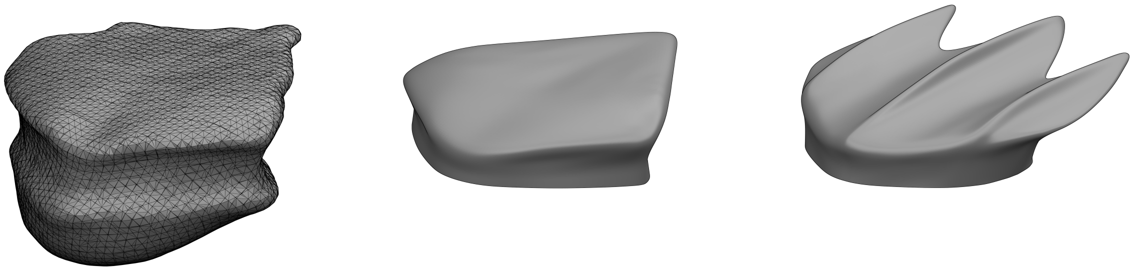

FIGURE 3.1: Shark skin denticle CAD models. A *Poracanthodes sp.* sample (left), a smoothed and symmetrical *Poracanthodes sp.* denticle (centre), and a mako-based ribletted denticle (right).

top, and cut-outs at the trailing edge, the overall dimensions have been kept consistent between the two.

Arrays of smooth and ribletted denticles were 3D printed at a 4 mm width and bonded to a 500 × 120 mm PVC sheet. The 4 mm denticle width equates to an $s^+ \approx 8 – 30$ over the range of Reynolds numbers tested. Further details on the denticle dimensions and fabrication process can be found in Appendix A.

3.2.1 Rig and plate design

Experiments were carried out using a recirculating flume (Figure 3.2). The test section of the flume has a width of 30 cm, and a length of 8.75 m, measured from downstream of a 20 cm long array of 35 mm diameter flow straightening steel tubes. The total flume depth is 30 cm, with the water filled to a constant depth of 26 cm. Water was recirculated using an inverter governed centrifugal pump . The pump frequencies tested corresponded to freestream velocities (U_∞) of 0.11 m s^{-1}, 0.21 m s^{-1}, 0.32 m s^{-1}, and 0.42 m s^{-1}. A removable plate assembly (CNC machined aluminium with a hard anodising coat), detailed in Figure 3.3, was attached in the centre of the flume, with a width of 140 mm and flat-section length of 500 mm. Its leading edge was 2.8 m downstream of the flow straighteners, and positioned at a height 18 cm from the base of the flume, measured from the bottom of the plate. The assembly was mounted on a bespoke two-axis gimbal, attached to aluminium struts which were joined to the top of the flume. Spirit levels (sensitivity of 0.02 mm m^{-1}) were used to ensure the plate was parallel to the flume base and LDA traverse. The leading and trailing edges were semi-circular to reduce the influence of blunt body effects on the boundary layer.

The plate assembly (Figure 3.3) was designed to allow different plates to be interchangeable. Experiments were carried out on three plates; a reference flat plate made of PVC, and the two 3D printed sharkskin surfaces described in Appendix A. The PVC inserts were held in place using two thin plates on either side, which lay flush with the plate when secured. The sharkskin protruded from the flat section such that the base of the sharkskin denticles lay flush with the securing plates. Boundary layer profiles were taken from beneath the plate, with the positive $y-$ direction taken as the downward plate-normal direction and the $x-$ direction as streamwise.

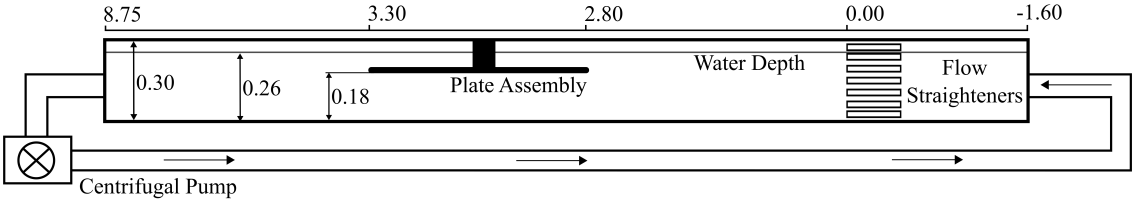

FIGURE 3.2: Schematic of the recirculating flume. Dimensions in m. (not to scale).

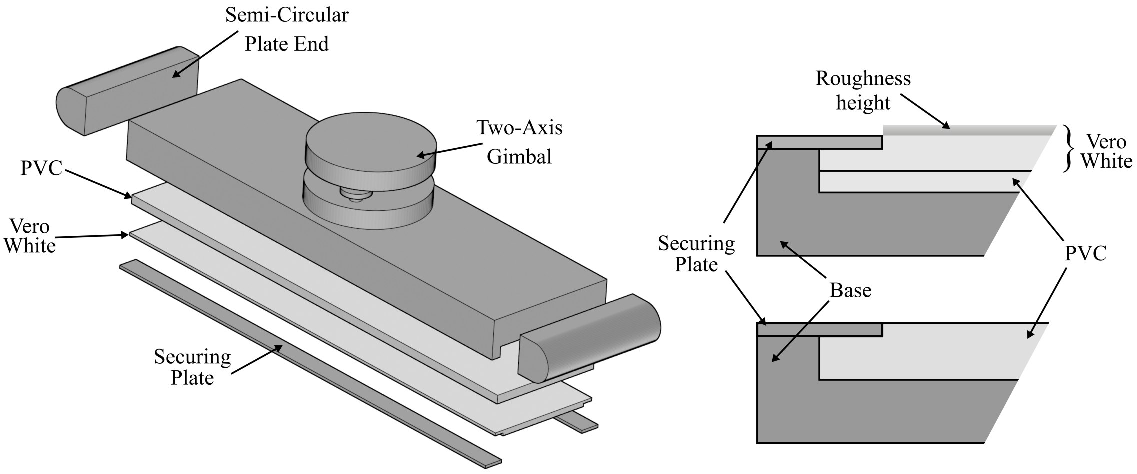

FIGURE 3.3: Plate assembly (left) and plate cross sections (right) for the 3D printed (upper) and smooth (lower) plates.

For each of the three plates and four flow rates experiments were typically carried out over 6-8 hours. Temperatures were recorded throughout the experiments with an average reading typically between 19.5 – 20.0 °C. The largest deviation during a set of measurements was 19.0 to 19.8 °C; the fluid viscosity was taken as the viscosity corresponding to average temperature throughout the measurement process on that particular day.

3.2.2 Measurement techniques

The flow was seeded with 10 µm diameter neutrally buoyant silver coated glass spheres. Particle velocities in the $x - y$ plane were measured by a two-component LDA (Dantec FibreFlow) with optical access via a glass side panel in the flume. Measurements were taken in coincident mode to allow calculation of cross-correlations, and a backscatter configuration was used.

The LDA probe had a diameter of 60 mm, a fixed focal length of 400 mm, a beam diameter of 1 mm, and a beam spacing of 38 mm. These equate to a measurement volume diameter of approximately 1 – 5 wall units and a length of 30 – 100 wall units, depending on the flow Reynolds number. The LDA probe was mounted to a three-axis ISEL system Traverse with a 410 mm maximum range. The minimum step size and precision of the motor were 10 µm. The LDA probe head, and subsequently the measurement volume, was rotated by 45° along the $z-$ axis, and 2.7° in the $x-$ axis. The $x-$ axis rotation allowed the LDA measurement volume to get close to the wall, while the $z-$ axis rotation was to reduce noise from reflections off the rough plate surfaces. Preliminary experiments found that when the LDA probe was aligned such that the streamwise and wall-normal velocities could be directly measured, the wall-normal velocity was consistently affected by noise near the wall which could not be easily filtered from the velocity field. This noise was entirely removed when rotating the probe by 45°, and transposing back to standard coordinates.

Profiles were measured at $x = 400\,\text{mm}$ and $z = 0$, where $x = 0$ corresponds to the leading edge of the plate and $z = 0$ corresponds to the plate centreline. Sensitivity to the exact $x-$ and $z-$ locations were checked by also measuring profiles at $(x, z) = (400, 1)$ and $(x, z) = (401, 0)$, corresponding to different locations on the same sharkskin denticle. No differences in profiles of velocity or Reynolds stresses were observed, within experimental accuracy.

A grid is created in the y direction with a minimum spacing of 0.0125 mm, which grows using a geometric scaling until y_{max} =75 mm. The point $y = 0$ lies just below the plate surface; since the plates are replaceable the exact wall position is unknown and estimated during post-processing. The first grid point y_0 corresponds to the closest position to the plate that could be achieved with the LDA probe, without observing large scattering in the data, within a tolerance of 0.0125 mm.

The raw data are passed through a moving average filter; a filter window of 16 points is used and data are removed from both the u and v time series if it falls outside of three standard deviations from the local mean. This typically removes 0.2 % of the data. Temporal statistics are calculated using the residence time as a weighting, in order to account for velocity biasing effects. A sampling time of 300 sec for the lowest flow rate is adopted, and 200 sec for the other flow rates. The total number of samples recorded over the sampling time was approximately 6500 for the lowest flow rate and 9000 for the highest flow rate, in the freestream. These sampling windows were chosen by assessing the convergence of statistics over a 10 min sampling period at several vertical positions. The Reynolds stresses converged to a temporal error of approximately 5 % for the sampling times chosen, when compared against the 10 min sampling period. Spatial filtering is adopted by assessing diagnostic plots, as per Alfredsson and Örlü (2010). While typically used for identifying wall effects for hot wire anemometry, the technique was found to be useful by identifying regions of the boundary layer which were affected by near wall reflections. These points were subsequently removed from the data series.

At x =400 mm boundary layers typically had a height of δ =30 mm. The Reynolds numbers based on the freestream velocity (U_∞) and momentum thickness (θ) varied between $Re_\theta \approx 400 - 1200$.

3.2.3 Parameterisation of the boundary layers

In order to calculate inner and outer length and velocity scales the freestream velocity, U_∞, boundary layer thickness, δ, friction velocity, u_τ, and wall-offset, Δ_y, must be estimated. For the flat plate the wall offset accounts for the unknown exact position of the wall in reference to the grid: $y = \tilde{y} - \Delta_y$, where y is the true vertical coordinate and $\tilde{y}$ corresponds to the grid. For the rough surfaces it also accounts for the offset of the virtual origin due to the presence of roughness. Three methods of determining the unknown parameters are presented here.

The first estimate of u_τ is calculated via a best-of-fit approach that minimises the root-mean-square (RMS) error between a composite velocity profile and the LDA data, as per Rodríguez-López, Bruce, and Buxton (2015). Due to the low Reynolds numbers a more typical Clauser (1956) approach is unsuitable due to the small overlap region. In contrast, a composite profile is valid for the entire boundary layer. The composite velocity profile U^+_{comp} is split into an inner U^+_{inner} and outer U^+_{outer} component (Coles, 1956), where the superscript $+$ denotes normalisation by inner scales u_τ and ν, and U is the mean streamwise velocity:

$$U^+_{\text{comp}} = U^+_{\text{inner}} + U^+_{\text{outer}}. \tag{3.1}$$

Typically the inner region is governed by the log-law:

$$U^+_{\text{inner}} = \frac{1}{\kappa} \ln y^+ + B \tag{3.2}$$

where κ and B are the log-law constants. However, this is only valid for $y^+ \gtrsim 30$ (Pope, 2001). In contrast the inner function of Musker (1979) is valid for the full inner region, dependent on the Von Kármán constant, κ, and the parameter a, which primarily governs the behaviour of U^+_{inner} in the overlap region:

$$\begin{aligned} U^+_{\text{inner}} = \frac{1}{\kappa} \ln\left(\frac{y^+ - a}{-a}\right) + \frac{R^2}{\alpha(4\alpha - a)} &\left[(4\alpha + a)\ln\left(-\frac{a}{R}\frac{\sqrt{(y^+ - \alpha)^2 + \beta^2}}{y^+ - a}\right)\right. \\ &\left. + \frac{\alpha}{\beta}(4\alpha + 5a)\left(\arctan\left(\frac{y^+ - \alpha}{\beta}\right) + \arctan\left(\frac{\alpha}{\beta}\right)\right)\right], \end{aligned} \tag{3.3}$$

where $\alpha = (-1/\kappa - a)/2$, $\beta = \sqrt{-2a\alpha - \alpha^2}$, and $R = \sqrt{\alpha^2 + \beta^2}$. This form of U^+_{inner} reduces to the $U^+ = y^+$ for $y^+ \lesssim 5$ and the log law (3.2) for $y^+ \gtrsim 30$. Further details on this function can be found in Musker (1979) and Chauhan, Nagib, and Monkewitz (2007). The outer component U^+_{outer} is dependent on κ, a wake strength parameter Π, and an empirical wake function $\mathcal{W}(\eta)$ dependent on the outer coordinate $\eta = y/\delta$:

$$U^+_{\text{outer}} = \frac{2\Pi}{\kappa}\mathcal{W}(\eta), \tag{3.4}$$

As per Coles (1956). A quartic wake function is used for $\mathcal{W}(\eta)$, developed by Lewkowicz (1982):

$$\mathcal{W}(\eta) = \eta^2(3 - 2\eta) - \frac{1}{2\Pi}\eta^2(1 - 3\eta + 2\eta^2). \tag{3.5}$$

This wake function was found to be most suitable for this problem, rather than more complex exponential forms such as that developed by Chauhan, Nagib, and Monkewitz (2007). This is due to the reasonably high levels of turbulence in the freestream, where the wake strength Π is either very small, or negative, and the quartic form of the wake function provides an excellent fit to the data for these values of Π.

The composite velocity profile U^+_{comp} is valid for $y \leq \delta$, but not for $y > \delta$ due to the behaviour of the wake function, a problem noted by Chauhan, Nagib, and Monkewitz (2007). In order to fit all collected data the coordinate transform of Sandham (1991) is adopted which ensures that for $\eta > 1$, $U_{\text{comp}} = U_\infty$. This takes the form

$$\frac{1}{(\widehat{y})^{1/n}} = \frac{1}{\delta^{1/n}} + \frac{1}{y^{1/n}}. \tag{3.6}$$

where the parameter $n = 0.02$ (Chauhan, Nagib, and Monkewitz, 2007) governs the behaviour of the transformed coordinate, $\widehat{y}$, at the boundary layer edge. In conventional inner and outer coordinates

$$\widehat{\eta} = \left[1 + \frac{1}{\eta^{1/n}}\right]^{-n}, \tag{3.7}$$

and

$$\widehat{y}^+ = \left[\frac{1}{(\delta^+)^{1/n}} + \frac{1}{(y^+)^{1/n}}\right]^{-n}. \tag{3.8}$$

From inspection one finds that for $y \to \infty$, $\widehat{\eta} \to 1$ and $\widehat{y}^+ \to \delta^+$. These transformed variables $\widehat{y}^+$ and $\widehat{\eta}$ are substituted directly into the composite velocity profile equations.

In order to fit the composite profile U^+_{comp} to the LDA boundary layer data 6 unknowns must be determined: u_τ, Δ_y, κ, a, Π, and δ. A differential evolution solver is adopted to minimise the RMS error

$$E_{\text{comp}} = \sqrt{\sum_{i=0}^{N}(U_i^+ - U^+_{\text{comp},i})^2} \tag{3.9}$$

between a given set of bounds for the unknown variables. These bounds were chosen as realistic limits for each variable, and it was ensured that the converged solution fell far from the edges of these bounds. The converged solutions for the unknowns lead to the first estimate of u_τ. However, with 6 unknowns the solution space of E_{comp} is very flat and large deviations in the unknowns can lead to reasonably good fits to the data. Ideally one would place constraints on the parameters a, κ and Π, but this would be inappropriate at the low Reynolds numbers herein (Nagib and Chauhan, 2008).

A second estimate is obtained by adopting the method of Hou, Somandepalli, and Mungal (2006), who obtained u_τ by a linear fit to profiles of the weighted total stress $T_{xy} = \tau_{xy}(1-\eta)$ where the total stress τ_{xy} is equal to the sum of viscous and Reynolds stresses:

$$\tau_{xy} = \nu\frac{dU}{dy} - \overline{u'v'}. \tag{3.10}$$

The linear fit of Hou, Somandepalli, and Mungal (2006) is given by

$$T^+_{\text{fit}} = m\eta + 1 \text{ for } \eta < \eta_{\text{Lim}}, \tag{3.11}$$

where m is the gradient of the linear fit and η_{Lim} is the limit of validity for the linear region. Hou, Somandepalli, and Mungal (2006) suggested $\eta_{\text{Lim}} = 0.5$ for their boundary layers but Mehdi and White (2011) noted that the linear region can be much smaller for some cases. Therefore a limit of $\eta_{\text{Lim}} = 0.3$ is specified. This best-fit method is therefore dependent on the unknowns u_τ, Δ_y, δ, and m. The RMS error between the data and the fit is given by

$$E_{\text{Lin}} = \sqrt{\sum_{i=0}^{N} (T^+_{xy,i} - T^+_{\text{fit},i})^2}. \tag{3.12}$$

E_{Lin} is minimised using a Nelder-Mead SIMPLEX algorithm (Gao and Han, 2012). Preliminary experiments found that the solution space of E_{Lin} is very flat due to its linear behaviour. For this reason the method is coupled with the composite fit and both E_{comp} (3.9) and E_{Lin} (3.12) are minimised in a segregated manner where u_τ is given by the linear fit to the weighted total stress and the other unknowns are determined by the composite profile fit. The two errors are minimised iteratively until the friction velocity converges to a relative tolerance of 0.001, leading to the second estimate of u_τ.

However, there is some dependence on η_{Lim} as noted by Mehdi and White (2011), and it is unclear whether this linear behaviour holds for all flat plate boundary layers. A more robust technique is that of Mehdi and White (2011) who derive an integral equation for the friction coefficient, $C_f = 2u_\tau^2/U_\infty^2$. A variation on this method provides the third estimate of u_τ. Assuming the boundary layer is steady and two-dimensional C_f can be calculated by (Mehdi and White, 2011)

$$C_f = 4\int_0^1 \frac{(1-\eta)}{U_\infty^2} \tau_{xy} d\eta - 2\int_0^1 \frac{(1-\eta)^2}{U_\infty^2} \frac{\partial \tau_{xy}}{\partial \eta} d\eta. \tag{3.13}$$

This method of calculating C_f (and subsequently u_τ) has the advantage of being an explicit equation for a given data set, and making few assumptions about the form of the boundary layer. However, calculating the derivative of τ_{xy} can lead to large errors due to the difficulties in achieving adequate convergence of $\overline{u'v'}$ in the near wall region. This problem is overcome by Mehdi and White (2011) by applying a Whittaker smoother (Whittaker, 1922) to profiles of T_{xy}, justified by noting its linear behaviour close to the wall and its monotonic and smooth decrease to zero as $y \to \delta$. A smoothed τ_{xy} is obtained from the smoothed T_{xy} by division of $(1-\delta)$ for evaluation of C_f. The smooth profile of τ_{xy} can subsequently be used to approximate its derivatives and the integral equation (3.13).

The integral equation (3.13) of Mehdi and White (2011) can be reformulated to

$$u_\tau^2 = \int_0^1 T_{xy} d\eta - \int_0^1 (1-\eta) \frac{dT_{xy}}{d\eta} d\eta. \tag{3.14}$$

The integral equation (3.14) is a more convenient formulation than (3.13) as τ_{xy} no longer appears in the integral, thus avoiding division by $(1-\eta)$ after smoothing profiles of T_{xy} which can otherwise lead to floating point precision errors at $\eta \approx 1$. Details on the Whittaker smoother can be found in Appendix B. Evaluation of (3.14) requires knowledge of Δ_y and δ in order to calculate η. This equation is therefore coupled with the composite profile method and E_{comp} (3.9) is minimised for a given u_τ calculated from (3.14). These equations are solved in a segregated and iterative manner until the friction velocity converges to a relative tolerance of 0.001, leading to the third estimate of u_τ.

For the smooth plate the three estimates of u_τ are taken as per the methods discussed. In order to ensure the composite profiles are suitable for the rough plates some small changes are made. At the three highest Reynolds numbers $\kappa = 0.42$ is obtained during the optimisation process for the smooth plate, which lies in the typical range of accepted values of κ (Nagib and Chauhan, 2008). For this reason the value of κ is fixed to 0.42 for the three highest Reynolds numbers for the rough plates, given that roughness only effects the offset of the log-law (treated via the parameter a). The Von Kármán constant, κ, is treated as a free variable for the lowest flow rates given how few points are in the overlap region. The same composite profile is adopted for the rough plate surfaces, given that the dimensionless roughness heights are very small for most of the flows tested. Subsequently the buffer region ($y^+ \sim 30$) follows the composite fit very well since it has not fully broken down over these transitionally rough surfaces (indeed, some of the cases appear hydraulically smooth). The highest flow rate tested does not follow this trend, due to the increased dimensionless roughness height. The buffer region is fully broken down, and therefore a log-law form of U^+_{inner} (3.2) is more appropriate where the offset parameter B is optimised instead of a. This is more in-line with typical methods for calculating the wall friction where the log-law is assumed to hold for all data below $y^+ \lesssim 0.2\delta$ (see e.g. Squire et al. (2016)).

Precision errors are estimated by four repeated experiments, two for the smooth plates and two for the rough, at the two extreme pump flow rates. Differences in Re_θ were at a maximum of 3.2 % over the four cases when compared to the reference data set. Differences in the friction velocity estimates are quantified individually. The estimate based solely on the fit to the composite profile (3.9) leads to differences of up to 45 %, clearly indicating that the method is unsuitable without placing constraints on some of the unknowns, or determining them independently. Errors in the Linear-fit to the near-wall T_{xy} led to differences of up to 3 %. This is improved further by the integral method (3.14) which leads to differences of a maximum of just 1.4 %. Note that this uncertainty is smaller than the estimated temporal error for the Reynolds stresses (5 %), a clear result of the Whittaker smoother.

TABLE 3.1: Flow conditions for all plates and flow rates. Cases are identified by a number 1-4 representing the flow rate, and an initial with 'F' representing the flat plate, 'S' the smooth denticle plate, and 'R' the ribletted denticle plate. Marker styles are used for all following figures.

	Plate	Re_θ	$u_{\tau,\mathrm{int}}$ (mm/s)	$u_{\tau,\mathrm{lin}}$ (mm/s)	$u_{\tau,\mathrm{comp}}$ (mm/s)	U_∞ (m/s)	I_u (%)	I_v (%)	κ	B
●	F1	487.8	5.62	5.69	5.54	0.11	5.1	4.2	0.58	8.86
▲	F2	719.5	10.45	10.67	10.24	0.21	5.8	4.5	0.42	6.3
★	F3	853.5	15.61	15.78	23.86	0.32	6.4	4.6	0.42	5.91
■	F4	1221.0	20.26	20.4	21.46	0.42	6.6	4.9	0.42	5.76
●	R1	409.9	5.83	5.79	5.85	0.11	5.0	4.2	0.55	8.55
▲	R2	646.6	10.72	10.76	9.71	0.21	5.7	4.3	0.42	5.72
★	R3	810.9	17.22	17.13	19.16	0.32	6.4	4.6	0.42	3.78
■	R4	1197.7	23.7	23.29	25.2	0.43	6.7	4.7	0.42	2.5
●	S1	417.2	5.91	5.9	6.05	0.11	5.0	4.4	0.51	7.23
▲	S2	693.7	11.22	11.39	9.24	0.21	5.8	4.4	0.42	4.65
★	S3	1029.1	18.36	18.46	20.72	0.32	6.4	4.6	0.42	2.14
■	S4	1227.3	26.03	26.05	26.51	0.43	6.8	4.7	0.42	0.39

3.3 Results and discussion

The flow conditions can be observed in Table 3.1, with key fitting parameters obtained through the optimisation process. The different plates and flow regimes are abbreviated by a letter and a number; The letter refers to the plate type with 'F' being the flat reference plate, 'R' the ribletted denticle array, and 'S' the smooth denticle array. The numbers refer to the imposed flow rates and subsequent Reynolds numbers, with '1' referring to the lowest Reynolds number cases and '4' the highest. Streamwise and wall-normal freestream turbulence intensities are also presented: I_u and I_v. As previously noted the optimised value of κ for all the flat plate flows is 0.42, apart from the lowest Reynolds number case where the overlap region is small. Three estimates of the friction velocity have been provided; one from the integral equation, one from the linear fit to the near wall weighted shear stress, and one from the unconstrained composite profile fit. The integral method and the linear fit method have good agreement; typical deviations from one another are less than 1 %, with a maximum of 2.1 % for the F2 case. Unsurprisingly the composite profile method leads to a large spread in deviations, a result of the underdetermined best-of-fit approach. The other parameters in Table 3.1 are those obtained when optimising the composite profile and the integral stress method, which is identified as the best estimate of u_τ due to its high repeatability and robustness (although the following analysis changes very little when adopting the linear-fit method instead).

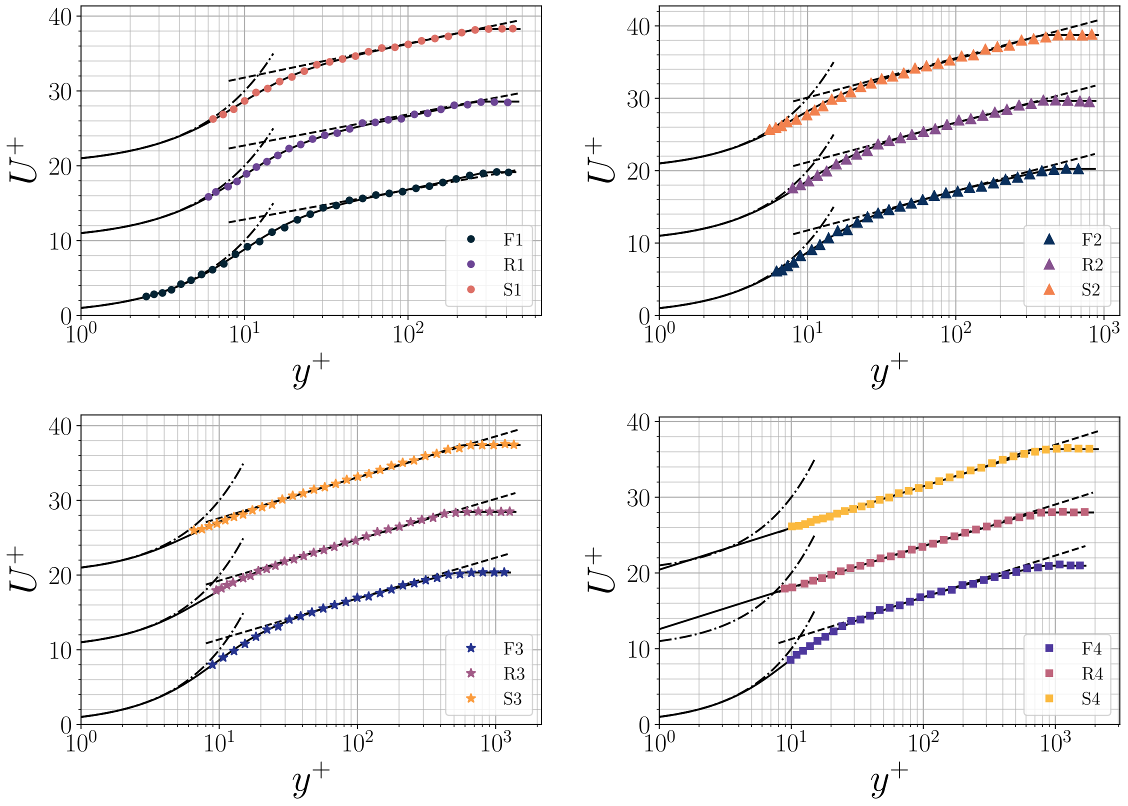

FIGURE 3.4: Composite profile fits. Line styles represent Composite profile (——), linear region (-·-·), and log-law (- - -). Note that profiles have been offset by 10 in the $y-$ axis.

3.3.1 Validation

Fits to the composite velocity profile can be observed in Figure 3.4 (For clarity when the $y-$ axis is scaled logarithmically every second data point is plotted for all presented profiles in this manuscript). Excellent agreement can be observed for all the cases. When considering the R1 and S1 cases it is clear that the roughness has negligible effect on the mean velocity. In contrast the R4 and S4 cases clearly indicate that the buffer region has fully broken down and the log-law holds for the full measured profile. The freestream turbulence intensities (I_u and I_v for streamwise and vertical intensities) reported in Table 3.1 account for the negative wake strengths that can be observed in the velocity profiles. The freestream velocity tends to U_∞ by dropping below the log-law, which is a property of the freestream turbulence, reported by Nagata, Sakai, and Komori (2011) and Thole and Bogard (1996), among others. Despite this, the composite profile captures the data well, and the inner-region of the boundary layer remains unchanged.

Profiles of the RMS velocity fluctuations for the flat plate cases can be observed in Figure 3.5, with comparisons against other literature data with similar Reynolds numbers and turbulence intensities. The RMS velocities follow the low turbulence intensity

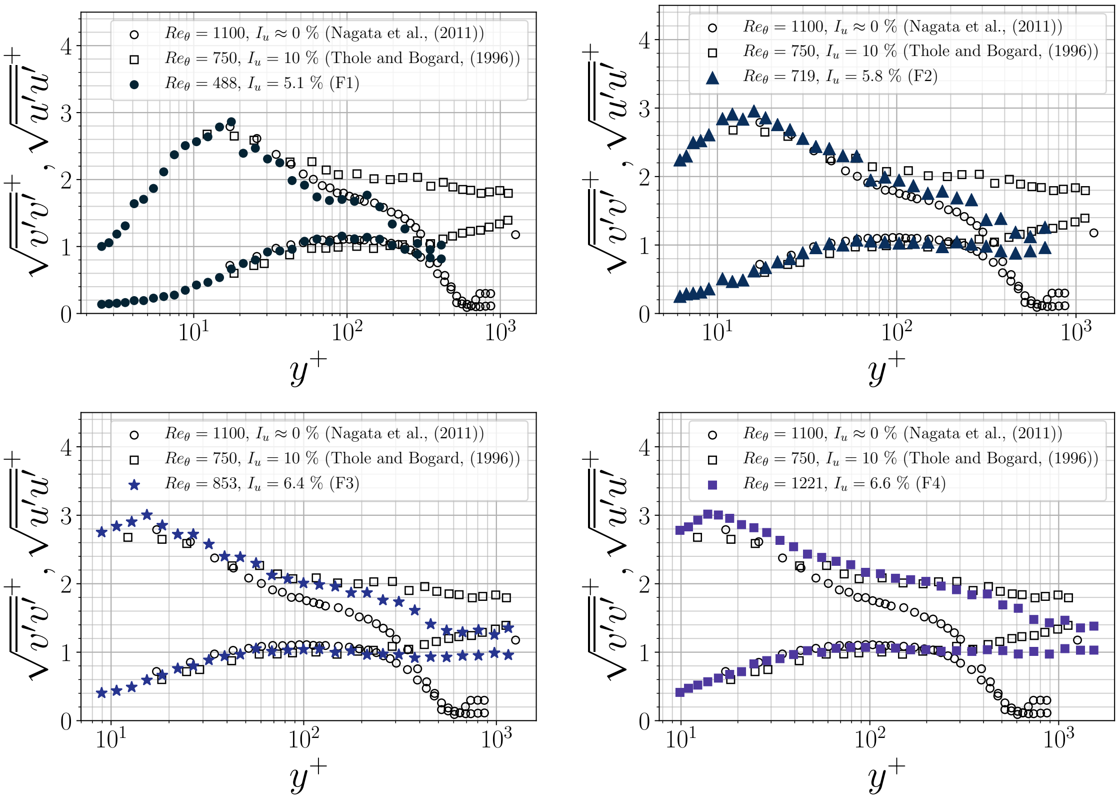

FIGURE 3.5: Flat plate Reynolds stress comparisons to literature data.

profile of Nagata, Sakai, and Komori (2011) well, until the wake region where the profiles do not decay to zero. Instead they tend to the freestream turbulence levels. The high turbulence intensity (10 %) profiles of Thole and Bogard (1996) show a similar but more extreme trend, where the turbulence levels in the freestream are greater for $\sqrt{\overline{v'v'}}^+$ than in the inner regions of the boundary layer. The turbulence levels herein are clearly more moderate than this where $\sqrt{\overline{v'v'}}^+$ reaches its maximum value well within the boundary layer.

Despite the low Reynolds numbers friction coefficients agree well with the correlation of Österlund et al. (2000):

$$C_f = \frac{2}{\left[\frac{1}{\kappa}\ln Re_\theta + B_0\right]^2}, \tag{3.15}$$

where Österlund et al. (2000) specify $B_0 = 4.08$. The agreement between the friction coefficients obtained using the integrated total shear stress method and the Österlund et al. (2000) correlation can be observed in Figure 3.6. Aside from case F2 the data agree well with the correlation, despite it being developed for $Re_\theta > 2500$, twice as large as the highest Reynolds number investigated here. With a small adjustment to B_0 to compensate for the lower Reynolds numbers slightly better agreement is obtained.

Profiles of the weighted shear stress can be observed in Figure 3.7. Firstly it is noted

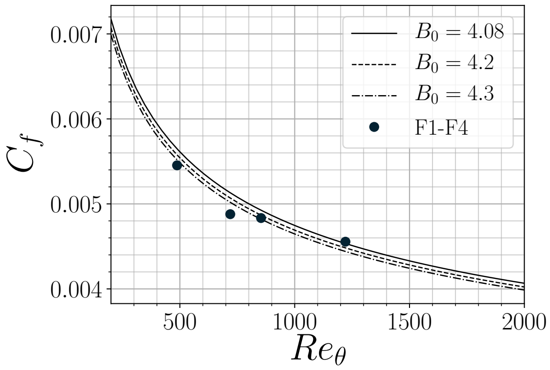

FIGURE 3.6: Österlund et al. (2000) correlation (3.15) compared to flat plate friction coefficients.

that the linear region identified by Hou, Somandepalli, and Mungal (2006) does not extend as far as $\eta \sim 0.5$. Scatter is also observed in the experimental values close to the wall, a feature of the difficulties in converging the Reynolds stresses $\overline{u'v'}$ associated with low sample rates very close to the wall. Despite this the Whittaker smoother obtains a robust and repeatable estimation of T_{xy}. An interesting feature of the F1 case is the small peak at $\eta \sim 0.4$, likely a result of scatter in $\overline{u'v'}$ and the low Reynolds number. However, the

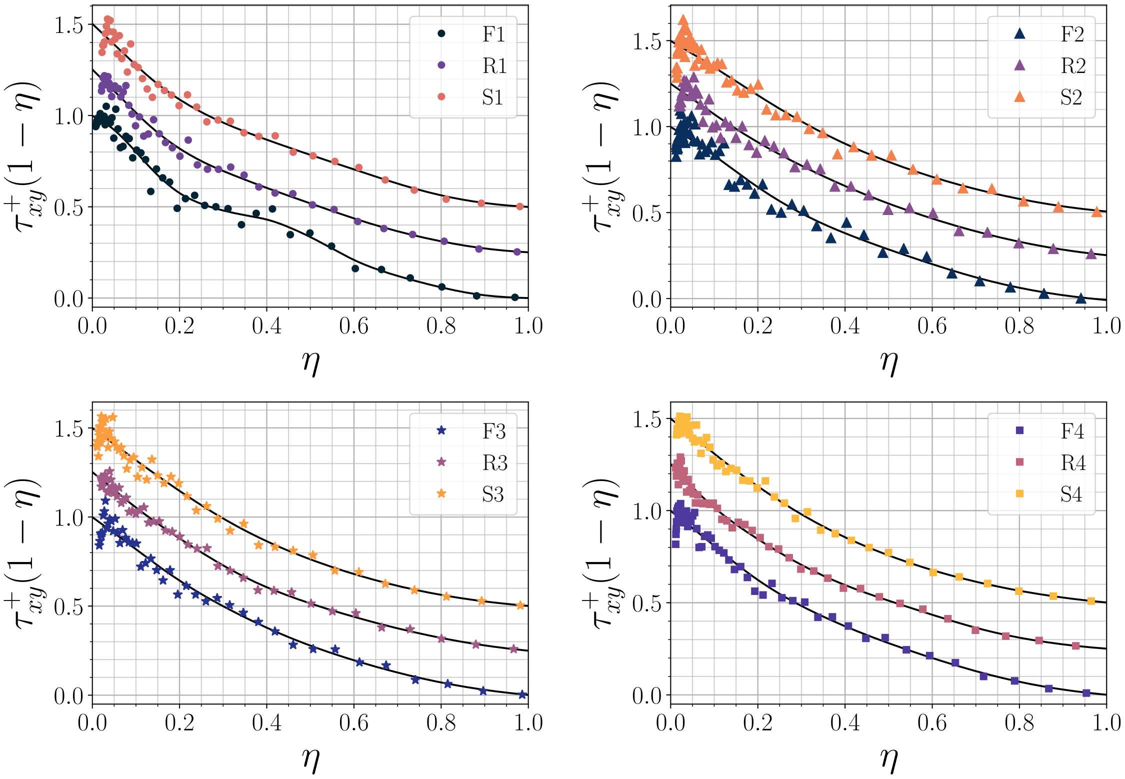

FIGURE 3.7: Weighted shear stress fits. Note that profiles have been offset by 0.25 in the $y-$ axis.

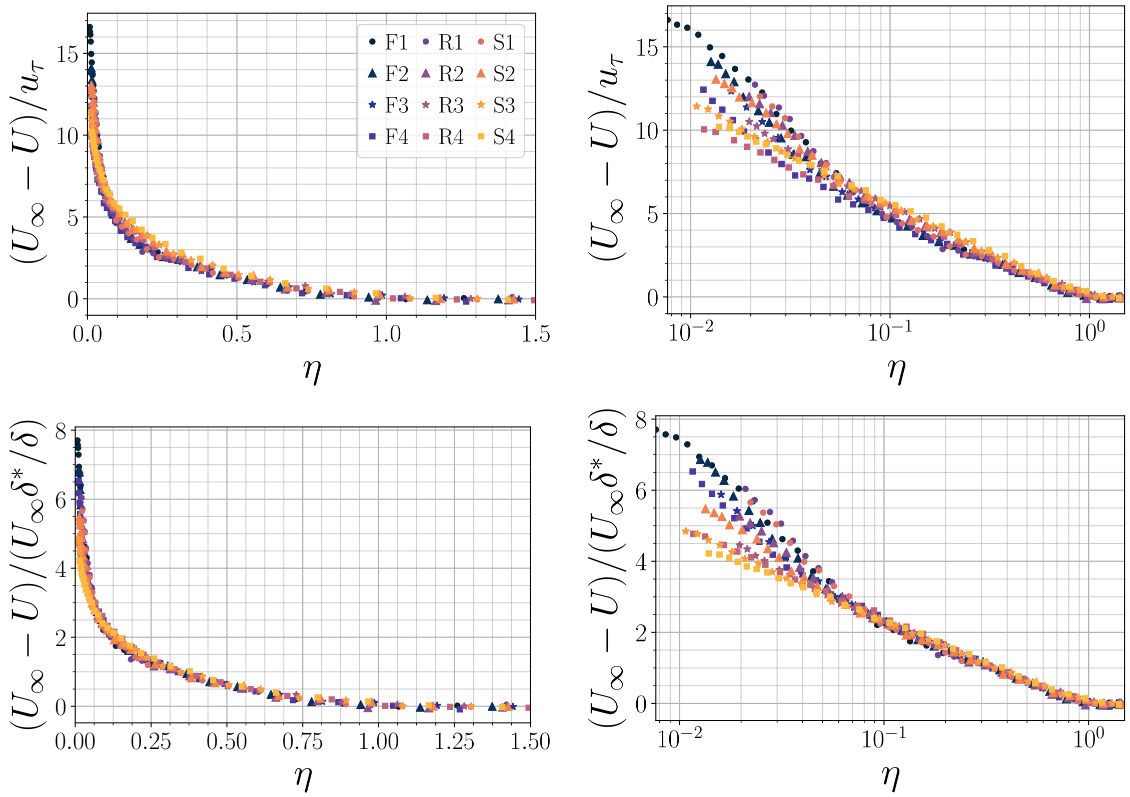

FIGURE 3.8: Outer scaling of velocity profiles.

integral balance used to calculate u_τ is not sensitive to the removal of the points that lead to that bump, since the largest contributions to the integrals are in the near wall region.

Outer scaling of the velocity profiles can be observed in Figure 3.8. The outer scaling $(U_\infty - U)/u_\tau$ shows similar profiles for all data sets in the outer region $\eta \gtrsim 0.1$ with small discrepancies for the high Reynolds number rough plate data. Deviations are known to be a function of the freestream turbulence intensity which alters the wake strength Π (Sharp, Neuscamman, and Warhaft, 2009). Another potential cause is the blockage ratio δ/k_0 where k_0 is the roughness height. When this ratio is small the roughness is large compared to the boundary layer thickness which has been reported to have an effect on the outer flow (Tani, 1987). The boundary layers herein lead to $\delta/k_0 \approx 25$ if k_0 is taken as the maximum roughness height. This is a little lower than the typical limit $\delta/k_0 = 40$ where roughness should have minimal impact on the outer flow (Jiménez, 2004), which could explain the slight discrepancies. When scaled by $(U_\infty - U)/(U_\infty \delta^*/\delta)$, as suggested by Castillo and Walker (2002), all data sets collapse onto a common curve (Figure 3.8).

3.3.2 Comparisons between the plates

Profiles of mean velocity, normalised in wall units, can be observed in Figure 3.9. It is clear that differences between the three plates are characterised by a downwards offset from the flat plate profile, as per any typical roughness. Cases R1 and R2 show negligible deviation from the flat plate profile, indicating hydraulically smooth behaviour. In contrast, the S1 case shows small deviation from the flat plate data, and the S2 case shows a large downward offset. As the Reynolds number increases the differences between the three plates gets larger, with the ribletted denticle plate consistently leading to a smaller downward offset than the smooth denticles, indicative of a lower coefficient of friction. These velocity profiles suggest that while both types of shark skin denticle behave like standard roughness, the ribletted denticles have a significantly lower impact on the flow than the smooth denticles.

Profiles of the RMS velocity fluctuations $\sqrt{\overline{u'u'}}^+$ and $\sqrt{\overline{v'v'}}^+$ can be observed in Figure 3.10. Profiles appear to diverge in the outer region of the flow due to the presence of freestream turbulence. When scaled in mixed units with the freestream turbulence levels subtracted from the RMS velocities (Figure 3.11) profiles collapse in the outer region. Differences in RMS velocities in the inner region are clearly a result of the roughness. Cases R1, S1, and R2 coincide with the flat plate profiles in Figure 3.10, indicative of hydraulically smooth behaviour. As the Reynolds number increases differences become more pronounced. The near-wall peak of $\sqrt{\overline{u'u'}}^+$ is reduced as the Reynolds number increases. The smooth denticles consistently lead to a smaller peak in $\sqrt{\overline{u'u'}}^+$ when compared to the ribletted case, ultimately resulting in a larger deviation from the flat plate. The near-wall peak of $\sqrt{\overline{v'v'}}^+$ is unaffected by the rough surfaces. As the Reynolds number increases the near-wall region lifts, indicative of a weaker impermeability condition at the virtual origin of the rough surface. Consistent with profiles of U^+ the smooth denticles lead to larger deviations from the flat plate profiles when compared to the ribletted denticles.

The principal Reynolds stresses $\overline{u'v'}^+$ are plotted in Figure 3.12. Consistent with the RMS velocity fluctuations differences are negligible between the flat plate and cases R1, S1, and R2. The remaining rough cases indicate similar behaviour to profiles of $\overline{v'v'}^+$; a slight lift in the near-wall region is observed, indicative of the weaker impermeability,

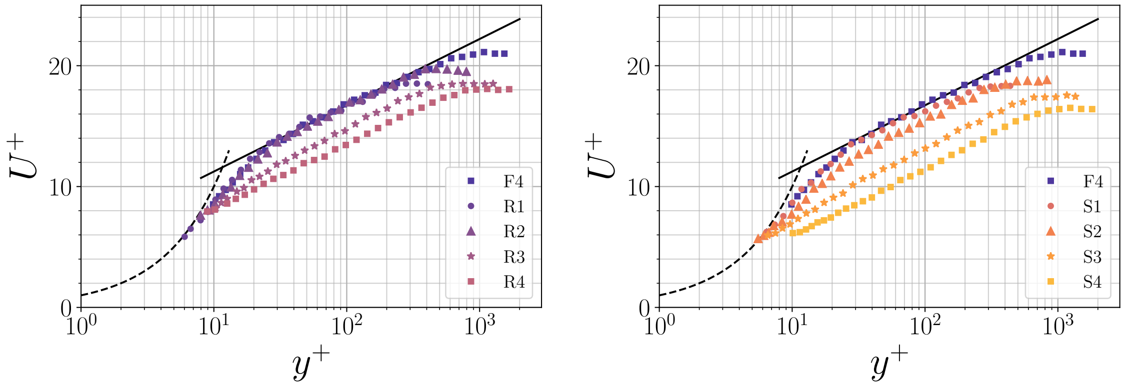

FIGURE 3.9: Mean velocity profiles. Line styles represent linear region (-··-·), and log-law using F4 constants (——).

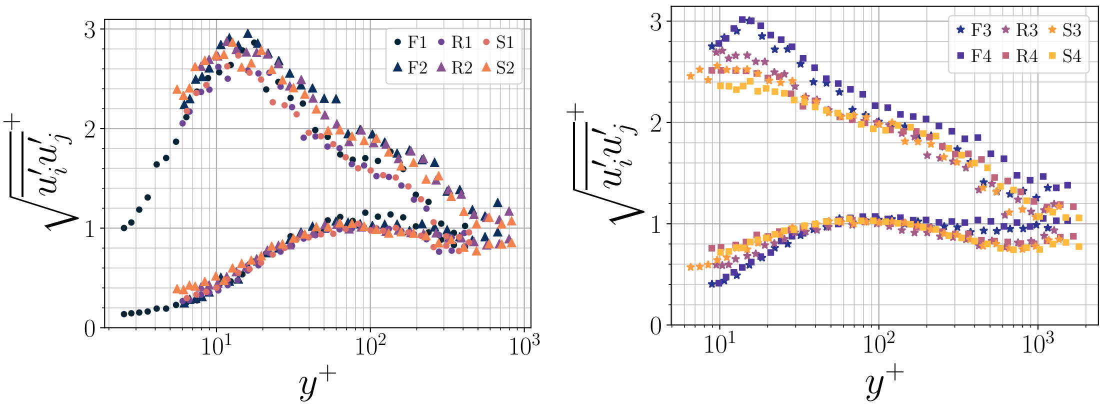

FIGURE 3.10: Reynolds stresses scaled in inner units. Upper curves are $\overline{u'u'}$ component, lower curves are $\overline{v'v'}$ component.

consistent with typical rough wall flows (Schultz and Flack, 2007).

Direct comparisons of the friction coefficients would be inappropriate due to the different Reynolds numbers Re_θ, most pronounced at the lowest Reynolds number cases; F1, S1, and R1 (Table 3.1). The correlation (3.15) of Österlund et al. (2000) is therefore adopted in order to establish empirical reference friction coefficients for the rough plate data sets. The constants of (3.15) are specified as $B_0 = 4.08$ as per Österlund et al. (2000) and $\kappa = 0.42$ as per the high Reynolds number data sets.

The relative change in skin friction coefficient for the ribletted denticle plate can be directly compared to previous studies by plotting its dependence against $s^+ = su_{\tau 0}/\nu$, where $u_{\tau 0}$ is the reference flat plate friction velocity, as per Figure 3.13. Two data sets of Bechert, Hoppe, and Reif (1985) also specify the denticle Angle of Attack (Θ). Data sets that do not report s^+ or an equivalent Reynolds number have been omitted from Figure 3.13 and subsequent analysis (e.g. Zhang et al. (2011a), Chen et al. (2014), and Domel et al. (2018)).

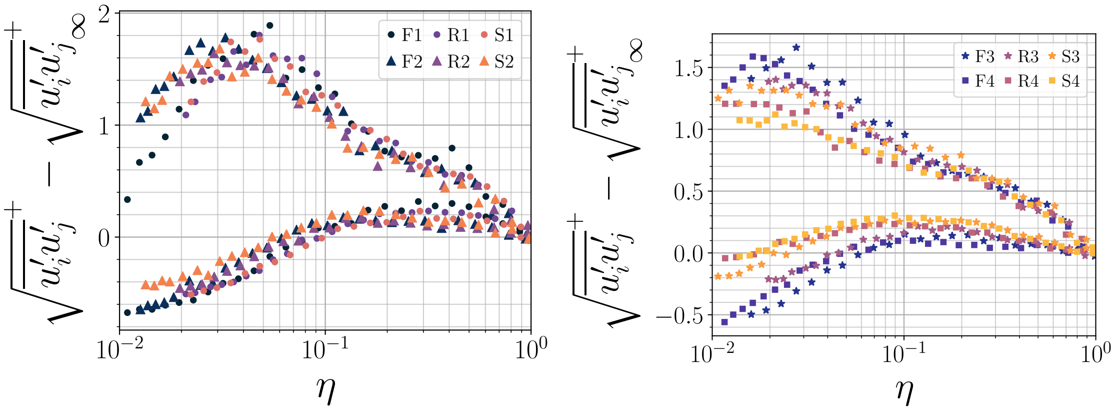

FIGURE 3.11: Reynolds stresses scaled in mixed units. Upper curves are $\overline{u'u'}$ component, lower curves are $\overline{v'v'}$ component.

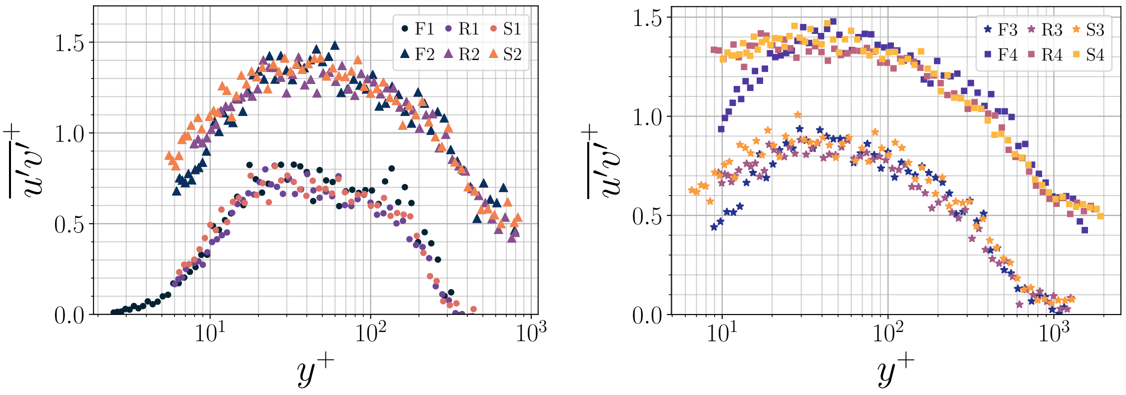

FIGURE 3.12: Reynolds stresses $\overline{u'v'}$ scaled in inner units. Data is offset by 0.5 for clarity.

The ribletted denticle plate leads to a relative change in drag coefficient in reasonable agreement with Wen, Weaver, and Lauder (2014) (Figure 3.13). A maximum drag reduction of 2 % is obtained, a little lower than the 3 % obtained by Bechert et al. (2000) for tightly packed hammerhead denticles. As s^+ increases beyond $s^+ \approx 20$ the ribletted denticles lead to a larger increase in drag than the denticles of Bechert et al. (2000). Levels of drag increase at high s^+ are in reasonable agreement with the silky shark and mako ($\Theta = 5^o$) data of Bechert, Hoppe, and Reif (1985). The largest deviations from the present ribletted denticle plate data are the DNS data of Boomsma and Sotiropoulos (2016) and

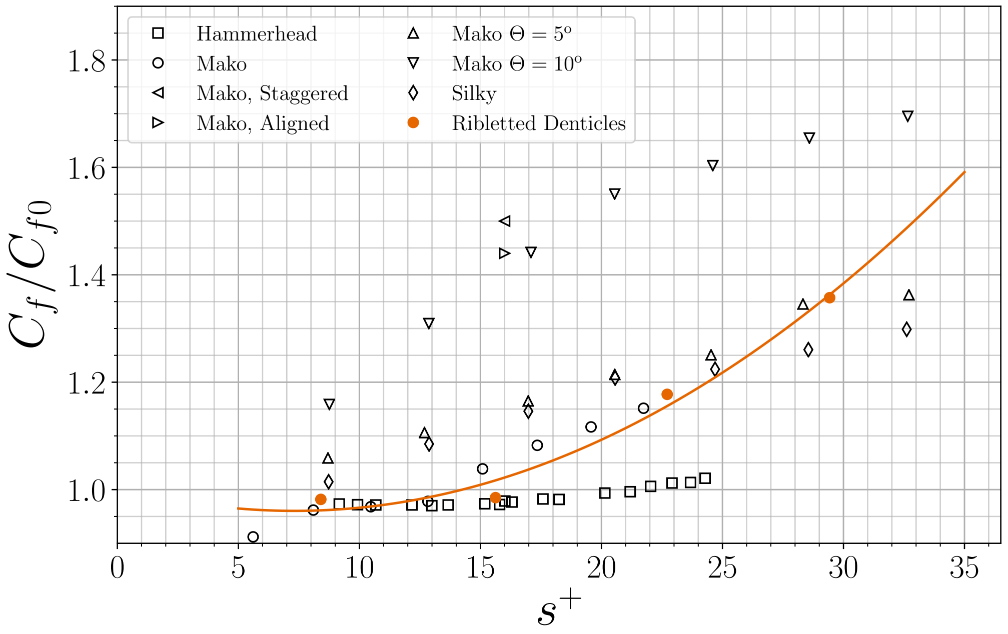

FIGURE 3.13: Relative change in drag for the ribletted denticles with comparisons against literature data. Data are from (◁, ▷) Boomsma and Sotiropoulos (2016), (□) Bechert et al. (2000), (▽, △, ◊) Bechert, Hoppe, and Reif (1985), (○) Wen, Weaver, and Lauder (2014).

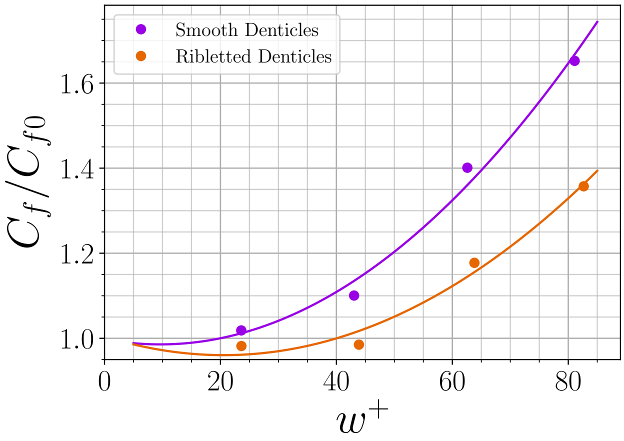

FIGURE 3.14: Relative change in drag for the replica shark skin plates.

the mako ($\Theta = 10^o$) data of Bechert, Hoppe, and Reif (1985) who both predict a significant increase in drag.

Differences in C_f are also presented as a function of dimensionless denticle width w^+ in order to make comparisons between the smooth and ribletted denticle plates (Figure 3.14). The smooth denticles consistently increase drag for the full range of w^+ tested, although only a small drag increase of 2 % is observed at $w^+ \approx 25$, suggesting that it is perhaps marginally hydraulically smooth. As w^+ increases both denticle plates lead to significant increases in drag, with the smooth denticle plate consistently leading to a larger C_f than the ribletted denticles. Furthermore, the differences between the two plates appears to increase as w^+ increases; at $w^+ \approx 80$ the smooth denticles lead to a C_f 20 % higher than the ribletted denticles.

3.3.3 Discussion

The dependence of C_f on s^+ in Figure 3.13 demonstrates that the length scale s is incapable of collapsing all the denticle data sets onto similar profiles. However, discrepancies between data sets can potentially be explained by considering differences in experimental procedures and fabrication techniques. The two largest discrepancies between the drag reduction data (Figure 3.13) reported herein and previous studies are with the DNS data of Boomsma and Sotiropoulos (2016) and the mako ($\Theta = 10^o$) data of Bechert, Hoppe, and Reif (1985). Disagreements between the present ribletted denticles and DNS data of Boomsma and Sotiropoulos (2016) can potentially be explained by considering the differences in denticle height, D_h. While s^+ is very similar between the present ribletted denticles and those of Boomsma and Sotiropoulos (2016) the denticle heights are vastly different: Boomsma and Sotiropoulos (2016) state $D_h = 1.37s$ while the present ribletted denticles have $D_h = 1.02s$. As a result, the denticles of Boomsma and Sotiropoulos (2016) protrude nearly 40 % further into the boundary layer than the present denticles. Furthermore, denticles are more closely packed in the present study. These differences could be the cause of larger pressure forces acting on the denticles of Boomsma and Sotiropoulos (2016) which contribute to a larger drag force.

Differences between the ribletted denticles and those of Bechert, Hoppe, and Reif (1985) could be associated with fabrication techniques. Fabrication methods have substantially improved since the experiments of Bechert, Hoppe, and Reif (1985) due to 3D printing capabilities; Bechert, Hoppe, and Reif (1985) readily admit that the regions between/beneath individual denticles is poorly captured by their fabrication technique. In contrast, the 3D printed models created in the present study are capable of accurately capturing the denticle surfaces (Appendix A).

For small s^+ the ribletted denticle data agree well with that of Bechert et al. (2000), but data sets diverge for $s^+ \gtrsim 20$. This deviation could potentially be explained by considering the forces subject to denticles as they increase in size. At high values of s^+ denticles are relatively large compared to the viscous region of the boundary layer, and so pressure forces on individual denticles may become a dominant contributor to skin friction. For example, 25 % of the friction drag acting on the denticles of Boomsma and Sotiropoulos (2016) was from pressure forces rather than viscous at $s^+ = 16$. One could hypothesise that a reduction of this force is directly linked to how well denticles shield each other from high velocity fluid, and so a loosely packed arrangement of denticles will naturally be subject to larger pressure forces than a tightly packed and overlapping arrangement. These pressure forces will become dominant as s^+ increases, perhaps explaining the divergence between the present data set and that of Bechert et al. (2000). The hammerhead denticles of Bechert et al. (2000) are very tightly packed, overlapping, and have 5 riblets on the denticle crown. In contrast, the ribletted denticles herein are more loosely packed and have three riblets on the crown. Therefore the denticles fabricated in this study are more three dimensional than those of Bechert et al. (2000) which more closely resemble a ribletted plate. At low s^+ viscous forces are much larger than pressure, and so the two types of denticle lead to reasonably similar levels of skin friction. As s^+ increases the present ribletted denticles become more exposed to high speed fluid while those of Bechert et al. (2000) remain shielded due to the overlapping, thus causing the divergence between the two data sets.

The turbulent boundary layers measured over the smooth denticles indicate behaviour typical of sand-grain roughness. At the lowest Reynolds number, corresponding to $w^+ \approx 25$, drag is increased by just 2 % for the smooth denticle array when compared to the flat plate, suggesting that the flow is close to hydraulically smooth. As w^+ increases, drag increases substantially. In contrast the ribletted denticles reduce drag by a modest 2 % relative to the flat plate up to $w^+ \approx 50$. As w^+ increases further drag is increased, but consistently less so than the smooth denticles. At $w^+ \approx 80$ drag is over 20 % higher for the smooth denticles when compared to the ribletted denticles. While profiles of C_f/C_{f0}

as a function of w^+ are similar for the smooth and riblетted denticles, they only appear to collapse as w^+ decreases to zero (an unsurprising result for vanishingly small roughness). Differences between the plates appear to increase as w^+ increases, suggesting that perhaps a length scale other than w should be sought. However, when scaled by mean or average denticle heights the trends observed in Figure 3.14 are consistent, due to the similarity in length scales between the smooth and ribletted denticles.

It is also important to consider experimental uncertainty when interpreting the relative changes in drag for the different surfaces (Figure 3.14). While repeatability errors for u_τ are just 1.5 % for the integral-stress method this is of a similar magnitude to the changes in drag coefficient for both denticle plates at small w^+. The drag reduction of 2 % for the ribletted denticles, relative to the flat plate, may therefore be somewhat due to uncertainty in the friction velocity. However, the differences in friction between the two denticle plates are substantial, especially at large w^+. As a result the ribletted denticles have a significantly lower impact on the turbulent boundary layer than smooth denticles.

These results suggest that the three-dimensionality of denticles is detrimental to flat plate skin friction drag, and perhaps denticles have not evolved to the benefit of drag reduction for attached boundary layer flows. Of course there could be other hydrodynamic functions of shark skin denticles. The ability of some denticles to prevent boundary layer separation via bristling is one such function (Lang et al., 2014). However, when riblets are present on the denticle crest the adverse effects of denticles are significantly diminished. Perhaps these riblet features have evolved as a secondary mechanism to control drag, while the primary purpose of the sharkskin denticles lies in their ability to prevent flow separation (Fletcher et al., 2014), or perhaps for non-hydrodynamic functions such as anti-fouling and abrasion resistance (Reif, 1985).

3.4 Conclusions

Through the use of 2D LDA the influence of both smooth and ribletted shark skin denticles on the turbulent boundary layer have been investigated for the first time. This has enabled the identification of the role of riblets in combination with complex 3D denticles. Two large arrays of denticles were 3D printed onto a flat plate submerged in a water flume. One set of denticles was smooth, based on an early shark ancestor *Poracanthodes sp.*, while the other had mako-based riblets added to the denticle crown, but maintained similar dimensions to the smooth denticle. Four boundary layer profiles were measured over each array of denticles, and a flat reference plate, allowing capture of a wide range of dimensionless riblet spacings: $s^+ \approx 8 - 30$. Profiles of the mean velocity and Reynolds stresses indicate that smooth denticles behave like a typical rough surface; effects on the mean streamwise velocity profile are characterised by a downwards shift of the overlap region, and the near-wall peak of $\overline{u'u'}^+$ is reduced as the dimensionless denticle width, w^+, increases. When riblets are added to the denticle crown the adverse effects of the 3D roughness are significantly reduced. A modest drag reduction of 2 % is observed for the riblетted denticles, which was maintained up to $w^+ \approx 50$ and $s^+ \approx 18$. In contrast the smooth denticle array led to an increased drag for all w^+ tested. At the highest w^+ the smooth denticles increased drag 20 % more compared to the ribletted.

These results demonstrate, for the first time, the role of riblets on scales. Smooth unribletted scales showed an increase in drag relative to a smooth flat plate, however, the incorporation of riblets on the scales led to a modest drag reduction of 2 %. The present study now enables us to conclude that riblets evolved as a mechanism to reduce or eliminate the skin friction increase due to the presence of scales (denticles). The combination of scales and riblets therefore appears to be relatively hydrodynamically efficient in terms of skin-friction drag, whilst also acting to maintain the attachment of the boundary layer around the curved body (Fletcher et al., 2014), and providing the other advantages associated with scales, anti-fouling, abrasion resistance, and defence against parasites (Reif, 1985).

Chapter 4

Numerical errors at the wall: On the sensitivity of RANS models to near wall cell size

The application of Reynolds Averaged Navier-Stokes (RANS) closures to riblets and shark skin denticles has been limited to date, with predictions often leading to non-physical solutions or suffering from poor documentation (discussed in Chapter 2). Before attempting to simulate flows over these complex rough surfaces it is important to consider the predictive capabilities and numerical properties of turbulence models in order to ensure changes in solutions can be directly attributed to the roughness geometry. Of particular importance is the discretisation error associated to near-wall cells. Consider a study of the flow over a ribletted surface with a dimensionless riblet spacing $s^+ = su_{\tau 0}/\nu$ (where $u_{\tau 0}$ is a reference flat plate friction velocity, s is the riblet spacing, and ν the kinematic viscosity) varying between $5 < s^+ < 50$ at a constant bulk flow Reynolds number. Over this range of s^+ the riblet spacing must vary by an order of magnitude given that the reference friction velocity $u_{\tau 0}$ is constant. For this to be the case the near-riblet cells must grow and shrink with the riblet size. As a result the near-wall cell sizes will vary significantly over the full range of s^+, especially when normalising these by a local friction velocity. Note that the drag reduction obtained for riblets in the viscous regime (see e.g. Figure 2.5) is of the order $1 - 5\,\%$ before reaching the optimum regime. For many engineering problems a discretisation error of $1\,\%$ on the friction coefficient would be neglected, but for riblets this error could significantly pollute drag reduction solutions. It is therefore important to quantify the sensitivity of RANS closures to the near-wall cell size. This is achieved through both analytical techniques and numerical simulations.

4.1 Introduction

Several decades have been spent developing turbulence models suitable for efficient integration through the boundary layer. While there is a vast range of different models, they generally require the solution to a transport equation for a scale determining variable;

the rate of turbulent dissipation, ε, or the specific rate of dissipation, ω. It is the choice and impact of this variable that is the focus of this chapter; in particular, how sensitive are boundary layer predictions to the dimensionless near wall cell size, $y_1^+ = u_\tau y_1/\nu$ (where u_τ is the friction velocity, ν is the fluid kinematic viscosity, and y_1 is the distance between the near-wall cell centre and the wall), and can deficiencies be mitigated against by solving for different scale determining variables?

Recently, Eça, Pereira, and Vaz (2018) investigated the 'rule of thumb', $y_1^+ \simeq 1$, by performing an extensive grid refinement study on a flat plate boundary layer, the NACA 0012 aerofoil, and the KVLCC2 tanker. Simulations were performed on several sets of geometrically similar grids, where the sensitivity to the near-wall cell size and the refinement level could be established. Eça, Pereira, and Vaz (2018) found that the $k-\omega$ SST (Menter, Kuntz, and Langtry, 2003) model, widely popular in engineering simulations (Menter, 2009), is extremely sensitive to the near wall cell sizes. Flat plate boundary layer results from the three finest sets of grids indicated that in order to achieve the same degree of mesh independence as the one equation model of Spalart and Allmaras (1992) and the two equation $k-\sqrt{k}l$ model of Menter, Egorov, and Rusch (2006), a cell size of an order of magnitude smaller was required for the ω based model. All of the test cases studied by Eça, Pereira, and Vaz (2018) led to the conclusions that grid dependency errors for the friction coefficient could reach at least 5 % for the SST model when $(y_1^+)_{avg} \approx 1$.

This is a disturbing result given that ω based models have been shown to predict boundary layers much better than their ε based alternatives (Wilcox, 2006), and have subsequently seen extensive use for the prediction of such flows (Menter, 2009). Eça, Pereira, and Vaz (2018) conclude by suggesting that simulations should either be carried out with $y_1^+ \simeq 0.1$, or a different turbulence model should be used. This conclusion is somewhat unsatisfying since such a strong limitation on near wall y_1^+ is not feasible for most engineering problems.

The significance of a grid dependency error of 5 % on the coefficient of friction is especially obvious when considering flows where viscous drag is large, for example the flow over aerofoils (Fischer and Ash, 1974). Small changes to the size of the surface elements could lead to differences in the predicted drag coefficient that are of the same order as differences observed when the aerofoil geometry is changed. The prediction of drag reducing surfaces may also be affected by this error. For example, ribletted surfaces have been experimentally shown to reduce viscous drag by up to 10 % (Dean and Bhushan, 2010); any attempt made to predict such a flow using an ω based model will have solutions significantly polluted by numerical error.

This chapter therefore aims to extend previous work on y_1^+ sensitivity to several other turbulence models, selected based on their different approaches to modelling boundary layer flows and tackling the closure problem at the wall. Analysis will be extended to boundary layer resolving ε based models which, like ω alternatives, also require analytical closure at the cells nearest the wall rather than at the domain boundary. It is currently unknown whether ε based algebraic closures also exhibit the same numerical errors observed by Eça, Pereira, and Vaz (2018).

In addition to this, the $k-\tau$ and $k-g$ models of Kalitzin, Gould, and Benton (1996), and the $k-\omega'$ model of Tomboulides et al. (2018), are promising alternatives to the $k-\omega$ model by solving for either $\tau = 1/\beta^*\omega$, where β^* is an empirical constant, $g = \sqrt{\tau}$, or $\omega' = \omega - \omega_w$, where ω_w is the leading order part of ω near the wall. These models are equivalent to $k-\omega$ but reduce to Dirichlet boundary conditions for the scale determining variables which could remove the near-wall numerical errors associated with ω models.

This chapter will investigate these models using both analytical and numerical techniques. The analytical methods will identify how the different models and variables behave in the near wall limit, and how this changes when introducing modifications such as damping functions or variable limiters. Numerical experiments will also be carried out in order to establish the influence of y_1^+ on the boundary layer solutions of a range of different turbulence models. These will be carried out on a 1D fully developed channel flow at a moderate bulk flow Reynolds number of $Re_b = 10\,864$, equating to a shear Reynolds number of $Re_\tau \approx 590$. This has several advantages over a flat plate developing boundary layer: firstly, since the grid is 1D, much smaller cell sizes will be able to be achieved. In addition to this, values of y_1^+ vary significantly over a flat plate developing boundary layer which therefore requires maximum/average values of y_1^+ to be used for analysis. A 1D grid will alleviate this issue by having a single value of y_1^+ at the wall for each grid. A quantification of the y_1^+ dependency error will allow engineers to select appropriate turbulence models based on how large a mesh dependency error they can accept. By covering a range of different turbulence models conclusions will be applicable to all models that reduce to the same asymptotic behaviour near the wall.

4.2 Model definitions and near wall behaviour

Several turbulence models are adopted in the present study, selected based on their different approaches to modelling near wall flow. Their limiting behaviour near the wall is investigated in order to establish differences between them, boundedness, and the asymptotic behaviour of k and the scale determining variable. This section also investigates the different methods of 'forcing' the correct asymptotic behaviour of k, whether by introducing time-scale limiters, damping terms in the transport equations, or damping individual model coefficients.

The models investigated are the $k-\omega$ model of Wilcox (1998), the low Reynolds number $k-\varepsilon$ model of Lam and Bremhorst (1981), the $k-\omega'$ model of Tomboulides et al. (2018), a modified version of the $k-\tau$ model of Kalitzin, Gould, and Benton (1996), a modified $k-g$ model of Kalitzin, Gould, and Benton (1996), and the $\overline{v^2}-f$ model of Durbin (1991), with the suggested modifications of Lien and Kalitzin (2001) and Davidson, Nielsen, and Sveningsson (2003). These are chosen due to the different ways in which their boundary conditions are treated, although the general form of the equations in the near wall limit is often consistent between many other models (i.e. ω based models such as SST and BSL reduce to the same form as that of Wilcox (1998) near the wall).

The models identified above are derived from the turbulent viscosity hypothesis which is used to close the Reynolds stresses in the Reynolds Averaged Navier-Stokes (RANS) equations:

$$\frac{D\overline{U}_j}{Dt} = -\frac{\partial \overline{P}}{\partial x_j} + \nu \nabla^2 \overline{U}_j - \frac{\partial \overline{u_i' u_j'}}{\partial x_i}, \tag{4.1}$$

and,

$$\frac{\partial \overline{U}_i}{\partial x_i} = 0, \tag{4.2}$$

where $\overline{P}$ is the ensemble averaged kinematic pressure, ν the kinematic molecular viscosity, $\overline{U}_i$ the ensemble averaged fluid velocity, and $u_i' = u_i - \overline{U}_i$ is the instantaneous velocity fluctuation. Density, ρ, is assumed constant and subsequently treated through the kinematic variables ν and $\overline{P}$. The Reynolds stresses, $-\overline{u_i' u_j'}$, are closed by

$$-\overline{u_i' u_j'} = 2\nu_t S_{ij} - \frac{2}{3} k \delta_{ij}, \tag{4.3}$$

where

$$S_{ij} = \frac{1}{2}\left(\frac{\partial \overline{U}_i}{\partial x_j} + \frac{\partial \overline{U}_j}{\partial x_i}\right) \tag{4.4}$$

is the symmetric velocity gradient tensor, $k = \frac{1}{2}\overline{u_i' u_i'}$ is the turbulent kinetic energy, and ν_t is the kinematic turbulent viscosity, the form of which is dependent on the adopted turbulence model. The models investigated in this chapter all solve for the transport of k and a scale determining variable, such as ε (in the case of $\overline{v^2} - f$, two additional transport equations are also solved). The transport of k is consistent between all turbulence models:

$$\frac{Dk}{Dt} = \mathcal{P} - \varepsilon + \frac{\partial}{\partial x_j}\left[\left(\nu + \frac{\nu_t}{\sigma_k}\right)\frac{\partial k}{\partial x_j}\right], \tag{4.5}$$

where the production of turbulent kinetic energy, $\mathcal{P} = -\overline{u_i' u_j'}\frac{\partial \overline{U}_i}{\partial x_j}$.

Near-wall behaviour is investigated by analysing a statistically steady, fully developed boundary layer flow with $\overline{U}_1(y) = U$ being the streamwise velocity. It is assumed that the flow is fully developed ($\partial/\partial x = 0$) and steady ($\partial/\partial t = 0$), which through continuity implies that $\overline{U}_2 = V = 0$. These assumptions will be adopted in the following sections where each of the selected models is addressed.

4.2.1 Near wall behaviour of ε based models

In the viscous sub-layer, ε balances viscous diffusion such that the transport of k (4.5) reduces to

$$\varepsilon \sim \nu \nabla^2 k, \tag{4.6}$$

which can subsequently be used to investigate the near wall behaviour of the scale determining variable. The no-slip condition leads to the following Taylor Series expansion of U and k:

$$\begin{aligned} U &\sim A_1 y + A_2 y^2 + \ldots, \\ k &\sim a_1 y^n + a_2 y^{n+1} + \ldots, \end{aligned} \tag{4.7}$$

where A_i and a_i are unknown coefficients. Note that the theoretical value of $n = 2$ is not guaranteed, and is dependent on the near wall solution of the scale determining variable (Wilcox, 2006). Substituting (4.7) into (4.6) leads to

$$\varepsilon \sim \nu[(n-1)na_1 y^{n-2} + n(n+1)a_2 y^{n-1} + (n+1)(n+2)a_3 y^n + \ldots]. \tag{4.8}$$

A special case arises for $n < 2$ where both ε and the leading order terms in the transport of k (4.5) are unbounded (i.e. grow with decreasing wall distance). This is precisely the result of the standard, unmodified, high Reynolds number $k - \varepsilon$ model of Launder and Spalding (1974) of which the transport of ε (See Appendix C.1) reduces to

$$0 = \underbrace{C_{\varepsilon 1} \frac{\varepsilon}{k} \nu_t \left(\frac{\partial U}{\partial y} \right)^2}_{\mathcal{O}(y^n)} - \underbrace{C_{\varepsilon 2} \frac{\varepsilon^2}{k}}_{\mathcal{O}(y^{n-4})} + \underbrace{\nu \frac{\partial^2 \varepsilon}{\partial y^2}}_{\mathcal{O}(y^{n-4})} . \tag{4.9}$$

Here the destruction of ε balances diffusion as $y \to 0$. Substituting (4.7) and (4.8) into (4.9) one obtains

$$C_{\varepsilon 2} \frac{\nu^2 n^2 (n-1)^2 a_1^2 y^{2n-4}}{a_1 y^n} \approx \nu^2 (n-3)(n-2)(n-1) n a_1 y^{n-4}, \tag{4.10}$$

to leading order. This reduces to a quadratic equation for n dependent only on $C_{\varepsilon 2}$. With $C_{\varepsilon 2} = 1.83$, typical for the standard $k - \varepsilon$ model (Launder and Sharma, 1974), the equation is satisfied by $n = 1.39$ (a result also obtained by the perturbation analysis of Wilcox (1998)). The poor prediction of n is partly why the standard $k - \varepsilon$ model is typically used with a log-law type wall function.

The near wall behaviour of the transport of ε changes significantly when modified as per the model of Lam and Bremhorst (1981) (Appendix C.1) or the $\overline{v^2} - f$ model of Durbin (1991) (Appendix C.7). Lam and Bremhorst (1981) introduce damping functions into the transport of ε; with some manipulation one finds that the transport of ε can only balance when $n = 2$:

$$0 = \underbrace{C_{\varepsilon 1} f_1 \frac{\varepsilon}{k} \nu_t \left(\frac{\partial U}{\partial y} \right)^2}_{\mathcal{O}(1)} - \underbrace{C_{\varepsilon 2} f_2 \frac{\varepsilon^2}{k}}_{\mathcal{O}(y^6)} + \underbrace{\nu \frac{\partial^2 \varepsilon}{\partial y^2}}_{\mathcal{O}(1)} . \tag{4.11}$$

In this case the value of n is ensured without dependence on the values of the empirical coefficients, since no other value of n allows (4.11) to balance. The damping functions also change the dominant balance in the transport of ε; instead of diffusion balancing destruction, it balances production, and therefore requires that $\nabla^2 \varepsilon < 0$. Note that damping functions are not applied to the diffusion term of (4.11) and yet it is $\mathcal{O}(1)$ rather than $\mathcal{O}\left(y^{n-4}\right)$ as per (4.9). This is due to the cancelled terms in the differentiation of (4.8) when $n = 2$.

In addition to achieving the correct scaling of k, the Lam and Bremhorst (1981) model is also bounded near the wall, whereby dominant terms are $\mathcal{O}(1)$. To leading order, (4.8) reduces to

$$\varepsilon \approx \frac{2\nu k}{y^2} + \mathcal{O}\left(y\right) \tag{4.12}$$

near the wall when $n = 2$. Despite tending to a finite value at the wall (since $k \sim y^2$) ε cannot be determined at $y = 0$ and must therefore be closed using either further modifications (for example the approach of Launder and Sharma (1974) who solve for $\tilde{\varepsilon} = \varepsilon - 2\nu(\nabla\sqrt{k})^2$), simplifications, or algebraic closures at the cells nearest the wall. The algebraic closure approach fixes ε at the cell centre closest to the wall:

$$\varepsilon_1 = \frac{2\nu k_1}{d^2} \tag{4.13}$$

where d is the distance to the wall. This method ensures correct scaling of k and ε although requires the solution to the transport of k (4.5). The typical approach adopted when using the model of Lam and Bremhorst (1981) is to specify Neumann boundary conditions:

$$n_i \frac{\partial \varepsilon}{\partial x_i} = 0 \tag{4.14}$$

at the wall, where n_i is the wall normal direction. This presents an issue when considering the balance of (4.11), whereby additional terms in the expansion of ε are required (i.e $\nabla^2 \varepsilon$ cannot be $\mathcal{O}(1)$ with Neumann boundary conditions). However, Patel, Rodi, and Scheuerer (1985) have shown that boundary layer predictions are insensitive to these boundary conditions due to the imposed damping functions; this conclusion will be investigated numerically in Section 4.3. It should also be noted that the damping functions adopted by the Lam-Bremhorst $k - \varepsilon$ model are a function of the wall-normal distance, y_w, which can be complicated to calculate when considering complex geometries.

The modifications to the transport of ε (4.9) adopted by the $\overline{v^2} - f$ model place a lower limit on the timescale k/ε such that it is clipped at the Kolmogorov timescale, $\tau_\eta =$

$C_T\sqrt{\nu/\varepsilon}$ where C_T is an empirical constant. Assuming $\overline{v^2}$ takes the form

$$\overline{v^2} \sim b_1 y^m + b_2 y^{m+1} + \ldots, \tag{4.15}$$

one finds that near the wall the transport of ε (See Appendix C.7) is balanced when $n = 2$ by

$$0 = \underbrace{\frac{C'_{\varepsilon 1}}{T}\nu_t\left(\frac{\partial U}{\partial y}\right)^2}_{\min\left[\mathcal{O}\left(y^{\frac{10-m}{2}}\right);\,\mathcal{O}\left(y^{\frac{2+m}{2}}\right)\right]} - \underbrace{C_{\varepsilon 2}\frac{\varepsilon}{T}}_{\mathcal{O}(1)} + \underbrace{\nu\frac{\partial^2\varepsilon}{\partial y^2}}_{\mathcal{O}(1)}. \tag{4.16}$$

This behaviour arises since $T = \max[k/\varepsilon; \tau_\eta]$ becomes $\mathcal{O}(1)$ near the wall, requiring that ε must be of the same order as $\nabla^2\varepsilon$ in order for (4.16) to balance. This also leads to no unbounded terms in the transport equations for k and ε, without requiring damping functions, or the computation of y_w. The authors of this model recommend using the algebraic closure approach of (4.13), consistent with the correct asymptotic scaling of k.

4.2.2 Near wall behaviour of the $k-\omega$ model

The $k-\omega$ model of Wilcox (1998) is detailed in Appendix C.2. Limiting behaviour of ω is derived from (4.6) using the asymptotic expansion of k (4.7):

$$\beta^* k\omega = \varepsilon \sim \nu\nabla^2 k, \tag{4.17}$$

which reduces to

$$\omega \sim \frac{(n-1)n\nu}{\beta^* y^2} + \frac{2na_2\nu}{\beta^* a_1 y} + \mathcal{O}(1). \tag{4.18}$$

Substituting this into the transport of ω (Appendix C.2) leads to

$$0 = \underbrace{\gamma\left(\frac{\partial U}{\partial y}\right)^2}_{\mathcal{O}(1)} - \underbrace{\beta\omega^2}_{\mathcal{O}(y^{-4})} + \underbrace{\nu\frac{\partial^2\omega}{\partial y^2}}_{\mathcal{O}(y^{-4})}. \tag{4.19}$$

Note that the dominant terms in this balance are unbounded, growing like $\mathcal{O}\left(y^{-4}\right)$. n can be determined by considering the balance of leading order terms, reducing to the quadratic:

$$\frac{\beta}{\beta^*}(n-1)n \sim 6. \tag{4.20}$$

For the standard $k-\omega$ model the coefficients are $\beta^* = 0.09$ and $\beta = 0.072$ (Wilcox, 1998) which leads to $n \sim 3.28$. This is clearly quite far from the asymptotic solution for k (despite this reasonable predictions of the velocity profile are still achievable (Wilcox, 1998)). The low Reynolds number corrections of Wilcox (2006) (Appendix C.2) changes the limiting behaviour such that as $y \to 0$, $Re_T \to 0$, and $\beta^* \approx \beta^*_\infty \frac{100}{27}\beta$. When this is substituted into the quadratic one obtains $n = 2$. It should be noted that there is a clear difference between the damping functions of the $k - \omega$ model and those of the Low Reynolds number $k - \varepsilon$ models; the $k - \omega$ model simply damps the coefficients of the equation between one finite value and another, whereas the $k - \varepsilon$ models significantly change the limiting behaviour of the ε transport equation. In addition to this, the damping functions of Wilcox (2006) don't require the calculation of y_w, unlike the $k - \varepsilon$ model of Lam and Bremhorst (1981).

Algebraic closures at the near-wall cells are required to evaluate ω near the wall which are derived from the transport of ω (4.19) in order to eliminate the dependence on n. The leading order balance of (4.19) can be rearranged to

$$\omega \approx \frac{\nu}{\beta\omega}\frac{\partial^2\omega}{\partial y^2}. \tag{4.21}$$

Substituting (4.18) into this expression yields another asymptotic expansion for ω:

$$\omega \sim \frac{6\nu}{\beta y^2} - \frac{8a_2\nu}{\beta a_1(n-1)y} + \mathcal{O}(1). \tag{4.22}$$

Equating the leading order terms of (4.18) and (4.22) leads to the quadratic equation for n, (4.20). The near-wall algebraic closure typically adopted for ω (Wilcox, 1998) is derived from the leading order term of (4.22):

$$\omega_1 = \frac{6\nu}{\beta d^2}. \tag{4.23}$$

where ω_1 is the value of ω at the cell centre closest to the wall. Of particular note is the singular behaviour of ω, which grows like $1/y^2$. Wilcox (2006) discusses the issues with discretising such functions, concluding that without care, the variable in question can be vastly over-predicted; over-predicting ω near the wall can have noticeable effects in the outer portions of the boundary layer. Wilcox (2006) suggests that this problem can be overcome by either using 'slightly-rough' wall boundary conditions, or by fixing the value of ω for all cells below $y^+ \approx 2.5$ (at which point the asymptotic solution is no longer valid). For complex geometries this second option is complicated to implement. Not only this, but enforcing such a condition is solution dependent which could lead to oscillatory solutions between consecutive iterations (Eça and Hoekstra, 2004). The alternative to enforcing (4.23) is to adopt slightly-rough wall boundary conditions, where the value of ω at the wall, ω_0, is related to a surface roughness height, k_s, by (Wilcox, 2006)

$$\omega_0 = \frac{40000\nu}{k_s^2}. \tag{4.24}$$

This method essentially fixes ω to a constant value on the wall. Wilcox (2006) argues that as long as k_s^+ is sufficiently small to be hydraulically smooth ($k_s^+ \lesssim 5$) the solution will still be valid for a smooth wall, but numerical errors will be significantly reduced as long as ω_1 is lower than that of the asymptotic solution (4.18). In essence, this method fixes the surface value of ω high enough that its approximation won't affect the freestream, but low enough to avoid discretisation errors. However, Eça and Hoekstra (2004) show that the use of slightly-rough wall boundary conditions does not reproduce the smooth wall solution, and is actually more sensitive to near wall cell size than its alternative.

4.2.3 Alternatives to the $k - \omega$ model

The recent model of Tomboulides et al. (2018) (Appendix C.3) decomposes ω into $\omega = \omega' + \omega_w$, where

$$\omega_w = \frac{6\nu}{\beta y_w^2}. \tag{4.25}$$

The motivation behind this decomposition is to avoid the numerical differentiation of the singularity, ω_w, by treating it algebraically. From inspection of (4.22) the behaviour of ω' is not entirely obvious, due to its dependency on the unknown coefficients a_1 and a_2:

$$\omega' = \omega - \omega_w \sim -\frac{8a_2\nu}{\beta a_1(n-1)y} + \mathcal{O}(1) \tag{4.26}$$

Tomboulides et al. (2018) state that $\omega' = 0$ at the wall, although this requires several terms in (4.26) to be zero. ω' can be written more generally:

$$\omega' = c_1 y^p + c_2 y^{p+1} + \cdots \tag{4.27}$$

Near the wall, the transport of ω' (see Appendix C.3) balances like

$$0 = \underbrace{\gamma\left(\frac{\partial U}{\partial y}\right)^2}_{\mathcal{O}(1)} - \underbrace{\beta\omega'^2}_{\mathcal{O}(y^{2p})} - \underbrace{\beta\omega_w^2}_{\mathcal{O}(y^{-4})} \underbrace{-2\beta\omega'\omega_w}_{\mathcal{O}(y^{p-2})} + \underbrace{\nu\frac{\partial^2\omega_w}{\partial y^2}}_{\mathcal{O}(y^{-4})} + \underbrace{\nu\frac{\partial^2\omega'}{\partial y^2}}_{\mathcal{O}(y^{p-2})}. \tag{4.28}$$

Through substitution of $\omega_w = 6\nu/\beta y_w^2$, and noting that for a boundary layer flow $y = y_w$, one observes that the leading order terms balance exactly and subsequently cancel from the balance of (4.28). This leads to

$$0 = \underbrace{\gamma\left(\frac{\partial U}{\partial y}\right)^2}_{\mathcal{O}(1)} - \underbrace{\beta\omega'^2}_{\mathcal{O}(y^{2p})} - \underbrace{\frac{12\nu\omega'}{y^2}}_{\mathcal{O}(y^{p-2})} + \underbrace{\nu\frac{\partial^2\omega'}{\partial y^2}}_{\mathcal{O}(y^{p-2})}. \tag{4.29}$$

By examining the possible balances of (4.29) one finds that the solution implied by the expansion of ω (4.22), $p = -1$, is not valid. Upon further inspection the only consistent solution is $p = 2$, resulting in

$$\gamma \left(\frac{\partial U}{\partial y} \right)^2 - \frac{12\nu\omega'}{y^2} + \nu \frac{\partial^2 \omega'}{\partial y^2} \sim 0. \tag{4.30}$$

c_1 can be determined by noting that $U^+ = y^+$ in the near wall region:

$$c_1 = \frac{\gamma u_\tau^4}{10\nu^3}, \tag{4.31}$$

which leads to

$$\omega' \sim \frac{\gamma u_\tau^4}{10\nu^3} y^2 + \mathcal{O}\left(y^3\right). \tag{4.32}$$

This clearly suggests that several coefficients of (4.22) are zero, and also means that the Dirichlet boundary conditions adopted by Tomboulides et al. (2018) are valid and consistent with the theoretical scaling of ω'.

However, the model is not only dependent on accurately calculating the wall-normal distance, y_w, but also its first and second derivatives (see Appendix C.3). Tomboulides et al. (2018) argue that since the terms involving y_w and its derivatives are only dominant near the wall, any discontinuities in derivatives of y_w further from the wall will have negligible influence on solutions. This argument is supported by noting that terms involving derivatives of y_w scale like y^{-3} or y^{-4}, but the authors fail to note that in the log-law region of the boundary layer this is not so much smaller than the dominant terms in the transport of ω'. This can be investigated by taking the log-law solutions noted by Wilcox (2006), derived from perturbation methods:

$$U^+ = \frac{1}{\kappa} \log y^+ + B, \qquad \nu_t = u_\tau \kappa y, \qquad k = \frac{u_\tau^2}{\sqrt{\beta^*}}, \qquad \omega = \frac{u_\tau}{\sqrt{\beta^*}\kappa y}. \tag{4.33}$$

Substituting these relations into the transport of ω' one finds that the production and destruction terms dominate in the log-region. By substituting these relationships into the transport equation for ω' (Appendix C.3) one finds that the largest term containing ω_w is $(\nu_t/\sigma)\nabla^2\omega_w$. With some manipulation one can relate this to the production term in the transport of ω':

$$\frac{\nu_t}{\sigma} \nabla^2 \omega_w \sim \frac{36\kappa^3}{\sigma\beta\gamma y^+} \left(\frac{\gamma(\omega' + \omega_w)}{k} \mathcal{P} \right). \tag{4.34}$$

Substituting typical values for κ, σ, β, and γ, (see Appendix C.2) into (4.34) one obtains

$$\frac{\nu_t}{\sigma} \nabla^2 \omega_w \sim \frac{30}{y^+} \left(\frac{\gamma(\omega' + \omega_w)}{k} \mathcal{P} \right). \tag{4.35}$$

Clearly, the influence of this diffusive term extends far into the log-layer; it is only reduced below 5 % of the production term at $y^+ = 600$. While Tomboulides et al. (2018) are correct in suggesting that terms dependent on derivatives of y_w are negligible far from the wall, they do still have some influence in the log-region of the boundary layer. Ultimately this suggests that if there are numerical issues concerning the calculation of y_w and its derivatives, the boundary layer solutions will be affected.

In order to make the equations more tractable, Tomboulides et al. (2018) simplify the equations by specifying $|(\nabla y_w)| = 1$ and $\nabla^2 y_w = 0$, an obvious deduction when considering boundaries normal to x or y, although the validity of specifying $\nabla^2 y_w = 0$ for more complex surfaces is not entirely obvious. Let us consider the wall-distance to a circle of radius r, with the origin placed at the centre of the circle. At any point outside this circle, the distance to the circle boundary will be given by

$$y_w = \sqrt{x^2 + y^2} - r, \tag{4.36}$$

which leads to

$$|\nabla y_w| = 1, \tag{4.37}$$

and

$$\nabla^2 y_w = \frac{1}{\sqrt{x^2 + y^2}} = \frac{1}{y_w + r}. \tag{4.38}$$

Clearly the Laplacian term is not zero, and at the boundary, $y_w = 0$, takes the value of $1/r$. This term appears twice in the transport of ω', both of which can be written like:

$$\nu \nabla^2 \omega_w = \frac{\nu \omega_w}{y_w^2} \left[6|\nabla y_w| - 2 y_w \nabla^2 y_w \right], \tag{4.39}$$

and

$$\frac{\nu_t}{\sigma} \nabla^2 \omega_w = \frac{\nu_t \omega_w}{\sigma y_w^2} \left[6|\nabla y_w| - 2 y_w \nabla^2 y_w \right]. \tag{4.40}$$

Substituting expressions for $|\nabla y_w|$ (4.37) and $\nabla^2 y_w$ (4.38) into these terms leads to

$$\left[6|\nabla y_w| - 2 y_w \nabla^2 y_w \right] = \frac{2r}{y_w + r} + 4. \tag{4.41}$$

Several conclusions can be drawn from this: Firstly, at $y_w = 0$, (4.41) takes the value of 6, consistent with the solution obtained when setting $\nabla^2 y_w = 0$. However, as $y_w \to \infty$, (4.41) tends to 4. Of course, far from the wall the terms containing ω_w are negligible, however the transition away from the solution of 6 is dependent on both the radius of the boundary and near wall distance. When $y_w \sim r$, the term is approximately 5, which is a significant deviation. Previous arguments have suggested that $(\nu_t/\sigma)\nabla^2 \omega_w$ is important in the log-layer, suggesting that if the wall radius is of $\mathcal{O}(100)$ wall units then taking $\nabla^2 y_w = 0$ will differ from the true solution. Relating this back to 'real' surfaces it is clear that very few CFD problems will ever consider resolving the flow over surfaces that vary by $\mathcal{O}(100)$ wall units (or smaller), but there are certainly cases which may be influenced by this approximation, such as rough-wall flows and flows over riblets.

There are other ways to mitigate against the numerical issues of ω based models; as noted by Kok and Spekreijse (2000), the unboundedness of the transport equation for ω (4.19) and its singular asymptotic behaviour, can be mitigated against by adopting the $k-\tau$ model of Kalitzin, Gould, and Benton (1996) (Appendix C.4). Substituting $\omega = 1/\tau$ into the transport of k (4.6) leads to

$$\frac{\beta^* k}{\tau} \approx \nu \nabla^2 k. \tag{4.42}$$

substituting the general expansion of k (4.7) into this balance and rearranging for τ leads to

$$\tau \sim \frac{\beta^* y^2}{(n-1)n\nu} - \frac{2\beta^* a_2 y^3}{n(n-1)^2 a_1 \nu} + \mathcal{O}\left(y^4\right). \tag{4.43}$$

The transport of τ (Appendix C.4) is derived by substituting $\omega = 1/\tau$ into the transport of ω (Appendix C.2), and balances like

$$0 = \underbrace{-\gamma\tau^2\left(\frac{\partial U}{\partial y}\right)^2}_{\mathcal{O}(y^4)} + \underbrace{\beta}_{\mathcal{O}(1)} \underbrace{-\frac{2\nu}{\tau}\frac{\partial \tau}{\partial y}\frac{\partial \tau}{\partial y}}_{\mathcal{O}(1)} + \underbrace{\nu\frac{\partial^2 \tau}{\partial y^2}}_{\mathcal{O}(1)}. \tag{4.44}$$

Equating $\mathcal{O}(1)$ terms leads to

$$0 = \beta - \frac{8\beta^*}{(n-1)n} + \frac{2\beta^*}{(n-1)n} \tag{4.45}$$

which reduces to the same quadratic as the $k-\omega$ model. This shows that the limiting behaviour of k is consistent between the two models, but Dirichlet boundary conditions can be adopted for τ, and all terms in the transport of τ are bounded as $y \to 0$. Boundedness is achieved without requiring significant modifications to the transport equation, such as damping functions or timescale limiters as previously discussed. This model can also be extended using the same low Reynolds number corrections as used by Wilcox (2006). When comparing the $k-\omega'$ model (Appendix C.3) and the $k-\tau$ model (Appendix C.4), both of which are mathematically equivalent, one can see how much simpler the $k-\tau$ formulation is. In comparison to $k-\omega$, $k-\tau$ adds only one extra term to the transport equation of the scale determining variable, and doesn't require accurate computation of the wall-normal distance, y_w.

Kalitzin, Gould, and Benton (1996) also derive a $k-g$ model (detailed in Appendix C.6) which solves for $g = \sqrt{\tau}$, arguing that since τ decreases quadratically with wall distance numerical errors may still be present due to discretisation errors near the wall. The near wall behaviour can be investigated by starting from (4.43):

$$g \sim \left[b_1 y^2 + b_2 y^3 + \mathcal{O}\left(y^4\right)\right]^{1/2}, \tag{4.46}$$

where

$$b_1 = \frac{\beta^*}{(n-1)n\nu}, \; b_2 = -\frac{2\beta^* a_2}{n(n-1)^2 a_1 \nu}. \tag{4.47}$$

A polynomial expansion on g leads to

$$g \sim b_1^{1/2} y + \frac{b_2}{2 b_1^{1/2}} y^2 + \mathcal{O}\left(y^3\right), \tag{4.48}$$

Substituting these expansions into the transport of g (Appendix C.6) leads to the following balance:

$$0 = \underbrace{-\frac{\gamma g^3}{2}\left(\frac{\partial U}{\partial y}\right)^2}_{\mathcal{O}(y^3)} + \underbrace{\frac{\beta}{2g}}_{\mathcal{O}(y^{-1})} \underbrace{-\frac{3\nu}{g}\frac{\partial g}{\partial y}\frac{\partial g}{\partial y}}_{\mathcal{O}(y^{-1})} + \underbrace{\nu\frac{\partial^2 g}{\partial y^2}}_{\mathcal{O}(1)}. \tag{4.49}$$

Unlike the other models the Laplacian term is not dominant near the wall. The behaviour of k and g can be determined by balancing leading order terms:

$$\beta \sim 6\nu \nabla g \nabla g, \tag{4.50}$$

which unsurprisingly returns the same quadratic for n as the ω and τ models:

$$\beta \sim \frac{6\beta^*}{n(n-1)}. \tag{4.51}$$

However, unlike the τ equation the dominant terms in the transport of g are unbounded (although less severely than in the ω case).

4.2.4 Summary

To summarise this section the most popular turbulence models for solving boundary layer flows require algebraic closure at the near-wall cells in order to ensure correct asymptotic behaviour. This is due to their dependence on the solution to a transport equation for either ε or ω, neither of which can be determined at the wall. In addition to this, without modifications the model transport equation for the scale determining variable is unbounded, growing like y^{-4} in the case of ω models. ε based models can be modified using timescale limiters or damping functions which ensure both boundedness, and correct scaling of k and ε near the wall. Both of these methods succeed by forcing $n = 2$ near the wall which results in cancelled terms in $\nabla^2\varepsilon$. This cannot be simply extended to ω based models since terms in the expansion of ω (4.18) cannot be cancelled. The damping functions introduced by Wilcox (2006) do not ensure boundedness of the transport of ω or alter its leading order balance, but the asymptotic scaling of k is corrected. Three models have been discussed which do address the singular behaviour of ω and its transport equation. The recent $k-\omega'$ model of Tomboulides et al. (2018) treats the singular component of ω algebraically, and reformulates the transport equation for ω

into one for $\omega' = \omega - \omega_w$. This section has shown that $k - \omega'$ is consistent with theory and avoids discretisation of singular functions. However, it is dependent on the calculation of the wall-distance y_w and its first and second derivatives, which are not trivial to calculate when considering complex geometries. The singular behaviour of ω can also be corrected by transforming the transport of ω to either transport of τ or g, as per Kalitzin, Gould, and Benton (1996). This retains the predictions of the ω model but significantly alters the numerical properties of the transport equations by ensuring boundedness (regarding the τ equation), and allowing Dirichlet boundary conditions at the wall for both τ and g. If the numerical errors observed by Eça, Pereira, and Vaz (2018) are entirely due to the singular behaviour of ω then the τ and g formulations may offer attractive alternatives to ω based models. Despite this, these models have seen little development or further use (Kok and Spekreijse, 2000; Kalitzin et al., 2005; Xiao et al., 2005) since their original publication; there is no reason why these could not be extended to include cross diffusion or SST type closures while maintaining their limiting behaviour near the wall.

4.3 Fully developed channel flow simulations

A 1D fully developed channel flow is simulated at a bulk Reynolds number of $Re_b = U_b\delta/\nu = 10\,864$, equating to a shear Reynolds number of $Re_\tau = u_\tau\delta/\nu \approx 590$, where δ is the channel half height and U_b is the bulk velocity. The flow is assumed steady state and incompressible. Turbulence models and boundary treatments are specified in Table 4.1 (See Appendices for model details). The $k-\tau$, $k-g$, and $k-\omega'$ models, unavailable with the official release, have been implemented in OpenFOAM 4.1 (Weller et al., 1998). Two $k-\tau$ cases are adopted, one with Dirichlet boundary conditions $\tau_0 = 0$ and one with an equivalent algebraic closure approach to $k-\omega$ (1), $\tau_1 = \beta d^2/6\nu$.

Equations are discretised and solved using OpenFOAM 4.1 (Weller et al., 1998); a second order upwind scheme is adopted for velocity convective terms, and a second order accurate Total Variation Diminishing (TVD) scheme is adopted for all other variables.

TABLE 4.1: Turbulence model definitions.

Label	Appendix	Model definition and treatment at the wall
LB1	C.1	$k-\varepsilon$ of Lam and Bremhorst (1981) with $n_i\frac{\partial \varepsilon_0}{\partial x_i} = 0$
LB2	C.1	$k-\varepsilon$ of Lam and Bremhorst (1981) with $\varepsilon_1 = 2\nu k_1/d^2$
$k-\omega$ (1)	C.2	$k-\omega$ with $\omega_1 = 6\nu/\beta d^2$
$k-\omega$ (2)	C.2	$k-\omega$ with 'slightly-rough' BC: $\omega_0 = 40000\nu/k_s^2$, $k_s^+ = 1$
$k-\omega$ (3)	C.3	$k-\omega'$ with $\omega_0' = 0$
$k-\tau$ (1)	C.4	$k-\tau$ model with $\tau_0 = 0$
$k-\tau$ (2)	C.4	$k-\tau$ model with $\tau_1 = \beta d^2/6\nu$
$k-g$	C.6	$k-g$ model with $g_0 = 0$
$\overline{v^2}-f$	C.7	$\overline{v^2}-f$ with $\varepsilon_1 = 2\nu k_1/d^2$

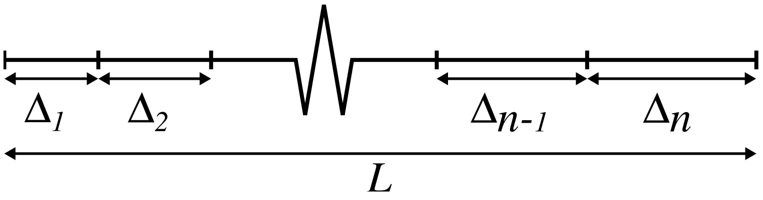

FIGURE 4.1: Mesh grading parameters.

Laplacian terms are discretised using standard Gaussian integration, and face gradients are calculated using linear interpolation. At the wall, first order approximations are made for calculating gradients, the importance of which will be discussed in the following section. The SIMPLEC scheme of Van Doormaal and Raithby (1984) is adopted to couple pressure and velocity equations. Convergence is determined by monitoring the friction velocity, u_τ. This converges to a value of approximately 1 (exact values are specific to each turbulence model) to a relative error of 1×10^{-7} for all cases. This corresponds to normalised residual errors of less than 1×10^{-10} for all variables.

Periodic boundary conditions are adopted in the streamwise and cross stream directions, and a source term is added to the momentum (4.1) equations. This source term takes an iterative form to ensure a fixed bulk flow rate, as per Murthy and Mathur (1997) (i.e. Re_b is fixed). The computational domain is such that a symmetric boundary condition is applied at $y = \delta$ and no-slip at $y = 0$.

5 sets of 6 geometrically similar meshes are created using a geometric grading to refine the near-wall cells. The geometric grading links 6 parameters by

$$r = \frac{\Delta_{i+1}}{\Delta_i}, \qquad R = \frac{\Delta_n}{\Delta_1} = r^{N-1}, \text{ and} \qquad L = \sum_{i=1}^{N} \Delta_i, \tag{4.52}$$

where Δ_1 is the cell width at the wall, Δ_n is the cell width at $y = \delta$, N is the number of cells, r is the ratio between consecutive cell sizes, and R is the ratio between the first and last cell size. These parameters are also defined in Figure 4.1. This study fixes the domain length, $L = \delta = 1$, N and R. The remaining parameters are calculated from (4.52). The 5 sets of meshes are distinguished by different stretching ratios, R, which varies between 1 and 10000, while the 6 meshes contain different numbers of cells, N,

TABLE 4.2: Set and mesh definitions.

Set	R	Mesh	N	$h_r = \frac{N_6}{N}$
S1	1.0	M1	250	4.00
S2	10.0	M2	400	2.50
S3	100.0	M3	550	1.82
S4	1000.0	M4	700	1.43
S5	10000.0	M5	850	1.18
		M6	1000	1.00

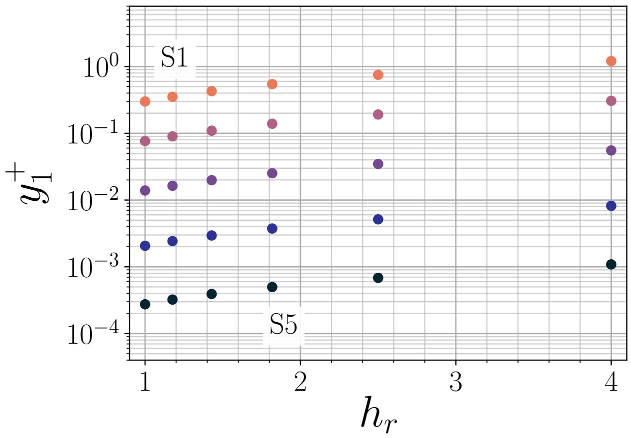

FIGURE 4.2: Variation of the near wall cell size y_1^+ for the different sets and grids (Table 4.2). Presented data are for the $k-g$ model. Colours represent different sets: ●, S1; ●, S2; ●, S3; ●, S4; ●, S5.

which varies between 250 and 1000. The grid and set definitions are detailed in table 4.2, which lead to a total of 30 grids. The 6 meshes cover a grid refinement ratio $h_r = N_6/N$ of 4, where N_6 is the number of cells in the finest mesh, M6. The maximum cell-cell ratio r is 1.038, corresponding to S5 M1 in Table 4.2. Figure 4.2 shows the variation of y_1^+ for the different grids. All but one of the meshes satisfies $y_1^+ < 1$, with a minimum value of $y_1^+ \approx 2.5 \times 10^{-4}$.

4.3.1 Solution dependence on h_r

In order to analyse solution dependence between the different sets of meshes and turbulence models the convergence of the friction velocity, u_τ, is investigated. The discretisation error can be expressed by (Eça and Hoekstra, 2014)

$$E = \phi_i - \phi_0 = \alpha h_i^p \tag{4.53}$$

where ϕ_i represents some scalar flow quantity (such as u_τ), ϕ_0 is the estimate of the exact solution, α is a constant to be determined, h_i is the typical cell size, and p is the observed order of convergence (Eça and Hoekstra, 2014). For second-order accurate discretisation schemes one should obtain $p = 2$. This can be reformulated in terms of the grid refinement ratio h_r to

$$\phi_i = \phi_0 + \alpha' h_r^p, \tag{4.54}$$

where α' is a constant (not equal to α). For each turbulence model (Table 4.1) and set of meshes (Table 4.2) the rate of convergence p and reference friction velocity $u_{\tau 0}$ are estimated through a best-of-fit procedure to (4.54). These fits can be observed in Figure 4.3, where the friction velocity for each of the 5 sets and turbulence models is plotted

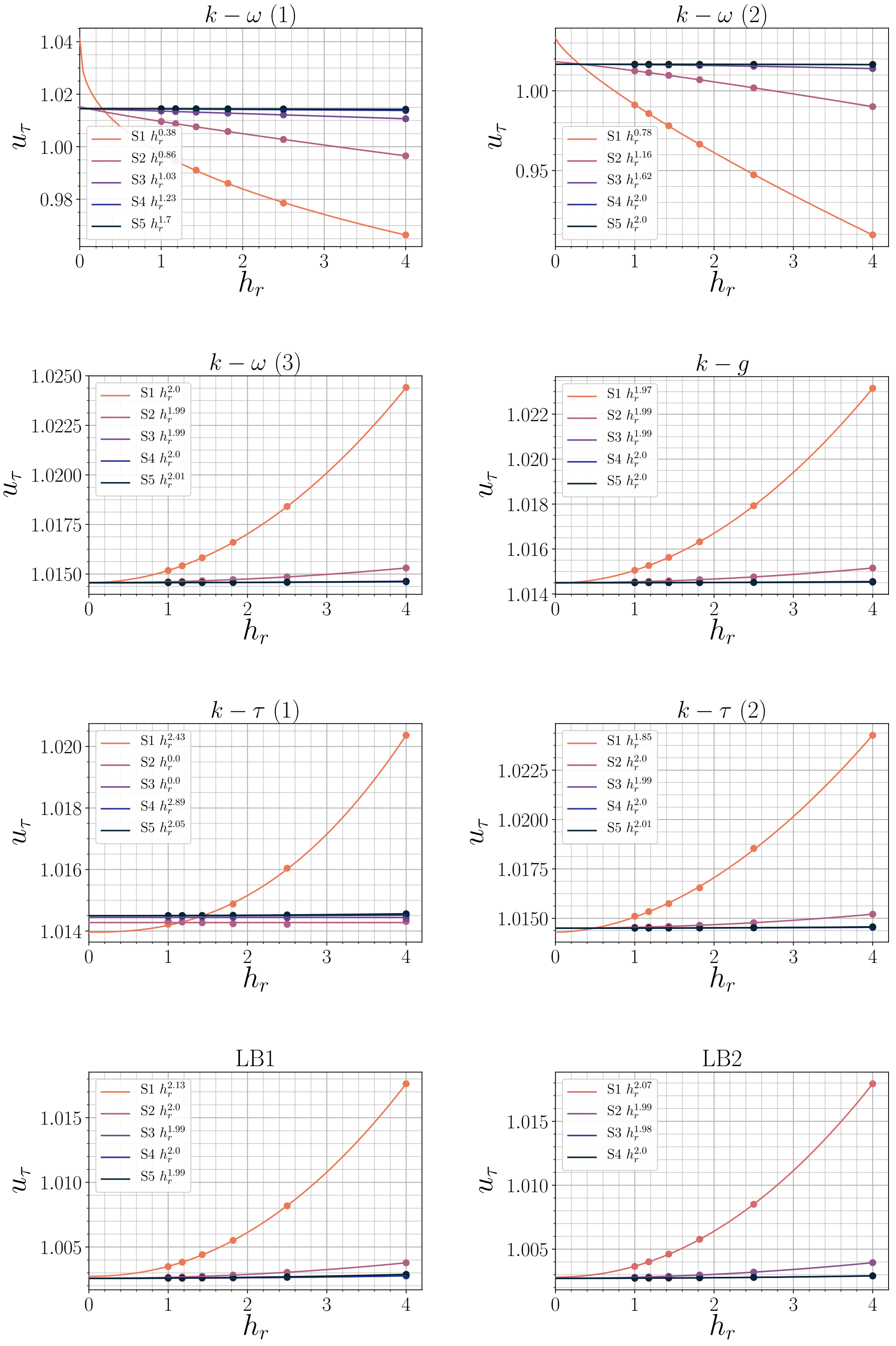

FIGURE 4.3: Convergence of the friction velocity as a function of the grid refinement ratio.

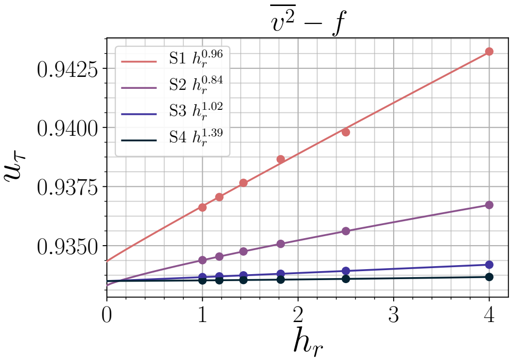

FIGURE 4.3: Convergence of the friction velocity as a function of the grid refinement ratio (cont.).

against the refinement ratio h_r. S5 data for the models LB2 and $\overline{v^2} - f$ have been omitted due to inadequate convergence; Oscillatory behaviour in u_τ is observed as a result of the analytical closure of ε_1 (Table 4.1) at the cell nearest the wall, likely due to its dependence on k.

All sets for the models $k - g$, $k - \omega$ (3), $k - \tau$ (2), LB1, and LB2 obtain approximately second order convergence, h_r^2. These models all obtain similar trends; all sets converge to a common $u_{\tau 0}$ (to plotting accuracy, with the exception of $k - \tau$ (2) S1), differences between sets are reduced as the set number (stretching ratio, R) increases, and solutions on sets S3, S4, and S5 are indistinguishable on the presented axis scales. The remaining cases, $k - \omega$ (1), $k - \omega$ (2), $k - \tau$ (1), and $\overline{v^2} - f$ obtain sub-optimal convergence. $k - \omega$ (1) and (2) behave in a similar fashion; sub-linear convergence is observed for set S1, which slowly tends towards second-order convergence at S5. $k - \omega$ (2) obtains a higher order of convergence than $k - \omega$ (1), achieving second-order convergence at S4 and S5 while $k - \omega$ (1) only obtains $h_r^{1.7}$ for S5. However, $k - \omega$ (2) leads to a much larger spread in solutions of u_τ, most noticeable for set S1. The $\overline{v^2} - f$ model obtains approximately linear convergence for all sets, with a minimum of $h_r^{0.84}$ and a maximum of $h_r^{1.39}$. However, the spread in values of u_τ is much smaller than for the $k - \omega$ (1) and (2) models. The $k - \tau$ (1) model appears to adopt non-trivial convergence for many of the sets. The rate of convergence appears to vary between $h_r^{2.89}$ and h_r^0, although this spread in results is a function of the simple polynomial estimate of the discretisation error (4.54). This behaviour will be investigated when discussing solution dependence on y_1^+.

4.3.2 Solution dependence on y_1^+

The dependence of u_τ on the near-wall cell size y_1^+ for $k - \omega$ and its mathematically equivalent models can be observed in Figure 4.4, for all sets and meshes. In general all solutions obtained from all sets collapse onto a common profile for each turbulence model. Deviations from this trend are most obvious for sets with large stretching ratios

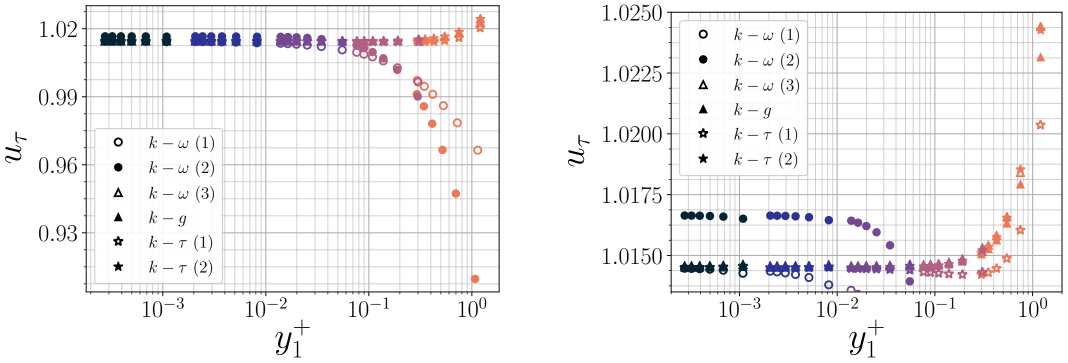

(A)

(B)

FIGURE 4.4: Friction velocity dependence on the near-wall cell size for $k-\omega$ and its mathematically equivalent models. (B) shows data from (A) with a different $y-$ axis scaling. Colours represent different sets, as per Figure 4.2: ●, S1; ●, S2; ●, S3; ●, S4; ●, S5.

(S4, S5), where deviations from this curve are a result of global refinement. However, for S1-S3 all solutions convincingly collapse onto a common curve, where $y_1^+ \gtrsim 0.01$. This suggests that for these highly refined meshes, solutions of u_τ are more sensitive to y_1^+ than the global refinement ratio, h_r, if $y_1^+ \gtrsim 0.01$. $k-\omega$ (1) and (2) lead to a larger spread in solutions of u_τ than any of the other models tested, when y_1^+ is large. As y_1^+ decreases all models except $k-\omega$ (2) collapse onto a common friction velocity, an unsurprising result given their mathematical equivalence and common model coefficients. An exception to this is the solutions of $k-\omega$ (2), which closes ω at the wall by adopting the slightly-rough boundary condition for ω_0. Clearly this has an effect on the converged solution of u_τ, even if the values chosen for ω_0 reflect hydraulically smooth roughness conditions.

Profiles of u_τ as a function of y_1^+ (Figure 4.4) coincide for all models that converge at the expected second-order rate; $k-g$, $k-\omega$ (3), and $k-\tau$ (2), again reflecting their mathematical equivalence. However, $k-\tau$ (1) behaves differently; there is a small undershoot of u_τ at $y_1^+ \approx 0.3$, explaining the peculiar convergence behaviour highlighted in Figure 4.3. This undershoot is removed when adopting the algebraic closure approach of $k-\tau$ (2), suggesting that this behaviour is entirely due to discretisation errors at the cell closest to the wall. First order approximations are made for calculations of gradients near the boundary due to complexities associated with implementing higher order schemes at the wall. For this reason, the discretisation of $\tau \sim y^2$, derived in Section 4.2, leads to a discretisation error that can only be removed by adopting higher order schemes. This reasoning is the motivation behind the formulation of $k-g$ (Kalitzin, Gould, and Benton, 1996); since $g \sim y$, gradients of g can be accurately calculated at the wall using first order approximations. This problem is eliminated when imposing the algebraic closure on τ_1 as per $k-\tau$ (2), since the transport of τ is no longer discretised at the cell closest to the wall. It should be noted that the suggestion of Kok and Spekreijse (2000) to reformulate the term

$$\frac{2}{\tau}\left(\nu + \frac{\nu_t}{\sigma}\right)\frac{\partial \tau}{\partial x_j}\frac{\partial \tau}{\partial x_j} \tag{4.55}$$

to

$$8\left(\nu + \frac{\nu_t}{\sigma}\right)\frac{\partial \sqrt{\tau}}{\partial x_j}\frac{\partial \sqrt{\tau}}{\partial x_j} \tag{4.56}$$

is not enough to entirely remove the discretisation errors associated with the quadratic behaviour of τ, since gradients of τ are also required in order to calculate $\nu\nabla^2\tau$. Interestingly, a result of this first order error is that solutions for S1 obtained using $k-\tau$ (1) are closer to $u_{\tau 0}$ than all other models. This error is also present for the $k-\omega'$ case, due to the quadratic behaviour of ω', but since ω is dominated by ω_w near the wall this error is negligible. Furthermore k is also non-linear near the wall; clearly there is no avoiding the discretisation of non-linear functions, and so if high order accuracy is required the discretisation schemes at the boundary-neighbouring cells should be changed before considering different turbulence models. $k-\tau$ (1) appears to converge more quickly than those that converge at h_r^2, but its undershoot of u_τ at $y_1^+ \approx 0.3$ slows down convergence. Despite this, the model is significantly less sensitive to y_1^+ than the $k-\omega$ formulation.

In order to assess discretisation errors as a function of y_1^+ the error $E = |(u_\tau - u_{\tau 0})/u_{\tau 0}|$ is defined, where $u_{\tau 0}$ is taken as the reference S5 friction velocity for a given turbulence model, estimated through the best of fit to the polynomial (4.54). All solutions obtained on M1-M6 for S4 and S5 agree with this reference friction velocity to within 0.069 % for $k-\omega$ (1) and (2), and within 0.0066 % for all other $k-\omega$ equivalents. E is plotted against y_1^+ for $k-\omega$ and its mathematically equivalent models in Figure 4.5.

$k-\omega$ (1) and (2) lead to significantly larger errors than any of the other models. $k-\omega$ (2) leads to an error of 10.52 % for S1 M1 ($y_1^+ = 1.07$) while $k-\omega$ (1) leads to an error

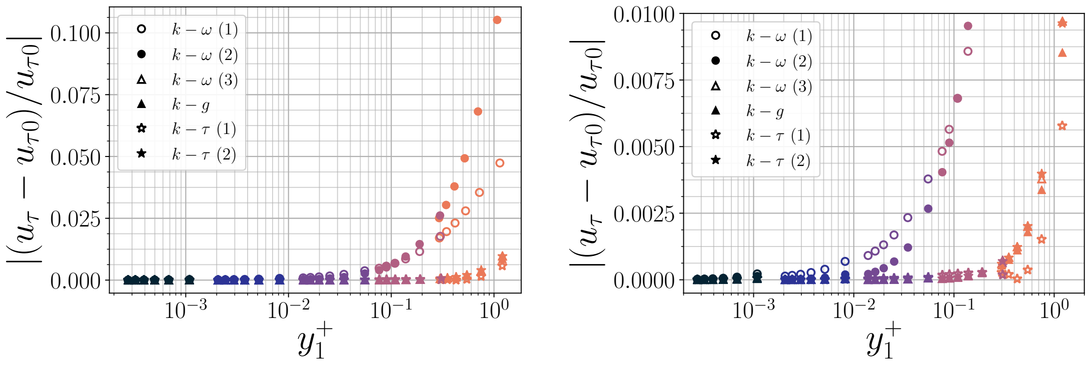

(A) (B)

FIGURE 4.5: Relative friction velocity error for $k-\omega$ and its mathematically equivalent models. $u_{\tau 0}$ is taken as the estimated exact solution (4.54) for S5, for respective turbulence models. (B) shows data from (A) with a different $y-$ axis scaling. Colours represent different sets, as per Figure 4.2: ●, S1; ●, S2; ●, S3; ●, S4; ●, S5.

of 4.74 % at S1 M1 ($y_1^+ = 1.14$). These relate to errors in the friction coefficient $C_f = \tau_w / \frac{1}{2}\rho U_\infty^2$ of 22.15 % for $k-\omega$ (2) and 9.7 % for $k-\omega$ (1). This is in agreement with the results of Eça, Pereira, and Vaz (2018), who obtained mesh dependency errors in C_f of at least 5 % when $y_{1,\mathrm{av}}^+ \simeq 1$, for all their flat plate cases for $k-\omega$ SST. All other models plotted in Figure 4.5 lead to u_τ errors of less than 1 % for all sets and meshes, which quickly drops to less than 0.1 % for S2-S5 ($y_1^+ \lesssim 0.3$). In order to obtain this low an error for the $k-\omega$ (1) and (2) models $y_1^+ \lesssim 0.015$ is required, a cell size of over an order of magnitude smaller than those required by its mathematically equivalent models. These results clearly show that the y_1^+ dependency error of the standard $k-\omega$ model is primarily due to the discretisation of the singularity; when reformulating the transport of ω to ω', τ, or g, the y_1^+ dependency error is significantly reduced.

$k-\omega$ (2) leads to the largest deviations in u_τ, although converges more rapidly to $u_{\tau 0}$ than the standard $k-\omega$ (1) model, a function of the higher convergence rates presented in Figure 4.3. This behaviour can be explained by examining ω_1 as y_1^+ decreases for both models. By specifying $\omega_0 = 40000\nu/k_s^2$ as per $k-\omega$ (2) the value of ω_1 is actually increased beyond the asymptotic solution $\omega = 6\nu/\beta y^2$ when the near-wall cell size y_1 is large. The threshold at which ω_1 is decreased for $k-\omega$ (2) relative to $k-\omega$ (1), lies between $y_1^+ \approx 0.14 - 0.18$ or cases S2 M2 - S2 M3, which also coincides with the region where the relative error in u_τ reduces below that of $k-\omega$ (1) for $k-\omega$ (2). Clearly then, the slightly-rough wall approach can only provide a lower sensitivity to y_1^+ if the value of ω_0 is small enough to limit the value of ω_1 below that of the asymptotic solution. For $k_s^+ = 1$ as per the data herein this actually leads to worse convergence unless $y_1^+ \lesssim 0.18$. This supports the claim of Eça and Hoekstra (2004) who find that the slightly-rough wall boundary condition is more sensitive to y_1^+ than the algebraic closure on ω_1.

The y_1^+ dependence of the ε based models can be observed in Figure 4.6. $u_{\tau 0}$ is taken

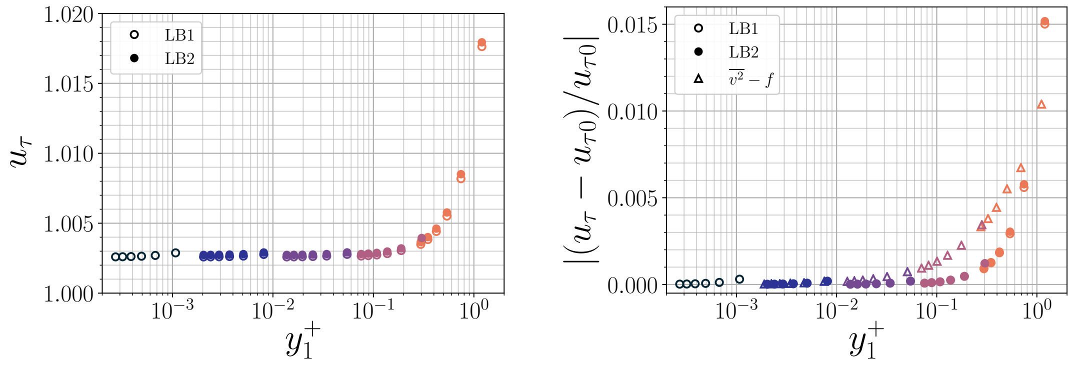

FIGURE 4.6: Friction velocity dependence on the near-wall cell size (left) and relative friction velocity errors (right) for ε based models, with $u_{\tau 0}$ taken as the estimated exact solution (4.54) for S5, for respective turbulence models. Colours represent different sets, as per Figure 4.2: ●, S1; ●, S2; ●, S3; ●, S4; ●, S5.

as the reference S5 friction velocity for LB1 and S4 for LB2 and $\overline{v^2} - f$. All solutions for LB1 obtained on M1-M6 for S4 and S5 agree with $u_{\tau 0}$ to within 0.03 %. All solutions for both LB2 and $\overline{v^2} - f$ obtained on M1-M6 for S4 agree with $u_{\tau 0}$ to within 0.02 %. Figure 4.6 indicates that the model of Lam and Bremhorst (1981) is insensitive to the treatment of ε at the wall; both LB1 and LB2 collapse onto very similar profiles regarding both absolute values of u_τ and its rate of convergence. Both LB1 and LB2 lead to relative errors in u_τ of 1.50 % and 1.52 % at S1 M1 ($y_1^+ \approx 1.2$) respectively, larger than the $\lesssim 1$ % error obtained by $k - \omega$ (3), $k - g$, and $k - \tau$ (1) and (2) for the same set and mesh. u_τ predictions of LB1 and LB2 converge to within 0.1 % of $u_{\tau 0}$ at $y_1^+ \approx 0.3$, as per $k - \omega$ (3), $k - g$, and $k - \tau$ (1) and (2). $\overline{v^2} - f$ converges at a slower rate due to its linear convergence with h_r (Figure 4.3). At $y_1^+ = 1.11$ the relative error in u_τ is 1.04 %, lower than LB1 and LB2. As y_1^+ decreases the $\overline{v^2} - f$ model slowly converges to $u_{\tau 0}$; to achieve a relative error of 0.1 % $y_1^+ \lesssim 0.1$ is required. While outperforming $k - \omega$ (1) and (2), $\overline{v^2} - f$ is outperformed by all other models.

4.3.3 Near wall behaviour

The mesh dependency of these models is clearly linked to the behaviour of these equations in the near wall limit. The behaviour of k near the wall can be observed in Figure 4.7 for the different turbulence models. Figure 4.7 (A) shows that for the ω, τ, and g based models the asymptotic solutions for n, obtained in Section 4.2, are in excellent agreement with the numerical solutions. However, the standard ω based models deviate from the asymptotic solution of k near the wall. This is unsurprising for $k - \omega$ (2), since ω_0 is fixed to a value much lower than the singular solution of the asymptotic behaviour. $k - \omega$ (1) underpredicts k for the first few cells and then collapses onto the asymptotic solution as y_1^+ increases. It should also be noted that the k solutions for the $k - \omega$ (3), $k - \tau$ (1) and

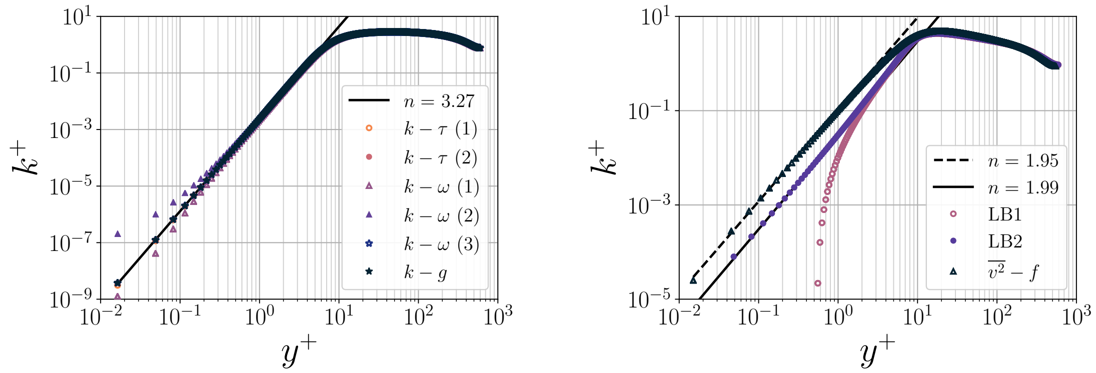

(A) (B)

FIGURE 4.7: Near wall k^+ predictions with data from case S3 M5. Legends correspond to Table 4.1.

(2), and $k - g$ models do not deviate from the asymptotic solutions, reinforcing the notion that the errors obtained when adopting the $k - \omega$ model are entirely numerical and associated with the singular behaviour of ω.

Figure 4.7 (B) shows the behaviour of the ε based models. Both the $\overline{v^2} - f$ model and the LB2 model agree strongly with the asymptotic solution of k, but the LB1 model shows a large deviation from $n = 2$: k rapidly decreases to zero below $y^+ \approx 1$. When adopting zero-gradient boundary conditions $k \approx 0$ for many cells close to the wall due to the neglected higher order terms in the expansion of ε (discussed in Section 4.2). Interestingly LB1 and LB2 solutions collapse further from the wall, strongly suggesting that the damping functions play a large role in forcing the correct behaviour of k and ε.

The near wall behaviour of $\omega = 1/\tau = 1/g^2 = \omega' + \omega_w$ can be observed for the ω, ω', τ and g based models in Figure 4.8, normalised by $\omega_w = 6\nu/\beta y^2$. The $k - \omega$ (1) model overpredicts ω by over 50 % in the second-to-closest cell to the wall (note that the first cell lies on the asymptotic solution due to the imposed algebraic closure). This is in strong agreement with the analysis of Wilcox (2006), who shows analytically that the discretisation of a function that goes like $\phi \sim 1/y^2$ can lead to an over-prediction of $\nabla^2\phi$ of 78 %. The S4 M5 case shows that eventually ω collapses onto ω_w below $y^+ \approx 1$, but for the S3 M5 and S2 M5 cases ω never reduces to ω_w before reaching the outer portions of the boundary layer. The mesh dependency error observed in Figures 4.3, 4.4, and 4.5 is related to this over-prediction; mesh independence is achieved for the $k - \omega$ model when the overprediction of ω is limited to the very near wall region where $y^+ \lesssim 1$. When cells are too large this over prediction extends beyond the viscous sub-layer and affects the outer portions of the flow. For completeness the $k - \omega$ (2) model has been included in Figure 4.8, although its lack of agreement with ω_w is unsurprising due to the specification

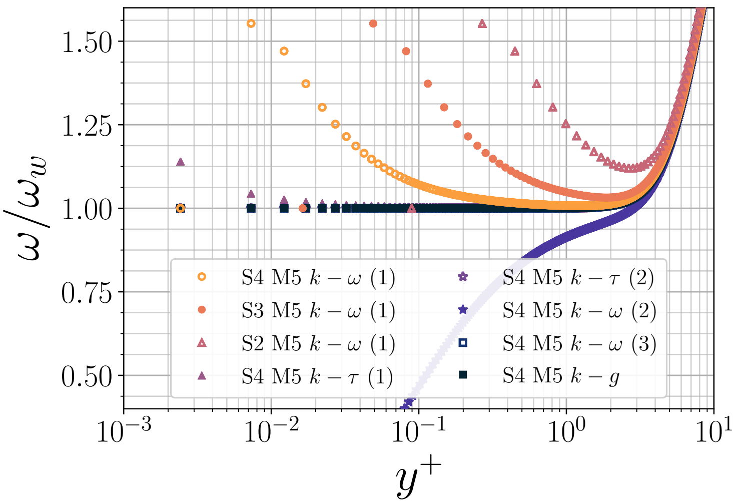

FIGURE 4.8: Near wall ω normalised by $\omega_w = 6\nu/\beta y^2$. Legends correspond to Tables 4.1 and 4.2.

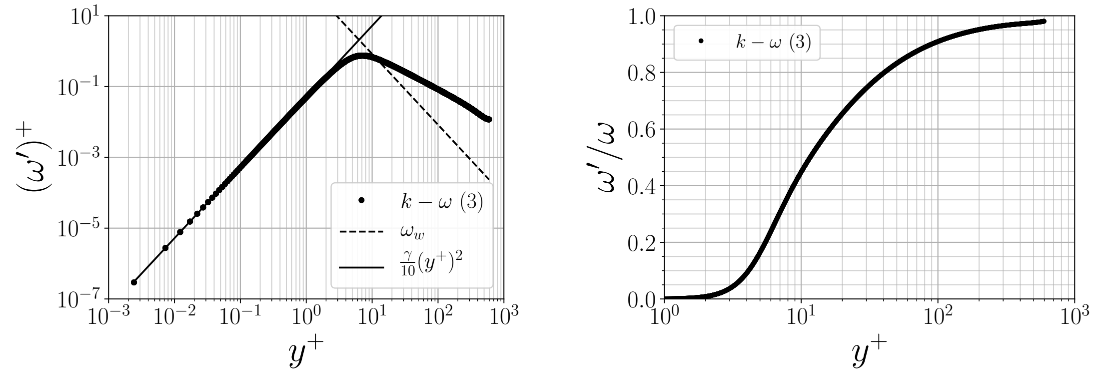

(A) (B)

FIGURE 4.9: ω' numerical data compared to asymptotic solution (A) and the contribution of ω' to ω (B). Data are from case S4 M5.

of the slightly-rough wall boundary condition.

The $k-\omega$ (3), $k-\tau$ (1) and (2), and $k-g$ models provide much better predictions of ω; the $k-\omega$ (3), $k-\tau$ (2), and $k-g$ models collapse onto ω_w until $y^+ \approx 2$, while the $k-\tau$ (1) model slightly over-predicts ω for the first few cells close to the wall. This is due to the first order approximations for the gradients at the boundary discussed in Section 4.3.2, which are mitigated against when adopting the algebraic closure approach $k-\tau$ (2).

Figure 4.9 shows how the analytical solutions of Section 4.2 compare against the numerical solutions of ω', for the $k-\omega$ (3) model. Clearly the fit is excellent, further validating the scaling arguments of Section 4.2. The contribution of ω' to ω is also plotted; the point at which ω' and ω_w are equal is at $y^+ \approx 10$. ω' is approximately 80 % of ω at $y^+ \approx 40$, supporting previous arguments that terms containing ω_w are still influential in the log-layer. It should be noted that contributions from ω_w never vanish entirely for the presented channel flow; at the channel centre $\omega_w \approx 0.05\omega$. It can therefore be concluded that particularly poor calculation of $\nabla^2 y_w$ would have noticeable consequences in the flow solution.

4.3.4 Extensions to the $k-\tau$ model

The model(s) of Kalitzin, Gould, and Benton (1996) have seen little use or development since their introduction, despite being promising alternatives to $k-\omega$. In contrast the $k-\omega$ model has seen significant improvements and extensions. For this reason a new $k-\tau$ model, based on the $k-\omega$ model of Wilcox (2006), has been implemented in OpenFOAM 4.1 (Weller et al., 1998). This is detailed in Appendix C.5.

It should be noted that there are arguments supporting the extensions of both the $k-\tau$ and the $k-g$ models; while the $k-g$ model is less sensitive to near-wall first order discretisation it is also unbounded, albeit significantly less so than $k-\omega$. In addition

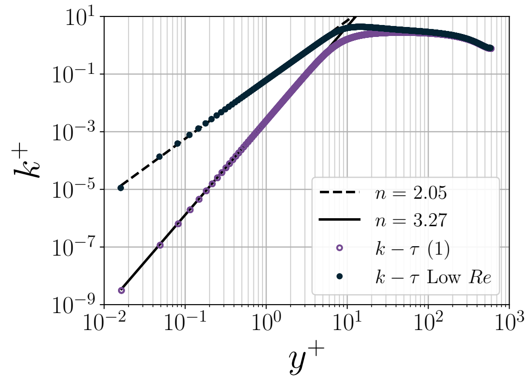

FIGURE 4.10: Near wall behaviour of k for the standard $k - \tau$ model (Appendix C.4) and the updated $k - \tau$ model (Appendix C.5) with Low Reynolds number corrections. Data are from case S3 M5.

to this, the algebraic closure approach of $k - \tau$ (2) mitigates against any small errors at the wall and can be easily extended to include log-law type closures. The $k - \tau$ model of Kalitzin, Gould, and Benton (1996) has therefore been extended to include updated coefficients and a cross diffusion term (See Appendix C.5) which have been shown to improve the behaviour of $k - \omega$ in freestream flows (Wilcox, 2006). The low Reynolds number corrections of Wilcox (2006) have also been implemented in the model in order to improve predictions of k near the wall. This is demonstrated in Figure 4.10, where the updated model with low Reynolds number corrections closely agrees with the asymptotic solution $n = 2$ near the wall, as predicted through the leading order arguments of Section 4.2.

4.3.5 Comparisons to DNS

Figure 4.11 compares the different turbulence models for the S4 M5 case to the DNS solution of Moser, Kim, and Mansour (1999). All $k - \omega$ and mathematically equivalent models collapse onto the same solution for both k^+ and U^+, which shows that there are negligible numerical errors between the different formulations far from the wall (Note that for the S4 M5 case the largest mesh dependency error for the friction velocity is for $k - \omega$ (1) at a value of 0.069 %).

Figure 4.11 also shows that the updated $k - \tau$ model (Appendix C.5), with the Low Re corrections of Wilcox (2006), provides much better predictions of k^+ compared to the standard model, although reasonable predictions of U^+ are achievable without these corrections. The LB models both collapse further from the wall, suggesting that the treatment of ε near the boundary has little impact in the freestream, a finding in agreement with Patel, Rodi, and Scheuerer (1985). The $\overline{v^2} - f$ model provides excellent predictions of the near wall gradients of k^+ and U^+ although it over-predicts the offset of U^+ in the log-layer. This is due to the underprediction of u_τ which results in a shear Reynolds number

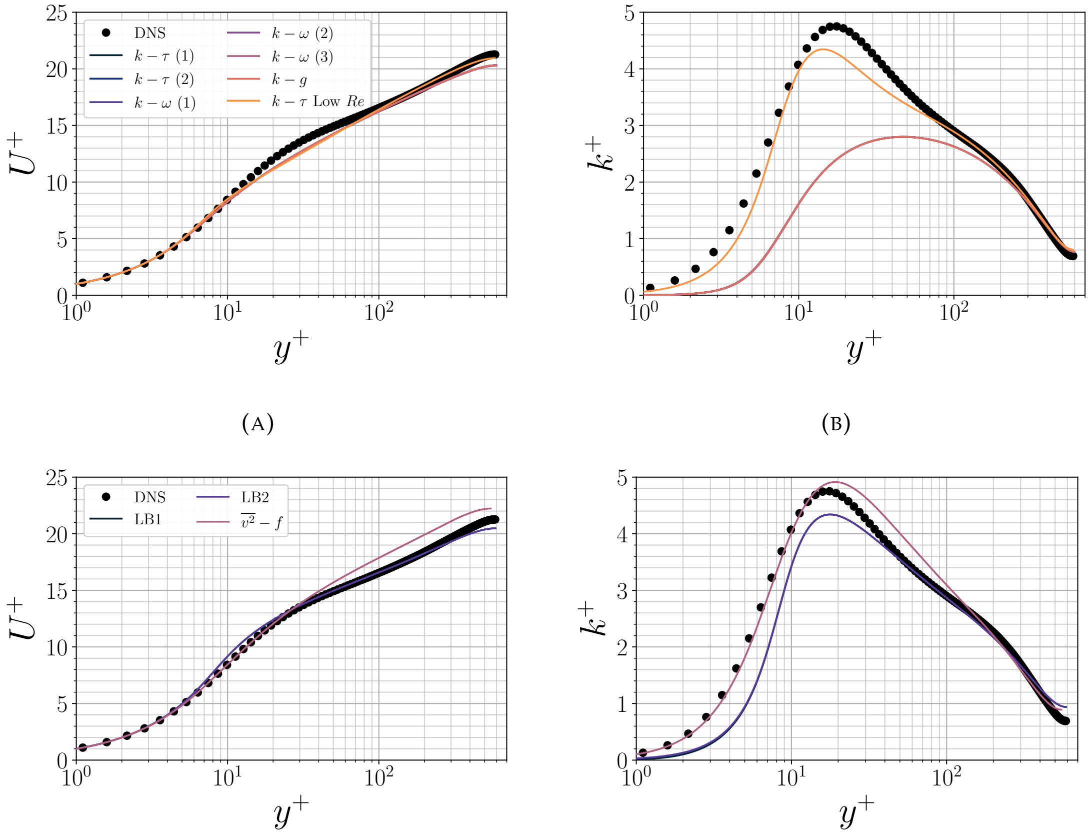

(A)

(B)

(C)

(D)

FIGURE 4.11: Profiles of U^+ and k^+ for all turbulence models, compared to the DNS of Moser, Kim, and Mansour (1999). Data are from case S4 M5. Note that $k-\omega$ (1), (2) and (3), $k-\tau$ (1) and (2), and $k-g$ data collapse onto common profiles, as do data from LB1 and LB2.

of $Re_\tau = 514$ rather than the target shear Reynolds number of $Re_\tau = 590$. There have been other modifications to the model which result in better predictions of U^+ profiles, such as the $\zeta - f$ model of Hanjalić, Popovac, and Hadžiabdić (2004).

4.3.6 Summary

In summary, this section has investigated the dependence of several turbulence models on the near-wall cell size y_1^+. 5 sets of 6 geometrically similar meshes have been created in order to investigate a range of y_1^+ varying between approximately 2.5×10^{-4} and 1, covering a grid refinement ratio of 4. Friction velocity errors of 4.74 % are obtained for the standard $k-\omega$ model at $y_1^+ \approx 1$, increasing to 10.52 % when slightly-rough wall boundary conditions are adopted. These equate to errors in the friction coefficient of 9.7 % and 22.15 % respectively, which could be significant in a number of industrial flows. In many engineering applications the y_1^+ dependency error associated with $k-\omega$ may be negligible, but Eça, Pereira, and Vaz (2018) have already shown that these errors can influence predictions of pressure and friction coefficients for aerofoils and ship hulls.

For $y_1^+ \approx 1$ errors of approximately 1.5 % are obtained for the $k - \varepsilon$ model of Lam and Bremhorst (1981), regardless of whether an algebraic expression for ε_1 is adopted, or a Neumann condition on ε_0. All other models investigated lead to friction velocity errors of $\lesssim$1 % for $y_1^+ \approx 1$. In order to achieve friction velocities within a 1 % error, a near-wall cell size of $y_1^+ \approx 0.1$ is required for the $k - \omega$ model, an order of magnitude smaller than all other models. The present work suggests that this problem could be overcome by adopting ω', τ or g based models. These retain the same boundary layer predictions of ω based models but achieve solutions without numerical error associated with the singular behaviour of ω. The $k - \tau$ (2), $k - g$, and $k - \omega$ (3) models outperform all of the other tested models. Of these three models the $k - \tau$ formulation should be developed further; the model is fully bounded at the wall and does not require computation of the wall-normal distance (or its derivatives).

While this study on the behaviour of these models near the wall is extensive, the flow is free from complexities such as freestream boundary conditions and strong separation. The numerical improvements of the τ formulation close to the wall do not guarantee globally better performance than ω models. Therefore, future work should be carried out in order to validate τ based models in a wider range of flows, and extend them to more complex closures such as Reynolds stress and SST.

4.4 Reynolds stress closures

So far this chapter has been limited to eddy-viscosity type RANS models of which one of the main modelling concerns is the closure of the rate of turbulent dissipation, ε. However, these models make a critical assumption that the Reynolds stresses can be approximated by a scalar eddy-viscosity,

$$-\overline{u_i'u_j'} = 2\nu_t S_{ij} - \frac{2}{3}k\delta_{ij}, \tag{4.57}$$

which is unable to correctly predict anisotropy in the Reynolds stresses, particularly near the wall. A review of literature concerning RANS predictions of the flow over riblетted plates (Chapter 2) suggested that accounting for anisotropy may be important for obtaining physical solutions, especially when riblets are small. This can be achieved by adopting a Reynolds Stress Model (RSM), which solves transport equations for each component of the Reynolds stress tensor. This can naturally resolve anisotropic flows, but comes with the expense of additional transport equations, and also additional terms that require modelling. In this section two Reynolds stress closures are detailed and investigated; a Stress-τ model, based on the Stress-ω model of Wilcox (2006), and the Elliptic-Blending SSG (EB-SSG) model of Manceau and Hanjalić (2002), updated by Manceau (2015). Both these models are suitable for integration through the full boundary layer, without requiring log-law type wall functions, but vary considerably in complexity. This section will extend previous analysis on eddy-viscosity models to Reynolds stress models, readily showing that as long as the underlying transport equations are similar, near-wall cell size dependency is affected little by the additional complexity.

4.4.1 The Reynolds stress equations

The general transport of $\overline{u_i'u_j'}$ is given by

$$\frac{D\overline{u_i'u_j'}}{Dt} = \mathcal{P}_{ij} + \Pi_{ij} + \mathcal{D}_{ij} - \varepsilon_{ij}, \tag{4.58}$$

where $\mathcal{P}_{ij}$ represents production, Π_{ij} represents the pressure-strain correlation, or redistribution tensor, $\mathcal{D}_{ij}$ represents the sum of turbulent transport and molecular diffusion, and ε_{ij} represents destruction. The production term is in closed form,

$$\mathcal{P}_{ij} = -\overline{u_i'u_k'}\frac{\partial \overline{U}_j}{\partial x_k} - \overline{u_j'u_k'}\frac{\partial \overline{U}_i}{\partial x_k}, \tag{4.59}$$

but the remaining terms require modelling.

There are two effects that are vital to consider when modelling near-wall flows with a Reynolds stress model. Wall-blockage is a phenomenon arising from the tendency of turbulence to become two-dimensional at the wall, where through continuity the wall-normal component of the turbulent kinetic energy becomes negligible compared to wall-parallel components (Manceau, 2015). Asymptotically the Reynolds stresses should behave like

$$\begin{aligned}
\overline{u'u'} &\sim a_1y^2 + a_2y^3 + \cdots, \\
\overline{u'v'} &\sim b_1y^3 + b_2y^4 + \cdots, \\
\overline{u'w'} &\sim c_1y^2 + c_2y^3 + \cdots, \\
\overline{v'v'} &\sim d_1y^4 + d_2y^5 + \cdots, \\
\overline{v'w'} &\sim e_1y^3 + e_2y^4 + \cdots, \\
\overline{w'w'} &\sim f_1y^2 + f_2y^3 + \cdots,
\end{aligned}$$

arising from the no-slip condition and continuity. This phenomenon is known as 2D turbulence, a purely kinematic effect that is not trivial to account for in near-wall modelling. Generally it is treated through the balance of ε_{ij} and Π_{ij} (see e.g. Jakirlić and Hanjalić, 2002).

The second effect arises from an increase in pressure fluctuations near the wall, which appears in the pressure-strain correlation which can be decomposed into (Hanjalić, 1994)

$$\Pi_{ij} = \Pi^1_{ij} + \Pi^2_{ij} + \Pi^w_{ij} = \overline{p' \left(\frac{\partial u'_i}{\partial x_j} + \frac{\partial u'_j}{\partial x_i} \right)}. \tag{4.60}$$

This decomposition follows from the exact Poisson equation for the fluctuating kinematic pressure p'. Π^1_{ij} represents a slow part, dependent only on velocity fluctuations, while Π^2_{ij} represents a rapid part, dependent on the mean velocity gradient (Pope, 2001). The third term is coined the wall-reflection term, accounting for the reflections of the pressure field at the wall (Hanjalić, 1994). This is only effective in the near-wall region, but Π_{ij} is crucially non-local in nature, arising from the elliptic (for incompressible flow) nature of the Poisson equation of p'. Π^w_{ij} is responsible for damping wall-normal components of the Reynolds stresses, and as such is usually implemented as a function of wall distance or the wall-normal direction, although some closures for Π_{ij} do not require models for Π^w_{ij} to obtain reasonable log-layer solutions (e.g. Speziale, Sarkar, and Gatski, 1991).

The Stress-τ model

Among the simplest Reynolds stress closures appropriate for resolving near-wall flows (without log-law wall functions) is the Stress-ω model of Wilcox (2006). Π_{ij} is modelled using the linear-pressure-strain correlation model of Launder, Reece, and Rodi (1975) (without a wall-reflection term, Π^w_{ij}):

$$\Pi_{ij} = \Pi^1_{ij} + \Pi^2_{ij}, \tag{4.61}$$

with

$$\Pi^2_{ij} = -2C_1 \varepsilon b_{ij}, \tag{4.62}$$

and

$$\begin{aligned} \Pi^1_{ij} = &+2(\hat{\alpha} + \hat{\beta})k \left(b_{ik}S_{jk} + b_{jk}S_{ik} - \frac{2}{3} b_{kl}S_{kl}\delta_{ij} \right) \\ &+2(\hat{\alpha} - \hat{\beta})k(b_{ik}\Omega_{jk} + b_{jk}\Omega_{ik}) + \left(\frac{4}{3}(\hat{\alpha} + \hat{\beta}) - \hat{\gamma} \right) kS_{ij}, \end{aligned} \tag{4.63}$$

and the mean rate of strain tensor S_{ij} is

$$S_{ij} = \frac{1}{2} \left(\frac{\partial \overline{U}_i}{\partial x_j} + \frac{\partial \overline{U}_j}{\partial x_i} \right), \tag{4.64}$$

and the mean rotation tensor is

$$\Omega_{ij} = \frac{1}{2} \left(\frac{\partial \overline{U}_i}{\partial x_j} - \frac{\partial \overline{U}_j}{\partial x_i} \right). \tag{4.65}$$

The remaining parameters $\hat{\alpha}$, $\hat{\beta}$, and $\hat{\gamma}$ are empirical constants. ε_{ij} is assumed isotropic and modelled by

$$\varepsilon_{ij} = \frac{2}{3}\beta^* k\omega\delta_{ij}, \tag{4.66}$$

which requires the solution to an additional transport equation for ω, identical to that of the two-equation $k-\omega$ model of Wilcox (2006) (Appendix C.2). Turbulent transport is modelled using an isotropic gradient diffusion hypothesis:

$$\mathcal{D}_{ij} = \frac{\partial}{\partial x_k}\left[\left(\nu + \frac{\nu_t}{\sigma^*}\right)\frac{\partial \overline{u_i'u_j'}}{\partial x_k}\right]. \tag{4.67}$$

From inspection of the transport of $\overline{u_i'u_j'}$ one observes that the underlying transport equations for k and ω are identical to the standard two-equation $k-\omega$ model of Wilcox (2006). Indeed, this was the primary motivation of Wilcox (2006); the construction of a simple and elegant extension of $k-\omega$ to a Reynolds stress closure. Low Reynolds number corrections can be readily applied in the same way as the typical $k-\omega$ model (Appendix C.2) which leads to better near-wall predictions of the turbulent kinetic energy.

There are two main issues with this choice of turbulence model in regard to near-wall modelling. Firstly, the model is dependent on the solution of a transport equation for ω, which as investigated in the previous section leads to significant numerical errors at the wall; a 10 % error was obtained for the coefficient of friction when near-wall cell sizes were $y_1^+ \approx 1$ for the standard $k-\omega$ model of Wilcox (1998). This numerical error is crucially retained for the Stress-ω model, given that it's underlying transport equations are identical to the standard two-equation model.

The second issue is its negligence of wall-reflection terms in Π_{ij}. Subsequently the model cannot account for either wall blockage or wall-reflection effects, i.e there are no corrections made to ensure turbulence tends to two-dimensionality as the wall distance decreases. This can be clarified by assessing the leading order balance of the transport of $\overline{u_i'u_j'}$. Near the wall, destruction must balance viscous diffusion and redistribution such that

$$\varepsilon_{ij} - \Pi_{ij}^1 \sim \nu\nabla^2\overline{u_i'u_j'}, \tag{4.68}$$

leading to

$$\frac{2}{3}(C_1+1)\beta^* k\omega\delta_{ij} - C_1\beta^*\omega\overline{u_i'u_j'} = \nu\nabla^2\overline{u_i'u_j'}. \tag{4.69}$$

Assessing the balance of the diagonal components, contributing to k, one observes that the above equation is only satisfied when all three terms balance, which requires the diagonal components of $\overline{u_i'u_j'}$ to be equal. It should also be noted that by taking the trace of this balance one obtains the same relationship between ω and k as the standard $k-\omega$ model, leading to the balance (4.19).

Despite these shortcomings, Wilcox (2006) has shown that the Stress-ω model obtains good agreement with the boundary layer log-law solutions, and with low Reynolds number corrections (Appendix C.2) predictions of turbulent kinetic energy are reasonable. In order to reduce model sensitivity to the near wall cell size the original model of Wilcox (2006) is reformulated, replacing the transport equation for ω with an equivalent one for τ. While this model removes the numerical issues associated with the singular behaviour of ω, the simple model for Π_{ij} is retained. The full Stress-τ model is detailed in Appendix C.8.

The Elliptic-Blending-SSG model (EB-SSG)

A significant simplification of the Stress-ω (and subsequently Stress-τ) model is its treatment of the near-wall balance of the Reynolds stresses. Satisfying the asymptotic near-wall balance of ε_{ij} and Π_{ij} is key to reproducing the two-component nature of near-wall turbulence (Manceau, 2015), which cannot be achieved using the linear isotropic models of the Stress-ω/Stress-τ models.

The second Reynolds stress closure adopted herein is the Elliptic Blending SSG (EB-SSG) of Manceau and Hanjalić (2002), updated by Manceau (2015) (Appendix C.9). This model satisfies the asymptotic balance of the transport of $\overline{u_i'u_j'}$ by solving for a blending parameter α calculated from an elliptic equation, representing the kinematic blocking effect by smoothly transitioning the near-wall asymptotic solutions of ε_{ij} and Π_{ij} into homogeneous freestream formulations. Π_{ij} is modelled by

$$\Pi_{ij} = (1-\alpha^2)\Pi_{ij}^{w} + \alpha^2\Pi_{ij}^{h}, \tag{4.70}$$

where superscript w represents a near-wall model and h represents a homogeneous model. The SSG model is adopted for Π_{ij}^{h}. ε_{ij} is modelled in a similar way:

$$\varepsilon_{ij} = (1-\alpha^2)\frac{\overline{u_i'u_j'}}{k}\varepsilon + \frac{2}{3}\alpha^2\varepsilon\delta_{ij} \tag{4.71}$$

where a near-wall anisotropic form is blended into an isotropic form, both dependent on the solution to a transport equation for ε. The model equation for the blending parameter α is

$$\alpha - L^2\nabla^2\alpha = 1, \tag{4.72}$$

where L is a turbulent length scale. This has the boundary condition $\alpha = 0$ at the wall. Subsequently the near-wall balance of $\overline{u_i'u_j'}$ is satisfied by

$$\frac{\overline{u_i'u_j'}}{k}\varepsilon - \Pi_{ij}^{w} \sim \nu\nabla^2\overline{u_i'u_j'}. \tag{4.73}$$

Π^w_{ij} is chosen such that the above balance leads to near exact[1] asymptotic solutions for the individual components of $\overline{u'_i u'_j}$:

$$\Pi^w_{ij} = -\frac{\varepsilon}{k}\begin{bmatrix} -\frac{5}{2}\overline{v'v'} & 5\overline{u'v'} & 0 \\ 5\overline{u'v'} & 5\overline{v'v'} & 5\overline{v'w'} \\ 0 & 5\overline{v'w'} & -\frac{5}{2}\overline{v'v'} \end{bmatrix}. \tag{4.74}$$

With $\varepsilon \sim 2\nu k/y^2$ one readily observes that the two-component limit of turbulence is obtained in the near-wall region.

The model solves for the scale determining variable ε using its asymptotic solution as a boundary treatment at the wall (further details are presented in Appendix C.9). If accurate representation of the near-wall turbulence is a necessity for the prediction of flows over riblets and shark skin denticles then the EB-SSG model is a more suitable candidate than the Stress-τ.

4.4.2 Numerical solutions

Here channel flow solutions are compared between the two Reynolds stress closures and two similar eddy-viscosity models. The most similar eddy viscosity model to EB-SSG is the $\overline{v^2} - f$ model; they both solve near identical equations for ε and both require the solution to an elliptic blending parameter to account for near-wall kinematic blocking. Similar behaviour between the two models should therefore be expected regarding grid independence. The Stress-τ model is most similar to the $k - \tau$ model, both with Low Reynolds number corrections; their transport equations for τ are identical, aside from slight differences between the model coefficients, and the underlying transport equation for k is identical for both models.

The numerical simulations are identical to those specified in Section 4.3, as are the techniques adopted for assessing convergence to the reference friction velocity $u_{\tau 0}$. Just like LB2 and $\overline{v^2} - f$, the EB-SSG model also obtained oscillatory solutions at very small cell sizes (Set 5) due to the algebraic closure of ε at the wall, such that those solutions have been omitted from the analysis. The convergence of u_τ for $\overline{v^2} - f$, EB-SSG, $k - \tau$, and Stress-τ, as a function of y_1^+ can be observed in Figure 4.12, for the two Reynolds stress closures and their similar eddy-viscosity models. The Stress-τ model obtains similar behaviour to $k - \tau$, although predicts the undershoot behaviour at a slightly larger value of y_1^+. It seems that the undershoot occurs at $y_1^+ \sim 1$, although present set definitions do not capture this. However, after this initial undershoot the convergence between the two models is nearly indistinguishable on the presented axis scales, both of which converge

---

[1] Note that this form of Π^w_{ij} actually predicts $\overline{u'v'} \sim \overline{v'w'} \sim y^4$ rather than the asymptotic solution y^3. While a model that obtains y^3 scaling is obtainable, Manceau and Hanjalić (2002) found that overall predictions were less satisfactory than when their chosen model was adopted.

to an error of less than 0.1 % at $y_1^+ \sim 0.1$. The Stress-τ model obtains a maximum error of less than 0.2 % for all cases ($y^+ \lesssim 1$).

Near identical behaviour is observed between the $\overline{v^2} - f$ model and the EB-SSG (Figure 4.12), both of which obtain errors of less than 0.7 % for all models ($y^+ \lesssim 1$). This converges to an error of less than 0.2 % at $y_1^+ \sim 0.1$. There is however one data point that does not agree with the $\overline{v^2} - f$ model, at $y^+ \sim 1$. The error does not continue its upward trend as y_1^+ increases and instead drops for the last data point. This perhaps suggests that further work should be carried out in quantifying how the EB-SSG model behaves for the cases $y_1^+ \sim 1 - 10$, since it seems that non-trivial effects are being introduced.

Comparisons to the DNS of Moser, Kim, and Mansour (1999) are presented in Figures 4.13 and 4.14. Similar profiles are obtained regarding U^+ and k^+ for both $k - \tau$ and Stress-τ models, with Low Reynolds number corrections (Figure 4.13). This is unsurprising given the underlying equations are so similar. The Stress-τ model does obtain slightly better predictions of the velocity profile in the buffer layer, and the general shape of k^+ is similar to the DNS, although the simple two-equation model actually converges to the DNS solution at a lower y^+ than the Stress-τ model.

Agreement is also good between the $\overline{v^2} - f$ and EB-SSG models for U^+ and k^+ (Figure 4.13), although this form of the $\overline{v^2} - f$ does lead to a significant underprediction of C_f that leads to the large velocity profile offset. In contrast the EB-SSG follows the DNS solution closely, only slightly underpredicting U^+ in the buffer region. k^+ profiles are very similar for both models.

Profiles of the Reynolds stresses (Figure 4.14) are where key differences between the two Reynolds stress models appear, given their significantly different approaches

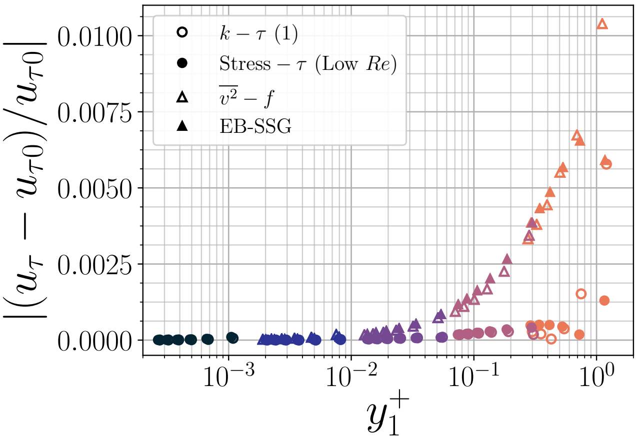

FIGURE 4.12: Friction velocity dependence on the near-wall cell size for Reynolds stress models, and similar eddy-viscosity models. $u_{\tau 0}$ is taken as the estimated exact solution (4.54) for S5 (or S4 for EB-SSG and $\overline{v^2} - f$), for respective turbulence models. Colours represent different sets, as per Figure 4.2: ●, S1; ●, S2; ●, S3; ●, S4; ●, S5.

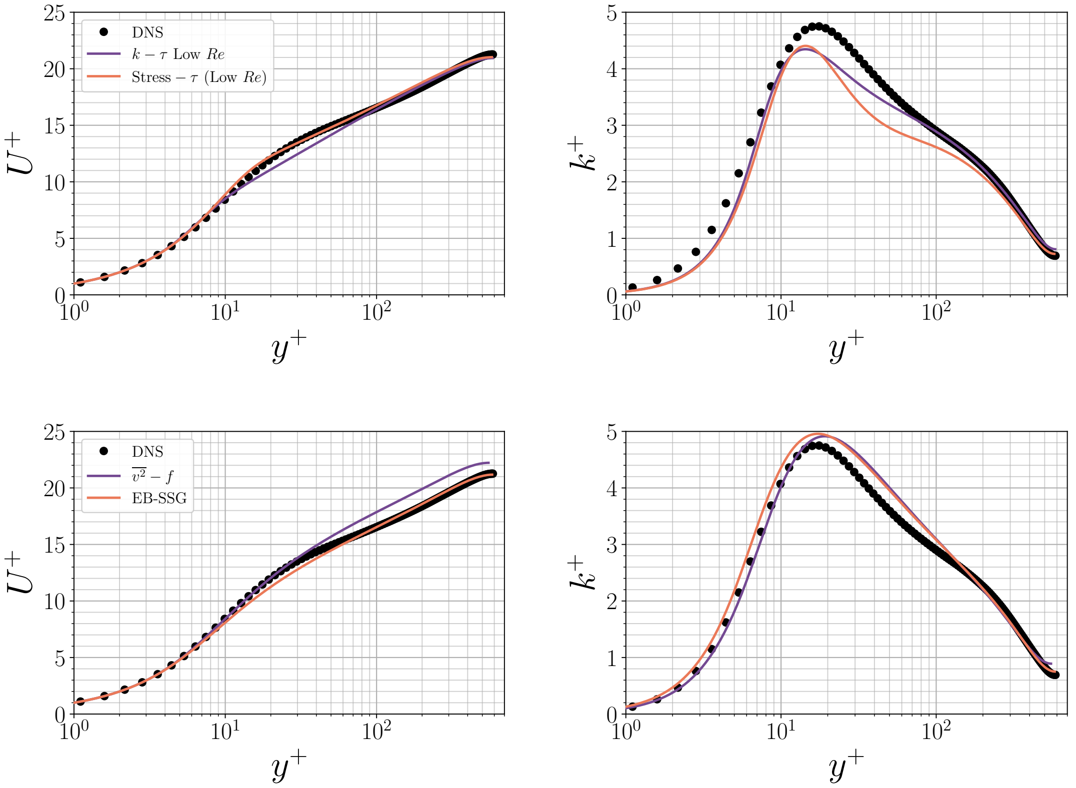

FIGURE 4.13: Profiles of U^+ and k^+ for Reynolds stress models and similar eddy-viscosity models, compared to the DNS of Moser, Kim, and Mansour (1999). Data are from case S4 M5.

to modelling the pressure-strain Π_{ij} and dissipation ε_{ij} tensors. (Note that the eddy-viscosity model profiles have been omitted due to their isotropic formulations). Differences are clearly vast when considering the diagonal components of $\overline{u_i'u_j'}^+$. The EB-SSG model obtains very close agreement with the DNS for all three components, only slightly overpredicting the peak of $\overline{w'w'}^+$. In contrast the Stress-τ model leads to very poor predictions; deviations in the three diagonal Reynolds stress components are limited to the log-layer and are essentially a small perturbation away from an isotropic turbulent kinetic energy. This is most obvious near the wall, where all three contributions to k^+ converge to a common profile. Clearly the two-component limit of near-wall turbulence is not obtained for this model. The main differences in the Reynolds stresses is limited to the log-layer which must have arisen from the LRR closure of Π_{ij}. In its present form the Stress-τ allows for some anisotropy in the flow, but wall-blockage and pressure-echo effects are not accounted for. Good predictions of the principal Reynolds stresses are obtained for both EB-SSG and Stress-τ (Figure 4.14).

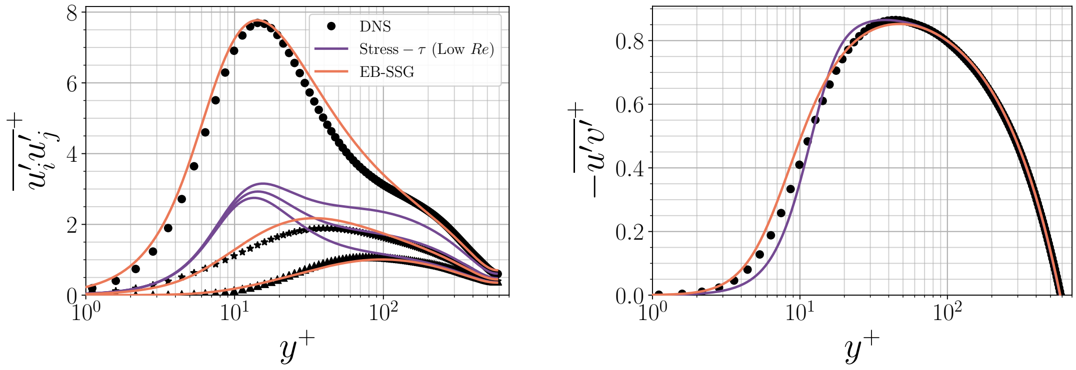

FIGURE 4.14: Profiles of Reynolds stresses for EB-SSG and Stress-τ, compared to the DNS of Moser, Kim, and Mansour (1999). Data are from case S4 M5. Diagonal Reynolds stresses (left) are: ●, $\overline{u'u'}^+$; ▲, $\overline{v'v'}^+$; ★, $\overline{w'w'}^+$.

4.5 Conclusions

In conclusion this chapter has analytically investigated the near wall behaviour of several turbulence models, addressing leading order balances, boundedness, and the limiting behaviour of k and the scale determining variables. Significant modifications are required in order to achieve reasonable predictions of the boundary layer with ε based models, typically in the form of damping functions or timescale limiters, both of which significantly alter the limiting behaviour of the transport of ε. In contrast, ω based models can achieve reasonable velocity profiles while retaining a simple form of the ω transport equation. Low Reynolds number corrections can be applied by damping the model coefficients, but these do not significantly alter the limiting behaviour of the transport equations. However, ω is singular at the wall, growing like $1/y^2$, and the leading order terms of the transport of ω are significantly unbounded. Discretisation errors associated with this behaviour can be mitigated against by solving transport equations for $\omega' = \omega - \omega_w$, $\tau = 1/\omega$, or $g = 1/\sqrt{\omega}$, which reduce to Dirichlet boundary conditions at the wall while retaining the excellent boundary layer predictions of the ω based models.

Channel flow simulations are carried out in order to investigate the solution dependence of these models on y_1^+, which is varied between approximately 2.5×10^{-4} and 1. Simulations are carried out at a fixed bulk Reynolds number of $Re_b = 10\,864$, equating to a shear Reynolds number of $Re_\tau \approx 590$. Friction velocity, u_τ, predictions (and subsequently the friction coefficient, C_f) are particularly sensitive to the near wall cell size. Most models exhibit an error of approximately 1 % when adopting the 'rule of thumb' $y_1^+ \approx 1$. The $k - \varepsilon$ model of Lam and Bremhorst (1981) obtains quadratic convergence of the friction velocity as a function of the refinement ratio, and is insensitive to the two types of boundary treatments tested. In contrast, the $\overline{v^2} - f$ model converges approximately linearly with the refinement ratio. At $y_1^+ \approx 1$ friction velocity errors are approximately 1 % for the $\overline{v^2} - f$ model, outperforming the 1.5 % error achieved by the model of Lam and Bremhorst (1981) despite its linear convergence with refinement ratio. The standard $k-\omega$ model requires a cell size of $y_1^+ \approx 0.1$ to reduce the friction velocity errors below 1 %, and exhibits an error of $\sim 4.74\,\%$ at $y_1^+ \approx 1$ for the friction velocity, equating to an error for the friction coefficient in excess of 10 %. This error has large implications in the context of engineering simulations based on the 'rule of thumb' $y_1^+ \simeq 1$. This error is entirely due to the singular behaviour of ω, which is mitigated against when adopting the $k-\omega'$, $k-\tau$, or $k-g$ model. These models achieve an error for the friction velocity of less than 1 % at $y_1^+ \approx 1$, and less than 0.1 % at $y_1^+ \approx 0.3$, outperforming all other models. When adopting highly resolved meshes solutions for $k-\omega$, $k-\omega'$, $k-\tau$, and $k-g$, all collapse, suggesting that solutions only differ due to numerical errors. There are two advantages of the $k-\tau$ formulation over $k-\omega'$ and $k-g$; the equations are fully bounded at the wall, and there is no dependence on the wall-normal distance. For these reasons, the original $k-\tau$ model is extended to include updated coefficients, a cross-diffusion term, and Low Reynolds number corrections; good agreement is obtained against channel flow DNS data. The $k-\tau$ closure has also been extended to a Reynolds Stress Model (RSM) by reformulation of the Stress-ω model of Wilcox (2006). This is a simple RSM with identical underlying transport equations as the two-equation $k-\tau$ model, which unsurprisingly leads to near identical friction velocity errors. For comparisons a further RSM was investigated, the EB-SSG model of Manceau (2015). Unlike the simple Stress-τ model, the EB-SSG accounts for near-wall anisotropy through an additional elliptic transport equation for a blending parameter. y_1^+ dependency for EB-SSG is similar to the $\overline{v^2}-f$, obtaining friction velocity errors of less than 1 % for $y_1^+ < 1$.

These new τ-based formulations offer a promising alternative to the popular ω models and could provide excellent boundary layer predictions at a feasible value of y_1^+. However, the numerical improvements of the τ formulation close to the wall do not guarantee globally better performance than ω models, and so future work should focus on the validation of this model in freestream and strongly separating flows.

Chapter 5

The scaling of secondary flows over longitudinal riblets

The prediction of flows over ribletted surfaces is a challenge for RANS type modelling that has yet to be overcome (see Section 2.3). Streamwise-aligned parallel riblets are a specific type of roughness that are two-dimensional in cross section, typically characterised by their inner-scaled spacing between consecutive peaks, $s^+ = su_{\tau 0}/\nu$, where s is the riblet spacing, $u_{\tau 0}$ is a reference flat plate friction velocity and ν the kinematic viscosity. Despite being considerably less geometrically complicated than shark skin denticles RANS predictions of the flow over riblets have often led to non-physical predictions of the viscous regime where $s^+ \lesssim 10$ (see e.g. Launder and Li, 1993; Djenidi and Antonia, 1993), and vastly different drag predictions when compared to DNS and experiments. Predictions improve when accounting for anisotropy by adopting Reynolds stress closures, but their investigation is limited to one small parameter study (Djenidi and Antonia, 1995). Before one can hope to predict the flow over complex 3D shark skin denticles it is vital to ensure that reasonable predictions of these simpler flows are attainable, and identify appropriate turbulence models.

This chapter investigates the predictive capabilities of three turbulence closures for a fully developed channel flow over sawtooth riblets, a geometry chosen due to its common occurrence in previous studies (e.g. Choi, Moin, and Kim, 1993; Launder and Li, 1993; Djenidi and Antonia, 1995; Bechert et al., 1997). The effects of riblet spacing and bulk flow Reynolds number are investigated, and results are validated against experimental and numerical data in order to identify whether adopted turbulence models are appropriate for the simulation of flows over shark skin denticles. Furthermore the identification of appropriate turbulence closures allows an investigation of the scaling of secondary flow that emerges near the riblet tips. Through both numerical and analytical techniques two distinct regimes which govern how the secondary flow scales with the riblet dimensions are identified. Firstly, a viscous regime where vorticity is produced by Reynolds stress anisotropy and dissipated by molecular viscosity, and secondly an inertial regime where viscous effects are negligible, necessitating the emergence of an effective turbulent viscosity.

5.1 Methodology

The geometry investigated is a fully developed channel flow over sawtooth riblets with a riblet spacing, s, twice that of the riblet height, h: $s = 2h$. The flow is fully developed in the streamwise (x) direction and is assumed steady state and incompressible. The flow domain has the two-dimensional cross section observed in Figure 5.1 and split into the blocks of Figure 5.2. Symmetry boundary conditions are applied to the $z-$ normal boundaries (spanwise) and the top boundary ($y = \delta$, where δ is the channel half-height) with no-slip conditions on the riblet surface. Periodic boundary conditions are applied to the remaining boundaries. Two Reynolds numbers are simulated: $Re_b = U_b\delta/\nu = 2825$ and $Re_b = 10864.85$, where U_b is the bulk flow velocity and ν the kinematic viscosity. These bulk flow Reynolds numbers approximately equate to $Re_\tau = u_\tau\delta/\nu \approx 180$ and $Re_\tau \approx 590$ for a smooth wall channel flow, where $u_\tau = \sqrt{\tau_w/\rho}$ is the friction velocity, τ_w is the wall shear stress and ρ is the fluid density. This study varies the riblet spacing s while maintaining a constant ratio $s/h = 2$. Presented simulations cover an s^+ range of approximately 5 to 50, which fully captures the expected drag reducing regime of sawtooth riblets (Bechert et al., 1997).

5.1.1 Turbulence closures

Three turbulence closures are adopted herein; the two equation $k-\tau$ model with low Reynolds number corrections, the Stress-τ model with low Reynolds number corrections, and the EB-SSG model. These are discussed in Chapter 4 and detailed in Appendices C.5, C.8, and C.9. The two τ based models have been chosen due to their excellent numerical properties near the wall, where solutions can be obtained with minimal numerical

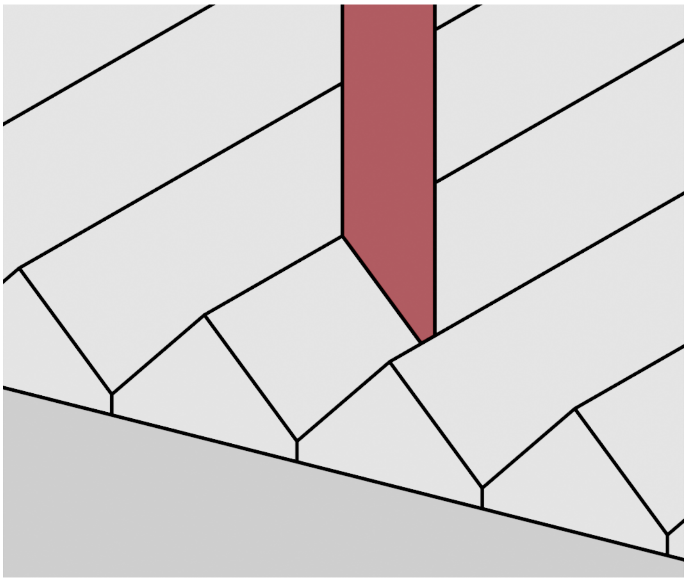

FIGURE 5.1: Fluid 2D domain above sawtooth riblets. Flow direction (x) is perpendicular to the 2D plane.

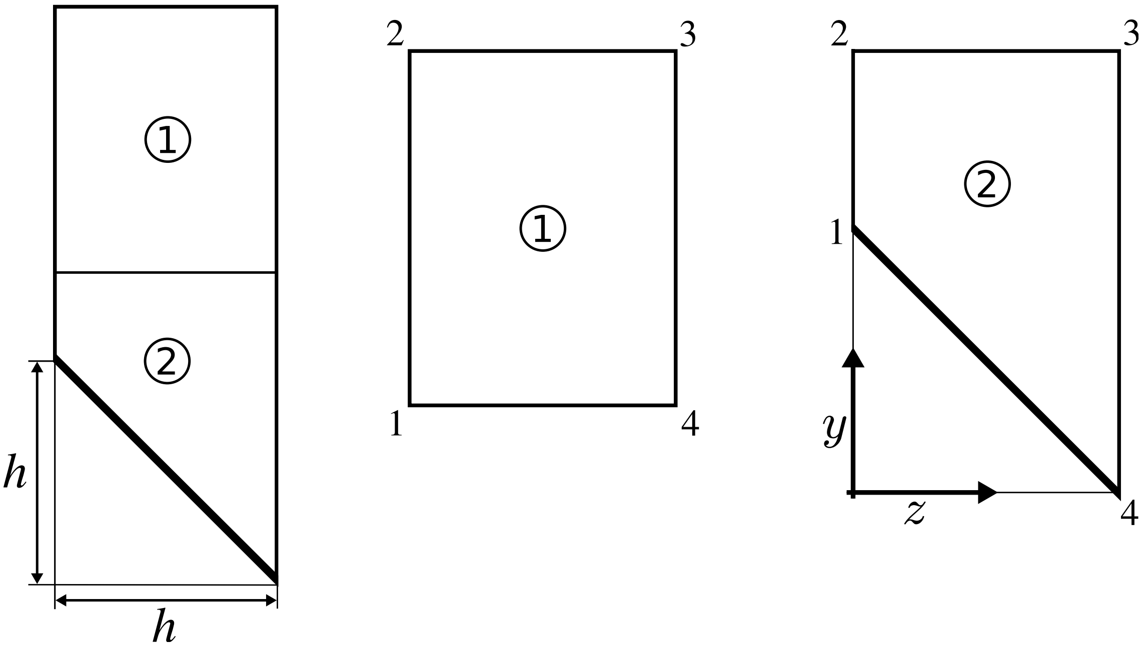

FIGURE 5.2: Fluid domain split into two blocks for the creation of a structured mesh. The thick line represents the riblet no-slip surface. $y-$ and $z-$ normal boundaries are treated with symmetry boundary conditions and $x-$ normal boundaries are periodic.

error associated to discretisation at near-wall cells (see Chapter 4 for details). Both these models require low Reynolds number damping in order to correct the behaviour of k and ν_t near the wall. The Stress-τ model has been introduced as a means to account for anisotropy in the flow. The model is a simple extension of the $k-\tau$ model, but allows for variation in the distribution of turbulent kinetic energy, which may be vital to achieve accurate predictions of the flow over riblets and shark scales. However, the Stress-τ model adopts a linear closure for the pressure-strain correlation (Launder, Reece, and Rodi, 1975), and does not account for near-wall kinematic blocking or pressure-echo effects, except through damping of the model coefficients. The EB-SSG model can account for these effects at the expense of numerical stability and computational costs. If it is important to correctly model near-wall anisotropy then the EB-SSG should perform better than Stress-τ.

5.1.2 Numerical techniques

The Reynolds numbers $Re_b = 2825$ and $Re_b = 10864.85$ are enforced by adopting an iterative source term in the momentum equation that ensures a fixed bulk velocity, U_b, as per Murthy and Mathur (1997). The channel half height is set to $\delta = 1$ and the fluid kinematic viscosity set to either $\nu = 1/180$ or $1/590$ depending on the Reynolds number. These correspond to $Re_\tau \approx 180$ and $Re_\tau \approx 590$ for a smooth-walled channel flow, with $u_\tau \approx 1$.

TABLE 5.1: Mesh statistics for a riblet height of $h^+ = 25$. Dimensions correspond to those of Figure 5.2. Inner length scales are approximated by the smooth wall u_τ.

	$Re_\tau \approx 180$						$Re_\tau \approx 590$					
	Block 1			Block 2			Block 1			Block 2		
	L^+	R	N	L^+	R	N	L^+	R	N	L^+	R	N
l_{12}	$\delta^+ - 80$	2	28	$80 - h^+$	10	82	$\delta^+ - 200$	2	54	$200 - h^+$	10	204
l_{23}	h^+	1	25	h^+	1	50	h^+	1	25	h^+	1	50
l_{34}	$\delta^+ - 80$	2	28	80	10	82	$\delta^+ - 200$	2	54	200	10	204
l_{14}	h^+	1	25	$\sqrt{2}h^+$	1	50	h^+	1	25	$\sqrt{2}h^+$	1	50

Equations are discretised and solved using OpenFOAM 4.1 (Weller et al., 1998). Convective terms are treated using a second order accurate TVD scheme, except velocity which adopts a second-order upwind scheme. Laplacian terms are discretised using standard Gaussian integration, with face gradients calculated using linear-interpolation. Corrections are made to account for non-orthogonality when calculating face fluxes. The SIMPLEC scheme of Van Doormaal and Raithby (1984) is adopted to couple pressure and velocity equations, with the friction velocity used to determine convergence. The friction velocity converged to a relative error of 1×10^{-7} for all cases, typically corresponding to normalised residual errors of less than 1×10^{-10}.

5.1.3 Meshing strategy

A blocking strategy, observed in Figure 5.2, is adopted to create a structured mesh. Vertices for each block are numbered and their edges given the notation l_{ab} with a and b representing a vertex pair. For each edge a geometric stretching function is adopted, where the edge length specified in approximate wall units, L^+ (estimated using the smooth wall channel flow u_τ), global expansion ratio, $R = \frac{\Delta_n}{\Delta_1}$, and number of elements, N, are specified. Further details on this stretching function can be found in Chapter 4. The lower block has a height of either 80 wall units or 200 wall units, depending on the Reynolds number. The grid definitions for $h^+ = 25$ (the largest riblets tested) are presented in Table 5.1 for each Reynolds number. In order to mesh a large h^+ range N and R are adjusted for block 2 edges l_{12} and l_{34} to ensure the near-wall cells scale with h^+ while maintaining the same cell size at the upper block edge. In other words, if h^+ is halved, the near-wall cell size is halved and R is doubled. N is subsequently adjusted to ensure Δ_n is constant for all meshes. For $h^+ = 25$ the grid has near-wall cell sizes corresponding to a maximum of $y_1^+ = 0.12$ for $Re_\tau \approx 180$ and $y_1^+ = 0.15$ for $Re_\tau \approx 590$. These are naturally reduced as h^+ decreases due to the scaling of the near-wall cell sizes. This range of y_1^+ should ensure friction velocity errors associated to the near-wall cell size are less than 0.25 % (see Chapter 4).

Grid independence is assessed by globally refining by a factor of 2 in all directions and comparing solutions of u_τ, $\overline{U}_x$, and k for the $k-\tau$ Low Re turbulence model, for both Reynolds numbers. Solutions of u_τ differ by 0.22 % between the two grids at $Re_\tau \approx 590$, and 0.19 % at $Re_\tau \approx 180$. Profiles of inner-scaled mean streamwise velocity, $\overline{U}_x^+$, and turbulent kinetic energy, k^+, can be observed in Figure 5.3. Differences between the two meshes are negligible, justifying the use of the base mesh statistics of Table 5.1 for parameter studies.

5.2 Results and discussion

The predicted drag reduction of sawtooth riblets is presented in Figure 5.4, where $C_f = 2u_\tau^2/U_b^2$ is the friction coefficient, and C_{f0} is the friction coefficient for the reference smooth channel. Drag reduction is achieved if C_f/C_{f0} is less than 1. A consistent trend observed for all turbulence models is that the higher Re_τ simulations lead to lower drag for the same value of s^+. This trend was also observed by Launder and Li (1993), and can potentially be explained by the differences in blockage ratio δ/h. However, the DNS solutions

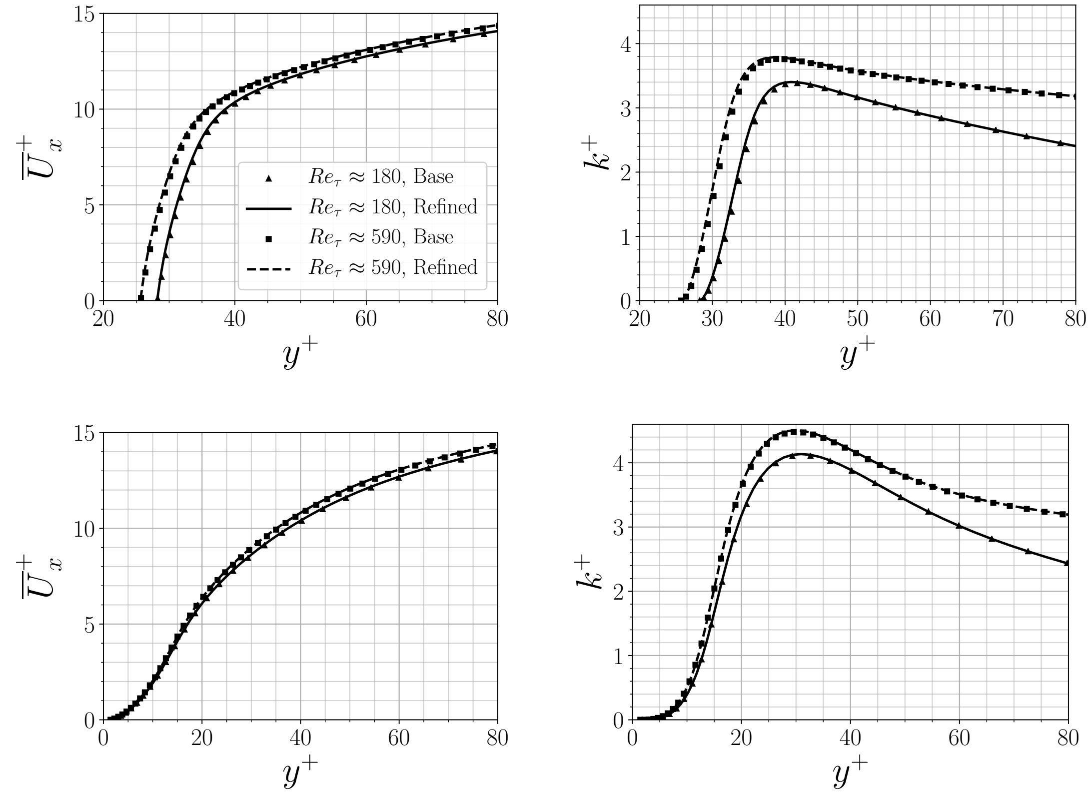

FIGURE 5.3: Demonstration of grid independence for the flow over sawtooth riblets. Profiles taken at riblet crest (upper) and riblet valley (lower). For clarity, every third data point has been plotted for the base mesh solutions.

of García-Mayoral and Jiménez (2012), also presented in Figure 5.4, suggest that differences between solutions at $Re_\tau \approx 180$ and $Re_\tau \approx 550$ should be fairly small. The DNS of García-Mayoral and Jiménez (2012) was carried out on blade-like riblets rather than sawtooth which could explain their insensitivity to Re_τ. While the blade-like riblets of García-Mayoral and Jiménez (2012) had the same height and spacing as the presented sawtooth riblets, their average height was half that of the sawtooth herein. The sawtooth riblets at $s^+ = 16$ and $Re_\tau = 180$ lead to blockage ratios of $\delta/h = 22.5$ and $\delta/\overline{h} = 45$, where $\overline{h}$ is the average riblet height, while the blade-like riblets lead to $\delta/h = 22.5$ and $\delta/\overline{h} = 90$ for the same spacing and Reynolds number. If it is assumed that the appropriate roughness height k_0 lies somewhere between these values then it seems reasonable that the blade-like riblets lead to blockage ratios close to or greater than the threshold $\delta/k_0 \approx 40$ as specified by Jiménez (2004), perhaps explaining why results are insensitive to further increases to Re_τ. In contrast, the sawtooth riblets lead to blockage ratios that will effect a large proportion of the boundary layer, providing explanation as to why drag is reduced more when the Reynolds number is increased.

The two-equation $k-\tau$ Low Re model predicts a drag increase for all riblet sizes at $Re_\tau \approx 180$, clearly far from the DNS and experimental data sets. At $Re_\tau \approx 590$ marginal drag reduction is achieved, but only for the $s^+ = 15$ case. The viscous region is particularly poorly predicted, where C_f/C_{f0} does not converge to 1 as s^+ decreases. The same behaviour is obtained for the Low Reynolds number $k-\varepsilon$ model adopted by Launder and Li (1993), suggesting that accounting for near-wall anisotropy is critical for the prediction of riblet flows.

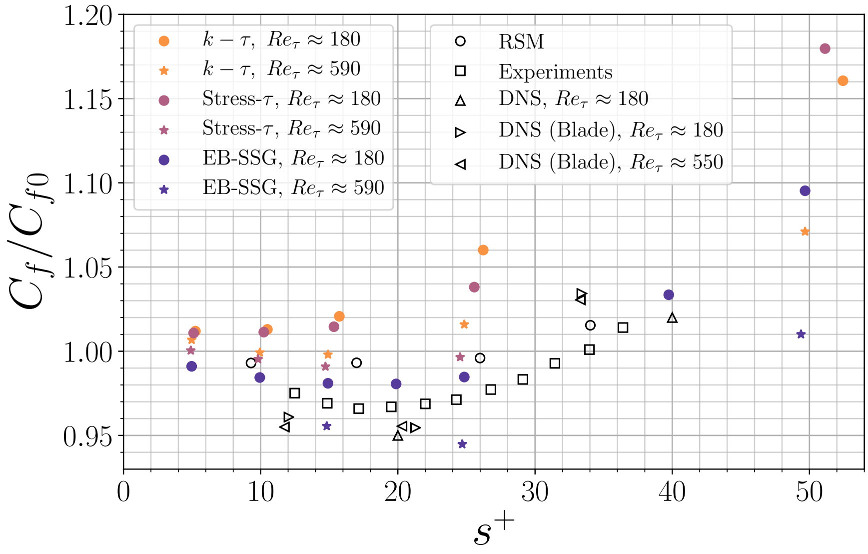

FIGURE 5.4: Predicted drag reduction of sawtooth riblets for different turbulence models. Data from (◁, ▷) García-Mayoral and Jiménez (2012), (□) Bechert et al. (1997), △ Choi, Moin, and Kim (1993), (○) Djenidi and Antonia (1995). RSM is an abbreviation for Reynolds Stress Model.

The Stress-τ model obtains similar solutions to the $k - \tau$. Their agreement can be explained by the similarity between their damping functions, used to correct the model behaviour close to the wall. The Stress-τ model leads to marginal drag reduction of similar levels to the Low Reynolds number Reynolds Stress Model (RSM) of Djenidi and Antonia (1995) at $Re_\tau \approx 590$, although converges to $C_f/C_{f0} = 1.0$ at $s^+ \approx 5$, as opposed to $s^+ \to 0$. This is inconsistent with the experiments and DNS, and raises the question - what happens as s^+ decreases further? Given that the solutions for the Stress-τ model are so similar to the $k - \tau$ model drag could be expected to increase as s^+ reduces to zero, inconsistent with theory.

In contrast, the behaviour $C_f/C_{f0} \to 1$ as $s^+ \to 0$ is well predicted by the EB-SSG model, for both Reynolds number cases. Drag reduction profiles for $s^+ \lesssim 20$ are reasonably well predicted when compared to the DNS and experimental results. At $Re_\tau \approx 180$ and $s^+ \approx 15$ the EB-SSG model predicts a drag reduction of 2 %, not far from the experimental values of 3 %. The full drag reducing regime appears of the same form as experiments and DNS. Of critical importance is the behaviour in the viscous limit as s^+ decreases; unlike other models the EB-SSG model obtains the linear regime for small s^+. At $Re_\tau \approx 590$ the EB-SSG model predicts a similar curve but with a larger drag reducing regime, and achieves a maximum drag reduction of approximately 5 %. While this is a little larger than experiments it is certainly within the limits of typical riblet behaviour (See e.g. Figure 2.5 in Section 2.3.). These results suggest that correctly accounting for near-wall anisotropy is vital for the prediction of flows over riblets.

Despite the large differences in C_f predictions, both the EB-SSG and Stress-τ models lead to near identical viscous stress distributions over the riblet surface, as observed in Figure 5.5, where the velocity gradient has been normalised by the reference flat plate friction velocity. By normalising in this way the regions where drag is increased and decreased relative to the reference plate can be identified; shear stresses above 1 indicate an increase in friction while values below 1 indicate regions of low shear stress relative to the flat plate. Both models predict that ∼80 % of the plate has a lower friction compared to the flat plate, while the riblet tips lead to larger shear stresses. Figure 5.5 clearly shows that differences between the two Reynolds stress closures are marginal, and can only be identified for the larger riblets ($s^+ = 25$) where the EB-SSG model predicts a slightly lower magnitude of shear stress compared to the Stress-τ model for $z/s \lesssim 0.1$. This may not seem intuitive given the large differences observed in the friction coefficient (Figure 5.4) but these large differences can be obtained when integrating the shear-stress distributions; the small differences in magnitude add up to create substantial differences in C_f. Given the similarities in the shear stress at the wall, differences in model predictions must arise further into the flow field.

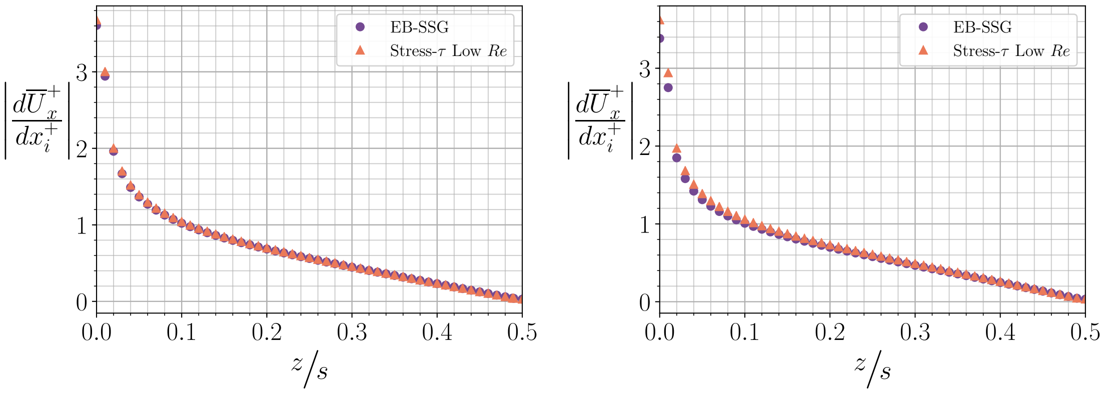

FIGURE 5.5: Viscous stresses at the wall for riblets of size $s^+ \approx 5$ (left) and $s^+ \approx 25$ (right) at $Re_\tau \approx 180$. Viscous stresses are normalised by respective flat plate friction velocities.

Comparisons between EB-SSG and Stress-τ Low *Re*

Here the near-riblet flow is investigated in order to establish the differences in predictions between the two Reynolds stress closures. Further analysis omits data for the $k - \tau$ Low *Re* model, given its similarities to the Stress-τ model. First, differences in the viscous stresses are quantified above the riblet surface as a function of the vertical inner-scaled coordinate y^+, observed in Figure 5.6. Several profiles in $z-$ have been plotted in order to capture the variation of these quantities in the spanwise direction. For comparisons the reference flat plate solutions have been added and variables have been scaled by the reference flat plate friction velocity. Profiles over the riblets have been offset in $y-$ by using the same virtual origin definition as Choi, Moin, and Kim (1993), who suggest that an appropriate virtual origin can be found by matching the location of maximum turbulent kinetic energy. Mathematically this leads to

$$y^+ = \tilde{y}^+ - (\tilde{y}_k^+ - y_{kf}^+) \tag{5.1}$$

where $\tilde{y}^+$ is the original coordinate with its origin at the riblet valley, the subscript k represents the point of maximum turbulent kinetic energy, and the subscript f represents the reference flat plate coordinate. The profiles of Figure 5.6 indicate that for small s^+ the two models provide similar predictions of the viscous stresses, with both collapsing to the flat plate reference solution for $y^+ \gtrsim 40$. This behaviour is unsurprising, given that the effect of roughness on velocity profiles is a simple shift to the log-law region while maintaining the same velocity gradient (Jiménez, 2004). Differences between the models are therefore limited to the regions close to the riblets. Dependence on z/s is also similar between the two models; there is strong dependence on z/s for $y^+ \lesssim 5$ which quickly tends to a spanwise-homogeneous solution for $y^+ \gtrsim 10$, although these regions are of course strongly dependent on the riblet size. At $z/s = 0$ (riblet tip) EB-SSG consistently leads to a greater viscous stress than at $z/s = 0.5$ (riblet valley) over the full

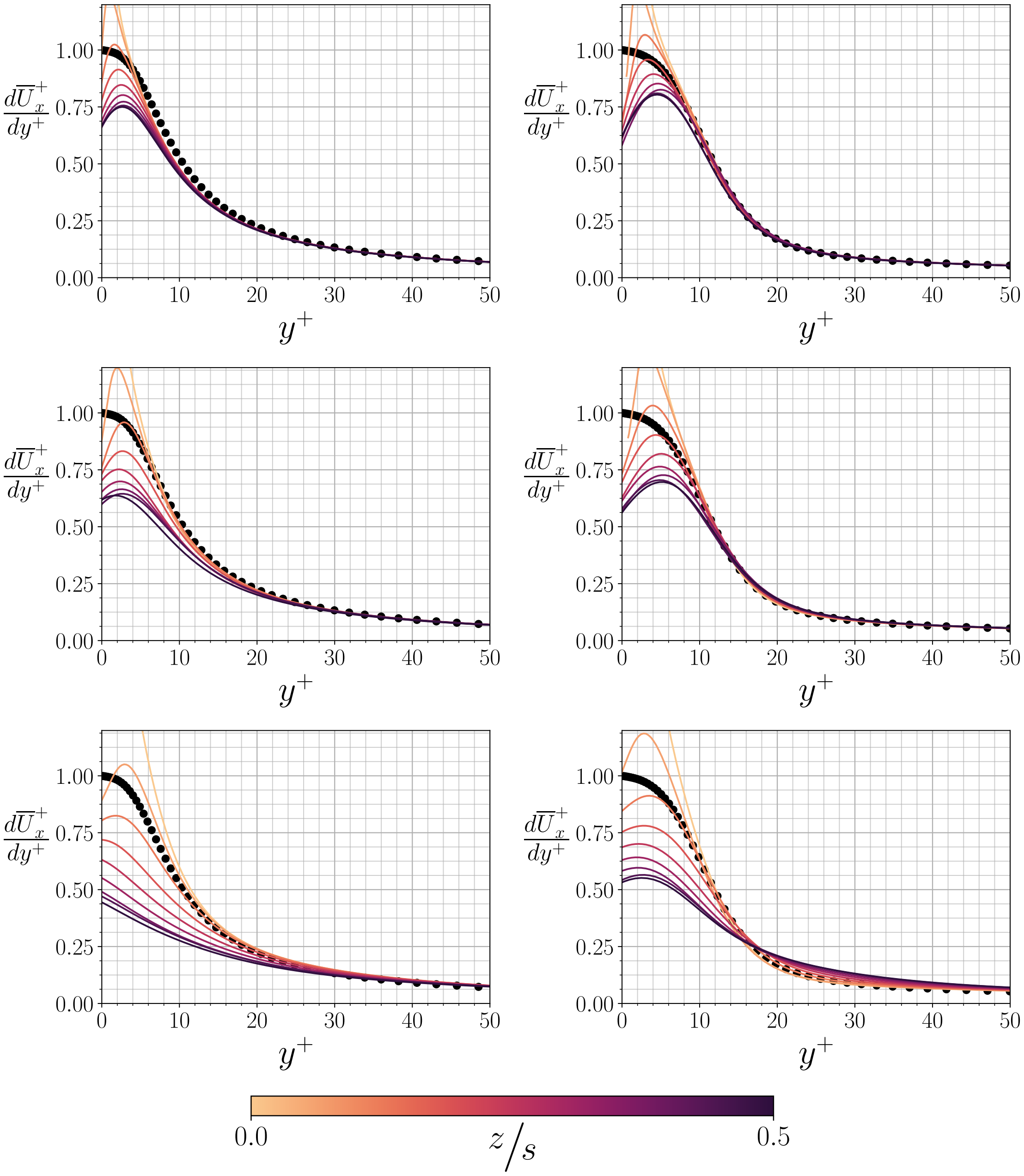

FIGURE 5.6: Viscous stress profiles above riblets of size $s^+ = 15$, $s^+ = 25$, and $s^+ = 50$ from top to bottom, at several z/s positions for EB-SSG (left) and Stress-τ (right). z/s positions are identified by the colour maps where the riblet tip lies at $z/s = 0$ and the valley lies at $z/s = 0.5$. • represents respective flat plate solutions for each model. The viscous stress is scaled by the reference flat plate friction velocity and the inner scaled coordinate y^+ is obtained from (5.1). All data are for $Re_\tau \approx 180$.

domain, until they eventually collapse into a spanwise-homogeneous state. In contrast, the Stress-τ model predicts that the viscous stresses at $z/s = 0$ converge to the flat plate solution quicker than at $z/s = 0.5$. This leads to two separate regions: Very close to the riblets viscous stress is largest above the riblet tip, but further from the riblet surface the stress above the valley becomes larger than that above the riblet tip. This behaviour is inconsistent with the DNS solutions of Choi, Moin, and Kim (1993) who report similar behaviour to that obtained by EB-SSG; there is no region where the viscous stresses are larger above the riblet valley than the riblet tip.

Similar behaviour is observed for $\overline{u'v'}$, the turbulent contribution to the total shear stress, shown in Figure 5.7. Dependence on z is minor for these Reynolds stresses when s^+ is small. Interestingly the behaviour of the two models only differs for $y^+ \gtrsim 20$, where the EB-SSG model consistently leads to a Reynolds stress magnitude lower than that of the reference plate. In contrast, the Stress-τ model collapses onto the flat plate solution for large s^+. This is a strange result given that the Stress-τ model predicts a relative change in skin friction greater than that of the EB-SSG model and yet obtains the same Reynolds stress scaling as the reference flat plate for $s^+ \lesssim 25$. Predictions differ for $s^+ \approx 50$ where the Stress-τ model predicts a significantly larger Reynolds stress for the riblets. The behaviour is very different to the EB-SSG; whereby it is the riblet valley that leads to the largest turbulent stress, rather than the riblet tip. Interestingly the convergence behaviour of the Reynolds stresses is opposite to that of the viscous stresses. Here the Stress-τ model obtains a consistently higher Reynolds stress at the riblet valley than above the riblet tip, for all y^+, while the EB-SSG obtains a higher Reynolds stress at the riblet tip for $s^+ \gtrsim 15$ but a higher Reynolds stress at the riblet valley for $s^+ \lesssim 15$. This behaviour is consistent with the DNS of Choi, Moin, and Kim (1993), and arises from the very steep gradient of $\overline{u'v'}$ at the riblet tip, which is properly captured by the EB-SSG model. Effectively the two contributions to the total stress are predicted in opposing ways by the Stress-τ model; there is a cross-over point that should not exist for the viscous stresses, and a lack of cross-over point for the turbulent stresses which should be present. In contrast, EB-SSG is able to correctly reproduce this behaviour.

Profiles of the root-mean-square (RMS) velocities are presented in Figure 5.8. Like the viscous and Reynolds stresses differences are observed in $z-$ close to the riblet surface which become homogeneous as y^+ increases. The effect of riblets on the distribution of turbulent kinetic energy is predicted differently by the two models. The Stress-τ model obtains a collapse of all components onto reference flat plate solutions for $s^+ \gtrsim 15$, except at large s^+. In contrast the EB-SSG model obtains collapse onto reference flat plate solutions for $\overline{v'v'}$ and $\overline{w'w'}$ but obtains a slightly lower magnitude for $\overline{u'u'}$, suggesting the the riblets have reduced the turbulent kinetic energy primarily in the streamwise direction. Differences between the two models are vast for $s^+ \approx 50$. While EB-SSG predicts transition to the homogeneous state at $y^+ \approx 20$ the Stress-τ model obtains significant variation in z for the full range of y^+ values plotted.

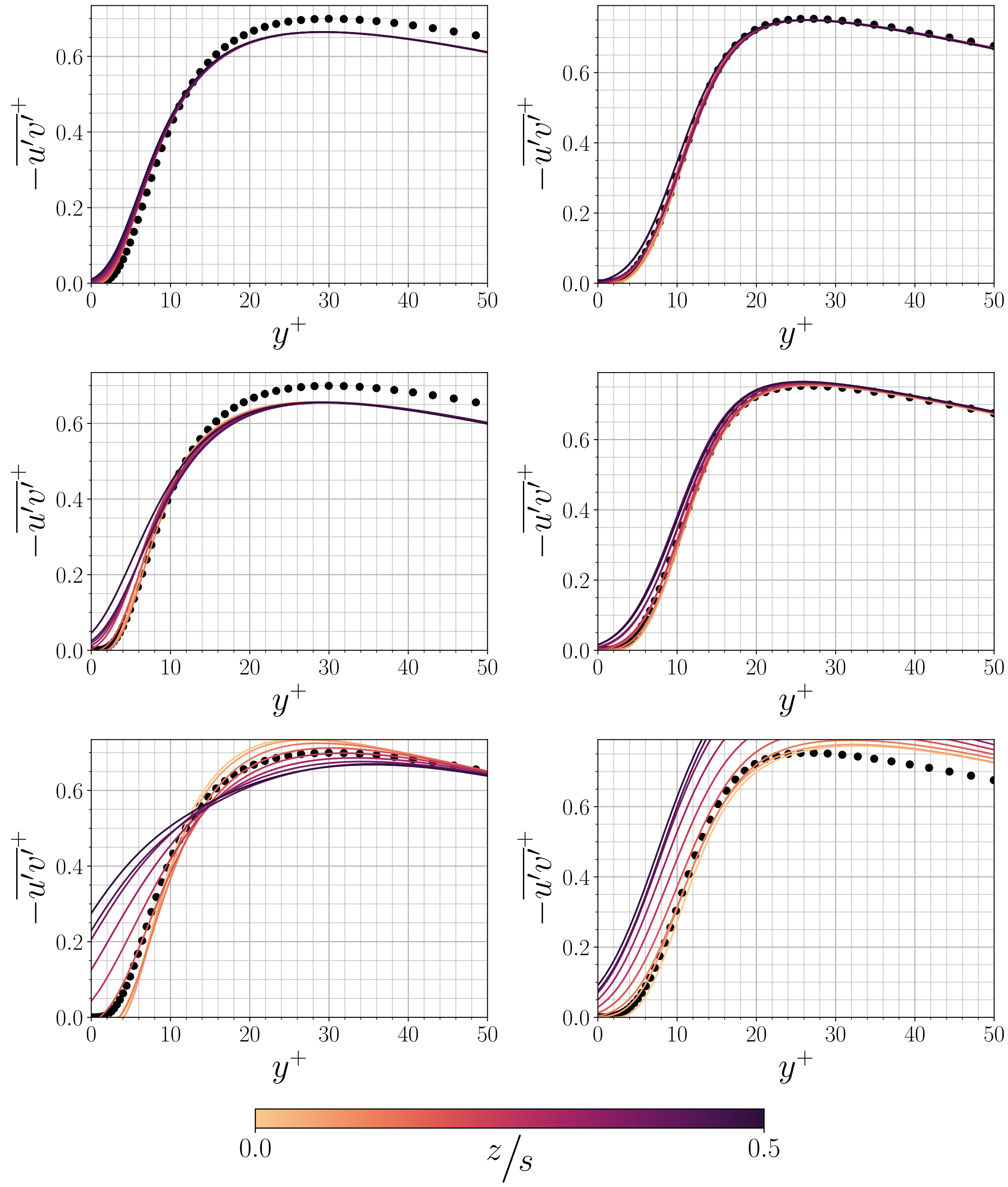

FIGURE 5.7: Reynolds stress profiles above riblets of size $s^+ = 15$, $s^+ = 25$, and $s^+ = 50$ from top to bottom, at several z/s positions for EB-SSG (left) and Stress-τ (right). z/s positions are identified by the colour maps where the riblet tip lies at $z/s = 0$ and the valley lies at $z/s = 0.5$. • represents respective flat plate solutions for each model. The Reynolds stress is scaled by the reference flat plate friction velocity and the inner scaled coordinate y^+ is obtained from (5.1). All data are for $Re_\tau \approx 180$.

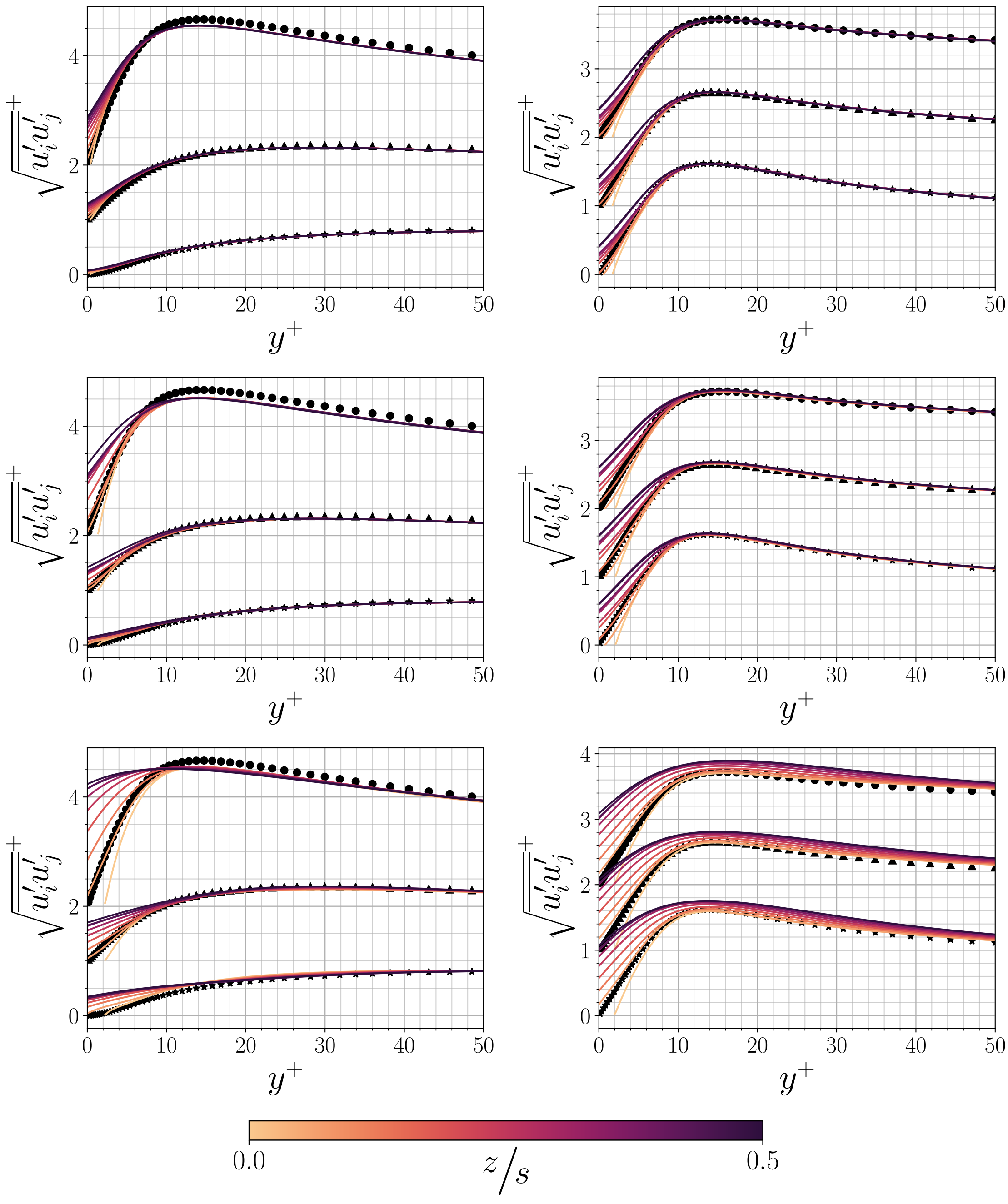

FIGURE 5.8: Root-mean-square velocity fluctuations above riblets of size $s^+ = 15$, $s^+ = 25$, and $s^+ = 50$ from top to bottom, at several z/s positions for EB-SSG (left) and Stress-τ (right). z/s positions are identified by the colour maps where the riblet tip lies at $z/s = 0$ and the valley lies at $z/s = 0.5$. Reference flat plate solutions are indicated by ● for $\overline{u'u'}$ components, ▲ for $\overline{w'w'}$ components, and ★ for $\overline{v'v'}$ components. Note that profiles have been shifted vertically by 1.0 for clarity. The RMS velocities are scaled by the reference flat plate friction velocity and the inner scaled coordinate y^+ is obtained from (5.1). All data are for $Re_\tau \approx 180$.

Further validation of EB-SSG is carried out by comparing profiles of the Reynolds stresses against the DNS solutions of Choi, Moin, and Kim (1993) at $s^+ = 20$ and $s^+ = 40$, two additional cases that have been run for the EB-SSG model. $u_{\text{rms}} = \sqrt{\overline{u'u'}}$ is compared between the EB-SSG model and the DNS at the riblet tip ($z = 0$) and the riblet valley ($z = s/2$) at $Re_\tau \sim 180$ in Figure 5.9. u_{rms} is normalised against the centreline velocity, although it should be noted that the simulations of Choi, Moin, and Kim (1993) were carried out on an asymmetric channel with riblets on one wall, such that the maximum velocity did not lie on the centreline. The origin for $\eta = y/\delta$ is taken at the point at which the flow velocity is zero; i.e at the riblet tip the origin is defined as $y_0 = h$, and at the riblet valley the origin is at $y = 0$. this definition is consistent with that of Choi, Moin, and Kim (1993). For $s^+ = 20$ the two data sets obtain very similar trends: In the very near-wall region, $\eta \lesssim 0.1$ the two data sets are very similar, and only differ slightly at their peaks, where the EB-SSG reaches a slightly larger maximum, potentially explained by the slight overprediction of C_f observed in Figure 5.4, and by the differences in U_c between the RANS simulation herein and the DNS of Choi, Moin, and Kim (1993). As η increases beyond this the DNS solutions seem to reduce at a slightly steeper gradient than the EB-SSG predictions, although the differences between the flat plate, riblet tip, and riblet valley profiles are qualitatively similar. The steeper decrease can be readily explained by examining the flat plate Reynolds stress profiles of Figure 4.14 in Section 4, where the EB-SSG model deviates from the DNS in the region after the peak of $\overline{u'u'}$ before collapsing back onto the DNS solution at larger y^+. Agreement is also good for $s^+ = 40$, except at the riblet valley which increases at a steeper gradient for EB-SSG than the DNS but achieves similar differences between the profiles at the riblet tip and reference flat plate for $\eta \gtrsim 0.2$.

Further validation is achieved by investigating the secondary flow features near the riblet tips that were reported by Choi, Moin, and Kim (1993) observed in Figure 5.10. Symmetrical vortex pairs are observed at the riblet tips, with fluid moving upwards at

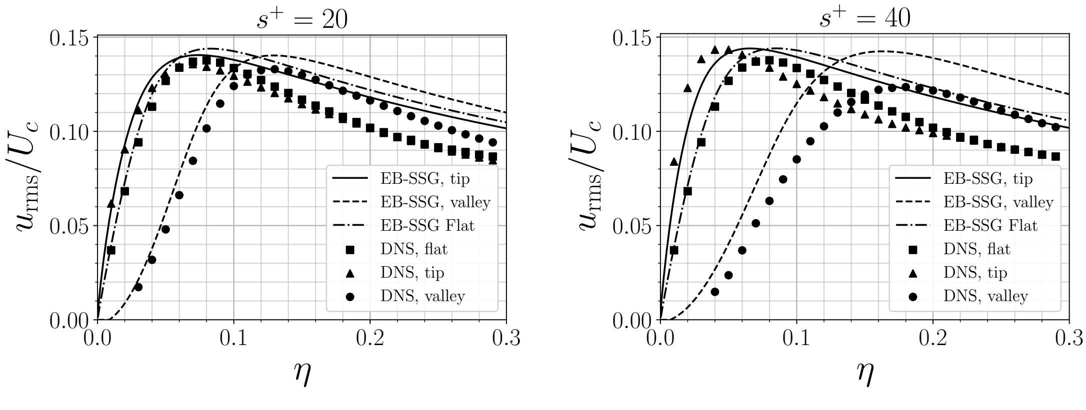

FIGURE 5.9: Comparisons of root-mean-square velocity fluctuations between EB-SSG and the DNS solutions of Choi, Moin, and Kim (1993) for sawtooth riblets at $Re_\tau \approx 180$.

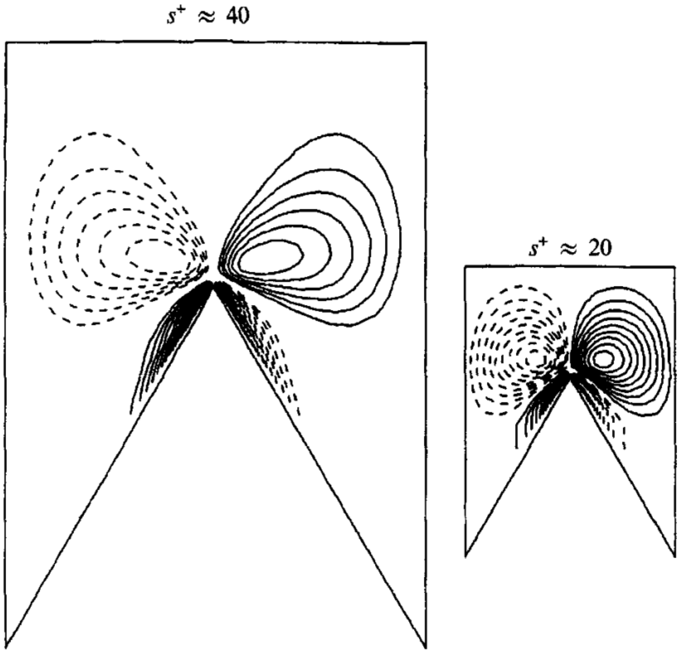

FIGURE 5.10: DNS secondary flow of Choi, Moin, and Kim (1993) over triangular riblets with a 60° ridge angle. Contours are vorticity $\Omega_x\delta/U_c$. Contour lines represent increments of 0.04 for $s^+ = 40$ and 0.02 for $s^+ = 20$. Values of $\Omega_x\delta/U_c$ at the vortex centres are 0.36 for $s^+ = 40$ and 0.19 for $s^+ = 20$. Negative contours are dashed.

the riblet tips and downwards at the valley. This is realised by the vorticity contours which show a positive peak just off-centre of the riblet tip. The secondary flow is fully embedded in half of a riblet section, such that the flow is symmetrical about the riblet tip and valley. Interestingly this secondary flow is well predicted for the EB-SSG model, but not for the Stress-τ model (Figure 5.11). The $k-\tau$ model obtains no secondary motion (not shown) while the Stress-τ model obtains a different and much weaker secondary flow pattern.

As discussed in Section 2.3 the mechanisms that drive and sustain these secondary flows are not well understood. Goldstein and Tuan (1998) have suggested that this flow is governed by the blocking of instantaneous spanwise fluctuations at the riblet tips, but if this were true then a steady-state RANS model should not be capable of obtaining these predictions. Numerical studies of the secondary flows generated by large scale spanwise-heterogeneous roughness have been investigated recently by Anderson et al. (2015) and Hwang and Lee (2018) (see Section 2.3 for details) who both concluded that vorticity is generated from the second kind of secondary flow (Prandtl, 1953); i.e through gradients of the Reynolds stresses. If this were the primary mechanism for generating secondary flows over riblets then this would explain why Reynolds stress models are capable of obtaining accurate predictions. These mechanisms will be investigated in the following section, as will the scaling of secondary flows with the riblet dimensions.

These results suggest that the EB-SSG model is highly capable of predicting the flow over riblets. Solutions obtained by EB-SSG are the most physical that have been reported for RANS-based models, leading to well predicted drag reduction profiles, secondary flows, and Reynolds stress profiles. In contrast, the two-equation $k-\tau$ model and the Stress-τ model lead to poor predictions. At $Re_\tau \approx 180$ both τ based models lead to increased drag for all s^+. This behaviour is associated to the treatment of near-wall anisotropy; clearly it is vital to capture kinematic blocking and pressure-echo effects if reasonable predictions of riblet flows are to be obtained, and neither of the τ based closures incorporate models for these effects.

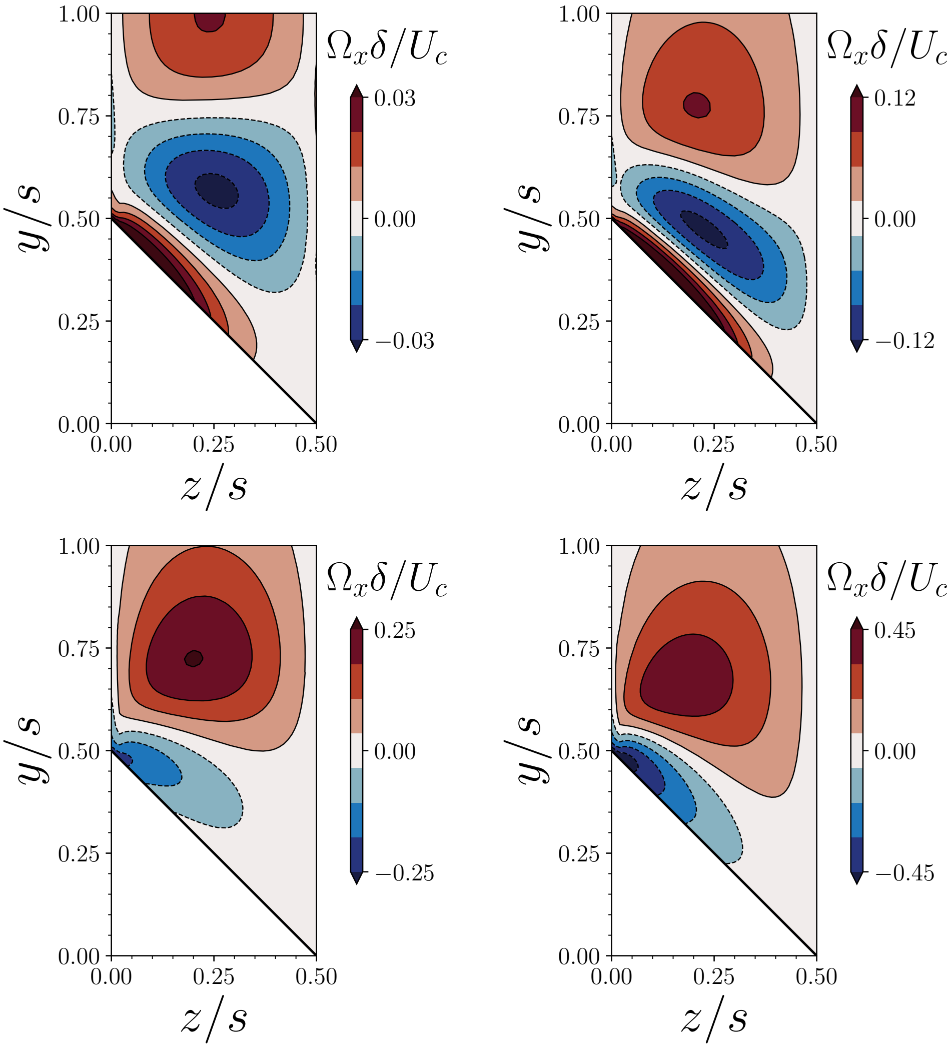

FIGURE 5.11: Contours of streamwise vorticity $\Omega_x\delta/U_c$ for $s^+ = 50$ (left) and $s^+ = 25$ (right) for the Stress-τ Low *Re* model (upper) and the EB-SSG model (lower). Data for $k-\tau$ Low *Re* are omitted, due to the streamwise vorticity being identically zero at all s^+.

5.3 Secondary flows over riblets

In this section the scaling of the vorticity field close to the riblet tips is investigated using analytical and numerical solutions obtained with EB-SSG. The mean streamwise vorticity is defined as

$$\Omega_x = \frac{\partial \overline{U}_z}{\partial y} - \frac{\partial \overline{U}_y}{\partial z} \tag{5.2}$$

and is identically zero for a fully developed flat plate boundary layer flow. However, when riblets are introduced a secondary flow develops at the riblet tips. There is clearly some s^+ dependence on the vorticity field when noting the different scale bars in Figure 5.11. The outer-scaling of the vorticity field, originally adopted by Choi, Moin, and Kim (1993) (See Figure 5.10) shows that the strength of the vorticity field approximately doubles when the riblet spacing doubles. This linear scaling with s^+ holds over a large range of s^+, as observed in Figure 5.12 where the inner-scaled streamwise vorticity $\Omega_x^+ = \nu\Omega_x/u_\tau^2$ has been normalised by s^+. The inner-scaled vorticity seems a more sensible choice than a scaling based on the outer variables U_c and δ, given that this vorticity field emerges close to the riblets and is present even for small s^+, and must therefore be independent of outer scales when riblets are small. Figure 5.12 clearly indicates that the Ω_x^+/s^+ is approximately self-similar for $s^+ < 40$, with the self-similarity breaking down at the larger riblet spacings. This appears true of both the location of maximum vorticity relative to the riblet tip, and the strength of the vorticity field. This is perhaps more obvious when plotting the maximum vorticity against s^+ for all simulations, and both Reynolds numbers, as in Figure 5.13. (Note that several additional cases have been run at $Re_\tau \approx 590$ in order to capture vorticity scaling at large s^+). Two distinct regimes are present in Figure 5.13; one at small s^+ where Ω_x^+ scales linearly with s^+, and one at large s^+ where Ω_x^+ decreases. While the linear scaling at small s^+ is well captured by the present simulations, the behaviour at larger s^+ is difficult to determine. It seems that as s^+ increases beyond $s^+ \approx 30$ the linear scaling breaks down until the vorticity strength reaches a maximum. At which point vorticity begins to decrease as s^+ increases further, although at a much slower rate than the initial increase. At larger s^+ it seems that the vorticity could tend to a constant value or it could decrease indefinitely. The breakdown region at $s^+ \approx 30$ appears independent of Reynolds number Re_τ, although the strength of the vorticity field does seem weakly Reynolds number dependent. This is likely attributed to the blockage ratios $\delta/\overline{h}$. Displayed on Figure 5.13 are two vertical lines that specify the limit $\delta/\overline{h} = 40$, which is the theoretical limit of Jiménez (2004) who suggested if blockage ratios are smaller than this then the roughness will affect the outer regions of the flow, rather than being confined to the inner region. The EB-SSG simulations operate up to a blockage ratio of $\delta/\overline{h} \approx 15$ at the largest s^+ values, which could have some effect on the vorticity field. Maintaining a blockage ratio of less than 40 would require much larger Reynolds numbers. However, the point at which the vorticity stops scaling linearly with s^+ is constant for both Reynolds numbers, despite operating in the low blockage ratio region for $Re_\tau \approx 180$, suggesting that the influence of blockage is minor. If blockage is having an effect then it will likely act to suppress the vorticity field which may be the cause of the reduced magnitude of $\Omega^+_{x,\max}$.

There are several questions that arise from analysis of Figure 5.13: What is the cause of the two different regimes at small and large s^+, and what is the mechanism that leads to the breakdown at $s^+ \approx 30$? Furthermore, as s^+ increases further, should vorticity vanish, or tend to a constant value? Some insight can be obtained by assessing the transport of

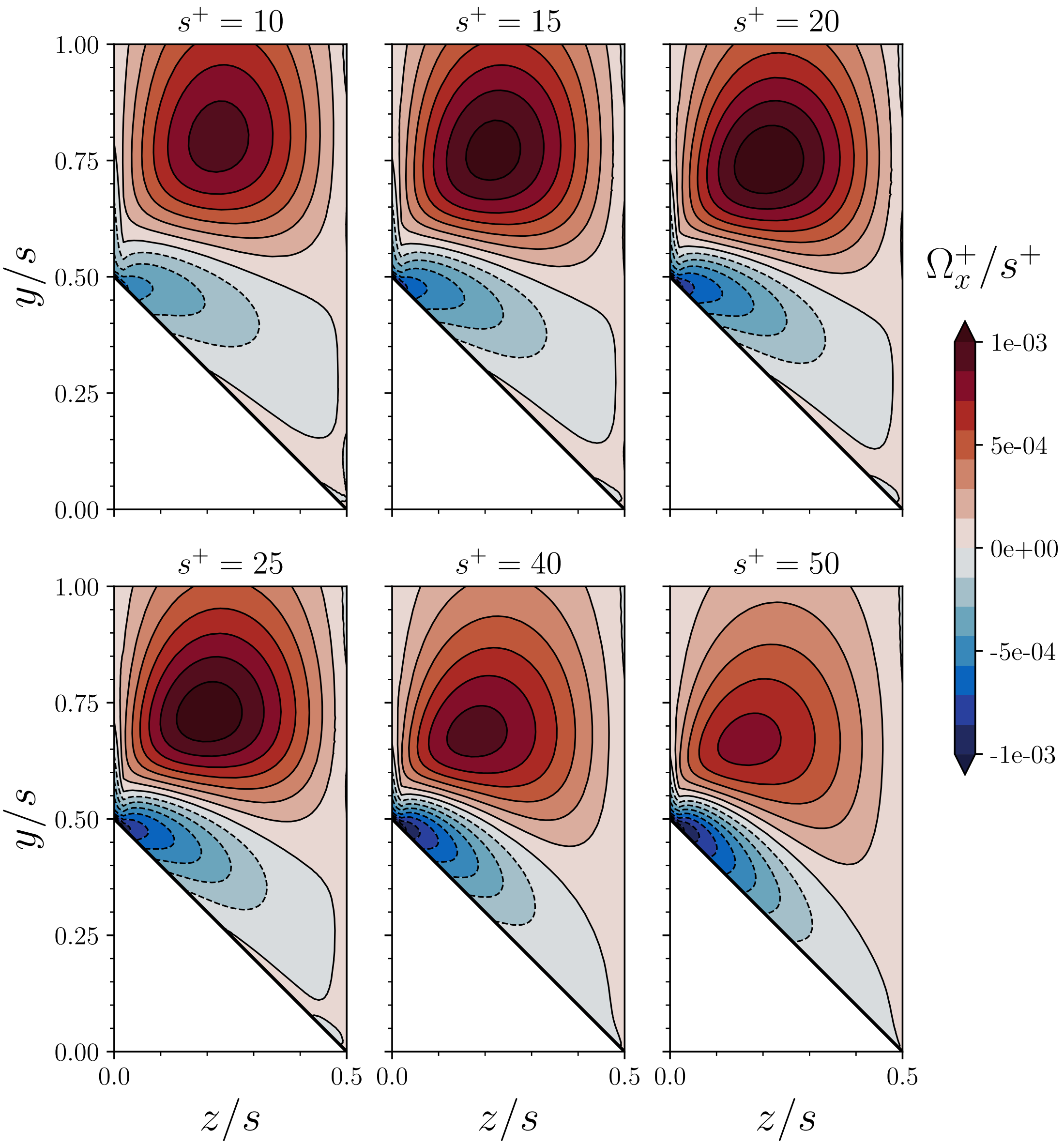

FIGURE 5.12: Inner-scaled streamwise vorticity normalised by the inner-scaled riblet spacing for EB-SSG at $Re_\tau \approx 180$.

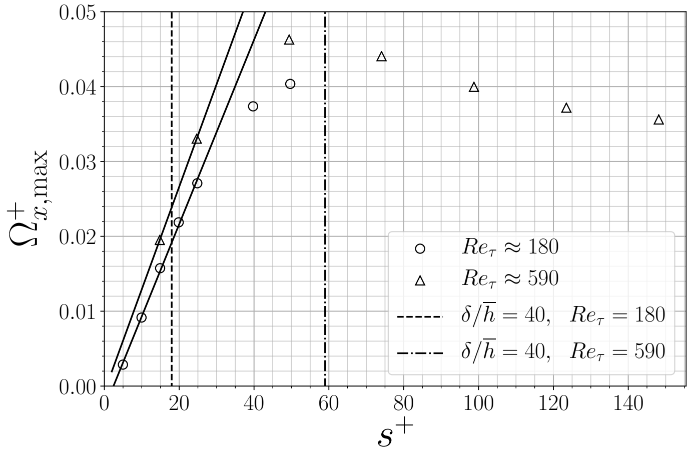

FIGURE 5.13: Scaling of the maximum streamwise vorticity for EB-SSG. Vertical lines represent the s^+ values that lead to a blockage ratio $\delta/\overline{h} = 40$, for each Reynolds number.

mean streamwise vorticity, governed by

$$\begin{aligned}\overline{U}_x\frac{\partial\Omega_x}{\partial x} + \overline{U}_y\frac{\partial\Omega_x}{\partial y} + \overline{U}_z\frac{\partial\Omega_x}{\partial z} &= \Omega_x\frac{\partial\overline{U}_x}{\partial x} + \Omega_y\frac{\partial\overline{U}_x}{\partial y} + \Omega_z\frac{\partial\overline{U}_x}{\partial z} \\ &+ \left(\frac{\partial^2}{\partial y^2} - \frac{\partial^2}{\partial z^2}\right)\left(-\overline{v'w'}\right) + \frac{\partial^2}{\partial y\partial z}\left(\overline{v'v'} - \overline{w'w'}\right) + \nu\nabla^2\Omega_x, \end{aligned} \tag{5.3}$$

where the first term represents convection of vorticity, the second term is often referred to as vortex stretching, the third and fourth terms represent inhomogenetic and anisotropic contributions of the Reynolds stresses to vorticity, and the final term represents viscous dissipation. The Reynolds averaged vorticity equation (5.3) can be obtained by taking the curl of the RANS momentum equations (4.1). For the two-dimensional fully developed flow over riblets (5.3) reduces to just

$$\underbrace{\overline{U}_y\frac{\partial\Omega_x}{\partial y} + \overline{U}_z\frac{\partial\Omega_x}{\partial z}}_{\Omega_x^C} - \underbrace{\left(\frac{\partial^2}{\partial y^2} - \frac{\partial^2}{\partial z^2}\right)\left(-\overline{v'w'}\right)}_{\Omega_x^{SS}} - \underbrace{\frac{\partial^2}{\partial y\partial z}\left(\overline{v'v'} - \overline{w'w'}\right)}_{\Omega_x^{NS}} - \underbrace{\nu\nabla^2\Omega_x}_{\Omega_x^V} = 0, \tag{5.4}$$

since the vortex stretching term and derivatives in x are identically zero. Here Ω_x^i represents a term in the balance of vorticity; Ω_x^C represents convection, Ω_x^{SS} represents contributions from the gradients of the off-diagonal Reynolds shear-stress $\overline{v'w'}$, Ω_x^{NS} represents contributions from gradients of the diagonal Reynolds normal-stresses, and Ω_x^V represents viscous diffusion. For a flat plate fully developed boundary layer flow it is obvious why there is no streamwise vorticity; derivatives in z are zero, as are vertical and spanwise velocities and the Reynolds stresses $\overline{v'w'}$.

The balance of the four vorticity budgets (5.4) for various s^+ can be observed in Figures 5.14 and 5.15, which have been normalised to the range ±1. Note that budgets are

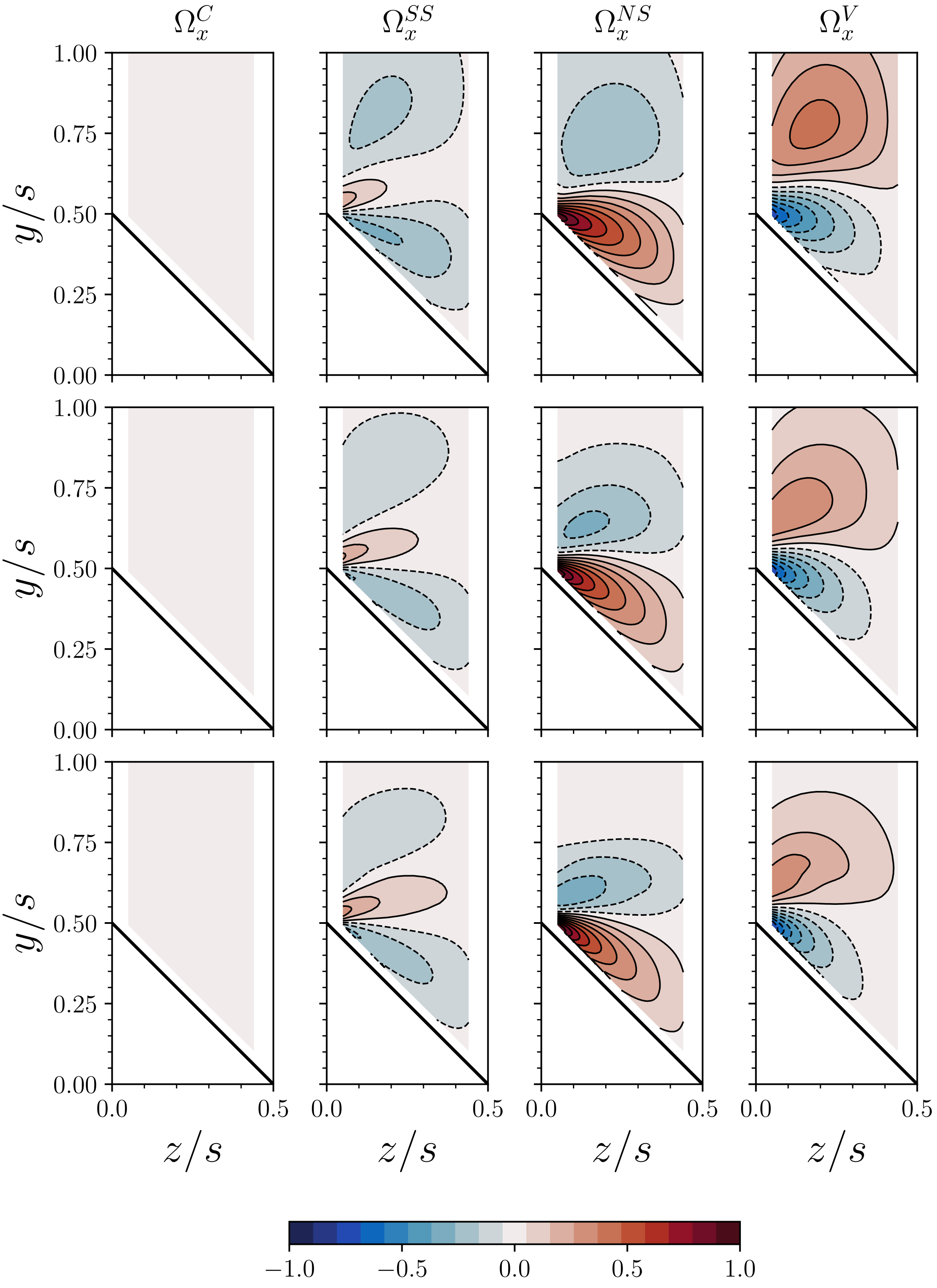

FIGURE 5.14: Transport of streamwise vorticity budgets (5.4) for EB-SSG at $Re_\tau \approx 180$. Cases are $s^+ \approx 5$ (upper), $s^+ \approx 15$ (middle), and $s^+ \approx 25$ (lower). Budgets for each case are normalised between -1 and 1.

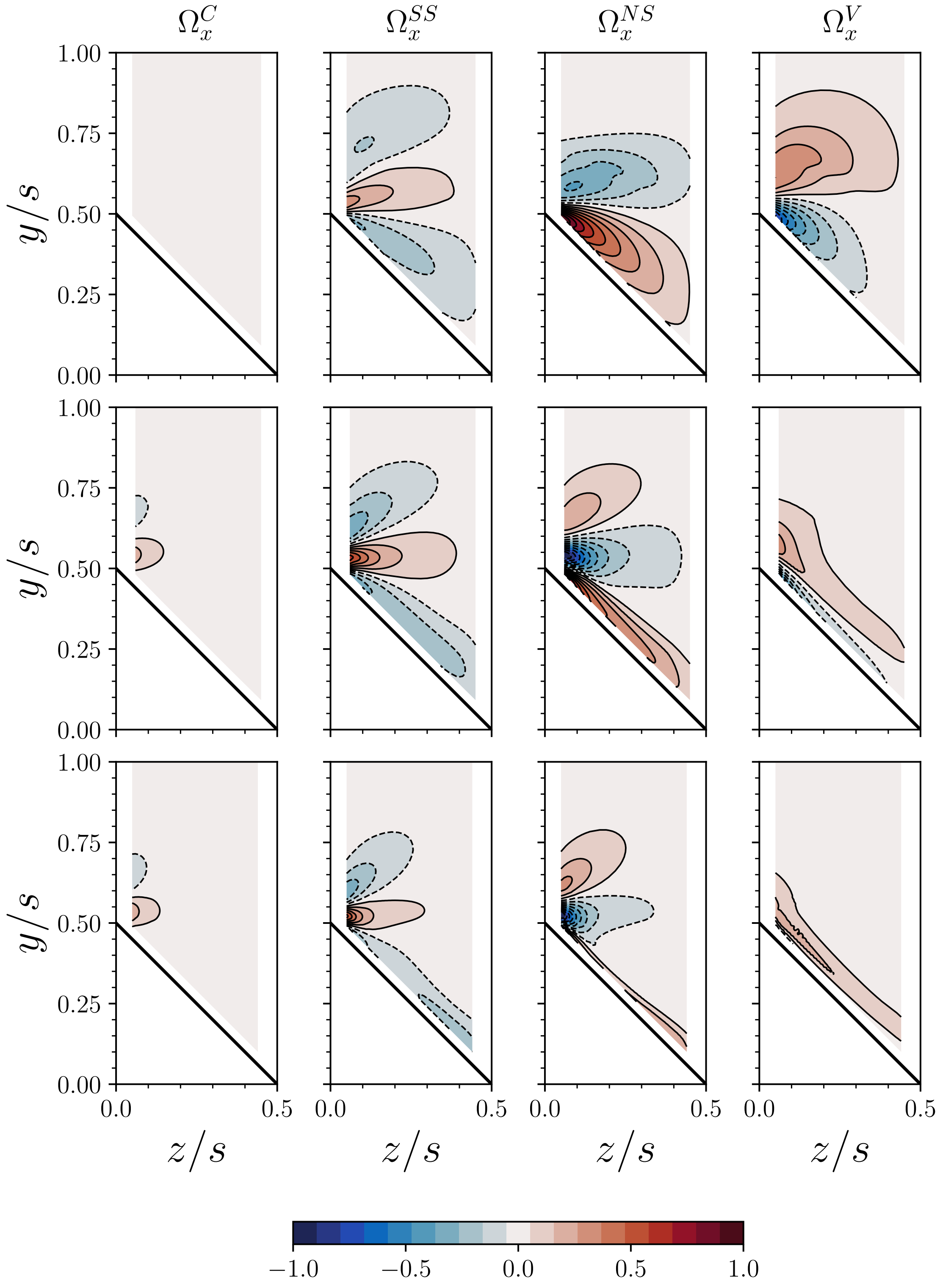

FIGURE 5.15: Transport of streamwise vorticity budgets (5.4) for EB-SSG at $Re_\tau \approx 590$. Cases are $s^+ \approx 25$ (upper), $s^+ \approx 75$ (middle), and $s^+ \approx 125$ (lower). Budgets for each case are normalised between -1 and 1.

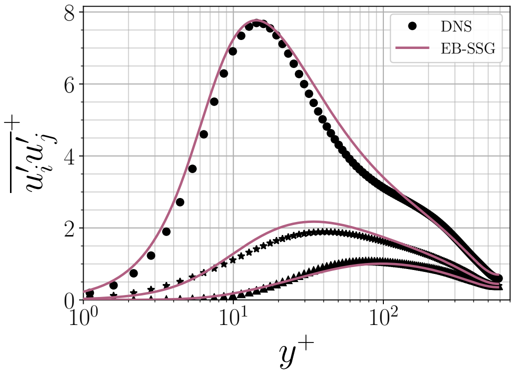

FIGURE 5.16: Profiles of diagonal Reynolds stresses for a smooth-walled channel flow with comparisons against the DNS of Moser, Kim, and Mansour (1999). Diagonal Reynolds stresses are: ●, $\overline{u'u'}^+$; ▲, $\overline{v'v'}^+$; ★, $\overline{w'w'}^+$.

not calculated at the cells closest to the boundaries due to their high order and subsequent numerical errors. Some distinct patterns emerge from these budgets which evolve as the riblet spacing increases. For small s^+ there is a dominant balance between vorticity generated by the anisotropy of the diagonal Reynolds stresses (Ω_x^{NS}) and viscous diffusion (Ω_x^V). Convection (Ω_x^C) of Ω_x is negligible for all s^+ except for $s^+ \gtrsim 75$ where it begins to contribute to the balance. The term containing derivatives of $\overline{v'w'}$ (Ω_x^{SS}) is of a lower magnitude for small s^+, mainly acting with viscous diffusion to balance Ω_x^{NS}. This seems a reasonable solution given that anisotropy in the Reynolds stresses exists for a flat plate case but $\overline{v'w'}$ is identically zero; it could therefore be expected that for small s^+ the term containing derivatives in $\overline{v'w'}$ will be small, since its existence can only arise due to the presence of the riblets themselves. It should be noted that the budgets for $s^+ \approx 25$ are near identical for both $Re_\tau \approx 180$ and $Re_\tau \approx 590$, indicating that the Reynolds number scaling is weak.

As s^+ grows the viscous diffusion term decreases while the anisotropic diagonal Reynolds stresses maintain a dominant role. In order to satisfy the streamwise vorticity balance the term containing derivatives of $\overline{v'w'}$ (Ω_x^{SS}) grows to become leading order for the larger s^+ cases. A consistent feature of all numerical solutions is that vorticity is produced by Reynolds stress anisotropy (Ω_x^{NS}), strongly suggesting that this secondary flow is of the second kind (Prandtl, 1953) [1]. The dominance of Ω_x^{NS} can potentially be explained by noting that the $\overline{v'v'} - \overline{w'w'}$ anisotropy is non-zero and quite large even for a flat plate boundary layer, due to kinematic blocking. This is demonstrated in Figure 5.16, where the diagonal Reynolds stresses of the reference smooth-walled channel flow are reported. The reason vorticity is not generated for the flat plate case is due to spanwise homogeneity. When riblets are small they act as a perturbation from the flat plate solution, introducing spanwise inhomogeneity and ultimately allowing the pre-existing

---

[1] This readily explains why the linear-pressure strain model and simple low Reynolds number damping of Stress-τ obtains poor predictions of secondary flows.

anisotropy to generate vorticity at the riblet surface. This suggests that the anisotropy arising from kinematic blocking is the primary mechanism that drives secondary flows in-between riblets.

The transition between dominant roles of Ω_x^{SS} and Ω_x^{V} provides a clear description of the two different regimes of Figure 5.13. At small s^+ the anisotropy in the Reynolds stresses generates vorticity near the riblets that is diffused by viscosity. It therefore seems appropriate to term the linear dependence on s^+ for small s^+ as the viscous regime. In contrast, at large s^+ viscous dissipation is negligible and the inhomogeneity of $\overline{v'w'}$ must act as a sink to balance the vorticity generate by the diagonal Reynolds stresses. This leads to what could be referred to as an inertial regime, a sensible choice given that it occurs when s^+, essentially a roughness Reynolds number, is large. In this regime convection also begins to grow and vorticity budgets begin to localise at the riblet tip.

The balance of the vorticity equation leads to a further description of the role of Ω_x^{SS}. On noting its role as an effective vorticity sink at high s^+ it is not a far reaching conclusion that perhaps it acts as an effective turbulent viscosity when molecular diffusion is too weak to effectively balance the vorticity production. This analogy is perhaps more obvious from a rearrangement of the RANS vorticity equation; by expanding the Laplacian operating on Ω_x one can obtain

$$\left(\frac{\partial^2}{\partial y^2} - \frac{\partial^2}{\partial z^2}\right)(-\overline{v'w'}) + \nu\nabla^2\Omega_x = \left(\hat{e}_y\frac{\partial}{\partial y} + \hat{e}_z\frac{\partial}{\partial z}\right)\cdot\left[\nu\left(\hat{e}_y\frac{\partial}{\partial y} + \hat{e}_z\frac{\partial}{\partial z}\right)\Omega_x + \left(\hat{e}_y\frac{\partial}{\partial y} - \hat{e}_z\frac{\partial}{\partial z}\right)(-\overline{v'w'})\right] \tag{5.5}$$

which leads to

$$\overline{U}_y\frac{\partial\Omega_x}{\partial y} + \overline{U}_z\frac{\partial\Omega_x}{\partial z} = \frac{\partial^2}{\partial y\partial z}\left(\overline{v'v'} - \overline{w'w'}\right) + \left(\hat{e}_y\frac{\partial}{\partial y} + \hat{e}_z\frac{\partial}{\partial z}\right)\cdot\left[\hat{e}_y\frac{\partial}{\partial y}\left(\nu\Omega_x - \overline{v'w'}\right) + \hat{e}_z\frac{\partial}{\partial z}\left(\nu\Omega_x + \overline{v'w'}\right)\right], \tag{5.6}$$

where $\hat{e}_y$ and $\hat{e}_z$ are unit vectors in the y and z directions, respectively. In this form it seems that $\overline{v'w'}$ acts to modify the molecular viscosity. At large s^+ the effective viscosity is dominated by the Reynolds stress term, and when s^+ vanishes molecular diffusion dominates. However, strictly this analogy is not entirely realised in the budgets of vorticity at smaller s^+. For the turbulent viscosity hypothesis to hold in its traditional definition one would expect the term to always act as diffusion to the balance of Ω_x. This does not necessarily require the term to be negative, given that the source of vorticity is not necessarily positive. However, the term should in principle act to oppose production of vorticity if the turbulent viscosity hypothesis is to hold. This is not entirely the case in Figure 5.14 for $s^+ = 15$ in the region $y/s \gtrsim 0.75$. Here the two Reynolds stress terms

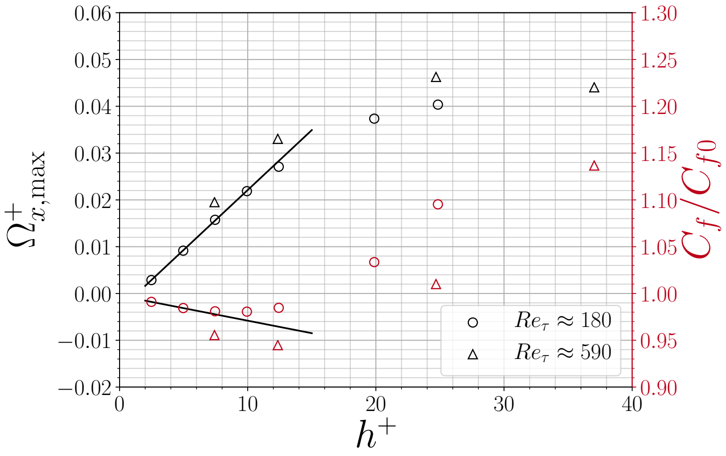

FIGURE 5.17: Scaling of the maximum streamwise vorticity and relative drag coefficient for EB-SSG as functions of the inner-scaled riblet height, $h^+ = s^+/2 = u_{\tau 0}h/\nu$. Data are from Figures 5.4 and 5.13.

Ω_x^{SS} and Ω_x^{NS} both contribute to the transport of vorticity with the same sign, and are balanced by viscosity. However, the typical behaviour closer to the riblet surface seems consistent with a turbulent viscosity, acting with molecular viscosity to diffuse away Ω_x.

This analogy adds some further insight to the two regimes identified by the vorticity budgets and the s^+ dependence of Ω_x. For small s^+ vorticity production is balanced by molecular diffusion, and at high s^+ it is balanced by turbulent diffusion. An open question remains: What governs the transition between the two regimes? One possible cause for this transition is some relation to the profiles of drag reduction, where at these intermediate values of s^+ there is a transition from a drag-reducing regime to a drag-increasing regime. The maximum streamwise vorticity and the relative drag coefficients are presented in Figure 5.17. Here the riblets have been characterised by their height (h) rather than spacing (s) in order to assess how far their tips protrude into the boundary layer. One observes that the viscous regime for the vorticity field lies within the drag reducing regime of the riblets, for both Reynolds numbers. While $\Omega^+_{x,\text{max}}$ and C_f/C_{f0} obtain linear behaviour for small h^+, the viscous regime for the relative drag coefficient appears to breakdown at a smaller h^+ than the maximum streamwise vorticity. In addition, the drag increasing regime does not seem to correspond directly to the inertial regime of Ω^+_x, where it decreases with increasing h^+. For example, as h^+ grows from $\approx 20-25$ both the maximum streamwise vorticity and the drag coefficient increase. This suggests that the different regimes for $\Omega^+_{x,\text{max}}$ and C_f/C_{f0} may not be directly related, although may arise from similar mechanisms. The breakdown of the viscous regime of vorticity could be explained by investigating the Reynolds stresses above a flat plate. The breakdown of the linear scaling of vorticity occurs at $h^+ \approx 10-20$ for both Reynolds numbers. For a flat plate at $y^+ = 15$ there is a peak in turbulent kinetic energy, in the buffer layer (See Figure 5.16), and the difference between $\overline{v'v'}^+$ and $\overline{w'w'}^+$ is near its maximum. Given that the vorticity source Ω_x^{NS} is dependent on the difference between $\overline{v'v'}^+$ and $\overline{w'w'}^+$ it seems reasonable that the transition from the viscous regime occurs as a result of the riblet tips protruding into the buffer layer and exposing the flow between riblets to high levels of turbulence. At this point turbulent diffusion becomes large, and eventually dominates over viscous diffusion as h^+ grows further.

Analytical solutions

The origins of the secondary flow have been identified through the numerical solutions; streamwise vorticity is produced by anisotropy in the Reynolds stresses, which is crucially inhomogeneous in the spanwise direction when riblets are present. Linear scaling with the riblet dimensions has also been observed at small s^+, although the precise mechanisms that lead to this behaviour are unknown. In addition to this it is unclear how vorticity scales at large s^+. Here the governing equations are investigated analytically in order to identify how the different variables scale in the viscous and inertial regimes. The governing equations are the continuity equation,

$$\frac{\partial \overline{U}_y}{\partial y} = -\frac{\partial \overline{U}_z}{\partial z}, \tag{5.7}$$

and the Reynolds-averaged transport of streamwise vorticity,

$$\overline{U}_y \frac{\partial \Omega_x}{\partial y} + \overline{U}_z \frac{\partial \Omega_x}{\partial z} = \left(\frac{\partial^2}{\partial y^2} - \frac{\partial^2}{\partial z^2} \right) \left(-\overline{v'w'} \right) + \frac{\partial^2}{\partial y \partial z} \left(\overline{v'v'} - \overline{w'w'} \right) + \nu \nabla^2 \Omega_x. \tag{5.8}$$

There are several unknown variables; $\overline{U}_y$, $\overline{U}_z$, $\overline{v'w'}$, $\overline{v'v'}$, $\overline{w'w'}$, and Ω_x, although several of these must be strongly related. Vertical and spanwise velocities are related to vorticity by

$$\Omega_x = \frac{\partial \overline{U}_z}{\partial y} - \frac{\partial \overline{U}_y}{\partial z}. \tag{5.9}$$

If it is assumed that secondary flow is confined by the riblet spacing (evident through all numerical solutions of Section 5.2) then the variables can be scaled by

$$y = hy^*, \qquad z = hz^*, \qquad \Omega_x = \Gamma \Omega_x^* \tag{5.10}$$

$$\overline{U}_y = V_\infty \overline{U}_y^*, \qquad \overline{U}_z = W_\infty \overline{U}_z^*, \tag{5.11}$$

where the superscript $*$ denotes a dimensionless variable, h is the riblet height (although the riblet spacing $s = 2h$ would also be appropriate), Γ represents a characteristic frequency governing the scaling of Ω_x, and V_∞ and W_∞ are characteristic velocity scales for vertical and spanwise flow, respectively. The continuity equation (5.7) leads to

$$W_\infty \sim V_\infty, \tag{5.12}$$

which when substituted into the definition of vorticity (5.9) leads to

$$\Omega_x \sim \frac{V_\infty}{h}\left(\frac{\partial \overline{U}_z^*}{\partial y^*} - \frac{\partial \overline{U}_y^*}{\partial z^*}\right). \tag{5.13}$$

Subsequently the recirculation frequency Γ which governs the secondary flow scales with the spanwise and vertical velocities by

$$\Gamma \sim V_\infty / h. \tag{5.14}$$

With some rearrangement V_∞ is found to scale with $h^+ = u_\tau h/\nu$ by

$$V_\infty \sim u_\tau \left(\frac{\Gamma \nu}{u_\tau^2}\right) h^+. \tag{5.15}$$

Numerical solutions have shown that $\Omega_x^+ = \Omega_x \nu / u_\tau^2 \sim s^+$ in the viscous regime, and by extension $\Omega_x^+ \sim h^+$. This requires

$$\Gamma^+ = \frac{\Gamma \nu}{u_\tau^2} \sim h^+, \tag{5.16}$$

suggesting that vertical and spanwise velocities must scale like $(h^+)^2$. This is precisely what is observed for small s^+, in Figures 5.18 and 5.19. Both vertical and spanwise components of velocity scale with $(s^+)^2$ in the viscous regime, with the vertical velocity approximately twice that of the spanwise. The quadratic scaling with s^+ breaks down at the same point at which the linear scaling of Ω_x breaks down ($s^+ \lesssim 30$), as observed in Figure 5.20. In the inertial regime the spanwise and vertical velocities scale sub-linearly with s^+. Their growth with s^+ to some fractional power is consistent with the scaling $\Gamma \sim V_\infty / h$ given that Ω_x^+ slowly decreases with s^+ in the inertial regime (Figure 5.13).

A further interesting result is that $\overline{v'w'}$ also scales in a near-identical way to $\overline{U}_z$, as shown in Figure 5.21. Deviations between $(\overline{v'w'}^+)_{\max}$ and $(\overline{U}_z^+)_{\max}$ are only clear in the inertial regime, but differences only lie in a small offset. A critical observation is that $(\overline{v'w'}^+)$ scales more strongly with s^+ than Ω_x^+ does, leading to $(\overline{v'w'}^+)$ vanishing in the viscous regime more quickly than Ω_x^+, and leading to a continued growth of $(\overline{v'w'}^+)$ at large s^+, while Ω_x^+ decreases. Knowing that these variables are all intricately linked and scale with Γ allow some analytical solutions at both small and large s^+ (or h^+) to be established.

Solutions for $0 < s^+ \ll 1$

For $0 < s^+ \ll 1$ riblets should have a negligible influence on the flow, such that the flow is governed by the flat plate solutions to leading order. Here the method of multiple scales is adopted, where the riblets act as a small perturbation to the flat plate solutions. There are three length scales that govern the flow over riblets; the boundary layer thickness, δ, the viscous or inner length scale, $\delta_\nu = \nu/u_\tau$, and a length scale associated to the riblets. Here the riblet height is chosen, $h = s/2$, rather than the spacing, s, although the same solutions are obtained regardless of this choice. These length scales lead to two inner-scaled Reynolds numbers: $\delta^+ = Re_\tau = \delta/\delta_\nu$, and $h^+ = h/\delta_\nu$, which describe the scale separation. Here it is assumed that $\delta^+ \gg 1$ and $0 < h^+ \ll 1$. The near-wall flow is therefore primarily governed by δ_ν, as per the typical boundary layer solution. Any influence of the boundary layer thickness is neglected, and the riblet length scale acts as a small perturbation to the flow. Mathematically the appropriate coordinates are

$$y = \delta_\nu f\left(y^+, y^*\right), \qquad z = \delta_\nu f\left(z^+, z^*\right), \tag{5.17}$$

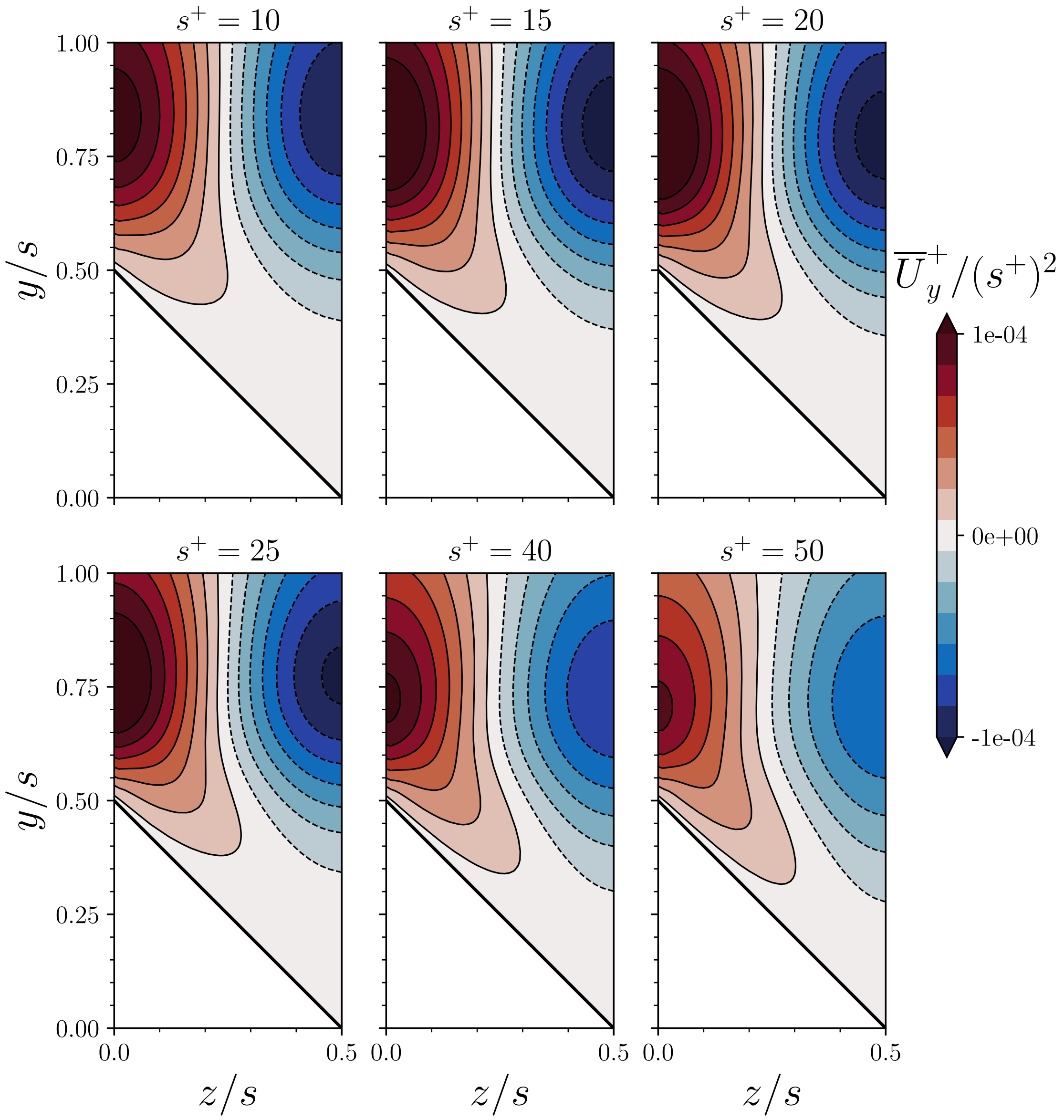

FIGURE 5.18: Inner-scaled vertical velocity normalised by the inner-scaled riblet spacing for EB-SSG at $Re_\tau \approx 180$.

where

$$y^+ = \frac{y}{\delta_\nu}, \qquad , y^* = h^+ \frac{y}{\delta_\nu}, \tag{5.18}$$

and

$$z^+ = \frac{z}{\delta_\nu}, \qquad , z^* = h^+ \frac{z}{\delta_\nu}, \tag{5.19}$$

such that y^* and z^* are much smaller than y^+ and z^+. Through the chain rule derivatives in y and z become

$$\frac{\partial}{\partial y} = \frac{1}{\delta_\nu}\left(\frac{\partial}{\partial y^+} + h^+ \frac{\partial}{\partial y^*}\right), \qquad \frac{\partial}{\partial z} = \frac{1}{\delta_\nu}\left(\frac{\partial}{\partial z^+} + h^+ \frac{\partial}{\partial z^*}\right), \tag{5.20}$$

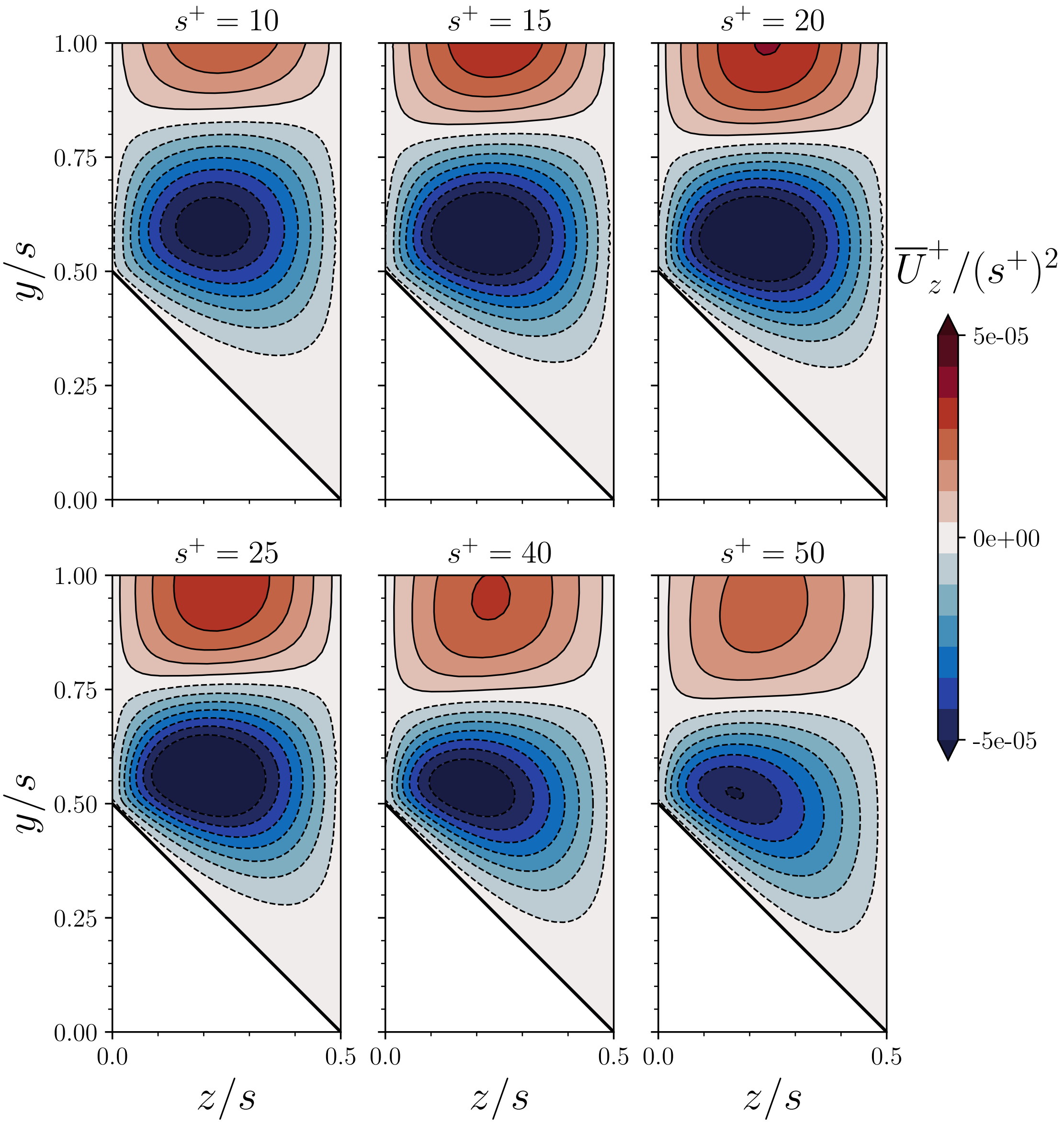

FIGURE 5.19: Inner-scaled spanwise velocity normalised by the inner-scaled riblet spacing for EB-SSG at $Re_\tau \approx 180$.

and second order derivatives become

$$\frac{\partial^2}{\partial y^2} = \frac{1}{\delta_\nu^2}\left[\frac{\partial^2}{\partial \left(y^+\right)^2} + 2h^+\frac{\partial^2}{\partial y^+ \partial y^*} + \left(h^+\right)^2\frac{\partial^2}{\partial \left(y^*\right)^2}\right], \tag{5.21}$$

$$\frac{\partial^2}{\partial z^2} = \frac{1}{\delta_\nu^2}\left[\frac{\partial^2}{\partial \left(z^+\right)^2} + 2h^+\frac{\partial^2}{\partial z^+ \partial z^*} + \left(h^+\right)^2\frac{\partial^2}{\partial \left(z^*\right)^2}\right], \tag{5.22}$$

$$\frac{\partial^2}{\partial y \partial z} = \frac{1}{\delta_\nu^2}\left[\frac{\partial^2}{\partial y^+ \partial z^+} + h^+\left(\frac{\partial^2}{\partial y^+ \partial z^*} + \frac{\partial^2}{\partial y^* \partial z^+}\right) + \left(h^+\right)^2\frac{\partial^2}{\partial y^* \partial z^*}\right]. \tag{5.23}$$

One observes that to leading order these derivatives are governed by the viscous length scale, consistent with flat plate boundary layer solutions. These derivatives are assigned the operators

$$\frac{\partial}{\partial y} = \frac{1}{\delta_\nu}\mathcal{D}_y, \qquad \frac{\partial}{\partial z} = \frac{1}{\delta_\nu}\mathcal{D}_z, \tag{5.24}$$

$$\frac{\partial^2}{\partial y^2} = \frac{1}{\delta_\nu^2}\mathcal{D}_{yy}, \qquad \frac{\partial^2}{\partial z^2} = \frac{1}{\delta_\nu^2}\mathcal{D}_{zz}, \qquad \frac{\partial^2}{\partial y \partial z} = \frac{1}{\delta_\nu^2}\mathcal{D}_{yz} \tag{5.25}$$

for clarity. Note that each of these operators contains $\mathcal{O}(1)$ and $\mathcal{O}(h^+)$ terms, while second derivatives contain a further $\mathcal{O}\left((h^+)^2\right)$ term. The small perturbation in length scales will also be felt by the Reynolds stresses $\overline{v'w'}$, $\overline{v'v'}$, $\overline{w'w'}$, the streamwise vorticity Ω_x, and subsequently the spanwise and vertical velocities $\overline{U}_y$ and $\overline{U}_z$. It is assumed these variables scale with a regular and spatially uniform perturbation series with $0 < h^+ \ll 1$ as the small parameter. The expansion for Ω_x is

$$\Omega_x \sim \Gamma f(h^+)\Omega_x^*, \qquad f(h^+) = a_2 h^+ + a_3 (h^+)^2 + \cdots, \tag{5.26}$$

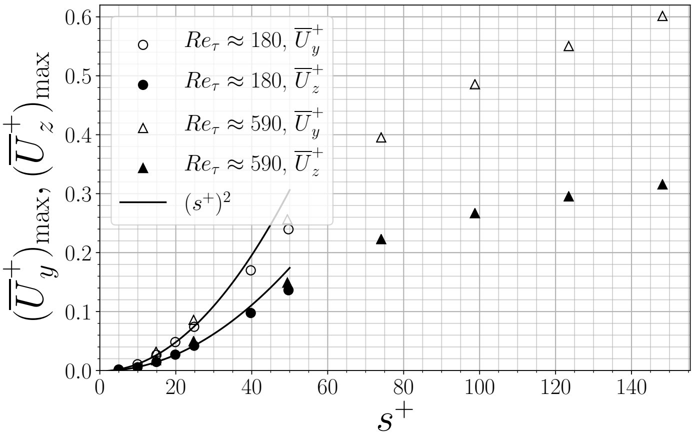

FIGURE 5.20: Scaling of the maximum vertical and spanwise velocities for EB-SSG.

where $f(h^+)$ is a spatially uniform expansion for small h^+. Note that its first coefficient $a_1 = 0$, which is required to maintain the flat plate boundary solution for vanishing h^+, where vorticity should also vanish.

The variables $\overline{U}_y$ and $\overline{U}_z$ are also assumed to scale with $f(h^+)$, given their relation to Ω_x through (5.15):

$$\overline{U}_y = h\Gamma f(h^+)\overline{U}_y^*, \qquad \overline{U}_z = h\Gamma f(h^+)\overline{U}_z^*. \tag{5.27}$$

Numerical solutions show that $\overline{v'w'}^+$ scales in a near identical way to $\overline{U}_z^+$ leading to the assumed scaling

$$\overline{v'w'} \sim u_\tau h\Gamma f(h^+)\overline{v'w'}^*, \tag{5.28}$$

or alternatively

$$\overline{v'w'} \sim u_\tau^2 h^+\Gamma^+ f(h^+)\overline{v'w'}^*. \tag{5.29}$$

The remaining terms are the two diagonal Reynolds stresses, which are assumed to scale by

$$\overline{v'v'} = u_\tau^2 g(h^+)\overline{v'v'}^*, \qquad \overline{w'w'} = u_\tau^2 g(h^+)\overline{w'w'}^*, \tag{5.30}$$

where the polynomial expansion $g(h^+)$ is defined as

$$g(h^+) \sim 1 + b_2 h^+ + b_3(h^+)^2 + \cdots . \tag{5.31}$$

Here the leading order coefficient of $g(h^+)$ is known, $b_1 = 1$, consistent with the flat plate boundary layer solution for $0 < h^+ \ll 1$. Note that it is assumed these expansions are spatially uniform, such that respective dimensionless variables denoted with the superscript $*$ contain spatial dependence.

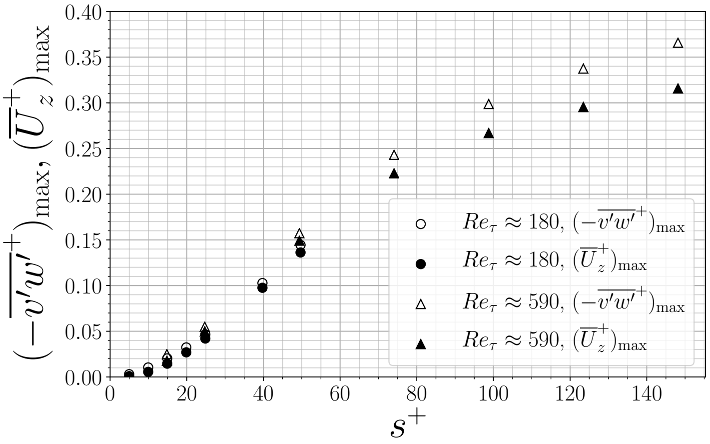

FIGURE 5.21: Scaling of the maximum off-diagonal Reynolds stress $\overline{v'w'}$ and spanwise velocity for EB-SSG.

Substituting these expansions into the RANS vorticity equation (5.8) leads to the balance

$$\begin{aligned} h^+ \left(\frac{\Gamma \nu}{u_\tau^2} f(h^+)\right)^2 \left[\overline{U}_y^* \mathcal{D}_y \Omega_x^* + \overline{U}_z^* \mathcal{D}_z \Omega_x^*\right] &= h^+ \frac{\Gamma \nu}{u_\tau^2} f(h^+) \left(\mathcal{D}_{yy} - \mathcal{D}_{zz}\right) \left(-\overline{v'w'}^*\right) \\ &+ g(h^+) \mathcal{D}_{yz} \left(\overline{v'v'}^* - \overline{w'w'}^*\right) + \frac{\Gamma \nu}{u_\tau^2} f(h^+) \left(\mathcal{D}_{yy} + \mathcal{D}_{zz}\right) \Omega_x^*. \end{aligned} \tag{5.32}$$

This equation provides some insight into how the vorticity budgets must balance for small h^+. Firstly it should be noted that this equation has maintained consistency with the flat plate solution; at $\mathcal{O}(1)$ only a single term could be non-zero, namely the anisotropic production term. However, knowing that derivatives in z^+ are zero to leading order a consistent solution is maintained.

At $\mathcal{O}(h^+)$ there are two possible contributions from the anisotropic production term, and one from viscous diffusion. These coefficients must balance like

$$1 \sim b_2 \sim \frac{\Gamma \nu}{u_\tau^2} a_2, \tag{5.33}$$

where the b_2 contribution arises from the $\mathcal{O}(1)$ term in the second order derivatives 5.25, and the first term arises from the $\mathcal{O}(h^+)$ term in the second order derivative. This balance can only be achieved if a_2 is non-zero. To leading order, Ω_x must therefore scale like

$$\Omega_x \sim \frac{u_\tau^2}{\nu} h^+ \Omega_x^* \tag{5.34}$$

or alternatively

$$\Omega_x^+ \sim h^+ \Omega_x^* \tag{5.35}$$

which is consistent with the numerical solutions in the viscous limit. This analytical solution arises from the requirement that viscosity must balance the vorticity produced by the anisotropy in the Reynolds stresses, and the production occurs at $\mathcal{O}(h^+)$. Even if all non-leading order coefficients of $g(h^+)$ were zero this balance would still hold, given the $\mathcal{O}(h^+)$ terms in the second order derivatives.

Despite this perturbation analysis being derived for $0 < h^+ \ll 1$ this scaling appears to hold up to reasonably large values of h^+, breaking down only when riblet tips begin to protrude into the buffer region of the boundary layer. This could be explained by noting that similar expansions on the viscous region of the flat plate boundary layer leading to the linear behaviour of streamwise velocity ($\overline{U}_x^+ \sim y^+$) also holds until the buffer region of the flow (Wilcox, 2006).

The only component of this analysis that is perhaps difficult to explain is the origin of the scaling of $\overline{v'w'}$; why should this be dependent on Γ? However, even if this dependence were removed, the leading order balance would still be $\mathcal{O}(h^+)$ between production due to anisotropy and diffusion due to molecular viscosity, as long as $\overline{v'w'}$ is smaller than

Ω_x.

Solutions for $s^+ \gg 1$

In the limit of large s^+ numerical solutions suggest that the vorticity field should either decrease with increasing s^+ or tend to a constant solution (see Figure 5.13). Here this is investigated analytically using a similar technique to the vanishing s^+ case. The governing length scales are as before: the boundary layer thickness δ, the viscous length scale $\delta_\nu = \nu/u_\tau$, and the riblet height h. Here it is assumed that for large h^+ solutions should be independent of the viscous length scale, leading to the dimensionless parameters

$$\frac{\delta}{h} \gg 1, \qquad h^+ = \frac{h}{\delta_\nu} \gg 1. \tag{5.36}$$

The boundary layer thickness is assumed large enough to have no influence on the flow close to the riblets. Here the leading order solution to the vorticity balance is sought, such that a single length-scale asymptotic approach is appropriate:

$$y \sim hy^*, \qquad z \sim hz^*. \tag{5.37}$$

Variables are scaled as in Section 5.3 but only their leading order behaviour is accounted for. Continuity and the definition of vorticity require that the relationship between vorticity and spanwise and wall-normal velocities still holds, leading to the scaling

$$\Omega_x \sim \Gamma\Omega_x^*, \qquad \overline{U}_y = h\Gamma\overline{U}_y^*, \qquad \overline{U}_z = h\Gamma\overline{U}_z^*. \tag{5.38}$$

Given the similarities between the numerical scaling of $\overline{U}_z$ and $\overline{v'w'}$ (see Figure 5.21) it is assumed the off-diagonal Reynolds stress scales like

$$\overline{v'w'} \sim u_\tau \Gamma h \overline{v'w'}^*, \tag{5.39}$$

consistent with Section 5.3. Furthermore it is assumed the diagonal Reynolds stresses still scale with the friction velocity:

$$\overline{v'v'} = u_\tau^2 \overline{v'v'}^+, \qquad \overline{w'w'} = u_\tau^2 \overline{w'w'}^+. \tag{5.40}$$

Substituting these into the vorticity equation leads to

$$\begin{aligned}(h^+)^2\left(\frac{\nu\Gamma}{u_\tau^2}\right)^2\left[\overline{U}_y^*\frac{\partial\Omega_x^*}{\partial y^*}+\overline{U}_z^*\frac{\partial\Omega_x^*}{\partial z^*}\right] &= h^+\left(\frac{\nu\Gamma}{u_\tau^2}\right)\left(\frac{\partial^2}{\partial(y^*)^2}-\frac{\partial^2}{\partial(z^*)^2}\right)\left(-\overline{v'w'}^*\right)\\ &+\frac{\partial^2}{\partial y^*\partial z^*}\left(\overline{v'v'}^+-\overline{w'w'}^+\right)+\left(\frac{\nu\Gamma}{u_\tau^2}\right)\left(\frac{\partial^2}{\partial(y^*)^2}+\frac{\partial^2}{\partial(z^*)^2}\right)\Omega_x^*.\end{aligned} \tag{5.41}$$

There is only one possible scaling of Γ that allows this equation to balance:

$$\frac{\nu\Gamma}{u_\tau^2} = \Gamma^+ \sim \frac{1}{h^+}. \tag{5.42}$$

With this scaling the only term that does not enter the leading order balance is viscous diffusion. Vorticity is therefore generated by the diagonal Reynolds stresses, which is balanced by turbulent diffusion and convection. This seems reasonable when assessing the numerical budgets of the vorticity equation in Figure 5.15, where convection starts to grow for the large s^+ cases. The numerical solutions are clearly not quite in the limit where convection is larger than viscous diffusion, but the general trend of the simulations suggests that convection could at some point become large. This would also be consistent with the LES of Anderson et al. (2015), who simulated the flow over large-scale heterogeneous roughness (Discussed in Section 2.3). Anderson et al. (2015) reported the dominant balance described by (5.41), where convective terms were required to advect vorticity generated by the Reynolds stress terms. This type of flow is analogous to widely spaced riblets in the limit of very large h^+, providing support for the analytical solution of (5.41).

Regarding the scaling of the variables at $h^+ \gg 1$ one should obtain

$$\Omega_x^+ \sim \frac{1}{h^+}, \qquad \overline{U}_y^+ \sim \overline{U}_z^+ \sim \overline{v'w'}^+ \sim 1. \tag{5.43}$$

This suggests that at large h^+ all variables governing the transport of vorticity are bounded and should tend to a constant value, with the exception of vorticity which should vanish at a rate of $1/h^+$.

Some of these features were obtained in the numerical solutions; firstly, the variables $\overline{U}_y^+$, $\overline{U}_z^+$, and $\overline{v'w'}^+$ do seem to scale at a rate of an order h^+ larger than vorticity. Numerical solutions also show vorticity decreasing with h^+, albeit sub-linearly. However, numerical solutions are only obtained up to $h^+ \approx 75$ ($s^+ \approx 150$) such that riblet tips only protrude slightly into the log-layer. The largest numerical h^+ data points are also obtained at a blockage ratio of $\delta/\overline{h} \approx 15$, below that of the limit specified by Jiménez (2004), $\delta/k_0 = 40$, which could also influence the secondary flow somewhat. This implies that the condition $\delta/h \gg 1$ adopted in the analytical solutions for $h^+ \gg 1$ are not realised for the numerical solutions. Therefore it is perhaps unsurprising that the scaling $\Omega_x^+ \sim 1/h^+$ is not obtained. However, it is certainly reasonable to suggest that profiles of $\overline{U}_y^+$, $\overline{U}_z^+$, and $\overline{v'w'}^+$ in Figures 5.20 and 5.21 will tend to a constant value at larger h^+, and that Ω_x would eventually scale like $1/h^+$ if numerical solutions were obtained at a higher Reynolds number, Re_τ.

The analytical solutions of the transport of streamwise vorticity for $h^+ \gg 1$ are therefore governed by the balance between convection, production due to Reynolds stress anisotropy, and turbulent diffusion, while viscous diffusion is negligible. In order to ensure convection is bounded and can be balanced by the remaining terms, the solution

$\Omega_x^+ \sim 1/h^+$ is required, which subsequently leads to solutions independent of h^+ for $\overline{U}_y^+$, $\overline{U}_z^+$, and $\overline{v'w'}^+$.

5.3.1 Discussion

The numerical and analytical solutions obtained for the flow over riblets have led to a significant understanding of how secondary flows are generated and sustained, and how they scale with the riblet dimensions. The near wall secondary flow arises from anisotropy of the Reynolds stresses, and as such are of the second kind of secondary flow (Prandtl, 1953). This anisotropy is inherent even for flat plate boundary layers, but riblets introduce the spanwise inhomogeneities responsible for vorticity production. At small riblet spacings ($s^+ \lesssim 30$) vorticity production is diffused by viscosity, and vorticity scales linearly with s^+. At large riblet spacings ($s^+ \gtrsim 75$) production is balanced by gradients of the Reynolds shear stress term $\overline{v'w'}$, and viscous diffusion is small. In this regime vorticity decreases with h^+ and convection begins to contribute to vorticity transport. These two distinct regimes are termed viscous and inertial regimes due to their dependence on the Reynolds number s^+, and are defined by how vorticity produced through anisotropy is balanced, either by molecular viscosity or by a 'turbulent viscosity' dependent on the Reynolds shear stresses $\overline{v'w'}$. The transition between these two regimes appears to coincide with the riblet tips protruding into the buffer layer, exposing the riblets to higher levels of turbulence.

Analytical solutions supported these results by investigating the vorticity scaling with riblet dimensions in the inertial and viscous regimes. The viscous regime was analysed using the method of multiple scales, finding that the linear behaviour $\Omega_x^+ \sim s^+$ observed in the numerical solutions are required in order to ensure vorticity vanishes with s^+ when riblets are negligibly small. The analytical solutions are also consistent with the numerical solutions concerning the leading order balance of the transport of vorticity, where the anisotropic Reynolds stress term is balanced by viscous diffusion at small s^+. Inertial regime predictions are also consistent with numerical solutions, finding that vorticity should scale like $1/h^+$ and all terms of the transport of vorticity are bounded. While the vorticity scaling of $1/h^+$ is not quite obtained from the numerical solutions, it seems reasonable that these solutions are consistent if Reynolds numbers were increased.

Goldstein and Tuan (1998) attributed the secondary flow over riblets to the blocking of instantaneous spanwise flow at the riblet tips, acting to deflect flow upwards. While this is an instantaneous process it may still be consistent with the present results. Numerical RANS solutions attribute vorticity production with gradients of the normal Reynolds stresses, which are crucially spanwise-inhomogeneous near riblets. This could be thought of as a spanwise-blocking, where riblet tips act to locally block the spanwise normal Reynolds stress, a kinematic effect similar to the kinematic blocking that leads to two-dimensional turbulence near walls (discussed in Section 2.1). Given that the present

EB-SSG model predictions lead to similar vorticity magnitudes and secondary flow structures as the DNS of Choi, Moin, and Kim (1993), perhaps the instantaneous blocking described by Goldstein and Tuan (1998) could alternatively be explained by the influence of the riblets on the Reynolds stress tensor.

An open question remains; what is the influence of the riblet-induced secondary flow on the friction coefficient? Secondary flows are known to have adverse effects on many flows; in ducts they distort the mean streamwise flow and lead to friction losses, despite their transverse velocities being only a few % of the streamwise mean flow (Speziale, 1986). Secondary flows also lead to significant drag and momentum loss over large scale spanwise-heterogeneous roughness (Anderson et al., 2015; Hwang and Lee, 2018). The large-scale roughness of Hwang and Lee (2018) is order δ in spacing and fully rough, rather than the order δ_ν spacings and hydraulically-smooth to transitionally rough ribletted surfaces herein, although the mechanisms driving the secondary flows are similar (Anderson et al., 2015; Hwang and Lee, 2018). However, the influence of the riblet-induced streamwise vorticity on drag is not well understood; Goldstein and Tuan (1998) directly attributed their existence to the degradation of drag reduction, although García-Mayoral and Jiménez (2011b) note that near-wall secondary flows can actually reduce drag by damping larger-scale swirling flow in the buffer layer. The present work suggests that while the friction coefficient and streamwise vorticity seem somewhat correlated they may not be directly related, just driven by similar mechanisms. This is evident in the contributions to drag and the budgets of streamwise vorticity: The viscous drag reduction regime breaks down when the turbulent shear stresses $\overline{u'v'}$ become large, i.e inertial effects become important above the riblet tips (García-Mayoral and Jiménez, 2011b). The viscous secondary flow regime breaks down when the turbulent shear stresses $\overline{v'w'}$ become important, eventually leading to the inertial regime where viscosity is negligible. While mechanisms leading to the regime changes of drag and vorticity are similar, there is mixed evidence of their direct correlation in Figure 5.17, in part due to unknown influence of Re_τ and the blockage ratio δ/h. These two processes are clearly similar, but do not necessitate a relationship between drag and the secondary flow. However, there must be some relationship between drag and vorticity dependent on the roughness dimensions, given that when roughness length scales are large the induced secondary flows can have substantial influence on the mean flow (Anderson et al., 2015). Future work should therefore be carried out in order to extend analysis to higher Reynolds numbers and bridge the gap in roughness length scales between the riblet flows herein and large-scale heterogeneous roughness.

5.4 Conclusions

RANS models have been successfully adopted for the prediction of ribletted channel flows with solutions in good agreement with DNS and experiments. Subsequently the secondary flows induced at the riblet tips have been thoroughly investigated regarding the mechanisms driving and sustaining them, and their scaling with the riblet dimensions. Simulations were carried out for sawtooth riblets, covering riblet spacings of approximately $5 < s^+ < 150$ at Reynolds numbers of $Re_\tau \approx 180$ and $Re_\tau \approx 590$. Investigation of riblet-induced secondary flows was carried out using the EB-SSG model of Manceau (2015), which correctly predicted the magnitude and extent of the secondary flow when compared to DNS solutions, unlike the $k - \tau$ and Stress-τ models, based on the ω models of Wilcox (2006). The primary mechanisms that induce streamwise vorticity have been identified as anisotropy in the near-wall Reynolds stresses, consistent with the second type of secondary flow (Prandtl, 1953). Two regimes have been identified which govern how vorticity produced by anisotropy is conserved: A viscous regime for small s^+ where vorticity production is balanced by viscous diffusion, and an inertial regime for large s^+ where vorticity production is balanced by an effective turbulent viscosity determined by the Reynolds shear stress $\overline{v'w'}$. The transition between the two regimes occurs at $s^+ \approx 30$, where riblet tips protrude into the buffer layer and cause increased turbulent mixing. Analytical solutions obtained a linear dependence of streamwise vorticity on the riblet height, h^+, in agreement with numerical solutions. This linear scaling arises as a condition that vorticity must vanish as h^+ decreases in order to obtain the flat plate boundary layer solution for vanishingly small roughness. In the inertial regime analytical solutions obtained a scaling such that streamwise vorticity should scale like $1/h^+$. While this limit is not reached for the numerical simulations there is evidence that this regime should occur if Reynolds numbers were increased and larger riblets could be simulated.

Chapter 6

Boundary layer flow over shark skin denticles: New mechanisms for drag reduction by riblets revealed by RANS-based modelling

The hydrodynamics of shark scales is poorly understood, even for the simplest of flows. Regarding shark scales subject to canonical boundary layer flows previous results vary considerably, with some authors claiming significant hydrodynamic efficiency (e.g. Domel et al., 2018) and others claiming a significant increase in drag when denticles are present (e.g. Boomsma and Sotiropoulos, 2016). Through a review of the literature in Chapter 2 two key reasons for these differences were identified; a lack of control of shark scale geometry and its influence on fluid dynamics, and a lack of flow field measurements close to the scales, where previous work has primarily adopted force balances. Of all previous studies only Bechert, Hoppe, and Reif (1985) and Fletcher (2015) have performed fluid dynamic experiments on more than one shark scale geometry, and only Boomsma and Sotiropoulos (2016), using Direct Numerical Simulation (DNS), have quantified the near-denticle flow field. This chapter presents a study adopting Reynolds Averaged Navier-Stokes (RANS) closures to model a fully developed boundary layer flow over shark scales. Three denticle geometries are investigated at different sizes with data validated against the experiments presented in Chapter 3. Unlike DNS, RANS models are significantly less computationally expensive and have the potential to carry out large parameter studies on scale geometry, although at present only one previous study using RANS models exists (Zhang et al., 2011a), which suffers from poor documentation and validation. Throughout this thesis RANS methodology has been validated for similar wall-bounded flows, concluding that the EB-SSG model (Appendix C.9) is capable of obtaining excellent predictions of flows over riblets. Extending this methodology to shark scales could prove instrumental in gaining an understanding of the effect of subtle changes to scale geometry on hydrodynamics, and obtaining flow field details that no experimental techniques are yet capable of. The focus of this chapter is to validate RANS methodology against experimental data, and investigate the role of riblets in combination with shark scales. Despite the considerable variability of shark scales (see e.g. Figure 2.9) only Fletcher (2015) has carried out fluid dynamic experiments on smooth shark scales without riblets, despite many sharks not possessing riblets. An open question is how do riblets operate when added to denticles? Do they behave as per longitudinal riblets, or are there other fluid dynamic effects introduced? The pursuit of methodology appropriate for quantifying effects of scale geometry on hydrodynamics could lead to a significantly better understanding of how scale morphology has evolved, and biomimicry of these surfaces could lead to improved fluid dynamic efficiency of engineering structures subject to high fluid drag.

6.1 Methodology

Alongside denticle models 3D printed in Chapter 3 an additional model has been created in order to investigate the effects of riblet geometry on the near-wall flow (Figure 6.1). This model is a cross between the two original models; riblets are present on the denticle crown but are shorter than those on the ribletted denticle of Chapter 3, and do not possess the cut-out regions on the trailing edge. Models are given the abbreviations SMO, SMR, and RIB, defined in the caption of Figure 6.1. Details and dimensions of the denticle models are presented in Appendix A.

A fully developed channel flow is simulated with shark scales present on the walls. The flow is assumed steady state and incompressible. Numerical techniques adopted are as per Section 5.1.2. The geometrical periodicity of shark scale arrays is exploited by assuming the Reynolds-averaged flow field over one scale is identical to all others. The domain can therefore be reduced to the small periodic and symmetrical section of Figure 6.2. The fluid domain therefore contains just one denticle, split up into four parts dependent on the array dimensions (defined in Appendix A). For the cases here the domain size, is $L_x \times L_z = 1.1w \times w$ where L_x and L_z are domain lengths in the streamwise (x)

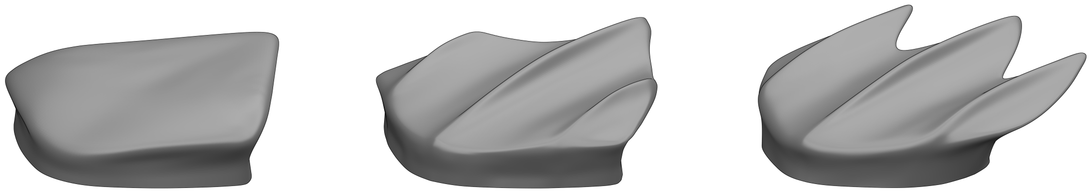

FIGURE 6.1: Denticle CAD models. Smooth (left) and ribletted (right) models are as per 3D printed models of Chapter 3. The central model is a derivative between the other two. Models are abbreviated SMO (smooth, left), SMR (smooth-ribletted, centre), and RIB (ribletted, right).

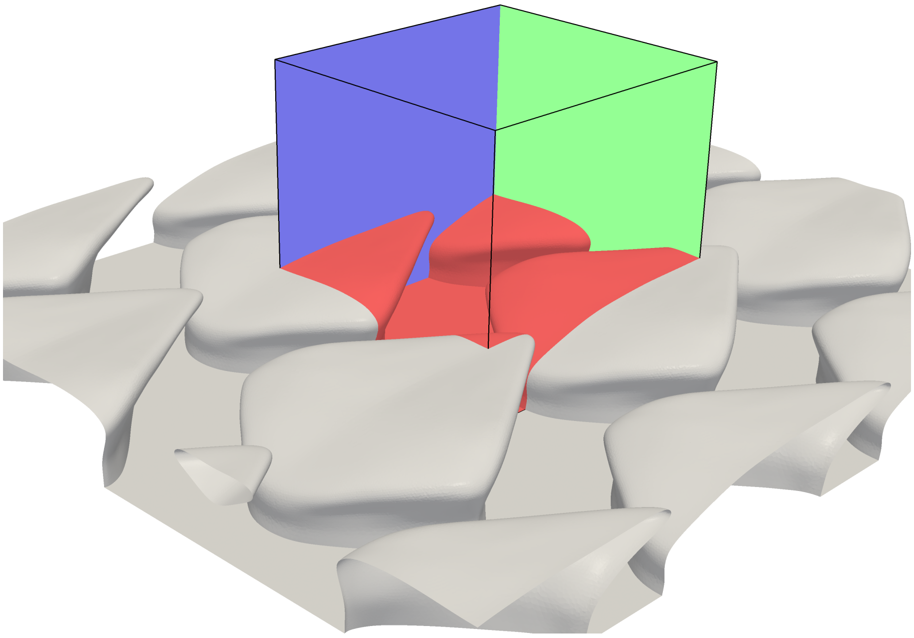

FIGURE 6.2: Array of smooth denticles. The CFD domain in the centre is periodic in the streamwise direction and symmetric at the spanwise boundaries.

and spanwise (z) directions, respectively, and w is the denticle width. Boundary conditions are periodic in the streamwise direction, symmetric in the spanwise direction, symmetric at the channel half-height $y = \delta$, and no-slip on the denticle surface. Bulk flow Reynolds numbers of $Re_b = U_b\delta/\nu = 2825$ and $Re_b = 10864.85$, where U_b is the bulk flow velocity and ν the kinematic viscosity, are imposed via an iterative forcing term as per the methodology of Chapters 4 and 5. These Reynolds numbers approximately equate to $Re_\tau = \delta u_\tau/\nu \approx 180$ and $Re_\tau \approx 590$ for a smooth wall channel flow, where $u_\tau = \sqrt{\tau_w/\rho}$ is the friction velocity, τ_w is the wall shear stress and ρ is the fluid density. The flow over denticles is simulated at four denticle widths covering the range $10 \lesssim w^+ \lesssim 70$, similar to the experimental values of Chapter 3, where the inner scaled denticle width is $w^+ = wu_{\tau 0}/\nu$, where $u_{\tau 0}$ is a reference flat plate friction velocity at the same bulk flow Reynolds number. Denticle dimensions are as per the experimental study (Chapter 3) but have been scaled to a specified w^+ using the flat plate estimations of u_τ/ν at $Re_b = 2825$ and $Re_b = 10864.85$. The turbulence models adopted are the $k - \tau$ model with low Reynolds number corrections (Appendix C.5), and the EB-SSG model (Appendix C.9). Given the similarities between Stress-τ and $k - \tau$ models for riblетted channels in Chapter 5 the less expensive two-equation model is adopted here. All other numerical methodology are as per Chapters 4 and 5. Reference smooth-walled channel flow simulations are obtained using the methodology described in Chapter 4, with bulk flow Reynolds numbers consistent with the denticle simulations.

ANSYS FLUENT 19.2 (2019) meshing software is adopted to create the body-fitted meshes around the shark scales. While a structured hex-mesh may be preferable, they are impractical when considering the complex riblletted denticles of Figure 6.1. Fluent Meshing is capable of creating smooth and high quality polyhedral meshes close to the scales. The meshes are constructed by creating a sub-domain of dimensions $L_x \times L_y \times L_z = 1.1w \times w \times w$, such that the polyhedral unstructured mesh is only present up to $y = L_z = w$. The remaining domain ($w \leq y \leq \delta$) is meshed using a structured hexahedral mesh to ensure cells are aligned with the mean flow direction. The hexahedral mesh is uniform in spacing in x and z, and a geometric stretching function is adopted in the y direction to blend small near-denticle cells into larger free-stream cells (this stretching function is detailed in Chapter 4). The near-denticle sub-domain is refined based purely on curvature; regions of high curvature, identified via a threshold surface-normal angle, are specified a smaller cell size which is blended into larger cells by a specified growth rate. Particular values of the threshold angle, minimum cell sizes, and growth rates, are determined through mesh sensitivity studies. 5 prism layers are grown normal to the no-slip surfaces to ensure larger near-wall gradients can be captured.

A disadvantage of the Fluent Meshing solver is that periodicity is not maintained between cell faces on the streamwise boundaries, thus a non-conformal periodic boundary condition is adopted, where fluxes are interpolated between the mismatched boundaries. A consequence of this is a much higher refinement requirement, such that numerical diffusion across the boundary is minimised. In addition, a non-conformal interface is present between the two sub-domains, such that prism layers and additional refinement are present at the interface, $y = w$. This meshing technique is validated by also creating a fully conformal structured mesh over the smooth denticle using ANSYS ICEM 19.2 (2019) software. The two meshing techniques can be observed in Figure 6.3. Note that despite adopting non-conformal boundaries, normalised residual errors for all variables converge to below 1×10^{-10}, and the friction velocity converges to a relative error of 1×10^{-7}, due to the high refinement levels at the boundaries. Both meshing strategies are assessed for mesh independence, and sensitivity to meshing strategy is determined.

Sensitivity to meshing strategy and refinement

Mesh statistics for three unstructured and three structured meshes are presented in Table 6.1, for the flow over smooth denticles at $w^+ \approx 45$ and $Re_\tau \approx 180$, using the $k - \tau$ model with low Reynolds number corrections. Here F is prescribed as a mesh created using FLUENT (unstructured) and I represents a mesh created using ICEM CFD. Friction velocities converge to $u_\tau \approx 1.14$ for $F3$ and $u_\tau \approx 1.13$ for I3, equating to an error of less than 1 % between the two meshing strategies. Mesh sensitivity is also determined through profiles of inner-scaled turbulent kinetic energy, k^+, and the inner-scaled mean velocity, $\overline{U}_i^+$, at two arbitrary sample lines at $(x, z) = (0.01, 0.01)$ and $(x, z) = (0.04, 0.22)$, in the $y-$ direction. These correspond to Line 1 and Line 2 in Figure 6.4. Line 1 is located near the domain origin (see Figure 6.3), and Line 2 is located at a position between denticles. Deviations in profiles of $\overline{U}_i^+$ and k are only present for I1 and F1 meshes, most notable

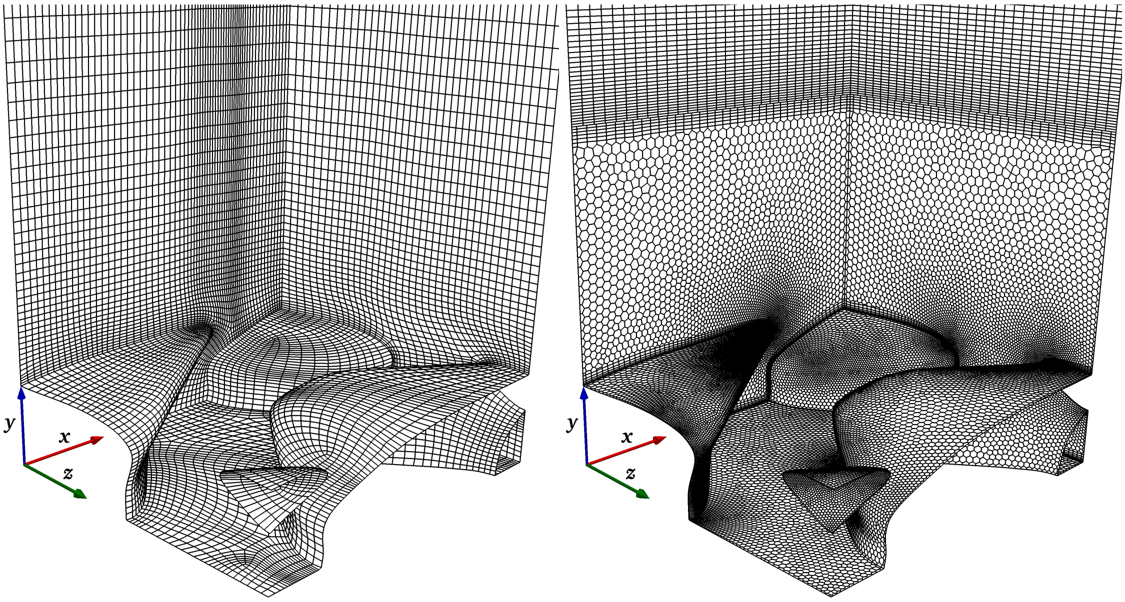

FIGURE 6.3: Structured (left) and unstructured (right) meshing strategies for a smooth denticle domain.

at the inflection points of the vertical velocity $\overline{U}_y^+$. The close agreement between the two meshing strategies validates the use of the unstructured non-conformal meshes for further studies, subsequently mesh F2 is used in the following sections for the smooth denticle (SMO) cases. Mesh independence is also assessed for the other two denticle models of Figure 6.1 using the unstructured strategy, where ribletted denticles are found to require significantly more cells in order to capture regions of high curvature. Meshes adopted for further analysis are detailed in Table 6.2. Note that $y_1^+ < 0.2$ for all adopted meshes, ensuring friction velocity errors associated to the near-wall cell size are approximately less than 0.25 % (see Chapter 4).

TABLE 6.1: Mesh statistics for three smooth-denticle (SMO) meshes at $Re_\tau \approx 180$ and $w^+ \approx 45$. N_cells represents the total number of cells, N_wall represents the number of elements on the denticle boundary, and Δ^+ represents typical cell sizes in wall units. F represents FLUENT unstructured meshes, I represents ICEM CFD structured meshes.

Case	N_cells	N_wall	Δ^+_avg	Δ^+_min	Δ^+_max
F1	108615	6932	1.777	0.007	5.429
F2	294663	17683	1.26	0.006	4.297
F3	431430	28550	1.107	0.005	5.17
I1	25746	1446	2.862	0.264	9.832
I2	150294	4534	1.556	0.081	4.968
I3	682702	16820	0.937	0.104	6.028

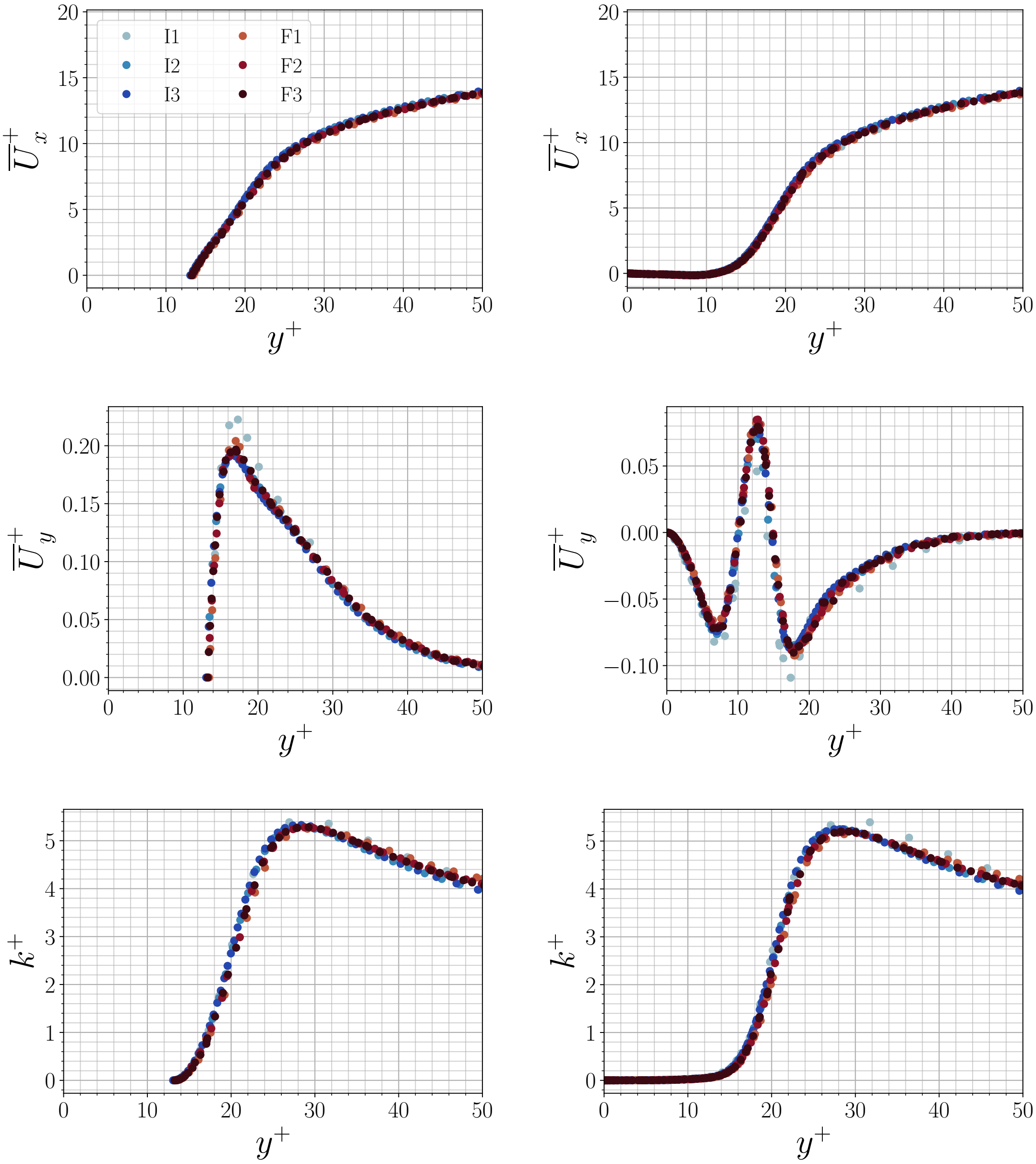

FIGURE 6.4: Mesh sensitivity for the flow over smooth denticles at $Re_\tau \approx 180$ and $w^+ \approx 45$, using the $k - \tau$ Low Reynolds number. Legend entries correspond to meshes defined in Table 6.1. Data are sampled in the $y-$direction at $(x, z) = (0.01, 0.01)$ and $(x, z) = (0.04, 0.22)$, corresponding to Line 1 (left) and Line 2 (right), respectively.

6.2 Results

For each denticle model four w^+ values are simulated at $Re_\tau \approx 180$ and $Re_\tau \approx 590$, covering the range $10 < w^+ < 70$. Due to computational expense, the EB-SSG model is only used for three denticle sizes at $Re_\tau \approx 180$ and $20 < w^+ < 70$. Results are presented in the following structure: Firstly, solutions are validated against experimental

TABLE 6.2: Mesh statistics for denticle meshes at $Re_\tau \approx 180$ and $w^+ \approx 45$. N_{cells} represents the total number of cells, N_{wall} represents the number of elements on the denticle boundary, and Δ^+ represents typical cell sizes in wall units. Denticle model abbreviations are as per Figure 6.1.

Case	N_{cells}	N_{wall}	Δ^+_{avg}	Δ^+_{min}	Δ^+_{max}
SMO	294663	17683	1.26	0.006	4.297
SMR	767198	48337	0.912	0.004	5.664
RIB	816812	56736	0.888	0.003	5.312

data of Chapter 3 by comparing friction coefficients, velocity profiles, and profiles of the Reynolds stresses. Secondly, the effect of riblets on the near-denticle flow is analysed in order to determine the influence of riblets in combination with shark skin denticles. This is achieved by investigating distributions of viscous and pressure forces on the denticles, denticle effects on the mean flow structures, and the influence of denticles on near-wall turbulence.

6.2.1 Validation

The drag force acting on the denticles has two components; viscous drag and pressure drag. These are defined by

$$F_i = F_{p,i} + F_{v,i} = \int_S -\overline{P} n_i \partial S + \int_S \nu \frac{\partial \overline{U}_i}{\partial x_j} n_j \partial S, \tag{6.1}$$

where F_i is a force vector, subscript p represents pressure components, subscript ν represents viscous components, S is the denticle surface, $\overline{P}$ is the mean kinematic pressure, and n_i is the local surface-normal vector. Note that the flat wall surface beneath the denticles is also included in the definition of S. There are therefore two contributions to the friction coefficient, which is decomposed by

$$C_f = C_{fp} + C_{fv} = \frac{F_{p,x}}{\frac{1}{2}U_\infty^2 A} + \frac{F_{v,x}}{\frac{1}{2}U_\infty^2 A} \tag{6.2}$$

where $A = L_x L_z$ is the reference surface area. The friction velocity is calculated from C_f. The friction coefficient as a function of dimensionless denticle width is compared against experimental data in Figure 6.5. The $k - \tau$ model with low Reynolds number corrections leads to reasonable predictions of the rough surfaces, where drag increases with w^+ and magnitudes of the drag increase are in good agreement with the experiments. However, there is little difference between the ribletted and smooth denticles at any value of w^+, contrary to the experiments. The effect of Re_τ and subsequently the blockage ratio δ/k_0 is to reduce the drag increase, consistently for both types of denticle.

The EB-SSG model leads to better predictions; as w^+ increases the difference between the two plates gets larger, with the ribletted denticles consistently leading to a reduced drag relative to the smooth, consistent with experiments. In addition, the magnitudes of drag increase appear in good agreement for the smooth denticles, although the drag appears slightly overpredicted for the ribletted denticles at small w^+. While experiments predict a drag decrease of approximately 2 % at $w^+ \approx 20$, the EB-SSG model predicts a drag increase of approximately 2 %. As a result, numerical solutions lead to a smaller difference in C_f between the two denticle plates when compared to the experiments, despite predicting the drag curve trends reasonably well. A possible explanation for this discrepancy is the different experimental conditions; while the present simulations are fully developed channel flows at a fixed bulk flow Reynolds number, the experimental flow was a developing boundary layer with a variable bulk flow Reynolds number. In addition, numerical solutions are somewhat influenced by the upper boundary at $y = \delta$, the influence of which is quantified by the blockage ratio δ/k_0 where k_0 is the roughness height, as discussed in Chapter 2. In particular, numerical solutions of the flow over sawtooth riblets (Chapter 5) were found to be somewhat dependent on blockage ratio, where the drag reduction of riblets was underpredicted for $Re_\tau \approx 180$ by 2 – 3 % when compared to experiments. Perhaps then the slight overprediction of drag for the ribletted denticles in Figure 6.5 is a result of the underprediction of the drag-reducing effects of riblets. However, the trends and magnitudes of C_f appear in good agreement between the EB-SSG model predictions and experiments. A critical result here is that deviations between the two plates appear to grow as w^+ increases, consistent between both experimental and numerical data.

Profiles of mean streamwise velocity and Reynolds stresses are also compared against experimental data for EB-SSG in Figures 6.6 to 6.9, for both smooth and ribletted denticles at $w^+ \approx 45$ and $w^+ \approx 67$. Direct comparisons between the data sets are not possible due to differences in experimental conditions, but deviations between rough plates and respective smooth-wall data can be readily compared. Here, the virtual origin has been approximated using the technique of Choi, Moin, and Kim (1993), described in Chapter

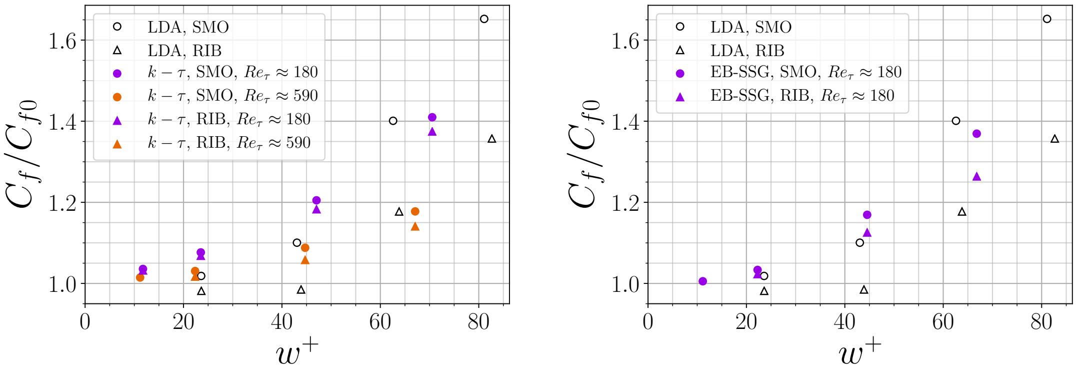

FIGURE 6.5: Relative friction coefficients for ribletted (RIB) and smooth (SMO) denticles with comparisons against the experimental data of Chapter 3. C_{f0} is the friction velocity for a reference flat plate.

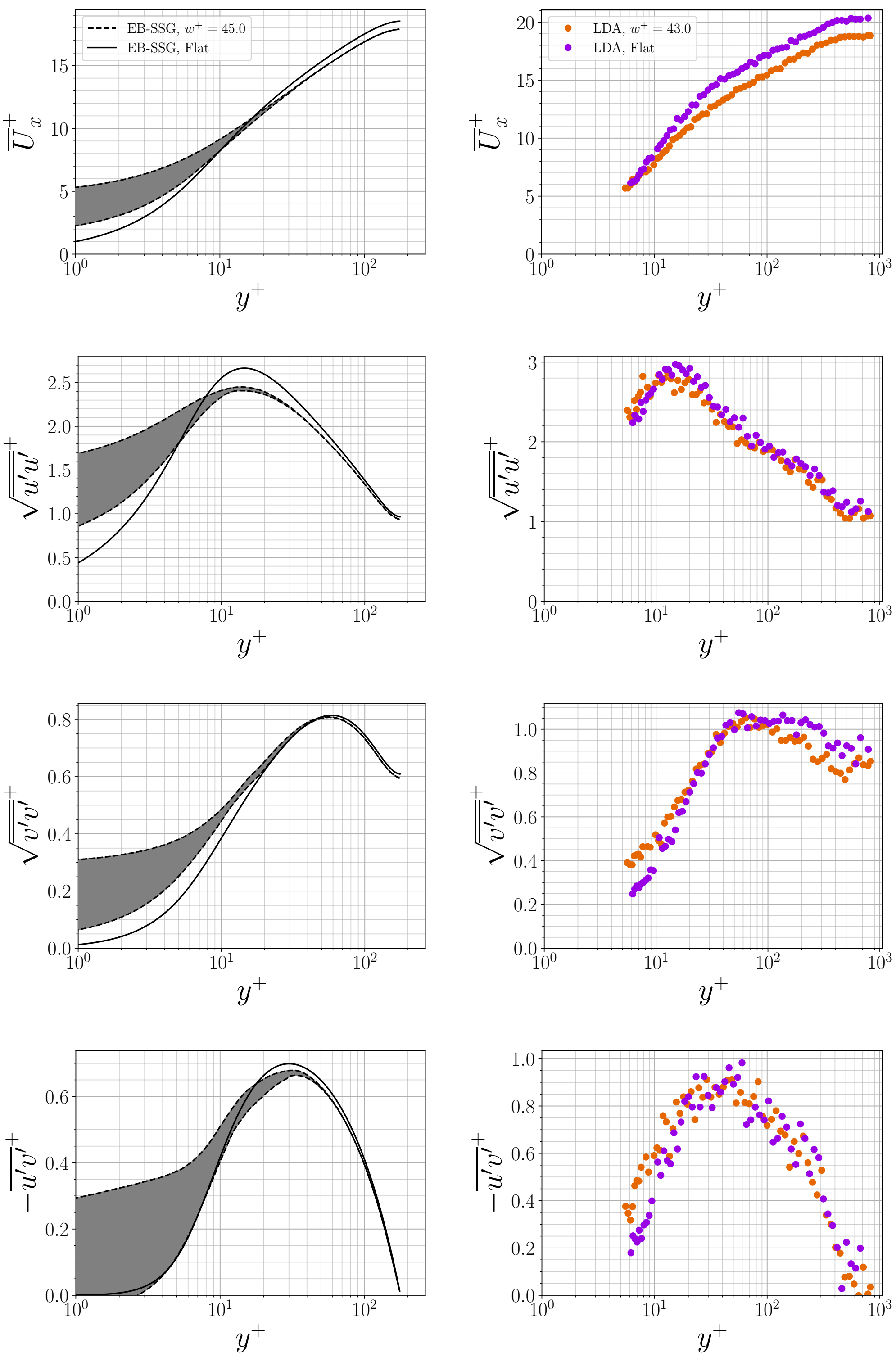

FIGURE 6.6: EB-SSG predictions (left) and experimental data (right) for the flow over smooth denticles at $w^+ \approx 45$. Numerical data are sampled at all mesh cell-centres, and lie in the grey region. Note that direct comparisons between numerical and experimental data sets are not appropriate, given their different bulk flow properties.

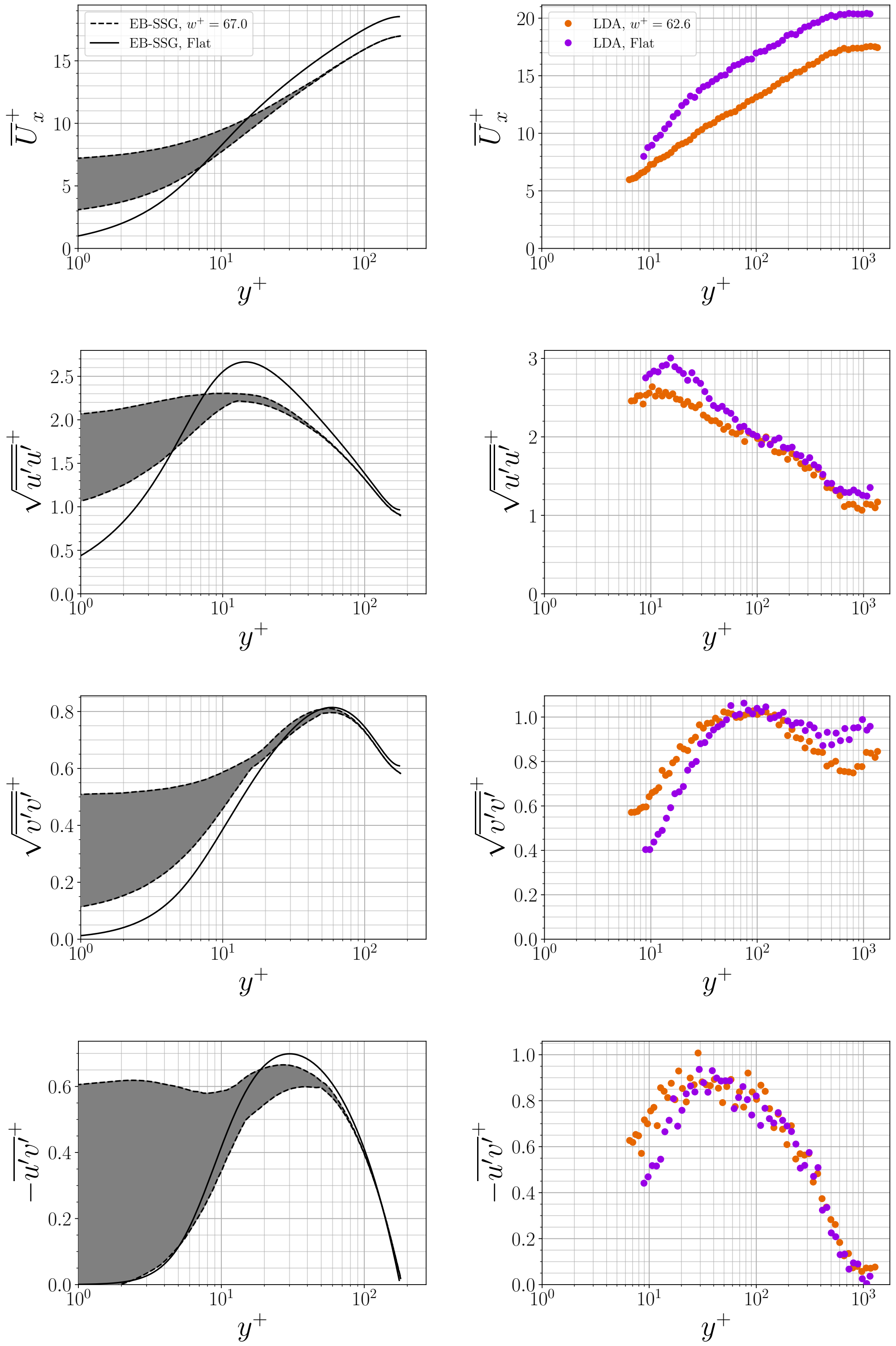

FIGURE 6.7: EB-SSG predictions (left) and experimental data (right) for the flow over smooth denticles at $w^+ \approx 67$. Numerical data are sampled at all mesh cell-centres, and lie in the grey region. Note that direct comparisons between numerical and experimental data sets are not appropriate, given their different bulk flow properties.

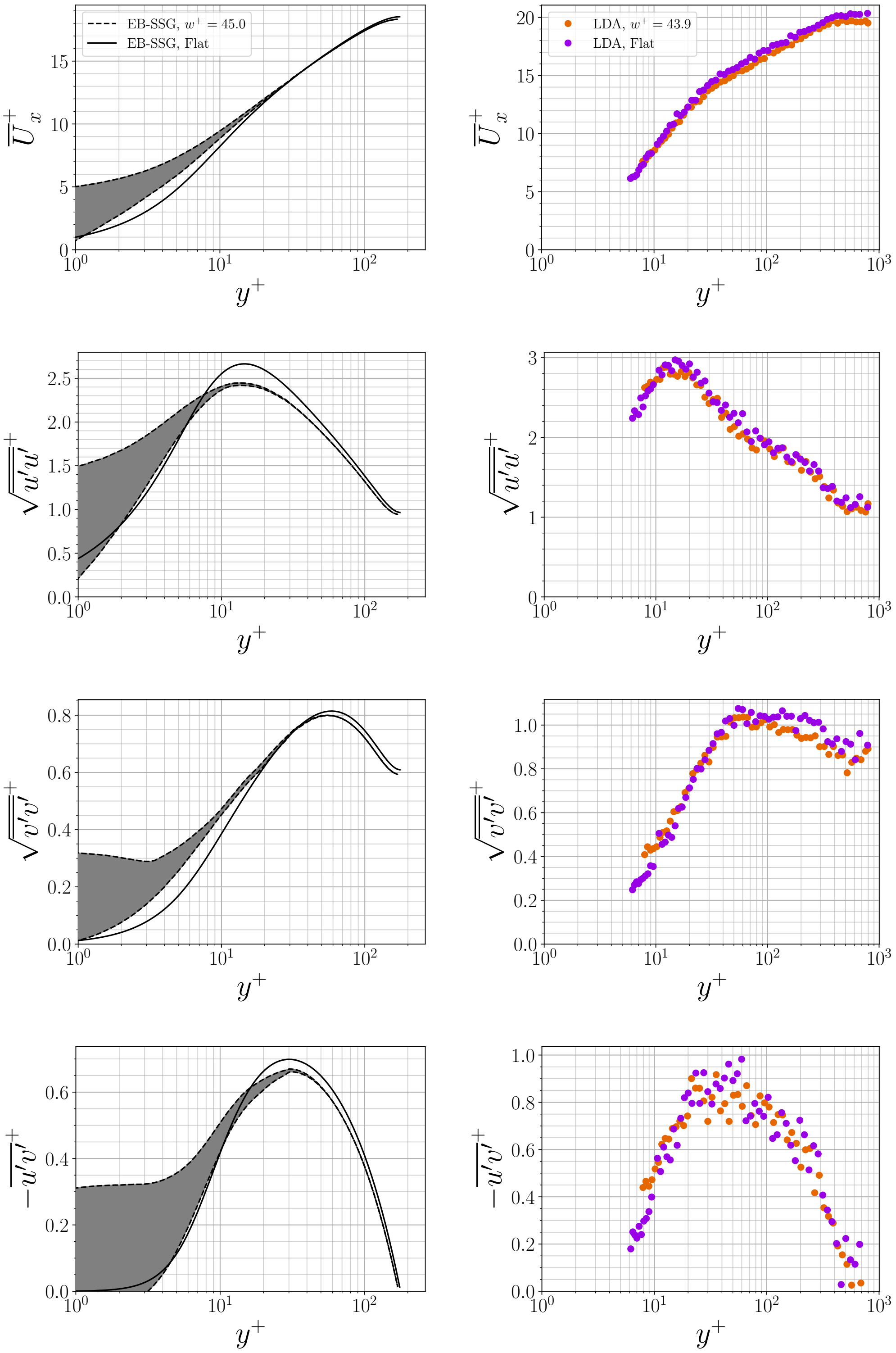

FIGURE 6.8: EB-SSG predictions (left) and experimental data (right) for the flow over ribletted denticles at $w^+ \approx 45$. Numerical data are sampled at all mesh cell-centres, and lie in the grey region. Note that direct comparisons between numerical and experimental data sets are not appropriate, given their different bulk flow properties.

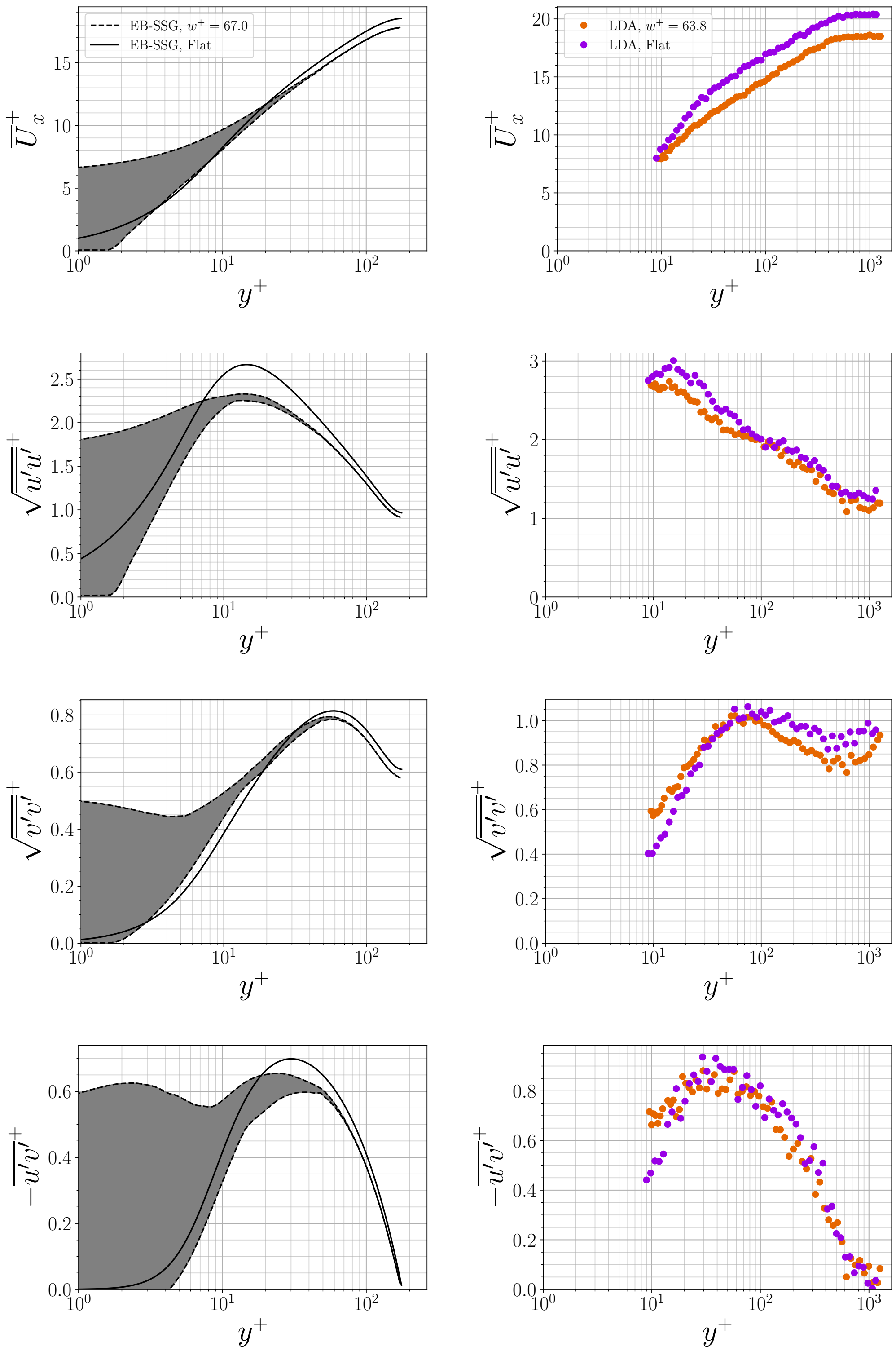

FIGURE 6.9: EB-SSG predictions (left) and experimental data (right) for the flow over riblletted denticles at $w^+ \approx 67$. Numerical data are sampled at all mesh cell-centres, and lie in the grey region. Note that direct comparisons between numerical and experimental data sets are not appropriate, given their different bulk flow properties.

5 (Section 5.2). Numerical data has been sampled at all coordinates in the domain, which lie within the grey region between the dotted curves. Results indicate that the influence of the rough surfaces on the mean velocity and Reynolds stresses is consistent between experiments and numerical predictions; the mean flow velocity is negatively offset from the flat surface profile, the maximum value of $\overline{u'u'}^+$ is reduced, and differences in $\overline{v'v'}^+$ and $\overline{u'v'}^+$ are characterised by a lifting of the near-wall region, due to a weaker impermeability condition. Regarding both smooth and ribletted denticle data the Reynolds stresses are in excellent agreement between experimental and numerical data. While the peak of $\overline{u'u'}^+$ is reduced a little more for the numerical solutions, predictions of $\overline{v'v'}^+$ and $\overline{u'v'}^+$ agree well. Note that the outer-region of the experimental measurements of $\overline{u'u'}^+$ and $\overline{v'v'}^+$ for the two plates diverges due to the presence of freestream turbulence, rather than differences between plates (discussed in Chapter 3). However, numerical solutions also predict a slightly larger decrease in the peak of $-\overline{u'v'}^+$ when compared to experiments. This could be partly due to the fairly large scatter in experimental measurements of $\overline{u'v'}^+$.

The good agreement between numerical and experimental data sets leads to confidence in the ability of EB-SSG to obtain reasonable predictions of these complex rough surfaces. In contrast, the two equation $k - \tau$ model fails to predict the large differences between the two denticle plates.

6.2.2 Pressure and viscous contributions to drag

Drag coefficients relative to reference flat plate values are presented in Figure 6.10, for all three denticle models, computed using the EB-SSG model. Interesting behaviour can be observed when introducing the denticle with smaller riblets (SMR), where the efficiency of the smaller riblets changes with respect to the other denticles as a function of w^+.

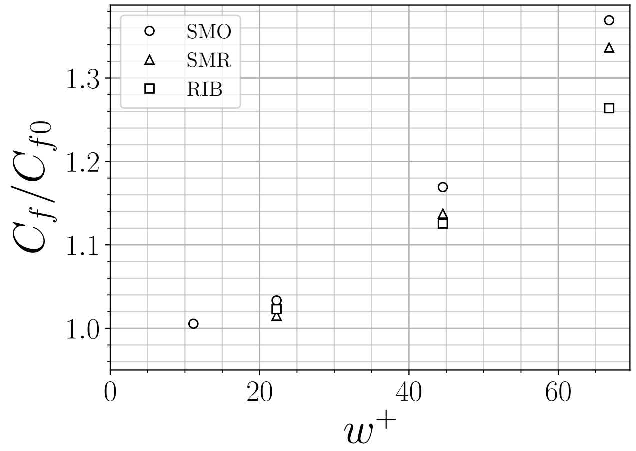

FIGURE 6.10: Friction coefficients relative to a reference flat plate for arrays of the three denticle models defined in Figure 6.1.

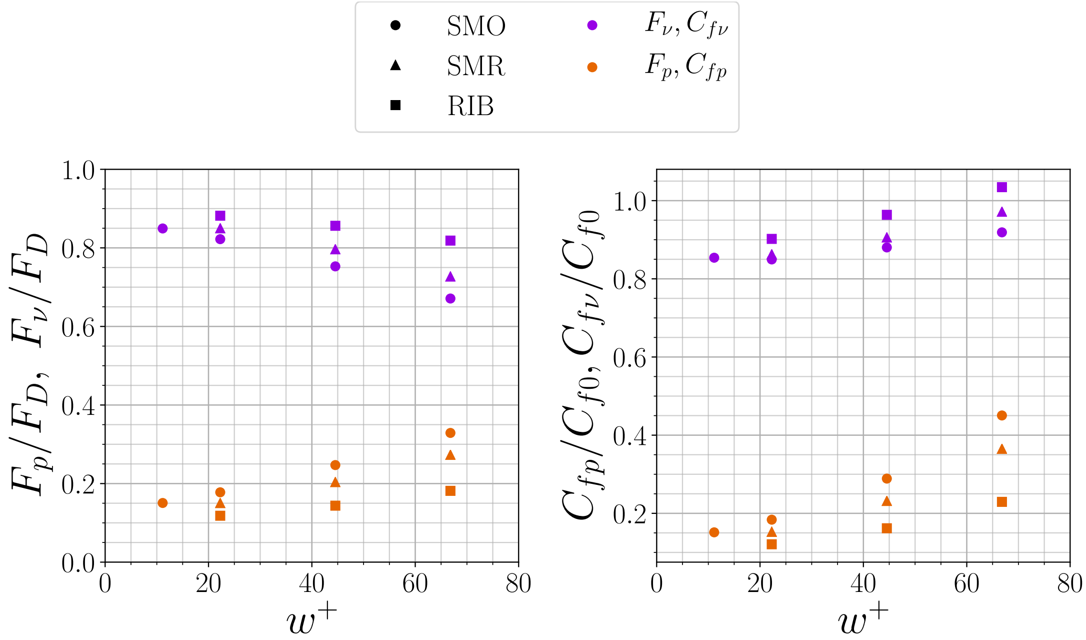

FIGURE 6.11: Contributions of pressure and viscous drag normalised by the total drag (left), and friction coefficients relative to reference flat plates (right). The sum of viscous and pressure friction coefficients (right) leads to the friction coefficients reported in Figure 6.10.

when w^+ is small the SMR denticles lead to the lowest drag compared to the others. As w^+ increases the RIB denticles become the most efficient. This seems a contradictory result, given that riblets are known to perform best at small riblet spacings (see data in Chapter 5), and as such one would expect the denticles with longer riblets (RIB) to out perform the SMR denticles at small w^+. Mechanisms leading to this change in regime may be identified by investigating the contributions of pressure and viscous components to the friction coefficient (6.2). These contributions can be observed in Figure 6.11. The relative contributions of viscous and pressure forces show that viscous forces dominate over pressure for all denticle models and all w^+ values reported. Viscous contributions account for approximately 80 % of the total drag force, and are largest at small w^+. As the denticle size increases pressure drag becomes more important, although for the range of w^+ investigated here pressure drag does not contribute more than 40 % of the total drag. Interestingly the denticle model that leads to the largest viscous drag is the denticle with long riblets (RIB). The effect of the riblets seems to be to reduce the pressure forces at the expense of viscous drag, contrary to what one may expect given their reduction of viscous forces for longitudinal ribletted plates and channels (See Chapter 5).

Contributions of pressure and viscous forces for the three denticle plates appears consistent for all w^+ values. smooth denticles (SMO) lead to the highest pressure drag but lowest viscous drag, the denticle with long riblets (RIB) leads to the highest viscous drag but lowest pressure drag, and the denticle with short riblets (SMR) lies between the other two denticles. While not immediately obvious, the regime change observed in Figure 6.10 can be identified by the contributions of pressure and viscous forces in Figure 6.11. Inspection of the pressure and viscous force coefficients for the three denticle plates at $w^+ \approx 20$ shows that while pressure drag is reduced for SMR denticles when compared to SMO denticles, there is little difference between respective viscous drag coefficients. In contrast, the RIB case leads to an approximately equal increase to viscous drag as the decrease to pressure drag, hence the SMR riblet appears overall more efficient.

Further insight can be gained through analysis of the distributions of local friction and pressure coefficients. While C_f is related to global forces calculated through the surface integrals of (6.1), the local streamwise pressure ($c_{p,x}$) and friction ($c_{f,x}$) coefficients are given by

$$c_{p,x} = \frac{\overline{P} - P_\infty}{\frac{1}{2}U_\infty^2} n_x, \quad c_{f,x} = \frac{\tau_{w,x}}{\frac{1}{2}U_\infty^2}, \tag{6.3}$$

where P_∞ is the mean kinematic pressure at $y = \delta$, n_x is the $x-$ component of the wall-normal unit vector, and the streamwise local shear stress $\tau_{w,x}$ is calculated by

$$\tau_{w,x} = \nu \frac{\partial \overline{U}_x}{\partial x_j} n_j. \tag{6.4}$$

Distributions of $c_{p,x}$ and $c_{f,x}$ for the three denticle models at $w^+ \approx 22$ and $w^+ \approx 67$ are presented in Figures 6.12 and 6.13. All 3D visualisations presented in this chapter are generated using PyVista software (Sullivan and Kaszynski, 2019). Surface contours of the local pressure coefficient (Figure 6.12) indicate regions of high pressure drag at the leading edge of the crown of each denticle model, just offset from the centreline due to the shielding of the upstream denticle. The SMO denticles consistently lead to the largest region of high pressure drag, where the peak of $c_{p,x}$ extends over a large portion of the denticle crown, and decreases towards the trailing edge. The RIB denticles have a much smaller region of high pressure, located at the leading edge of the outer riblet. The SMR denticles lead to pressure distributions somewhere between the other two; while the maximum pressure is of a similar magnitude to the SMO denticles, the region of high pressure is much more local to just the leading edge of the outer riblet, and quickly dissipates further downstream. While relatively high pressure is found over approximately half of the SMO denticles crown, the SMR denticles obtain a much lower pressure. There are also contributions to the pressure coefficient at the denticle trailing edges, but to a lesser extent than the leading edge given that they are much thinner.

The relative change in pressure coefficient between SMO and SMR denticles appears consistent at both $w^+ \approx 22$ and $w^+ \approx 67$, whereby the peak values are similar but the SMR denticles lead to a more local high pressure region, and therefore a lower total pressure drag. However, the relative difference between SMO and RIB denticles appears to grow as w^+ increases; at $w^+ \approx 67$ the RIB denticles lead to much smaller peak pressure coefficients than SMO and SMR denticles, and are much more local to the outer riblet

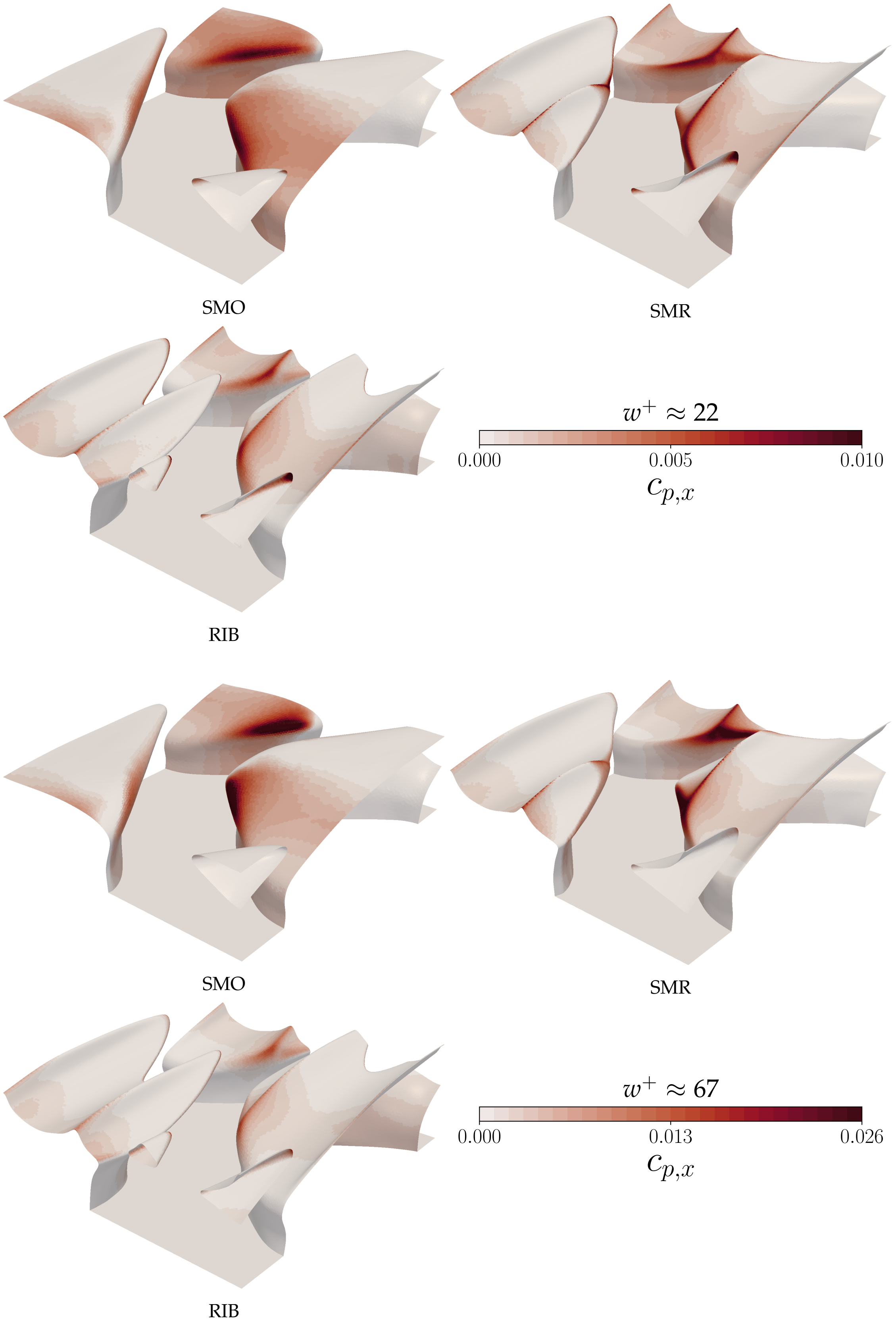

FIGURE 6.12: Local streamwise pressure coefficients for the three denticle models, SMO, SMR, and RIB, at $w^+ \approx 22$ and $w^+ \approx 67$. Flow direction is approximately from lower left to upper right for each model.

leading edges. These observations are consistent with the total pressure coefficients of Figure 6.11, where the relative change in pressure coefficient is similar between SMO and SMR denticles for all w^+, but grows between SMO and RIB denticles as w^+ increases.

Contours of the local streamwise friction coefficients are presented in 6.13. Here the friction coefficient colour maps have been scaled asymmetrically about $c_{f,x} = 0$ in order to highlight regions of negative friction, i.e regions of backflow. Note that the strength of the backflow is over an order of magnitude smaller than the maximum positive values of $c_{f,x}$. A smooth change in friction coefficient is observed for the smooth denticles (SMO) at $w^+ \approx 22$, which peaks towards the edge of the denticle crown, just downstream of the widest section. When riblets are added, the peak friction occurs at the riblet tips, at significantly higher magnitudes than the remaining denticle surface. A slightly lower friction relative to the SMO denticles is observed in the riblet valleys for both RIB and SMR denticles, although not low enough to compensate for the increased friction at the tips. The increased friction at the riblet tips is the cause of the increased viscous friction coefficient $C_{f,\nu}$, observed in Figure 6.11. It should be noted that for $w^+ \approx 22$, $s^+ \approx 8$ for both SMR and RIB denticles, which should be in the drag reducing regime if they were to behave like a typical ribletted surface. While longitudinal riblets do have high viscous stress at the tips this is compensated by significantly lower stresses between riblets (see Chapter 5), which is not the case here. Differences between friction coefficients at $w^+ \approx 67$ are consistent with those at $w^+ \approx 22$; SMO denticles have a smooth and gradual change in friction over the denticle crown, while the ribletted denticles have much higher friction at the tips. While it may seem like SMR denticles have larger regions of high stress than RIB denticles, they have a smaller surface area over which viscous friction can act, and subsequently lead to slightly lower global friction coefficient, $C_{f,\nu}$. An interesting feature of the SMR and SMO denticles at $w^+ \approx 67$ is that there are regions of positive friction coefficient on the lower wall, where the outer fluid is able to penetrate more deeply between denticles than for the RIB denticles. The larger outer riblet prevents this behaviour for the RIB denticles.

The distribution of $c_{f,x}$ also highlights regions of backflow, where the local friction coefficient is negative (Figure 6.13). The SMO denticles lead to the largest regions of backflow, and the highest magnitude of negative $c_{f,x}$. The backflow regions of the SMR denticles are similar in size as the RIB denticles, although the magnitude appears slightly lower for the RIB denticles. This suggests that the shape of the outer denticle has a small influence on flow separation. The backflow region increases in size with increasing w^+, but the differences between the three denticles appears consistent regardless of w^+.

The contributions of viscous and pressure drag to the total friction coefficients in Figure 6.11 can now be explained. Viscous forces appear smallest for the unribletted SMO denticles. Distributions of $c_{f,x}$ reveal that this is due to high viscous stress at the riblet tips for both SMR and RIB denticles. While longitudinal riblets compensate for increased viscous stress at the tips with considerably lower stress between riblets, this is not the

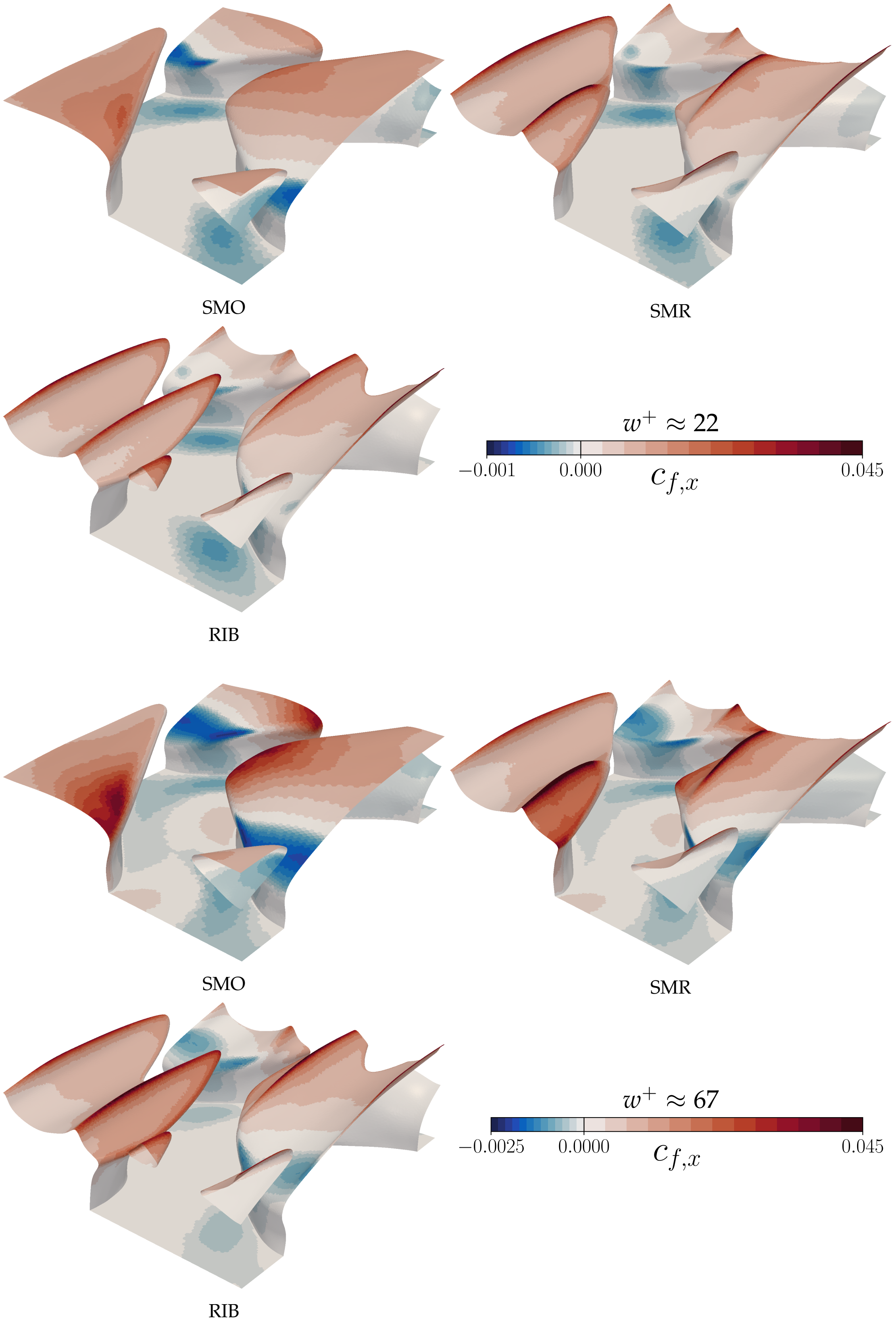

FIGURE 6.13: Local streamwise friction coefficients for the three denticle models, SMO, SMR, and RIB, at $w^+ \approx 22$ and $w^+ \approx 67$. Colour maps are scaled asymmetrically about $c_{f,x} = 0$ to highlight regions of backflow. A linear scaling is adopted for both halves of the colour map. Flow direction is approximately from lower left to upper right for each model.

case for the 3D denticles. Viscous stresses are larger for RIB denticles than SMR denticles due to the additional surface area of the longer riblets.

Pressure drag is largest for the SMO denticles and smallest for the RIB denticles, and distributions of $c_{p,x}$ illustrate the reasons for this. The SMO denticles lead to a large region of high pressure on the upstream tip of the denticle crown, towards the side of the denticle. It seems reasonable that this region is subject to relatively high speed fluid passing between denticles and impinging on the exposed surface. The SMO denticle leads to high $c_{p,x}$ over a large portion of the denticle crown. The SMR denticle leads to a similar peak of $c_{p,x}$ in the same location, coinciding with the leading edge of the riblet tip. However, $c_{p,x}$ is significantly lower over the remaining denticle, leading to an overall reduced pressure drag. The RIB denticle leads to the same location of maximum $c_{p,x}$ but with a much lower magnitude. Here the longer riblet seems to help shield the downstream denticle somewhat, restricting the ability of high speed fluid to impinge on the downstream denticle. These simulations therefore suggest that the ability of riblετted denticles to reduce drag relative to smooth denticles lies in a trade-off between pressure-drag and viscous-drag, where a reduction of pressure drag seems to be compensated by an increase to viscous drag. However, at $w^+ \approx 22$ the SMR denticles obtain near identical viscous drag solutions as the SMO denticles, while also obtaining a small decrease to pressure drag. The overall effect of this is a more efficient denticle than when longer riblets are present (i.e the RIB denticle), when denticle sizes are small ($w^+ \lesssim 30$).

6.2.3 Mean flow velocities

A $y-$normal slice through the domain beneath the denticle crown reveals a high momentum pathway (HMP) passing between denticles, with flow separation behind the denticle base (Figure 6.14). The streamwise velocity colour maps in Figure 6.14 have been scaled asymmetrically in order to reveal and compare regions of back flow, the magnitudes of which are approximately an order of magnitude smaller than the high momentum fluid passing between denticles. The SMO denticles lead to the HMP of highest mean velocity magnitude, followed by SMR and then RIB denticles. The RIB denticles lead to a considerably weaker HMP than the other two denticles. At $w^+ \approx 67$ the HMP curvature is much tighter, where the higher momentum fluid separates from the denticle base earlier. It seems here that the backflow is partly due to flow separating from the denticle base, rather than from separation of fluid above the denticle crown. The region of separating fluid therefore grows with w^+, where higher momentum fluid detaches from the denticle base earlier. Flow separation is also dependent on the denticle geometry; SMO denticles lead to the highest magnitude of negative velocity, although the shape of the recirculation region appears consistent between SMO and SMR denticles. In contrast, the RIB denticles lead to little flow separation, potentially due to the weaker momentum fluid beneath the denticle crown.

$x-$normal slices of mean streamwise velocity are presented in Figure 6.15. SMO and

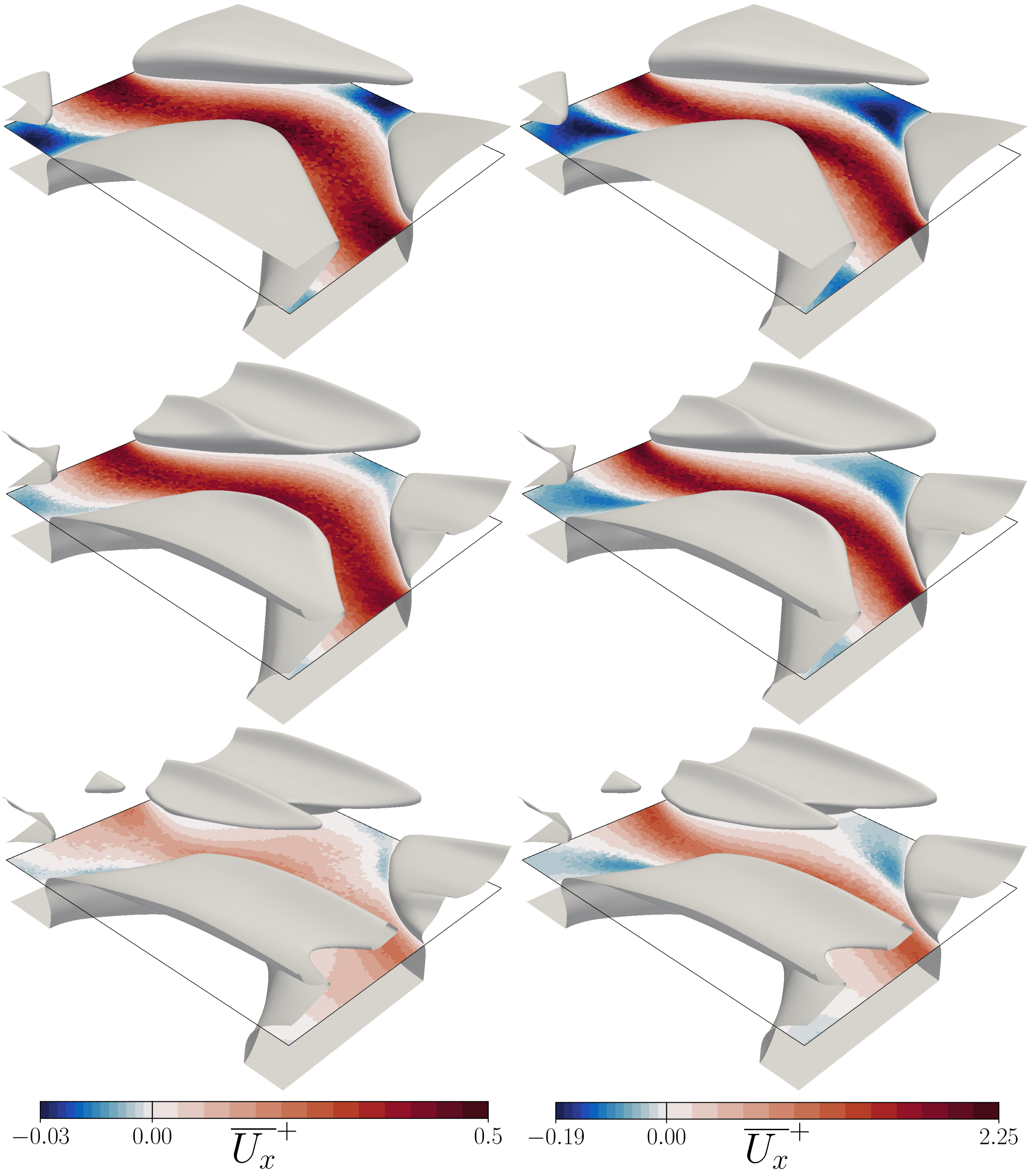

FIGURE 6.14: A $y-$normal slice beneath the denticle crown at $w^+ \approx 22$ (left) and $w^+ \approx 67$ (right). Denticle models are SMO (top), SMR (centre), and RIB (bottom). Contours are mean streamwise velocity, scaled asymmetrically about $\overline{U}_x^+ = 0$ to highlight regions of flow separation. A linear scaling is adopted for both halves of the colour map. Flow direction is approximately from upper left to lower right for each model.

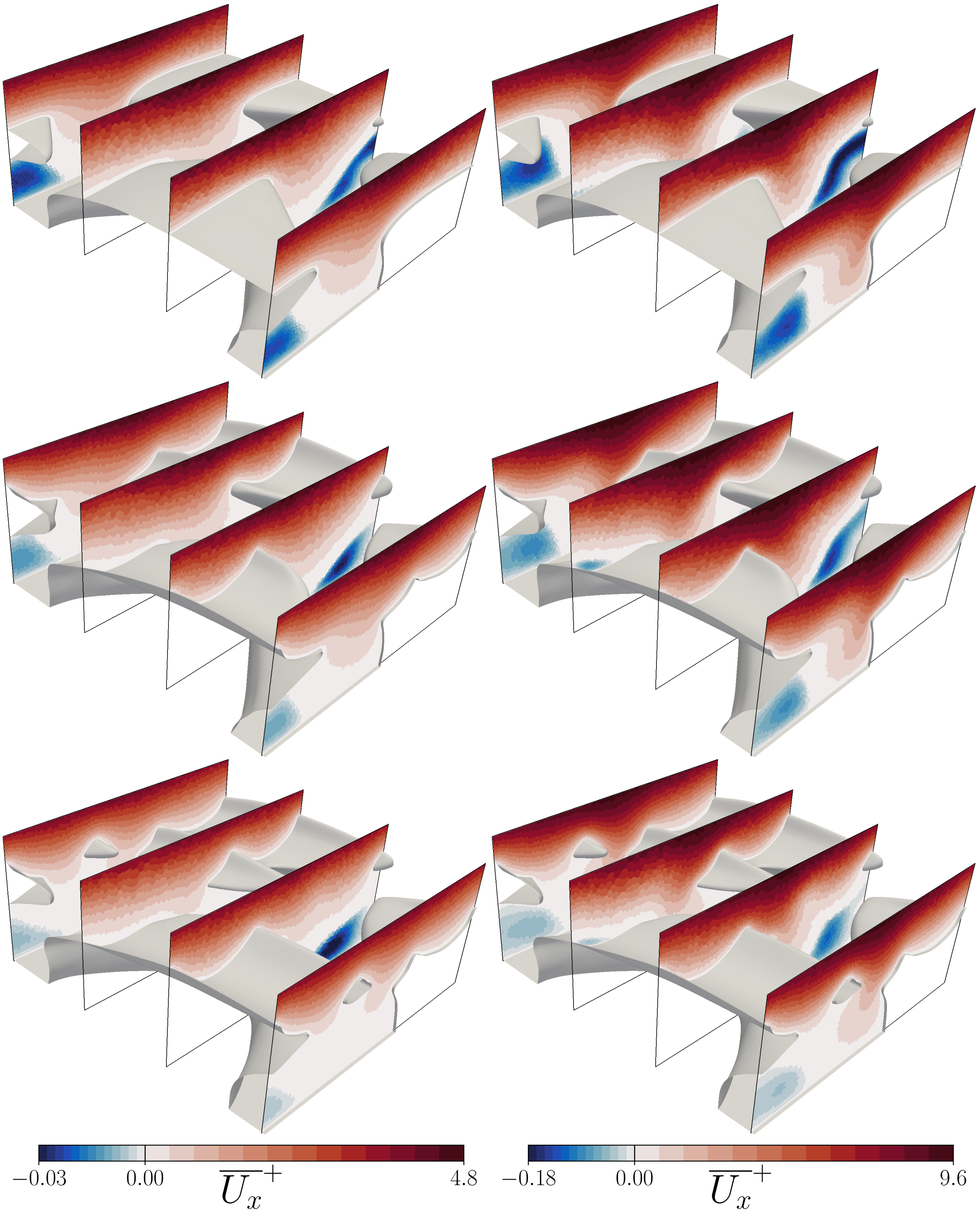

Figure 6.15: $x-$normal slices of the near-denticle flow at $w^+ \approx 22$ (left) and $w^+ \approx 67$ (right). Denticle models are SMO (top), SMR (centre), and RIB (bottom). Contours are mean streamwise velocity, scaled asymmetrically about $\overline{U}_x^+ = 0$ to highlight regions of flow separation. A linear scaling is adopted for both halves of the colour map. Flow direction is approximately from upper left to lower right for each model.

SMR denticles lead to very similar distributions of mean streamwise flow, main differences lying above the denticle crown, where the SMO denticles lead to an even distribution of flow and the SMR denticles lead to high gradients at the riblet tips and lower velocity fluid in the valleys. This occurs over the whole denticle crown, including the leading edge where pressure drag is reduced for the SMR denticle when compared to the SMO denticle (Figure 6.12). This suggests that riblet tips are acting to protect the riblet valleys from relatively high velocity impinging fluid, leading to the reduction of local pressure coefficient in Figure 6.12 at the expense of higher pressure at the riblet tips. Note that the HMP between denticles has a velocity magnitude of approximately 10 % of the fluid just above the denticle crown. The RIB denticles lead to similar profiles above the denticle crown as SMR denticles, but the flow beneath the crown is significantly weaker.

Contours of spanwise and vertical components of velocity can be observed on the same $x-$normal planes in Figures 6.16 and 6.17. All three denticles lead to similar and complex flow patterns. However, it should be noted that these are not indicative of secondary or tertiary flows, since the mean flow direction is not necessarily aligned with x in the roughness sub-layer. The vertical velocity contours of Figure 6.16 show large regions of high magnitude downward velocity between the denticles, peaking at the edges of the wide section of the crown. It seems then that the HMP is at least partly driven by a vertical flux of fluid from above the roughness, drawing fluid between the denticles. Fluid beneath the trailing edge of the denticle crown is typically moved upwards, while flow shedding from the top of the denticle crown's trailing edge is convected downwards. Flow travelling over the top of denticles moves upwards, due to the positive angle of attack of the denticles. Differences between SMO and SMR mainly exist above the denticle crown, where the riblets have a significant influence on the vertical and spanwise flow. The SMO denticles lead to a large region of high magnitude vertical velocity near the widest region of the scale. When riblets are added (SMR and RIB denticles), this region is broken down such that high magnitude vertical velocities occur only at the tip of the riblet, with an overall reduction in vertical velocity in the riblet valleys. In addition, the riblets on the SMR denticle also change the region of downward flow at the edge of the crown, where the riblet appears to constrict the region of downward flow to just the edges of the denticle. In contrast, the SMO denticle leads to downward flow over a larger portion of the denticle. The effect of w^+ on the flow is consistent for all denticles; a higher w^+ leads to a suppression of vertical flow such that peaks in $\overline{U}_y^+$ occur closer to the denticle surface. This is unsurprising since at higher w^+ the denticles are exposed to higher momentum fluid which, like the HMPs, will be affected less by small changes in curvature.

Contours of spanwise flow (Figure 6.17) reveal the motion of the HMP, where the largest magnitudes of spanwise flow occur between denticles. The positive and negative values correspond to the local direction of the HMP, observed in Figure 6.14. Above the denticle crown the spanwise flow appears consistent between the SMO and SMR

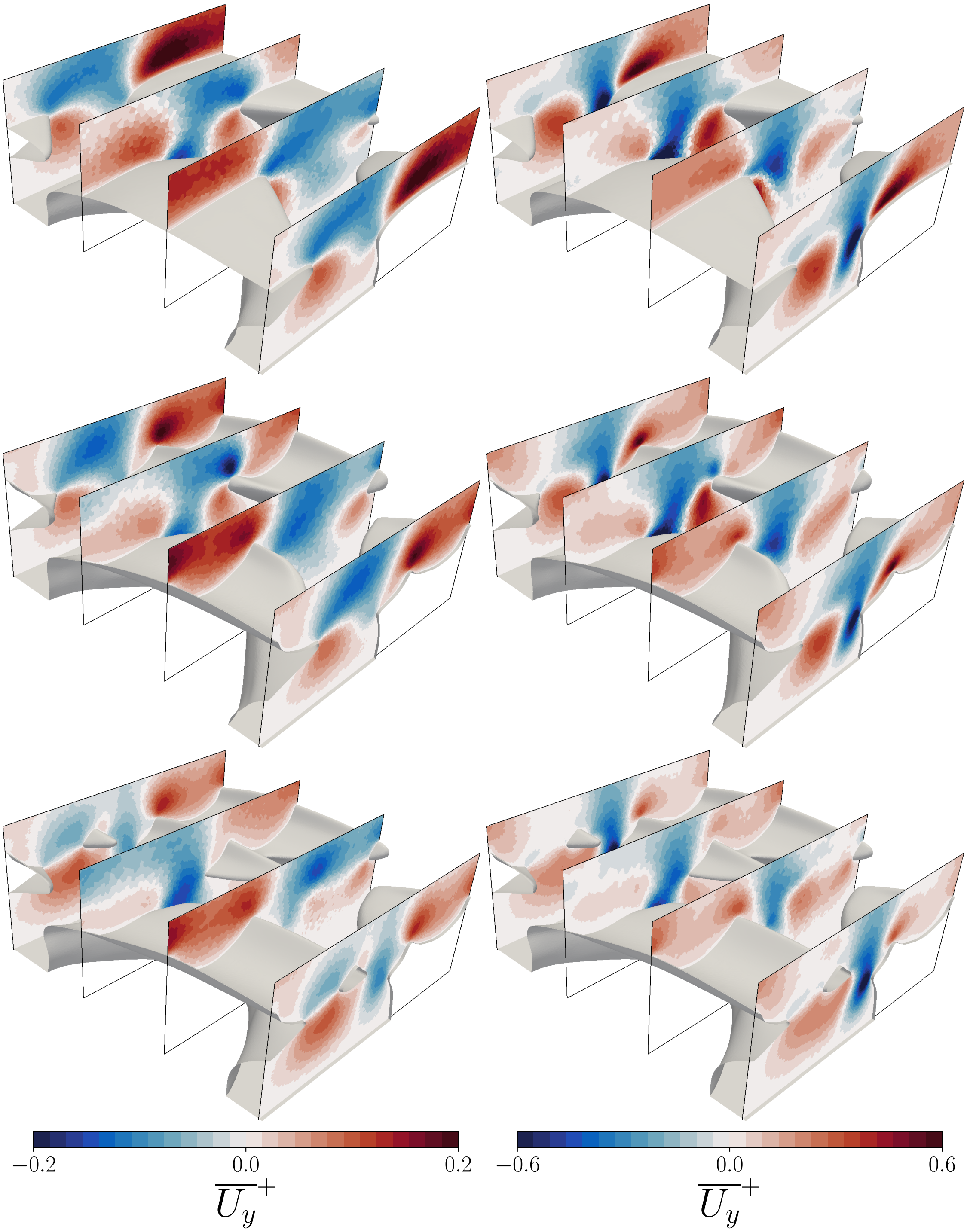

FIGURE 6.16: x−normal slices of the near-denticle flow at $w^+ \approx 22$ (left) and $w^+ \approx 67$ (right). Denticle models are SMO (top), SMR (centre), and RIB (bottom). Contours are mean vertical velocity. Flow direction is approximately from upper left to lower right for each model.

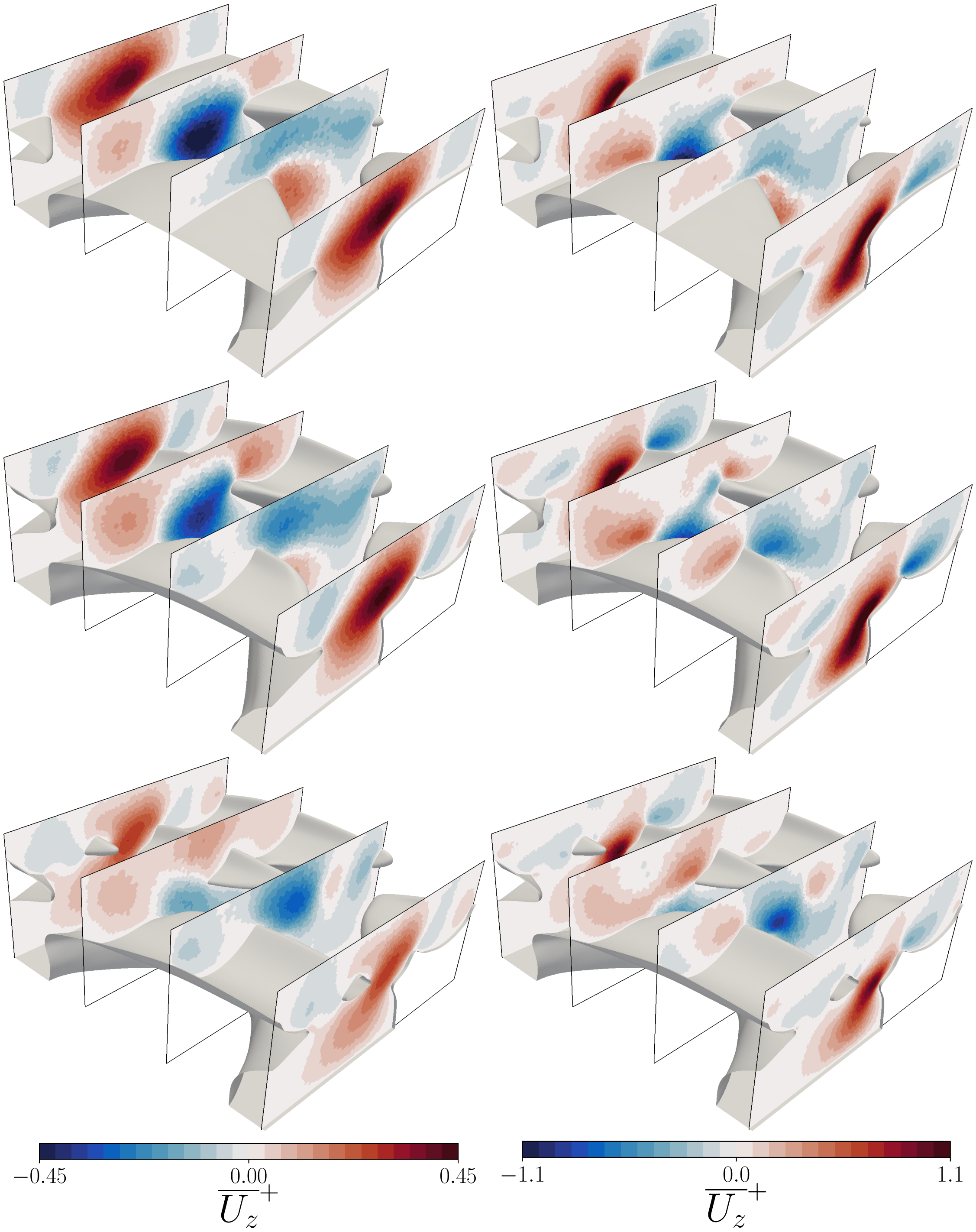

FIGURE 6.17: $x-$normal slices of the near-denticle flow at $w^+ \approx 22$ (left) and $w^+ \approx 67$ (right). Denticle models are SMO (top), SMR (centre), and RIB (bottom). Contours are mean spanwise velocity. Flow direction is approximately from upper left to lower right for each model.

denticles. The RIB denticles appear to weaken spanwise flow and break up the larger coherent regions of spanwise and vertical flow. An interesting feature of the spanwise and vertical flows is that when riblets are introduced the stress-induced secondary flows that are produced by longitudinal riblets (see Chapter 5) are not present. One would expect to observe spanwise flow moving towards riblet tips and deflecting upwards, but this is not always the case when inspecting Figures 6.16 and 6.17. This, along with the increase to viscous drag, suggests that riblets are not acting as they do when applied to plates and channels.

The fluid impinging on each denticle originates from the widest section of the upstream denticles outer edge, as observed in Figure 6.18. The fluid is drawn beneath the roughness height between each denticle and is then ejected upwards as it impinges on the following denticle. The HMP originates from the downward flow at the exposed denticle edge and is responsible for the impinging flow on each denticle crown. It is interesting to note that the impinging flow at the denticle crown's leading edge does not originate

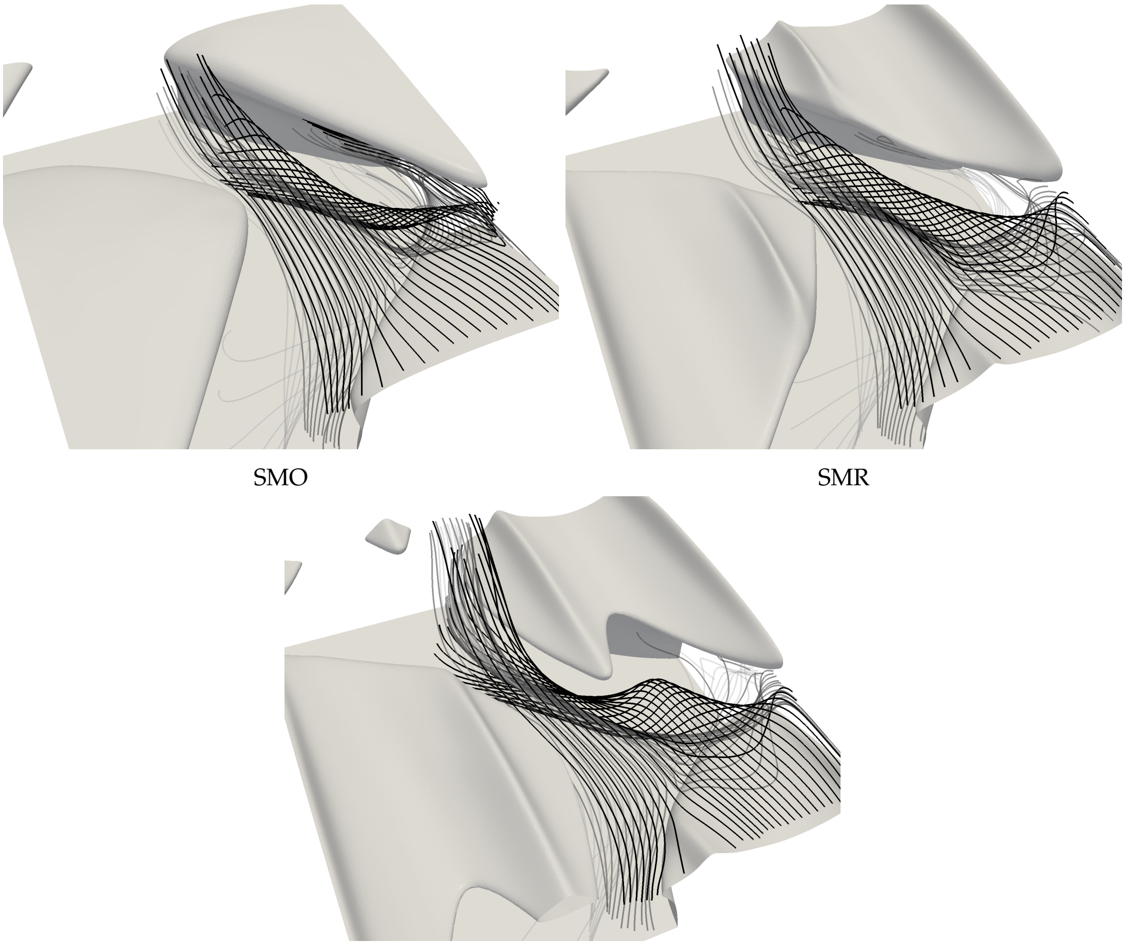

FIGURE 6.18: Streamlines indicating the origin of flow impinging on the denticle crown at $w^+ \approx 67$. Flow direction is approximately from top to bottom for each model.

from the trailing edge of the denticle directly upstream. Flow detaching from above the denticle trailing edge is convected in the streamwise direction, likely due to its relatively high momentum.

The influence of riblets is subtle when comparing streamlines above the SMO and SMR denticle. The main differences exist at the impingement region, where the outer riblet acts to deflect the flow around it, while the streamlines over the SMO denticle appear uniform. This deflection leads to a relative increase in pressure at the outer riblet (Figure 6.12), and shields the valley from high velocity fluid (Figure 6.15). In addition, the back flow region appears slightly larger for the SMR denticle (although significantly weaker in strength when considering local friction coefficients of Figure 6.13), consistent with the lower velocities between riblet tips of Figure 6.15. The origin of impinging flow is consistent between all three denticles, despite the partial shielding of the RIB denticles outer riblet, which only act to distort the streamlines that pass around/beneath it.

The vertical and spanwise velocity contours of Figures 6.16 and 6.17, and the streamlines of Figure 6.18, indicate regions of swirling flow, particularly at the outer edge of the denticles. The swirling flow is quantified by computing iso-contours of swirl strength, λ_{ci}^+, which is a scalar equal to the imaginary part of the complex eigenvalue of the inner-scaled velocity gradient tensor. Mathematically the inner-scaled velocity gradient tensor can be decomposed by

$$\frac{\partial \overline{U}_i^+}{\partial x_j^+} = \begin{bmatrix} \boldsymbol{v}_r & \boldsymbol{v}_{cr} & \boldsymbol{v}_{ci} \end{bmatrix} \begin{bmatrix} \lambda_r^+ & 0 & 0 \\ 0 & \lambda_{cr}^+ & \lambda_{ci}^+ \\ 0 & -\lambda_{ci}^+ & \lambda_{cr}^+ \end{bmatrix} \begin{bmatrix} \boldsymbol{v}_r & \boldsymbol{v}_{cr} & \boldsymbol{v}_{ci} \end{bmatrix}^{-1} \tag{6.5}$$

where λ_r^+ is the real eigenvalue with a corresponding eigenvector $\boldsymbol{v}_r$ and $\lambda_{cr}^+ \pm \lambda_{ci}^+ i$ are the conjugate pair of the complex eigenvalues with complex eigenvectors $\boldsymbol{v}_{cr} \pm \boldsymbol{v}_{ci} i$ (Zhou et al., 1999). Regions of swirling flow are identified by non-zero swirl strengths, λ_{ci}^+. This has the advantage of eliminating regions having vorticity but no local spiralling motion (i.e shear layers), and being frame invariant. Iso-contours of λ_{ci}^+ are presented in Figure 6.19. Here, regions of particularly strong swirling have been identified by applying a transparency filter mapped to the values of λ_{ci}^+. The swirling flows, while complex, are largely dominated by one region of high swirl strength at the edge of each denticle. For a given w^+, each denticle has similar values of maximum swirl strength, although it should be noted that this is due to the inner-scaling of the velocity gradient (6.5), where the resulting dimensional swirl strength has been scaled by ν/u_τ^2. If normalised by $u_{\tau 0}$ instead the differences in swirl strength would be vast, with the SMO denticle leading to significantly higher swirling than the other denticles, due to the higher friction coefficient (Figure 6.10). However, when scaled by respective friction velocities the structure of swirling flow still varies significantly over the different denticles. Interestingly no circular flow exists in the region behind the denticle base where flow separation occurs, and most swirling flow occurs above the denticle crown. The swirling flow beneath the

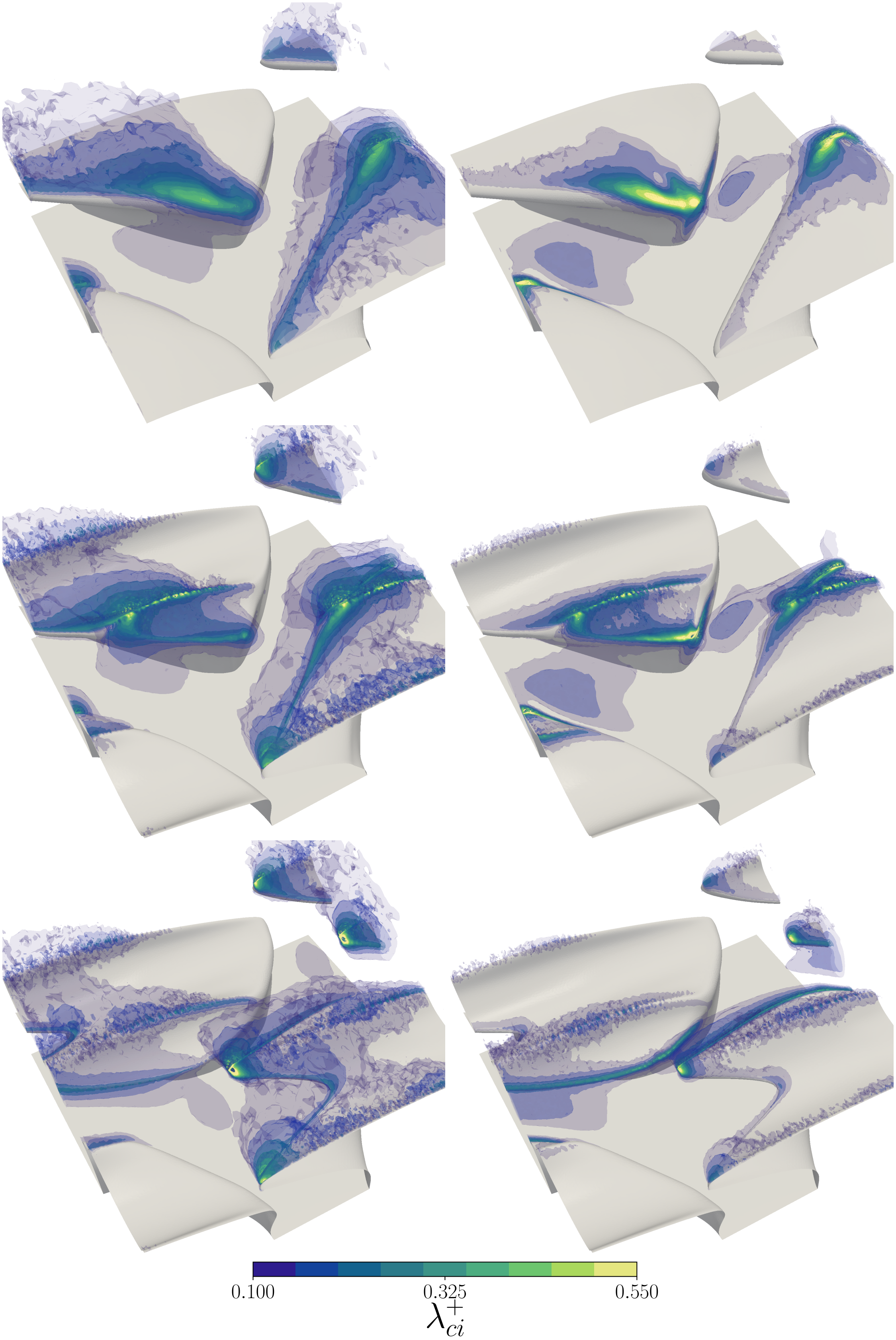

FIGURE 6.19: Iso-contours of swirl strength λ_{ci}^{+}. Contours are partially transparent to visualise three-dimensionality of swirling structures. Cases are $w^{+} \approx 22$ (left) and $w^{+} \approx 67$ (right). Denticle models are SMO (top), SMR (centre), and RIB (bottom). Flow direction is approximately from right to left for each model.

denticle crowns is located primarily along the path of the HMP, between denticles and just downstream of the large patch of high magnitude swirl, which can be most clearly observed for the SMO and SMR denticles at $w^+ \approx 67$. However, the strength of this swirling flow is significantly weaker than those above and along the edge of the denticle crowns. When compared to Figures 6.12 and 6.13 the regions of high swirl strength are somewhat correlated to regions of high viscous friction, likely due to the large near-wall velocity gradients.

The SMO denticle consistently leads to the largest region of high magnitude swirling, located at approximately the widest point of the denticle crown. This high magnitude swirling covers a significant proportion of the denticle crown surface, and is only negligible along the denticle centreline and at the leading edge, where flow separation is present (see Figure 6.13). A reasonably high magnitude of swirling is present on the full trailing edge of the denticle, likely due to the formation of a shear layer as high speed fluid detaches from the denticle crown and mixes with low speed fluid beneath it.

Swirling flow structures over the SMR denticles are similar to those over the SMO denticles but with more localised thin regions of high swirl strength present on the riblet tips. There is also reasonably high swirl at the trailing edge, although in a thinner region when compared to the SMO denticles. The outer riblet tips lead to the highest magnitude of swirl, peaking at the trailing edge of the riblet, where flow detaches from the denticle crown. Similarities between SMO and SMR denticles are perhaps unsurprising given their similar shapes. The introduction of riblets seems to break up the region of high swirl, perhaps helping align fluid with the streamwise direction. There is also a small amount of swirl generated at the central riblet tip, although of a lesser magnitude than the outer riblets, likely due to the lower local friction (see Figure 6.13).

The RIB denticles lead to much weaker swirling with a maximum swirl strength present at the very downstream tips of the outer riblets. Swirling at the outer edge is significantly reduced. There is some weak swirl generated at the riblet tips, similar to that observed on the SMR denticle. In addition, there is little swirling beneath the denticle crown, most obvious when comparing the $w^+ \approx 67$ cases. Two reasons could lead to this behaviour: Firstly, the longer riblets lead to slightly more shielding, thus reducing the flow that can penetrate beneath the denticle crowns. Secondly, the riblets act to align the flow and restrict the swirling generated at the widest part of the denticle, and on the denticle crown between riblets. Perhaps this is due to the restricted spanwise-motion of the riblets, where swirl generated at the outer edge cannot 'spill' over onto the inner-denticle crown surface.

The effect of denticle size seems to be consistent over all three denticle models; at large w^+ the swirl strength is increased but more localised. Low magnitude swirl is suppressed by the higher momentum fluid close to the denticle surface, such that overall swirl is reduced over much of the denticle. However, regions of high swirl are actually enhanced. The relative magnitude of swirling beneath the denticle seems to increase with

w^+, likely due to the higher momentum fluid that is able to penetrate beneath the denticle crowns.

An immediate question arises from this analysis; what effect does swirling have on the efficiency of a denticle? Any momentum lost to swirling flow will be detrimental to overall efficiency, but two further adverse effects of secondary flows are suggested here. Firstly, the swirling at the outer edge of the denticle crown is responsible for driving the downward motion observed in Figure 6.16 that draws high momentum fluid above the denticles downwards and into the gaps between them, leading to the HMP. This will have adverse effects on both pressure drag and viscous drag, where higher momentum fluid will impinge on the denticles, and also lead to larger velocity gradients close to the surface. Secondly, the swirling above the denticle crown will lead to larger velocity gradients and therefore enhance production of turbulent kinetic energy (TKE). TKE production will enhance momentum transfer close to the surface and subsequently increase both pressure and viscous drag on the denticle surface. The introduction of riblets leads to a restriction on the swirl strength, and subsequently reduces momentum transfer close to the surface. While there is sufficient evidence for this first mechanism, through the velocity and swirl strength contours of the present section, the second mechanism requires support from analysis of the near-denticle turbulence fields.

6.2.4 Turbulence predictions

Contours of inner-scaled turbulent kinetic energy (k^+) are presented in Figure 6.20. k^+ peaks above the region between denticles, and is strongest for SMO denticles, followed by SMR and then RIB denticles. Above the SMO denticles k^+ is fairly homogeneous, but when riblets are present there is some spatial dependence, where k^+ is low in the riblet valleys. This occurs more-so for the RIB denticles, which also protect the flow beneath the denticle crowns from high turbulence. Note that for the denticle sizes presented here the flow appears fairly laminar beneath the denticle crown, except in the exposed region between denticles. This is perhaps unsurprising for the $w^+ \approx 22$ cases, where the maximum denticle heights here are approximately $D_h^+ \approx 6$ for the SMO denticles and $D_h^+ \approx 8$ for the SMR and RIB denticles, and therefore protrude only slightly into the buffer layer. However, at $w^+ \approx 67$ the denticles have heights closer to 23 wall units. While turbulent kinetic energy is much stronger near the denticles at $w^+ \approx 67$, the denticle crowns are still able to maintain a small region of laminar flow.

While not explicitly linked, the turbulence levels close to the wall have a large effect on drag, by enhancing momentum transfer close to the walls and subsequently increasing both velocity gradients leading to viscous stress, and increasing the momentum loss due to pressure drag, where higher momentum fluid can impinge on exposed surfaces. It is therefore important to identify mechanisms that lead to the differences in k^+ distributions above the three denticle geometries. This is achieved by investigating differences in the budgets of k^+ transport, which is derived by taking the trace of the Reynolds stress

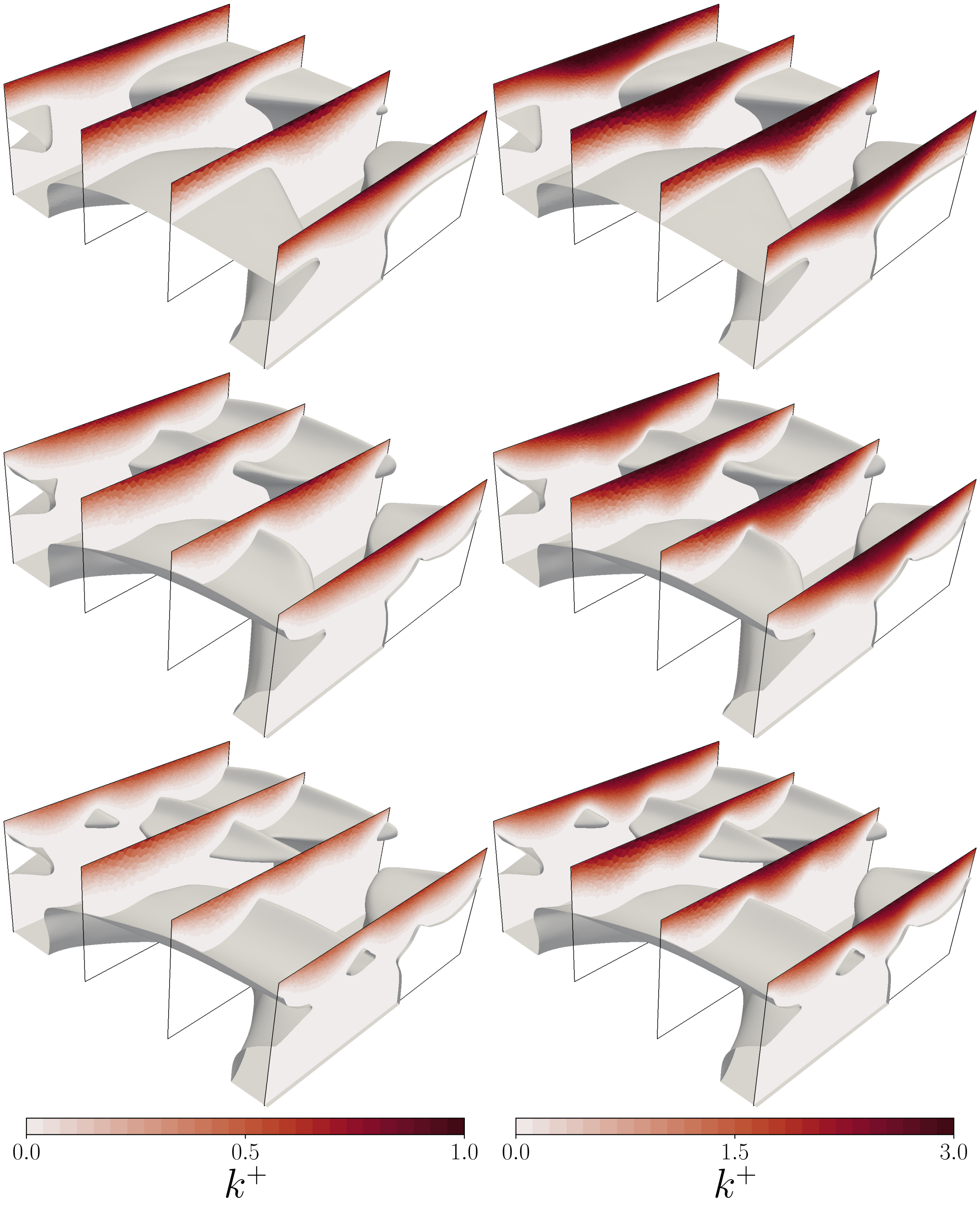

FIGURE 6.20: $x-$normal slices of the near-denticle turbulent kinetic energy at $w^+ \approx 22$ (left) and $w^+ \approx 67$ (right). Denticle models are SMO (top), SMR (centre), and RIB (bottom). Flow direction is approximately from upper left to lower right for each model.

transport equations for the EB-SSG model (Appendix C.9), leading to

$$(\mathrm{D}_t k)^+ = \frac{Dk^+}{Dt^+} = \mathcal{P}^+ - \varepsilon^+ + \mathcal{D}_T^+ \tag{6.6}$$

where convection of k^+ is balanced by production, $\mathcal{P}^+ = \frac{1}{2}\mathcal{P}_{ii}$, the rate of turbulent dissipation, ε^+, and the sum of turbulent and viscous diffusion,

$$\mathcal{D}_T = \frac{1}{2}\mathcal{D}_{ii} = \frac{1}{2}\frac{\partial}{\partial x_l}\left[\left(\frac{C_\mu}{\sigma_k}\overline{u_l' u_m'}T + \nu\delta_{lm}\right)\frac{\partial\overline{u_i' u_i'}}{\partial x_m}\right], \tag{6.7}$$

and the superscript + represents normalisation in inner units: ν/u_τ^4. For further details of this transport equation see Appendix C.9.

Analysis of turbulent kinetic energy transport budgets is limited to the $w^+ \approx 67$ case, since the small denticles lead to reasonably similar but weaker and more homogeneous budgets, due to the low magnitude of turbulent kinetic energy. Distributions of the four budgets for the SMO denticle are presented in Figure 6.21. In the immediate vicinity of the denticle surface the rate of turbulent dissipation (ε^+) balances diffusion ($\mathcal{D}_T^+$), a necessity through asymptotic analysis and imposed through the boundary conditions of ε (discussed in Chapter 4). Near the wall diffusion is positive, where turbulence is diffused from the outer regions to the near-wall regions, and subsequently balanced by the rate of dissipation. Regions of strong viscous shear lead to the peaks in ε and $\mathcal{D}_T^+$ at the widest part of the denticles. Typically diffusion of k^+ is negative, contributing to the removal of k^+ produced by velocity gradients and convected from other regions of the flow. This behaviour leads to the sign change observed for $\mathcal{D}_T^+$ in Figure 6.21, and is typical of wall-bounded flows (see e.g. Mansour, Kim, and Moin, 1988).

Further from the wall turbulent production ($\mathcal{P}^+$) dominates and is particularly strong at the trailing edges of the denticle crown. At these regions production of turbulent kinetic energy is so large it must be balanced by all other terms. Contours of $\mathcal{P}^+$ also reveal small regions of weak negative production, particularly downstream of the denticle trailing edge, and close to the region of high local pressure coefficient (Figure 6.12). This is not consistent with typical smooth-walled channels but is known to exist for boundary layers in adverse pressure gradients, flows subject to curvature, and regions of flow separation (Cimarelli et al., 2019).

The most interesting feature of the budgets of turbulent kinetic energy transport is the structure of convective and productive terms, which both have a large influence on turbulence near the denticles. There are regions of both positive and negative convection of turbulent kinetic energy. At the front of the denticle crown convection is negative in sign, such that k^+ is transported towards these regions and must be balanced by dissipation and diffusion. At the denticle crown's trailing edge convection is positive, such that k^+ is transported away from this region to be dissipated elsewhere. In this region production of k^+ is so large that convection is required to transport it to regions it can be dissipated/diffused. Regions of high negative convection are present at the exposed regions of the denticles where fluid impinges on the outer edge and the local pressure coefficient is large (Figure 6.12).

Budgets of the transport of turbulent kinetic energy for the SMR and RIB denticles can be observed in figures 6.22 and 6.23. The magnitude of the budgets appears consistent between all three denticles, suggesting that the inner-scaling ν/u_τ^4 is an appropriate normalisation. the most notable changes are in the vicinity of the riblets, where the peaks in ε^+ and $\mathcal{D}_T^+$ are local to the riblet tips, due to the higher local viscous shear. Other differences between the three denticles are smaller, where the general structure of the transport budgets are similar. However, regions of negative convection at the widest section of the denticle is lower in magnitude for SMR and RIB denticles than SMO denticles, such that

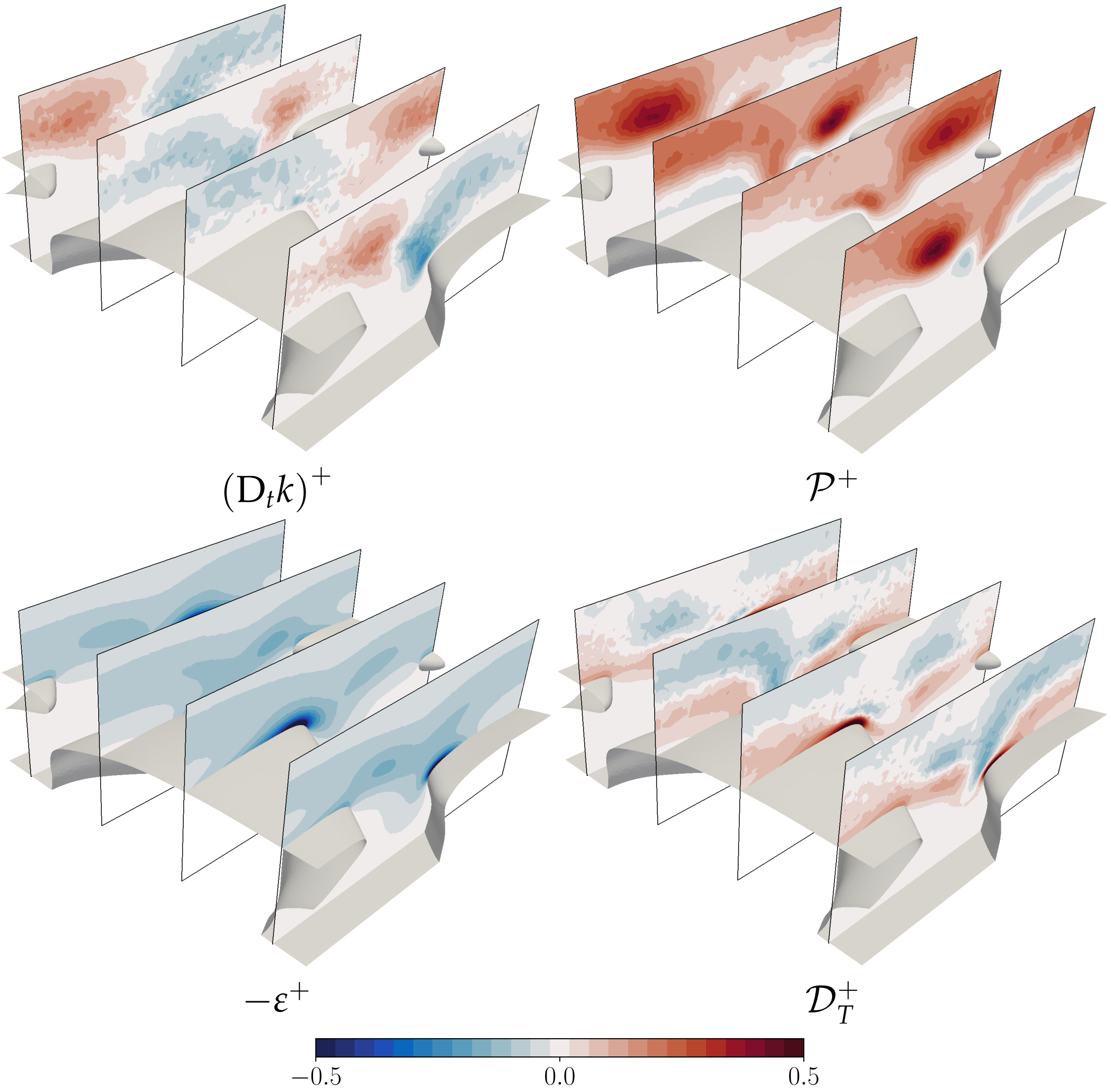

FIGURE 6.21: Budgets of the transport of k^+ at $w^+ \approx 67$ for the SMO denticle. Terms are as per equation (6.6). Flow direction is approximately from upper left to lower right for each model.

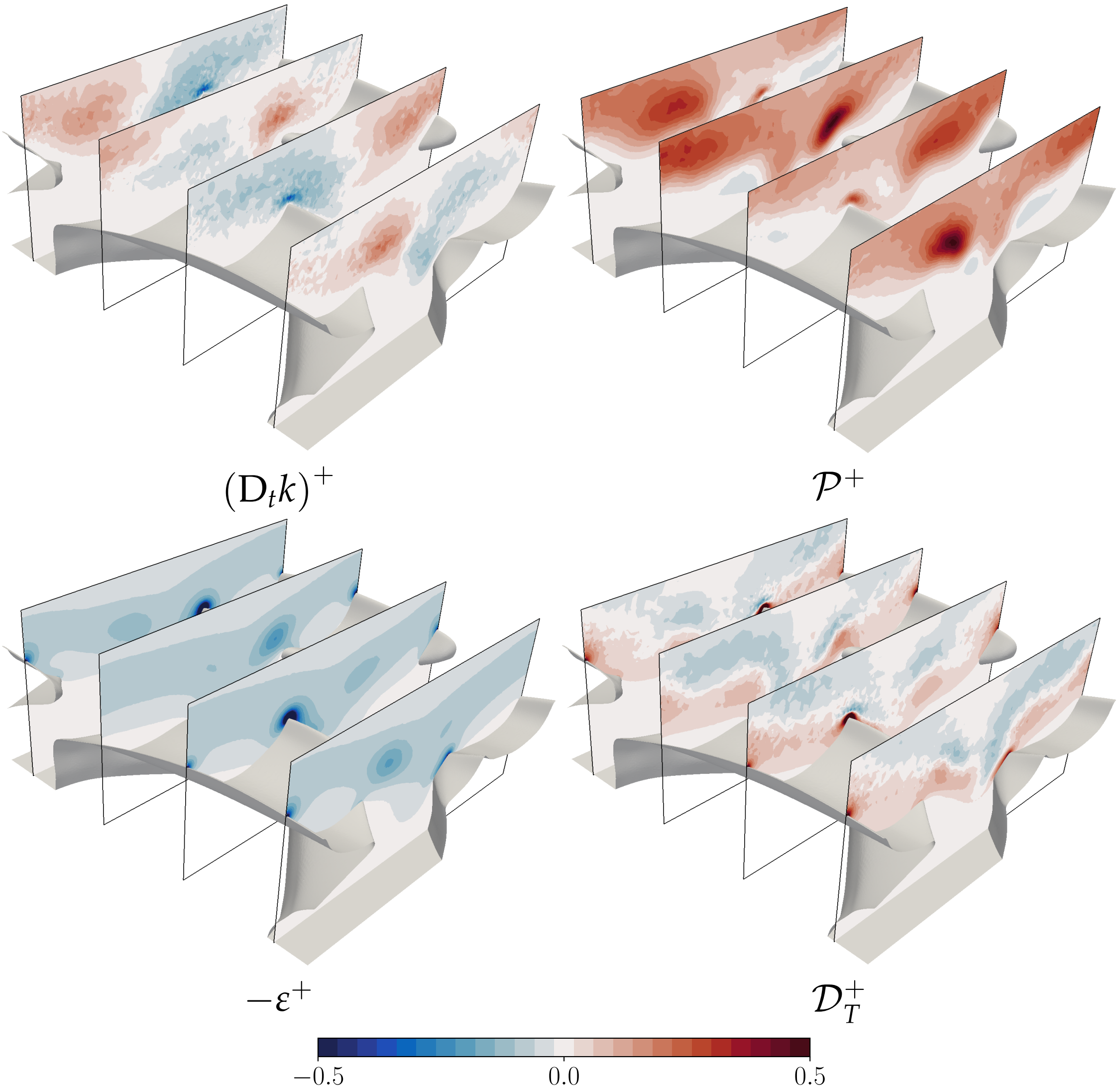

FIGURE 6.22: Budgets of the transport of k^+ at $w^+ \approx 67$ for the SMR denticle. Terms are as per equation (6.6). Flow direction is approximately from upper left to lower right for each model.

there is less turbulent kinetic energy transported to these regions. Positive convection and peaks in production appear similar for all three denticles, although the structure of these budgets is difficult to distinguish using 2D slices through the domains. Differences in the structure of production and convection of turbulent kinetic energy can be better identified through iso-contours of respective budgets, as per Figures 6.24 and 6.25. Here regions of particularly strong magnitudes of $\mathcal{P}^+$ and $(D_t k)^+$ are displayed, and highlighted using a transparency map. There is a large region of production downstream of the trailing edges of the denticles, although its precise form is different for each denticle model. The SMO denticle leads to the largest region of high magnitude production, with its maximum located downstream of the widest part of the denticle, and high magnitude

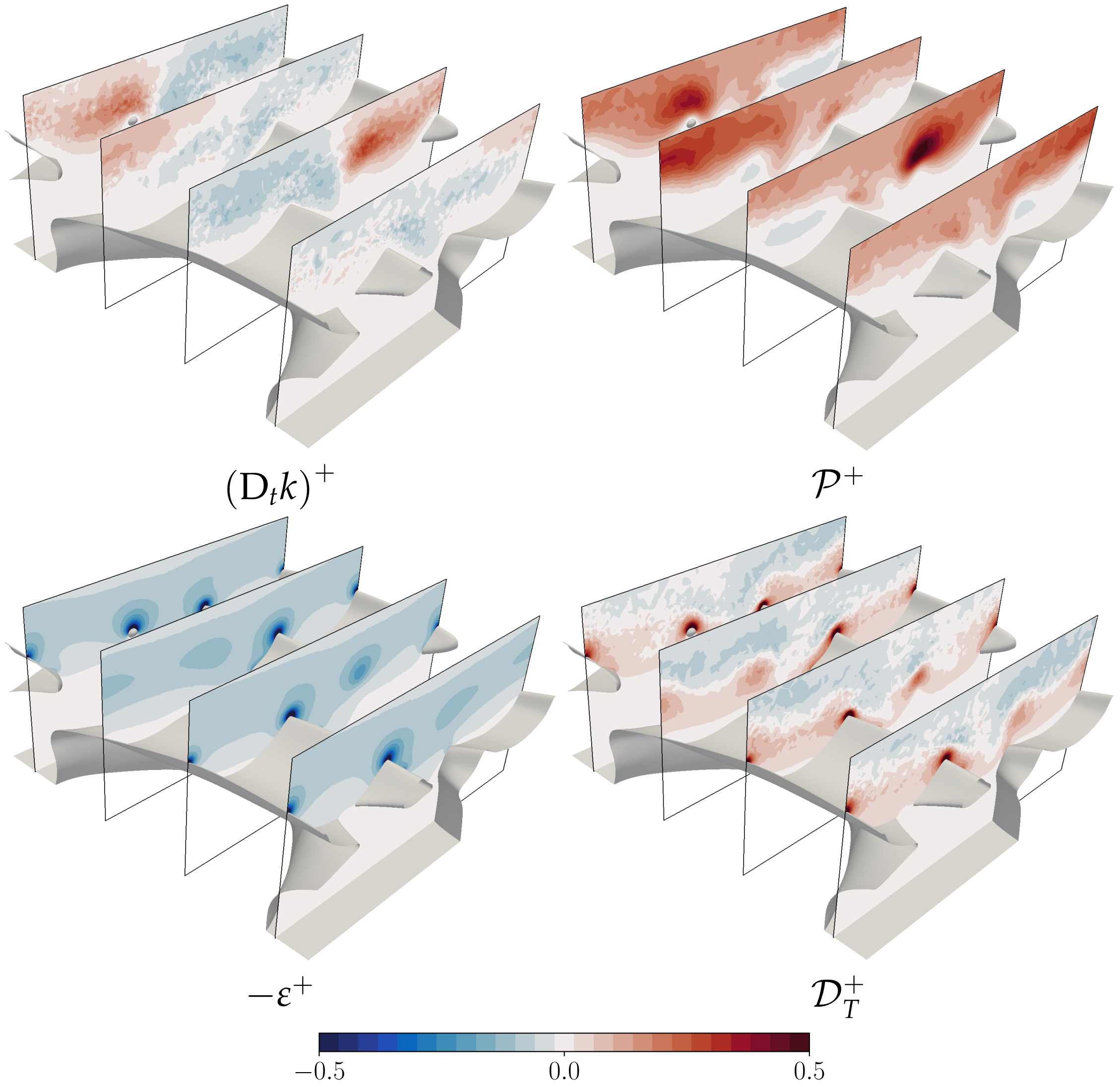

FIGURE 6.23: Budgets of the transport of k^+ at $w^+ \approx 67$ for the RIB denticle. Terms are as per equation (6.6). Flow direction is approximately from upper left to lower right for each model.

production spans the full length of the trailing edge. When moving from the widest region of the denticle to its centreline the production of TKE decreases in magnitude and spreads over a larger region. The SMR denticle leads to similar behaviour, although the structure of the high production region is somewhat broken down at the riblet valleys, and regions of high production are local to the riblet tips. The RIB denticle leads to a very different structure of k^+ production, where high magnitudes of $\mathcal{P}^+$ are local to the trailing edge of the riblet tips; little turbulence is produced at the edges of the denticle. Of the three denticle models only SMO leads to notable production at the outer-crown edge.

Regions of positive convection correspond to those of high turbulent production, consistent for all three denticles. Clearly the two budgets are strongly related; where $\mathcal{P}$ is

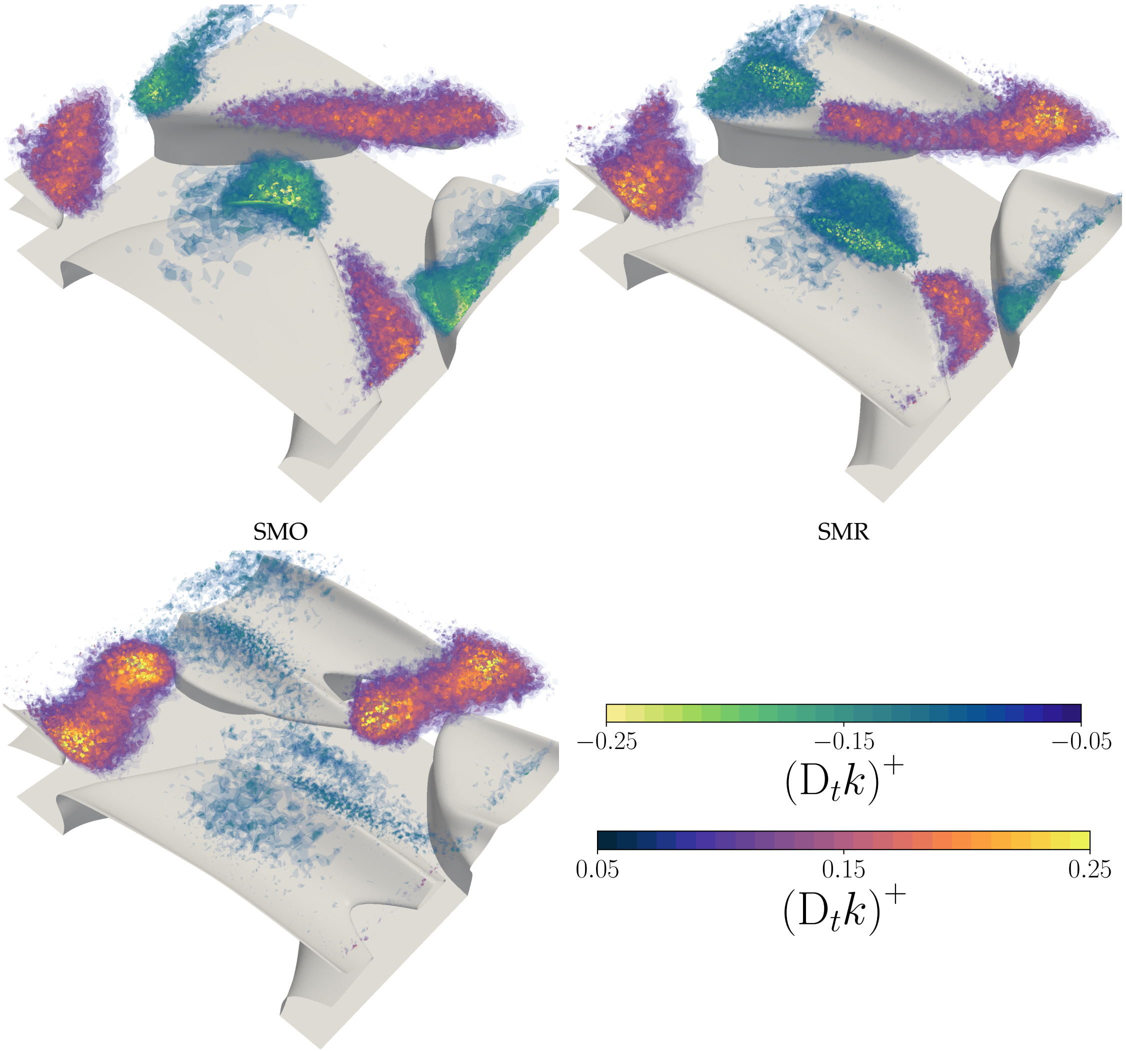

SMO

SMR

RIB

FIGURE 6.24: Local budgets of turbulent kinetic energy convection for the three denticle models, SMO, SMR, and RIB, at $w^+ \approx 67$. Positive and negative regions are identified through different colour maps, and a transparency map is adopted to highlight regions of strong convection. Flow direction is approximately from upper left to lower right for each model.

large, convection must act to transport turbulence to other regions where it can be dissipated/diffused. regions of negative convection are coherent for SMO and SMR denticles, and are located at the outer-region of the denticle crown for the SMO denticle, and the outer riblet for the SMR denticle. These regions are somewhat correlated to the regions of high local pressure coefficient (see Figure 6.12), which is perhaps unsurprising given that these are the regions of the denticle most exposed to impinging fluid. The RIB denticles lead to no regions of particularly strong negative convection, perhaps due to the restriction of swirling fluid (see Figure 6.19) and the shielding effect of the longer riblet structures.

There is certainly some correlation between the regions of strongly swirling fluid and

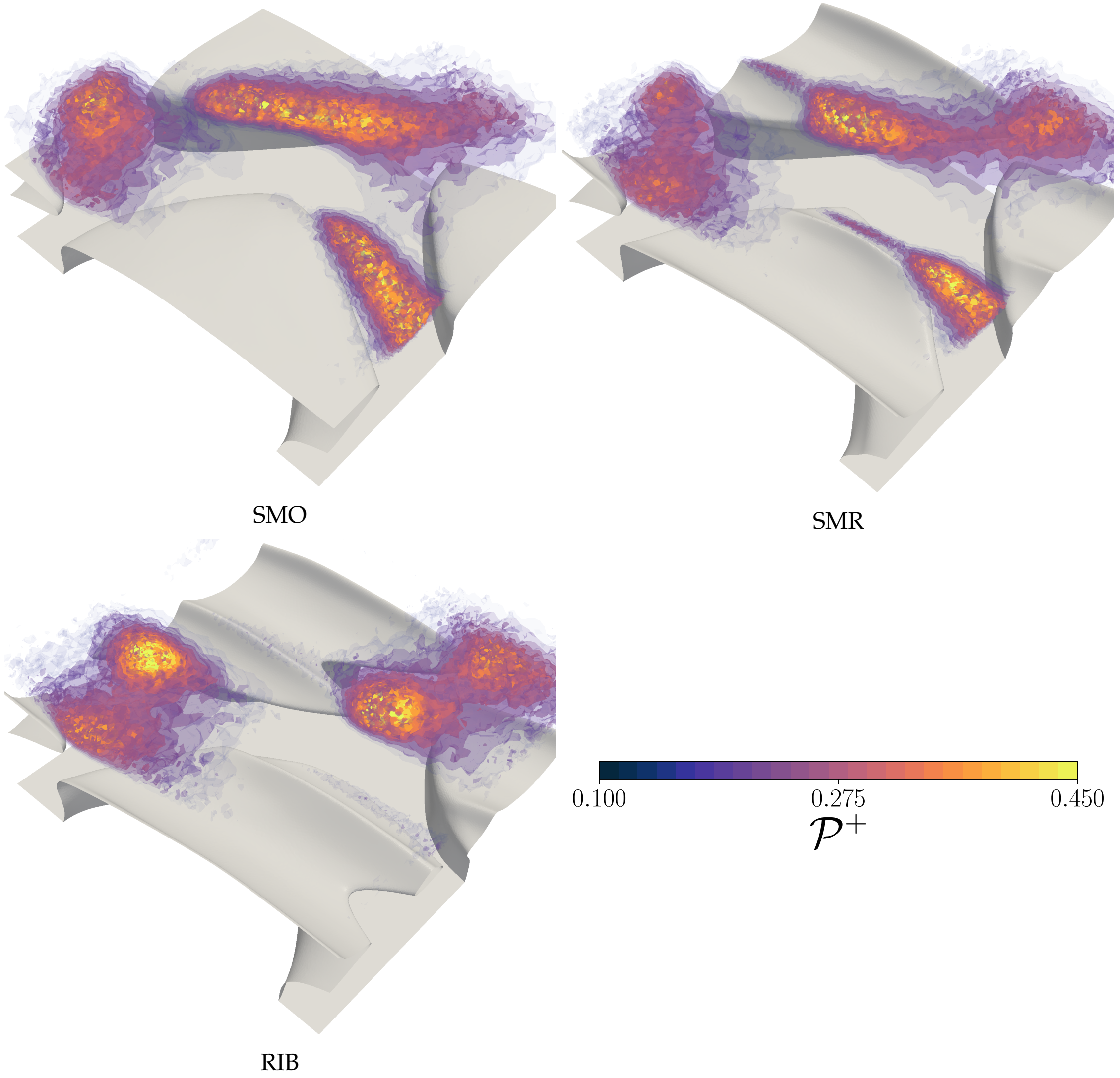

FIGURE 6.25: Local budgets of turbulent kinetic energy production for the three denticle models, SMO, SMR, and RIB, at $w^+ \approx 67$. A transparency map is adopted to highlight regions of strong production. Flow direction is approximately from upper left to lower right for each model.

the structure of turbulent kinetic energy production and convection, observed when comparing Figure 6.19 with Figures 6.24 and 6.25. The SMO denticles lead to large peaks in swirl strength at the widest part of the denticle, with swirl generated along the full trailing edge of the denticle crown. Turbulence production is at its highest just downstream of the widest part of the denticle crown, and is large for the full trailing edge of the denticle. SMR denticles lead to similar behaviour as SMO denticles, but regions of high $\mathcal{P}^+$ are more local to the region just downstream of the riblets, and lower downstream of the riblet valleys, as per the regions of high and low swirl strength. This suggests that by restricting the swirling motion of the fluid, riblets act to break up the region of high turbulence production at the trailing edge of the denticle. The RIB denticles lead to even smaller regions of turbulence production, just downstream of the riblet tips. These are precisely downstream of the regions of peak swirling, and little turbulence is produced at the outer edges of the denticle crown.

6.3 Discussion

For the first time, RANS predictions of the flow over smooth and ribletted denticles have been obtained with good agreement against experimental data. While the two-equation $k - \tau$ model, derived from the two-equation $k - \omega$ model of Wilcox (2006) in Chapter 4, obtained little difference between drag forces acting on smooth (SMO) and ribletted (RIB) denticles, the EB-SSG model of Manceau (2015) obtained good predictions of the two denticle models, particularly at larger w^+ values. However, EB-SSG does appear to overpredict the drag force acting on the ribletted denticles at low w^+, where a 2 % increase in C_f is obtained for the numerical solutions, compared to a 2 % decrease in C_f measured in the laboratory experiments (see Figure 6.5). Differences can be explained by considering differences in flow conditions; while the present RANS simulations are for a fully developed channel flow, the experiments were carried out on a developing boundary layer, on a 3D printed surface. When taking into account precision errors, the gap between data sets is reasonably small.

Clearly accounting for near-wall anisotropy is necessary for obtaining the key differences between smooth and ribletted denticles. This is unsurprising given the result of Chapter 5, where only the EB-SSG model was successful in predicting the drag reducing effects of longitudinal riblets, a significantly simpler roughness geometry. However, the general profile of the drag increase obtained for denticles is well predicted for the $k - \tau$ model; the magnitudes are reasonable when compared to experiments, where drag increases with increasing w^+. Perhaps then, the ability of the $k - \tau$ model breaks down when introducing the riblets, where only EB-SSG is able to model the flow correctly.

A key result gained from these simulations is that pressure-drag is vital to consider when investigating the flow over shark skin denticles. While longitudinal riblets are primarily associated with the reduction of viscous drag, here they operate in a different manner; rather than decreasing viscous drag they actually increase it, but greatly reduce pressure-drag relative to smooth denticles, especially at larger values of w^+. It seems then that the drag reduction observed when riblets were added to the smooth denticles in the experiments of Chapter 3 were primarily due to decreased pressure-drag. These results are consistent with typical $K-$type roughness theory, where at large roughness heights friction is dominated by pressure forces acting on roughness elements; these simulations and experiments suggest that a reduction of pressure forces by introducing riblets may lead to significant efficiency gains for a shark skin surface.

The increase in viscous friction coefficient is straightforward to explain. When riblets are introduced viscous forces (Figure 6.13) are large at the riblet tips, typical of longitudinal riblets when applied to flat plates. However, while longitudinal riblets see this increase in viscous forces at the tips compensated for by a significant viscous drag reduction in the riblet valleys, this is not the case when applied to the shark skin denticles modelled herein. The ribletted denticles lead to only slightly lower viscous drag between riblets when compared to the smooth denticle, which therefore leads to an overall increase to viscous drag. This may not be typical of all ribletted denticles; Bechert et al. (1997) have shown that small changes to the riblet geometry, such as tip-rounding, can have significant effects on drag reduction, but these results do reveal that the reduction of viscous drag is not always the only role of riblets.

The decrease of pressure-forces are explained by considering differences between the three denticle models: The smooth and ribletted denticles as per the experiments (SMO and RIB), and a ribletted denticle with shorter riblets (SMR). Distributions of local pressure coefficients (Figure 6.12) revealed peaks in pressure-drag at the exposed leading-edge of the SMO denticle, at the widest part of the crown. The SMO denticle led to a large high pressure-region, which slowly decreased towards the back of the denticle. The exposed denticle edge has a smaller peak in $c_{p,x}$ for SMR denticles, and smaller still for RIB denticles. Riblets lead to more localised peaks in $c_{p,x}$, particularly at the leading edge of the outer riblets. The longer riblets of the RIB denticle acts to partially shield the downstream denticle, therefore reducing the amount of fluid that can impinge on the exposed surface which therefore reduces pressure drag. However, shielding is not the only mechanism that leads to a reduced pressure drag, and cannot explain why the SMR denticle also leads to reduced pressure drag when compared to the SMO denticle.

Inspection of the mean streamwise velocity reveals a high momentum pathway (HMP), where relatively high speed fluid passes between denticles, and is responsible for sustaining a back-flow region and increased drag due to impinging fluid on the denticle base. This HMP is reduced in strength when riblets are added, particularly for the RIB denticle. In addition, streamlines reveal that flow impinging on denticle crowns originates from the HMP, beneath the denticles. Riblet tips act to protect the riblet valleys from relatively high momentum fluid, therefore reducing local pressure forces at the expense of increased pressure drag at the riblet tips. Furthermore, swirling flows are generated at the outer and trailing edges of the denticle. When riblets are present these swirling flows are broken up and the large region of high swirl strength is reduced and localised to the riblet tips. These appear different in form to the secondary flows investigated over longitudinal riblets in Chapter 5, and are instead driven by impinging flow at the outer edge of the denticle crown. Swirling flow is strongest at the widest part of the SMO denticle, and generates downward flow between denticles. This draws high momentum fluid downwards into the HMP and therefore increases the pressure forces at the exposed regions of the denticles. Riblets act to restrict the swirling flow, making it local to just the riblet tips and the trailing edges. Riblets act to help maintain streamwise-aligned flow, and therefore weaken the downward fluid velocities and the HMP. The longer riblets of the RIB denticle restrict the downward motion more-so than SMR due to the longer riblets.

Another role of riblets is identified by the RANS solutions, where their presence significantly alters the way turbulence is transported near the denticle surface. Turbulence enhances momentum transfer close to the wall and is therefore detrimental to drag. The SMO denticles lead to large regions of turbulence production at the denticles trailing edge. Production is so large here that convection is required to move turbulent kinetic energy away to regions it can be dissipated. SMO denticles also lead to regions of strong negative convection at the exposed region of the denticle, where turbulence is transported and must be balanced by diffusion and dissipation. These large regions of turbulence production appear strongly correlated to the swirling fluid, where the region of maximum production lies just downstream of the region of maximum swirl strength, at the widest part of the SMO denticle. When riblets are added to the denticle crown the region of large swirl strength is broken down and turbulence production becomes more local to the riblet tips. The RIB denticles lead to the smallest regions of swirl, and therefore turbulence production, and convection.

This work has identified several related roles of riblets by investigating differences between smooth and ribletted denticles. Riblets act to reduce swirling flow by restricting spanwise motion and maintaining streamwise-aligned flow near the denticle surface. By doing so riblets reduce the amount of flow that is drawn into the regions between denticles, leading to the HMP, and also reduce the strong velocity gradients associated with swirling that can lead to turbulence production. Both these effects contribute to the reduced pressure drag near the wall by minimising momentum transfer. These effects, in combination with the shielding of downstream denticles and the protection of riblet valleys from high momentum fluid, lead to the reduced drag of the ribletted denticles, relative to the smooth denticles, in the experiments of Chapter 3.

The numerical and experimental results both lead to common conclusions regarding the role of riblets in combination with shark skin denticles. Smooth denticles appear to increase flat plate skin friction, consistent with $K-$type roughness theory. However, when riblets are added to the crown drag is reduced relative to the smooth denticle, more-so at large w^+. The RANS solutions identify several mechanisms that lead to this behaviour; riblets restrict swirling motion above the denticle crown, reduce the regions of high turbulence production, and longer riblets act to protect the roughness sub-layer from high speed fluid. These results suggest that the primary function of shark skin denticles is not for flat plate drag reduction, given that present data shows that smooth denticles consistently increase drag. The experimental data of Chapter 3 do show that ribletted denticles may reduce drag relative to flat plates, but this drag reduction is marginal, especially when compared to longitudinal ribletted plates. Perhaps then the primary role of denticles is for defence against parasites, prevention of abrasion, or anti-fouling, while riblets act to minimise hydrodynamic costs. However, there could also be other hydrodynamic benefits to denticles; the flow over a shark consists of regions of favourable and unfavourable pressure gradients, flow separation, and developing boundary layers. Denticles may have evolved to the benefit of these flow conditions; for example, present data have shown that denticles lead to peaks in turbulence production at their trailing edges, which could help maintain flow attachment and help boundary layer transition. The riblets may therefore act to reduce the adverse effects of denticles, by helping maintain streamwise-aligned flow, reducing turbulence production, and reducing swirl. Present data suggests that this is primarily achieved through a reduction of pressure-drag, but it seems plausible that riblets could also act to reduce viscous drag, if the tip shapes were better optimised. This work has demonstrated that riblets in combination with denticles do not act as they do when applied to smooth walls, and can be responsible for significant performance gains through effects that lead to reductions in pressure drag. This work therefore leads to two key areas that require further research; firstly the extension of analysis to other denticle geometries, and secondly an extension to more complex flow conditions, such as adverse and favourable pressure gradients.

6.4 Conclusions

For the first time predictions of boundary layer flows over smooth and ribletted shark scales have been obtained using RANS closures, with solutions in good agreement with experimental data. While the two equation eddy-viscosity $k-\tau$ model is unable to capture the large performance differences between smooth and ribletted denticles, the EB-SSG Reynolds stress model of Manceau (2015) obtains good predictions of drag. Like the experimental results of Chapter 3, smooth denticles are found to increase drag substantially when compared to a flat plate. When riblets are added performance is improved, although they do not lead to overall reduction in drag when compared to a flat plate.

Pressure drag is found to be vital to consider, especially when considering the effects of riblets on the rough-wall flow. While longitudinal riblets are typically associated with a reduction of viscous drag, when applied to denticles the RANS predictions indicate an increased viscous drag. The ribletted denticles lead to a large increase in viscous stress at the riblet tips, without a significant decrease of viscous stresses in the riblet valleys. Performance gains for ribletted denticles are found to be associated with a reduction of pressure drag. While results may not be indicative of all riblet geometries, they do show that the role of riblets is not limited to just a reduction of viscous forces.

The reduced pressure drag associated with riblets is found to be due to two mechanisms: Firstly, riblets act to protect the denticle crowns from high momentum fluid, and secondly, riblets help maintain streamwise-aligned flow near the rough surface. Without riblets the flow over denticles is found to impinge strongly on the exposed outer-edge of the denticle crown, and leads to high magnitudes of swirling over much of the denticle surface, and regions of enhanced production of turbulent kinetic energy at the trailing edge. This swirling leads to regions of strong downward vertical velocities which draws high momentum fluid from above the denticles to the regions between them. Riblets are found to reduce swirling substantially, leading to reduced flow velocities between denticles and smaller regions of high TKE production.

These results lead to new insight into the hydrodynamic functions of shark scales. Flat plate drag reduction does not appear to be a priority for shark scales, given that smooth scales substantially increase it, suggesting that denticles may have evolved to help defend against parasites, prevent abrasion, and for their anti-fouling properties. There could however be other hydrodynamic functions, given that the flow over a shark will also consist of regions of adverse and favourable pressure gradients, flow separation, and developing boundary layers. Riblets may therefore act to reduce the adverse effects of denticles by helping maintain streamwise-aligned flow near the rough surfaces, and helping shield exposed regions of the downstream denticles, thus minimising the hydrodynamic cost of providing other benefits of scales.

There is still much variability in shark scale geometry that has not been considered in this study, such as denticle spacings and aspect ratios. These will of course have a large effect on denticle performance. Two key areas for future research are therefore identified; extension of RANS models to more denticle geometries, and extension to more complex flow conditions such as flow separation.

Chapter 7

Conclusions and outlook

The influence of shark scales and riblets on the turbulent boundary layer has been investigated throughout this thesis using both experimental and numerical techniques. This study is motivated by potential biomimetic applications, where an understanding of the influence of shark scales on the boundary layer could prove invaluable for the design of engineering structures subject to high fluid drag. Through a review of the literature regarding hydrodynamic studies on shark scales several knowledge gaps were identified, arising from a poor understanding of the influence of denticle geometry on the turbulent boundary layer, and a lack of flow field data. The combination of these issues led to a large spread in results with some authors claiming denticles are detrimental to skin friction and others stating that they can be highly efficient. The lack of studies regarding denticle geometry motivated the use of RANS models which are able to carry out large parameter studies, and an experimental study adopting LDA to measure turbulent boundary layers over arrays of two different types of shark skin denticles. However, RANS models require significant validation, especially given that RANS predictions of flows over simpler geometries such as riblets can often lead to non-physical solutions. The validation of RANS models motivated two additional chapters, focused on the behaviour of RANS models near solid boundaries, and obtaining accurate predictions of the flow over riblets. These two studies led to a significant understanding of different RANS formulations regarding near-wall corrections and numerical stability, and how secondary flows at the tips of riblets are generated and sustained, and how they scale with riblet dimensions.

7.1 Experiments on shark skin denticles

Chapter 3 investigated the influence of denticles on a turbulent boundary layer flow using 2D LDA. Turbulent statistics were measured above 3D printed arrays of smooth and riblетted denticles of widths covering the typical drag reducing regime of longitudinal riblets. The study was carried out in order to investigate the role of riblets in combination with denticles. Smooth denticles were found to behave like a typical $K-$type rough surface; drag was greater than that of the flat plate, and increased with denticle size. This was also realised through the mean velocity and Reynolds stress profiles, where the mean streamwise velocity profile was offset downwards from the reference flat plate, indicative of increased skin friction. When riblets were added to the denticle drag was reduced for all denticle widths compared to the smooth denticles, but only a 2 % reduction in drag was obtained when compared to a reference flat plate, with a transition to increased drag at an inner-scaled denticle width of $w^+ \approx 40$. However, differences between the two denticle plates grew with increasing w^+, reaching a 20 % difference in friction coefficient C_f at $w^+ \approx 80$. Not only is this difference larger than that obtained for longitudinal riblets relative to a flat plate, but the efficiency increased over the present range of denticle widths, rather than decreased as per longitudinal riblets. As a result the ribletted denticles had a significantly lower impact on the turbulent boundary layer than smooth denticles.

These results suggest that the three-dimensionality of denticles is detrimental to flat plate skin friction drag, given that smooth unribletted denticles increased drag substantially relative to a smooth plate. Denticles may have therefore evolved for non-hydrodynamic functions such as anti-fouling and abrasion resistance, or for their effects on other flows such as adverse/favourable pressure gradients. However, when riblets are present on the denticle crown drag is reduced substantially, suggesting that they have evolved as a mechanism to reduce the adverse effects of denticles and lead to an overall hydrodynamically efficient surface.

7.2 Numerical errors at the wall

Chapter 4 investigated the near-wall behaviour of RANS models, assessing their limiting behaviour close to the boundary, and their sensitivity to the near-wall cell size. In particular, RANS models were assessed based on their scale determining variable, typically the rate of turbulent dissipation, ε, or the specific rate of turbulent dissipation, ω. The study was motivated by the recent work of Eça, Pereira, and Vaz (2018), who showed that numerical errors in excess of 5 % could be obtained for the friction coefficient when using the $k - \omega$ SST model with near-wall cell sizes of $y_1^+ \approx 1$, a typical 'rule of thumb' common in the CFD industry. If this model were to be used for the prediction of flows over riblets or shark skin denticles an error of 5 % would significantly pollute solutions, given that drag reduction is typically of the same magnitude as this discretisation error.

Chapter 4 therefore extends previous work by investigating nine eddy-viscosity turbulence models/near-wall treatments, and two Reynolds stress models. An extensive analytical study is carried out determining model boundedness, consistency with asymptotic near-wall solutions, and examining alternatives to the popular ω based turbulence models. Channel flow simulations are presented adopting 5 sets of 6 geometrically similar grids with a y_1^+ range of approximately 2.5×10^{-4} to 1. Results show that friction velocities and coefficients are extremely sensitive to the near-wall cell size. Most models attain a discretisation error for the friction velocity of approximately 1 % when adopting the 'rule of thumb' $y_1^+ \lesssim 1$. However, the $k-\omega$ model leads to errors of approximately 5 %, which is made worse when adopting 'slightly-rough' wall boundary conditions. A cell size of $y_1^+ \approx 0.1$ is required to obtain errors of 1 %, due to its sub-linear rate of convergence. In contrast, the mathematically equivalent models $k-g$, $k-\omega'$, and $k-\tau$, lead to errors of less than 1 % at $y_1^+ \approx 1$, reducing to less than 0.1 % for $y_1^+ \lesssim 0.3$. Differences are due to the near-wall behaviour; ω is singular at the wall while the variables τ, g, and ω' are zero. These alternative formulations retain the excellent boundary layer predictions of the $k-\omega$ model but without introducing large discretisation errors at the wall associated with the singularity. There are two advantages of the $k-\tau$ formulation over $k-\omega'$ and $k-g$; the equations are fully bounded at the wall, and there is no dependence on the wall-normal distance. For these reasons, the original $k-\tau$ model is extended to include updated coefficients, a cross-diffusion term, and Low Reynolds number corrections. The $k-\tau$ closure has also been extended to a Reynolds Stress Model (RSM) by reformulation of the Stress-ω model of Wilcox (2006). This is a simple RSM with identical underlying transport equations as the two-equation $k-\tau$ model, which unsurprisingly leads to near identical friction velocity errors. For comparisons a further RSM was investigated, the EB-SSG model of Manceau (2015). Unlike the simple Stress-τ model, the EB-SSG accounts for near-wall anisotropy through an additional elliptic transport equation for a blending parameter. y_1^+ dependency for EB-SSG is similar to the $\overline{v^2}-f$, obtaining friction velocity errors of less than 1 % for $y_1^+ < 1$.

These new τ-based formulations offer a promising alternative to the popular ω models and could provide excellent boundary layer predictions at a feasible value of y_1^+. However, the numerical improvements of the τ formulation close to the wall do not guarantee globally better performance than ω models, and so future work should focus on the validation of this model in freestream and strongly separating flows.

7.3 The scaling of secondary flows over longitudinal riblets

Chapter 5 investigated the flow over streamwise-aligned parallel sawtooth riblets using RANS models, in order to determine the mechanisms driving and sustaining secondary flow at the riblet tips, and how vorticity scales with the riblet dimensions. Simulations adopted three turbulence models of varying complexity: The $k-\tau$ model, the Stress-τ model, and the EB-SSG model. Friction coefficient predictions showed that only the EB-SSG model can obtain good agreement with experiments and DNS. $k-\tau$ and Stress-τ led to poor predictions of the viscous regime, where the friction coefficient should tend to the reference flat plate solution as the riblet size decreases. In addition, there were large discrepancies between the secondary flow predictions of the two τ based models and the DNS of Choi, Moin, and Kim (1993), while the EB-SSG model correctly predicted the size and magnitude of the vorticity field. Subsequently the EB-SSG model was adopted for further analysis of the secondary flow.

Results show that anisotropy of the Reynolds stresses is responsible for vorticity production, consistent with the second type of secondary flow (Prandtl, 1953). While anisotropy is inherent in the boundary layer even for flat plates, riblets perturb the flow leading to the inhomogeneities required for vorticity production. Two regimes have been identified which govern how vorticity produced by anisotropy is conserved: A viscous regime for small s^+ where vorticity production is balanced by viscous diffusion, and an inertial regime for large s^+ where vorticity production is balanced by an effective turbulent viscosity determined by the Reynolds shear stress $\overline{v'w'}$. The viscous regime leads to a linear dependence of vorticity on the riblet size s^+, while vorticity decreases with s^+ in the inertial regime. The transition between the two regimes occurs at $s^+ \approx 30$, where riblet tips protrude into the buffer layer and cause increased turbulent mixing.

Analytical solutions obtained a linear dependence of streamwise vorticity on the riblet height, h^+, in agreement with numerical solutions. This linear scaling arises as a condition that vorticity must vanish as h^+ decreases in order to obtain the flat plate boundary layer solution for vanishingly small roughness. In the inertial regime analytical solutions obtained a scaling such that streamwise vorticity should scale like $1/h^+$. While this limit is not reached for the numerical simulations there is evidence that this regime should occur if Reynolds numbers were increased and larger riblets could be simulated.

The relationship between the vorticity field and the friction coefficient is difficult to establish. While there is evidence that the two quantities are related, present solutions show that the viscous and inertial regimes of the two variables are not entirely correlated, although this may be due to the limited Reynolds numbers and therefore influence of the blockage ratio δ/h. However, large-scale roughness of a similar form to riblets can lead to significant distortion of the mean flow (e.g. Hwang and Lee, 2018) and subsequently has a large influence on drag. It therefore seems reasonable that there must be some relationship between the secondary flow and the friction coefficient. Further work should therefore be carried out in order to bridge the gap in length scales between the riblet type roughness herein, and the large scale heterogeneous roughness of Hwang and Lee (2018).

7.4 Boundary layer flow over shark skin denticles

RANS predictions of the flow over shark skin denticles are presented in Chapter 6, where a parameter study on the influence of riblet geometry and denticle size on hydrodynamics is carried out, validated against the experimental data of Chapter 3. For the first time RANS predictions of boundary layer flows over smooth and ribletted shark scales have been obtained in good agreement with experiments, leading to the identification of several new mechanisms responsible for drag reduction when riblets are present. Simulations of the flow over three denticle models are presented; a smooth unribletted denticle (SMO), a denticle with short riblets (SMR), and a denticle with long riblets (RIB). While denticle plates appear to increase drag relative to smooth plates, ribletted denticles significantly reduce drag when compared to smooth denticles due to a reduced pressure drag acting on roughness elements. Pressure drag becomes important for these rough surfaces as w^+ grows, and is primarily due to a high momentum pathway that passes between denticles and impinges on the edges of the denticle crowns. Swirling flow is found to draw high momentum fluid from above the denticles to the regions between them, which is subsequently ejected back into the boundary layer after impinging on the downstream denticle.

When riblets are added performance is improved, although they do not lead to overall reduced drag when compared to a flat plate. Unlike longitudinal riblets viscous drag is found to increase when riblets are added to the denticle. The ribletted denticles lead to a large increase in viscous stress at the riblet tips, without a significant decrease of viscous stresses in the riblet valleys. The performance improvements of riblets is associated with a reduction in pressure drag, which is realised through several mechanisms. Firstly, the long riblets of the RIB denticle lead to a better shielding of the downstream denticle, and therefore partially block high momentum fluid from passing beneath the denticle crowns. However, this mechanism does not explain why the SMR denticle also reduces pressure drag, given that its platform area is so similar to the SMO denticle. It is found that riblet tips also act to protect the riblet valleys from high momentum impinging fluid, at the expense of increased pressure at the riblet tips. Further reductions of pressure drag occur due to the ability of riblets to maintain streamwise-aligned flow in their vicinity. This is realised through analysis of swirl strength, where the SMO denticles lead to large patches of high magnitude swirl at the outer-trailing edge of the denticle crown. This swirling leads to regions of strong downward vertical velocities which draw high momentum fluid from above the denticles to the regions between them. Riblets are found to reduce swirling substantially, leading to reduced flow velocities between denticles and smaller regions of high TKE production, ultimately reducing momentum transfer and therefore drag.

These results lead to new insights regarding the hydrodynamic functions of shark scales. The drag relative to flat plates does not appear to be a priority for shark scales, given that smooth denticles substantially increases drag relative to a flat plate. The experimental data of Chapter 3 do show that ribletted denticles may reduce drag relative to flat plates, but this drag reduction is marginal, especially when compared to longitudinal ribletted plates. Small changes to riblet geometry could reduce drag further, but it seems unlikely that drag would be reduced below that of the longitudinal riblets. Perhaps then the primary role of denticles is for defence against parasites, prevention of abrasion, or anti-fouling. There could of course be other hydrodynamic benefits to denticles; the flow over a shark consists of regions of favourable and unfavourable pressure gradients, flow separation, and developing boundary layers. The primary function of denticles may be to improve hydrodynamics of these flow conditions, while riblets have evolved to reduce the adverse effects of denticles by helping maintain streamwise-aligned flow, reducing turbulence production, and reducing swirl.

7.5 Further work

There are many opportunities for further work regarding each of the objectives stated in Chapter 1. Chapter 4 identified a family of turbulence models that tackle the closure problem at the wall by reformulating the $k-\omega$ transport equations. Channel flow results showed that numerical errors were significantly reduced when adopting these models with no sacrifice to model performance, due to their mathematical equivalence to the popular $k-\omega$ model. However, the flows presented in this thesis are free from issues such as sensitivity to freestream boundary conditions, and adverse pressure gradients that lead to large scale flow separation. It is unclear how the models identified herein will behave when extended to these more complex flow conditions, which should certainly be tested in future work.

Chapter 5 investigated the scaling of the secondary flow above riblets, identifying driving mechanisms and the dependency of vorticity on the riblet size. The driving mechanisms were found to be similar to those identified by Hwang and Lee (2018) who investigated the flow over large scale spanwise-heterogeneous roughness, which differs from riblets only by their length scales and spacings. An interesting study would bridge the gap in length scales between these two different rough surfaces. This would also help identify the influence of the secondary flow on the mean flow.

A large area of further work could be the extension of analysis to more denticle models in order to investigate the influence of denticle spacings and other geometric properties. This is applicable to both the experiments in Chapter 3 and the RANS simulations of Chapter 6. Present results have shown that riblets can act to reduce pressure drag when applied to denticles, but the underlying denticle geometries have been changed little. RANS models present an opportunity to carry out a parameter study at fairly little expense, such that other geometries could be investigated.

However, perhaps the largest conclusion from the present work is that shark scales do not appear beneficial to hydrodynamics when subject to flat plates and channel flows; the key hydrodynamic benefits have been observed when riblets have been added, which have been hypothesised to counter the adverse effects of having the denticle type roughness. While further investigations on denticle geometry subject to flat plate boundary layers would be insightful, perhaps shark scales have evolved to the benefit of more complex flow conditions, such as adverse pressure gradients. There is evidence for this, as identified through the literature review of Chapter 2, although modelling such flows is not straight forward; the small periodic domain adopted herein is unlikely to be applicable, and due to the large differences in length scales between the separating flow over a shark and the small denticles computational domains would be vast. However, experimental and numerical studies of such flows would be beneficial to the field, especially given the prevalence of boundary layer separation in engineering flows.

References

Alfredsson, P. H. and R. Örlü (2010). “The diagnostic plot — a litmus test for wall bounded turbulence data”. In: *European Journal of Mechanics- B/Fluids* 29.6, pp. 403–406.

Anderson, W., J. M. Barros, K. T. Christensen, and A. Awasthi (2015). “Numerical and experimental study of mechanisms responsible for turbulent secondary flows in boundary layer flows over spanwise heterogeneous roughness”. In: *Journal of Fluid Mechanics* 768, pp. 316–347.

ANSYS FLUENT 19.2 (2019). *User's and theory guide*. ANSYS, Inc., Canonsburg, Pennsylvania, USA.

ANSYS ICEM 19.2 (2019). *User's and theory guide*. ANSYS, Inc., Canonsburg, Pennsylvania, USA.

Barros, J. M. and K. T. Christensen (2014). “Observations of turbulent secondary flows in a rough-wall boundary layer”. In: *Journal of Fluid Mechanics* 748, R1.

Bechert, D., G Hoppe, and W.-E. Reif (1985). “On the drag reduction of the shark skin”. In: *1985 AIAA Shear Flow Control Conference, Boulder, CO,* paper no. AIAA–85–0564.

Bechert, D., M Bruse, W Hage, J. T. Van der Hoeven, and G Hoppe (1997). “Experiments on drag-reducing surfaces and their optimization with an adjustable geometry”. In: *Journal of Fluid Mechanics* 338, pp. 59–87.

Bechert, D., M Bruse, W Hage, and R Meyer (2000). “Fluid mechanics of biological surfaces and their technological application”. In: *Naturwissenschaften* 87.4, pp. 157–171.

Benhalilou, M. and N. Kasagi (1999). “Numerical prediction of heat and momentum transfer over micro-grooved surface with a nonlinear k–ε model”. In: *International Journal of Heat and Mass Transfer* 42.14, pp. 2525–2541.

Bixler, G. D. and B. Bhushan (2013). “Fluid drag reduction with shark-skin riblet inspired microstructured surfaces”. In: *Advanced Functional Materials* 23.36, pp. 4507–4528.

Blender (2017). *Blender v2.78c - a 3D modelling and rendering package*. Blender Foundation. Blender Institute, Amsterdam. URL: `http://www.blender.org`.

Boomsma, A and F Sotiropoulos (2016). “Direct numerical simulation of sharkskin denticles in turbulent channel flow”. In: *Physics of Fluids* 28.3, p. 035106.

Brazeau, M. D. (2009). “The braincase and jaws of a Devonian ‘acanthodian’and modern gnathostome origins”. In: *Nature* 457.7227, p. 305.

Budker, P. (1971). *The Life of Sharks*. Columbia University Press.

Castillo, L. and D. J. Walker (2002). “Effect of upstream conditions on the outer flow of turbulent boundary layers”. In: *AIAA Journal* 40.7, pp. 1292–1299.

Chauhan, K., H. Nagib, and P. Monkewitz (2007). "On the composite logarithmic profile in zero pressure gradient turbulent boundary layers". In: *45th AIAA Aerospace Sciences Meeting and Exhibit*, p. 532.

Chen, H., X. Zhang, L. Ma, D. Che, D. Zhang, and T. Sudarshan (2014). "Investigation on large-area fabrication of vivid shark skin with superior surface functions". In: *Applied Surface Science* 316, pp. 124–131.

Cheng, H. and I. P. Castro (2002). "Near wall flow over urban-like roughness". In: *Boundary-Layer Meteorology* 104.2, pp. 229–259.

Chien, K.-Y. (1982). "Predictions of channel and boundary-layer flows with a low-Reynolds-number turbulence model". In: *AIAA Journal* 20.1, pp. 33–38.

Choi, H., P. Moin, and J. Kim (1993). "Direct numerical simulation of turbulent flow over riblets". In: *Journal of Fluid Mechanics* 255, pp. 503–539.

Chu, D. C. and G. E. Karniadakis (1993). "A direct numerical simulation of laminar and turbulent flow over riblet-mounted surfaces". In: *Journal of Fluid Mechanics* 250, pp. 1–42.

Cimarelli, A, A Leonforte, E De Angelis, A Crivellini, and D Angeli (2019). "On negative turbulence production phenomena in the shear layer of separating and reattaching flows". In: *Physics Letters A* 383.10, pp. 1019–1026.

Clauser, F. H. (1956). "The turbulent boundary layer". In: *Advances in Applied Mechanics* 4, pp. 1–51.

Coles, D. (1956). "The law of the wake in the turbulent boundary layer". In: *Journal of Fluid Mechanics* 1.2, pp. 191–226.

Davidson, L, P. V. Nielsen, and A. Sveningsson (2003). "Modifications of the $\overline{v^2} - f$ model for computing the flow in a 3D wall jet". In: *Turbulence Heat and Mass Transfer* 4, pp. 577–584.

Dean, B. and B. Bhushan (2010). "Shark-skin surfaces for fluid-drag reduction in turbulent flow: a review". In: *Philosophical Transactions of the Royal Society of London A: Mathematical, Physical and Engineering Sciences* 368.1929, pp. 4775–4806.

Díez, G, M Soto, and J. Blanco (2015). "Biological characterization of the skin of shortfin mako shark Isurus oxyrinchus and preliminary study of the hydrodynamic behaviour through computational fluid dynamics". In: *Journal of Fish Biology* 87.1, pp. 123–137.

Djenidi, L and R. Antonia (1993). "Riblet flow calculation with a low Reynolds number $k - \varepsilon$ model". In: *Further Developments in Turbulence Management*. Springer, pp. 267–282.

Djenidi, L and R. Antonia (1995). "Riblet modelling using a second-moment closure". In: *Applied Scientific Research* 54.4, pp. 249–266.

Domel, A. G., G. Domel, J. C. Weaver, M. Saadat, K. Bertoldi, and G. V. Lauder (2018). "Hydrodynamic properties of biomimetic shark skin: Effect of denticle size and swimming speed". In: *Bioinspiration & Biomimetics* 13.5, p. 056014.

Durbin, P. A. (1991). "Near-wall turbulence closure modeling without 'damping functions'". In: *Theoretical and Computational Fluid Dynamics* 3.1, pp. 1–13.

Eça, L and M Hoekstra (2004). "On the grid sensitivity of the wall boundary condition of the $k - \omega$ turbulence model". In: *Journal of Fluids Engineering* 126.6, pp. 900–910.

Eça, L, F. Pereira, and G Vaz (2018). "Viscous flow simulations at high Reynolds numbers without wall functions: Is $y^+ \approx 1$ enough for the near-wall cells?" In: *Computers & Fluids* 170, pp. 157–175.

Eça, L. and M. Hoekstra (2014). "A procedure for the estimation of the numerical uncertainty of CFD calculations based on grid refinement studies". In: *Journal of Computational Physics* 262, pp. 104–130.

Eilers, P. H. (2003). "A perfect smoother". In: *Analytical Chemistry* 75.14, pp. 3631–3636.

Feld, K., A. N. Kolborg, C. M. Nyborg, M. Salewski, J. F. Steffensen, and K. Berg-Sørensen (2019). "Dermal denticles of three slowly swimming shark species: Microscopy and flow visualization". In: *Biomimetics* 4.2, p. 38.

Fischer, M. C. and R. L. Ash (1974). "A general review of concepts for reducing skin friction, including recommendations for future studies". In: *NASA Tech. Memo* X-2894.

Flack, K. A., M. P. Schultz, and T. A. Shapiro (2005). "Experimental support for Townsend's Reynolds number similarity hypothesis on rough walls". In: *Physics of Fluids* 17.3, p. 035102.

Fletcher, T., J. Altringham, J. Peakall, P. Wignall, and R. Dorrell (2014). "Hydrodynamics of fossil fishes". In: *Proc. R. Soc. B*. Vol. 281. 1788, p. 20140703.

Fletcher, T. M. (2015). "The Evolution of Speed: an empirical and comparative analysis of drag-reducing scales in early fishes". PhD thesis. University of Leeds.

Gao, F. and L. Han (2012). "Implementing the Nelder-Mead simplex algorithm with adaptive parameters". In: *Computational Optimization and Applications* 51.1, pp. 259–277.

García-Mayoral, R. and J. Jiménez (2011a). "Drag reduction by riblets". In: *Philosophical Transactions of the Royal Society of London A: Mathematical, Physical and Engineering Sciences* 369.1940, pp. 1412–1427.

García-Mayoral, R. and J. Jiménez (2011b). "Hydrodynamic stability and breakdown of the viscous regime over riblets". In: *Journal of Fluid Mechanics* 678, pp. 317–347.

García-Mayoral, R. and J. Jiménez (2012). "Scaling of turbulent structures in riblet channels up to $Re_\tau = 550$". In: *Physics of Fluids* 24.10, p. 105101.

Goldstein, D. B. and T.-C. Tuan (1998). "Secondary flow induced by riblets". In: *Journal of Fluid Mechanics* 363, pp. 115–151.

Hanjalić, K (1994). "Advanced turbulence closure models: a view of current status and future prospects". In: *International Journal of Heat and Fluid Flow* 15.3, pp. 178–203.

Hanjalić, K, M Popovac, and M Hadžiabdić (2004). "A robust near-wall elliptic-relaxation eddy-viscosity turbulence model for CFD". In: *International Journal of Heat and Fluid Flow* 25.6, pp. 1047–1051.

Hou, Y., V. S. Somandepalli, and M. Mungal (2006). "A technique to determine total shear stress and polymer stress profiles in drag reduced boundary layer flows". In: *Experiments in Fluids* 40.4, pp. 589–600.

Huser, A. and S. Biringen (1993). "Direct numerical simulation of turbulent flow in a square duct". In: *Journal of Fluid Mechanics* 257, pp. 65–95.

Hwang, H. G. and J. H. Lee (2018). "Secondary flows in turbulent boundary layers over longitudinal surface roughness". In: *Physical Review Fluids* 3.1, p. 014608.

Jackson, P. (1981). "On the displacement height in the logarithmic velocity profile". In: *Journal of Fluid Mechanics* 111, pp. 15–25.

Jakirlić, S and K Hanjalić (2002). "A new approach to modelling near-wall turbulence energy and stress dissipation". In: *Journal of Fluid Mechanics* 459, pp. 139–166.

Jiménez, J. (2004). "Turbulent flows over rough walls". In: *Annu. Rev. Fluid Mech.* 36, pp. 173–196.

Kalitzin, G, A. Gould, and J. Benton (1996). "Application of two-equation turbulence models in aircraft design". In: *AIAA paper* 960327.

Kalitzin, G., G. Medic, G. Iaccarino, and P. Durbin (2005). "Near-wall behavior of RANS turbulence models and implications for wall functions". In: *Journal of Computational Physics* 204.1, pp. 265–291.

Kok, J. C. and S. P. Spekreijse (2000). "Efficient and accurate implementation of the $k-\omega$ turbulence model in the NLR multi-block Navier-Stokes system". In: NLR-TP-2000-144.

Lam, C. and K Bremhorst (1981). "A modified form of the k-ε model for predicting wall turbulence". In: *Journal of Fluids Engineering* 103.3, pp. 456–460.

Lang, A. W., M. T. Bradshaw, J. A. Smith, J. N. Wheelus, P. J. Motta, M. L. Habegger, and R. E. Hueter (2014). "Movable shark scales act as a passive dynamic micro-roughness to control flow separation". In: *Bioinspiration & Biomimetics* 9.3, p. 036017.

Launder, B. and D. Spalding (1974). "The numerical computation of turbulent flows". In: *Computer Methods in Applied Mechanics and Engineering* 3.2, pp. 269–289.

Launder, B. E. and S. Li (1993). "On the prediction of riblet performance with engineering turbulence models". In: *Applied Scientific Research* 50.3-4, pp. 283–298.

Launder, B. E., G. J. Reece, and W Rodi (1975). "Progress in the development of a Reynolds-stress turbulence closure". In: *Journal of Fluid Mechanics* 68.3, pp. 537–566.

Launder, B. E. and B. Sharma (1974). "Application of the energy-dissipation model of turbulence to the calculation of flow near a spinning disc". In: *Letters in Heat and Mass Transfer* 1.2, pp. 131–137.

Launder, B. E. and N Shima (1989). "Second-moment closure for the near-wall sublayer-Development and application". In: *AIAA Journal* 27.10, pp. 1319–1325.

Lee, S.-J. and S.-H. Lee (2001). "Flow field analysis of a turbulent boundary layer over a riblet surface". In: *Experiments in Fluids* 30.2, pp. 153–166.

Lee, Y., J. A. Nelder, and Y. Pawitan (2006). *Generalized linear models with random effects: unified analysis via H-likelihood*. Chapman and Hall/CRC.

Leonardi, S., P. Orlandi, and R. A. Antonia (2007). “Properties of d-and k-type roughness in a turbulent channel flow”. In: *Physics of Fluids* 19.12, p. 125101.

Lewkowicz, A. (1982). “An improved universal wake function for turbulent boundary layers and some of its consequences”. In: *Zeitschrift fuer Flugwissenschaften und Weltraumforschung* 6, pp. 261–266.

Lien, F.-S. and G. Kalitzin (2001). “Computations of transonic flow with the $v^2 - f$ turbulence model”. In: *International Journal of Heat and Fluid Flow* 22.1, pp. 53–61.

Luchini, P., F. Manzo, and A. Pozzi (1991). “Resistance of a grooved surface to parallel flow and cross-flow”. In: *Journal of Fluid Mechanics* 228, pp. 87–109.

Luo, Y., Y. Liu, J. Anderson, X. Li, and Y. Li (2015). “Improvement of water-repellent and hydrodynamic drag reduction properties on bio-inspired surface and exploring sharkskin effect mechanism”. In: *Applied Physics A* 120.1, pp. 369–377.

Manceau, R. (2015). “Recent progress in the development of the Elliptic Blending Reynolds-stress model”. In: *International Journal of Heat and Fluid Flow* 51, pp. 195–220.

Manceau, R. and K. Hanjalić (2002). “Elliptic blending model: A new near-wall Reynolds-stress turbulence closure”. In: *Physics of Fluids* 14.2, pp. 744–754.

Manceau, R., M. Wang, and D. Laurence (2001). “Inhomogeneity and anisotropy effects on the redistribution term in Reynolds-averaged Navier–Stokes modelling”. In: *Journal of Fluid Mechanics* 438, pp. 307–338.

Mansour, N. N., J. Kim, and P. Moin (1988). “Reynolds-stress and dissipation-rate budgets in a turbulent channel flow”. In: *Journal of Fluid Mechanics* 194, pp. 15–44.

Medjnoun, T., C. Vanderwel, and B. Ganapathisubramani (2018). “Characteristics of turbulent boundary layers over smooth surfaces with spanwise heterogeneities”. In: *Journal of Fluid Mechanics* 838, pp. 516–543.

Mehdi, F. and C. M. White (2011). “Integral form of the skin friction coefficient suitable for experimental data”. In: *Experiments in Fluids* 50.1, pp. 43–51.

Mejia-Alvarez, R and K. T. Christensen (2013). “Wall-parallel stereo particle-image velocimetry measurements in the roughness sublayer of turbulent flow overlying highly irregular roughness”. In: *Physics of Fluids* 25.11, p. 115109.

Menter, F. R. (2009). “Review of the shear-stress transport turbulence model experience from an industrial perspective”. In: *International Journal of Computational Fluid Dynamics* 23.4, pp. 305–316.

Menter, F. R., Y. Egorov, and D Rusch (2006). “Steady and unsteady flow modelling using the $k - \sqrt{kl}$ model”. In: *Ichmt Digital Library Online*. Begel House Inc.

Menter, F. R., M. Kuntz, and R. Langtry (2003). “Ten years of industrial experience with the SST turbulence model”. In: *Turbulence, Heat and Mass Transfer* 4.1, pp. 625–632.

Moser, R. D., J. Kim, and N. N. Mansour (1999). “Direct numerical simulation of turbulent channel flow up to $Re_\tau = 590$”. In: *Physics of Fluids* 11.4, pp. 943–945.

Murthy, J. and S Mathur (1997). "Periodic flow and heat transfer using unstructured meshes". In: *International Journal for Numerical Methods in Fluids* 25.6, pp. 659–677.

Musker, A. (1979). "Explicit expression for the smooth wall velocity distribution in a turbulent boundary layer". In: *AIAA Journal* 17.6, pp. 655–657.

Myong, H. K. and N. Kasagi (1990). "Prediction of anisotropy of the near-wall turbulence with an anisotropic low-Reynolds-number k-epsilon turbulence model". In: *ASME Transactions Journal of Fluids Engineering* 112, pp. 521–524.

Nagata, K., Y. Sakai, and S. Komori (2011). "Effects of small-scale freestream turbulence on turbulent boundary layers with and without thermal convection". In: *Physics of Fluids* 23.6, p. 065111.

Nagib, H. M. and K. A. Chauhan (2008). "Variations of von Kármán coefficient in canonical flows". In: *Physics of Fluids* 20.10, p. 101518.

Nikuradse, J. (1933). "Laws of flow in rough pipes". In: *VDI Forschungsheft*, p. 361.

Örlü, R., J. H. Fransson, and P. H. Alfredsson (2010). "On near wall measurements of wall bounded flows—the necessity of an accurate determination of the wall position". In: *Progress in Aerospace Sciences* 46.8, pp. 353–387.

Österlund, J. M., A. V. Johansson, H. M. Nagib, and M. H. Hites (2000). "A note on the overlap region in turbulent boundary layers". In: *Physics of Fluids* 12.1, pp. 1–4.

Patel, V. C., W. Rodi, and G. Scheuerer (1985). "Turbulence models for near-wall and low Reynolds number flows- a review". In: *AIAA Journal* 23.9, pp. 1308–1319.

Perlin, M., D. R. Dowling, and S. L. Ceccio (2016). "Freeman scholar review: passive and active skin-friction drag reduction in turbulent boundary layers". In: *Journal of Fluids Engineering* 138.9, p. 091104.

Perry, A. and J. D. Li (1990). "Experimental support for the attached-eddy hypothesis in zero-pressure-gradient turbulent boundary layers". In: *Journal of Fluid Mechanics* 218, pp. 405–438.

Perry, A. E., W. H. Schofield, and P. N. Joubert (1969). "Rough wall turbulent boundary layers". In: *Journal of Fluid Mechanics* 37.2, pp. 383–413.

Pope, S. B. (2001). *Turbulent Flows*. IOP Publishing.

Prandtl, L. (1953). *Essentials of fluid dynamics: with applications to hydraulics, aeronautics, meteorology and other subjects*. Blackie & Son.

Raupach, M., R. Antonia, and S Rajagopalan (1991). "Rough-wall turbulent boundary layers". In: *Applied Mechanics Reviews* 44.1, pp. 1–25.

Reif, W.-E. (1985). *Squamation and Ecology of Sharks*. Senckenbergische Naturforschende Gesellschaft.

Rodríguez-López, E., P. J. Bruce, and O. R. Buxton (2015). "A robust post-processing method to determine skin friction in turbulent boundary layers from the velocity profile". In: *Experiments in Fluids* 56.4, p. 68.

Rosen, M. W. and N. E. Cornford (1971). "Fluid friction of fish slimes". In: *Nature* 234.5323, p. 49.

Sandham, N. (1991). *An alternative formulation of the outer law of the turbulent boundary layer*. Tech. rep. Tech. Rep. No. DLR IB 221-91 A 10, DLR Göttingen.

Sansom, I. J., N. S. Davies, M. I. Coates, R. S. Nicoll, and A. Ritchie (2012). "Chondrichthyan-like scales from the Middle Ordovician of Australia". In: *Palaeontology* 55.2, pp. 243–247.

Schultz, M. P. and K. A. Flack (2003). "Turbulent boundary layers over surfaces smoothed by sanding". In: *Journal of Fluids Engineering* 125.5, pp. 863–870.

Schultz, M. and K. Flack (2007). "The rough-wall turbulent boundary layer from the hydraulically smooth to the fully rough regime". In: *Journal of Fluid Mechanics* 580, pp. 381–405.

Sharp, N. S., S Neuscamman, and Z Warhaft (2009). "Effects of large-scale free stream turbulence on a turbulent boundary layer". In: *Physics of Fluids* 21.9, p. 095105.

Shih, T.-H., W. W. Liou, A. Shabbir, Z. Yang, and J. Zhu (1995). "A new $k - \varepsilon$ eddy viscosity model for high Reynolds number turbulent flows". In: *Computers & Fluids* 24.3, pp. 227–238.

Spalart, P. and S. Allmaras (1992). "A one-equation turbulence model for aerodynamic flows". In: *30th Aerospace Sciences Meeting and Exhibit*, p. 439.

Speziale, C. G. (1986). "The dissipation rate correlation and turbulent secondary flows in noncircular ducts". In: *J. Fluids Eng., Transactions of ASME* 108, pp. 118–120.

Speziale, C. G., S. Sarkar, and T. B. Gatski (1991). "Modelling the pressure–strain correlation of turbulence: an invariant dynamical systems approach". In: *Journal of Fluid Mechanics* 227, pp. 245–272.

Squire, D., C Morrill-Winter, N Hutchins, M. Schultz, J. Klewicki, and I Marusic (2016). "Comparison of turbulent boundary layers over smooth and rough surfaces up to high Reynolds numbers". In: *Journal of Fluid Mechanics* 795, pp. 210–240.

Sullivan, C. B. and A. Kaszynski (2019). "PyVista: 3D plotting and mesh analysis through a streamlined interface for the Visualization Toolkit (VTK)". In: *Journal of Open Source Software* 4.37, p. 1450. DOI: `10.21105/joss.01450`. URL: `https://doi.org/10.21105/joss.01450`.

Suzuki, Y. and N. Kasagi (1994). "Turbulent drag reduction mechanism above a riblet surface". In: *AIAA Journal* 32.9, pp. 1781–1790.

Tani, I (1987). "Turbulent boundary layer development over rough surfaces". In: *Perspectives in Turbulence Studies*. Springer, pp. 223–249.

Thole, K. and D. Bogard (1996). "High freestream turbulence effects on turbulent boundary layers". In: *Journal of Fluids Engineering* 118.2, pp. 276–284.

Thom, A. (1971). "Momentum absorption by vegetation". In: *Quarterly Journal of the Royal Meteorological Society* 97.414, pp. 414–428.

Tomboulides, A, S. Aithal, P. Fischer, E Merzari, A. Obabko, and D. Shaver (2018). "A novel numerical treatment of the near-wall regions in the k- ω class of RANS models". In: *International Journal of Heat and Fluid Flow* 72, pp. 186–199.

Townsend, A. (1976). *The structure of turbulent shear flow*. Cambridge University Press.

Van Doormaal, J. and G. Raithby (1984). "Enhancements of the SIMPLE method for predicting incompressible fluid flows". In: *Numerical Heat Transfer* 7.2, pp. 147–163.

Vanderwel, C. and B. Ganapathisubramani (2015). "Effects of spanwise spacing on large-scale secondary flows in rough-wall turbulent boundary layers". In: *Journal of Fluid Mechanics* 774, R2.

Vanderwel, C., A Stroh, J Kriegseis, B Frohnapfel, and B. Ganapathisubramani (2019). "The instantaneous structure of secondary flows in turbulent boundary layers". In: *Journal of Fluid Mechanics* 862, pp. 845–870.

Walsh, M (1982). "Turbulent boundary layer drag reduction using riblets". In: *20th Aerospace Sciences Meeting*, p. 169.

Walsh, M. J. (1990). "Effect of detailed surface geometry on riblet drag reduction performance". In: *Journal of Aircraft* 27.6, pp. 572–573.

Weller, H. G., G. Tabor, H. Jasak, and C. Fureby (1998). "A tensorial approach to computational continuum mechanics using object-oriented techniques". In: *Computers in Physics* 12.6, pp. 620–631.

Wen, L., J. C. Weaver, and G. V. Lauder (2014). "Biomimetic shark skin: design, fabrication and hydrodynamic function". In: *Journal of Experimental Biology* 217.10, pp. 1656–1666.

Wen, L., J. C. Weaver, P. J. Thornycroft, and G. V. Lauder (2015). "Hydrodynamic function of biomimetic shark skin: effect of denticle pattern and spacing". In: *Bioinspiration & Biomimetics* 10.6, p. 066010.

Whittaker, E. T. (1922). "On a new method of graduation". In: *Proceedings of the Edinburgh Mathematical Society* 41, pp. 63–75.

Wilcox, D. C. (2006). *Turbulence Modeling for CFD*. Vol. 3. DCW Industries, Inc.

Wilcox, D. C. (1998). *Turbulence Modeling for CFD*. Vol. 2. DCW Industries, Inc.

Willingham, D., W. Anderson, K. T. Christensen, and J. M. Barros (2014). "Turbulent boundary layer flow over transverse aerodynamic roughness transitions: induced mixing and flow characterization". In: *Physics of Fluids* 26.2, p. 025111.

Xiao, Z., H. Chen, S. Fu, and F. Li (2005). "Computations with $k - g$ model for complex Configurations at High-Incidence". In: *Journal of Aircraft* 42.2, pp. 462–468.

Yakhot, V., S. Orszag, S. Thangam, T. Gatski, and C. Speziale (1992). "Development of turbulence models for shear flows by a double expansion technique". In: *Physics of Fluids A: Fluid Dynamics* 4.7, pp. 1510–1520.

Yang, S.-Q., S. Li, H.-P. Tian, Q.-Y. Wang, and N. Jiang (2016). "Tomographic PIV investigation on coherent vortex structures over shark-skin-inspired drag-reducing riblets". In: *Acta Mechanica Sinica* 32.2, pp. 284–294.

Yokojima, S. and N. Shima (2010). "Applicability of elliptic-relaxation method to free-surface turbulence". In: *Fluid Dynamics Research* 42.3, p. 035505.

Zhang, D.-Y., Y.-H. Luo, L. Xiang, and H.-W. Chen (2011a). “Numerical simulation and experimental study of drag-reducing surface of a real shark skin”. In: *Journal of Hydrodynamics, Ser. B* 23.2, pp. 204–211.

Zhang, D., Y. Li, X. Han, X. Li, and H. Chen (2011b). “High-precision bio-replication of synthetic drag reduction shark skin”. In: *Chinese Science Bulletin* 56.9, pp. 938–944.

Zhao, D.-Y., Z.-P. Huang, M.-J. Wang, T. Wang, and Y. Jin (2012). “Vacuum casting replication of micro-riblets on shark skin for drag-reducing applications”. In: *Journal of Materials Processing Technology* 212.1, pp. 198–202.

Zhou, J., R. J. Adrian, S Balachandar, and T. Kendall (1999). “Mechanisms for generating coherent packets of hairpin vortices in channel flow”. In: *Journal of Fluid Mechanics* 387, pp. 353–396.

Zuliana, S. U. and A. Perperoglou (2017). “Two dimensional smoothing via an optimised Whittaker smoother”. In: *Big Data Analytics* 2.1, p. 6.

Appendix A

Denticle fabrication

Three denticle CAD models are presented in Figure A.1, a smooth denticle based on a *Poracanthodes sp.* (extinct shark relative) sample, and two ribletted denticles with similar dimensions as the smooth denticle. The two ribletted denticles differ only by the shape of their riblets, with one having mako-type cut out regions at the trailing edge, and the other more closely resembling the smooth denticle. These are given the abbreviations defined in the caption of Figure A.1. Denticle dimensions are presented in A.3 for all three models. The denticle array patterns can be found in Figure A.3. The smooth (SMO) and ribletted (RIB) denticles are 3D printed in the experimental study of Chapter 3, while all three models are used in the numerical study of Chapter 6. Arrays of smooth (SMO) and ribletted (RIB) denticles were 3D printed at a 4 mm width, in 5 sections of 98 × 120 mm, and bonded to a 500 × 120 mm PVC sheet using a medium viscosity epoxy-resin (Opti-Tec 5013) to ensure the glue thickness was negligible. A thin 10 × 120 mm 3D printed flat section was added to the end of the denticle arrays to ensure the full 500 mm plate was covered. A Stratasys Objet Connex printer was used to manufacture the sharkskin, printing in vero-white resin in 16 µm layers. The array dimensions were changed slightly at the joint between two plates in order to minimise the impact of any large gaps. This is illustrated in Figure A.4. A 3D printed ribletted denticle array is presented in Figure A.5, along with a close up image taken with a scanning Electron Microscope (SEM) of a single denticle. The denticle is well captured at a width of 4 mm, with small amounts of roughness on the leading edge.

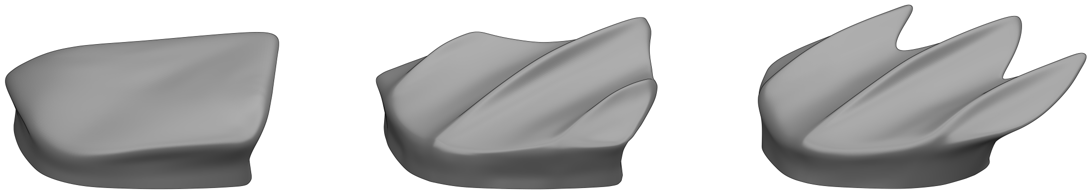

FIGURE A.1: Denticle CAD models. Smooth (left) and ribletted (right) models are as per 3D printed models of Chapter 3. The central model is a derivative between the other two. Models are abbreviated SMO (smooth, left), SMR (smooth-ribletted, centre), and RIB (ribletted, right).

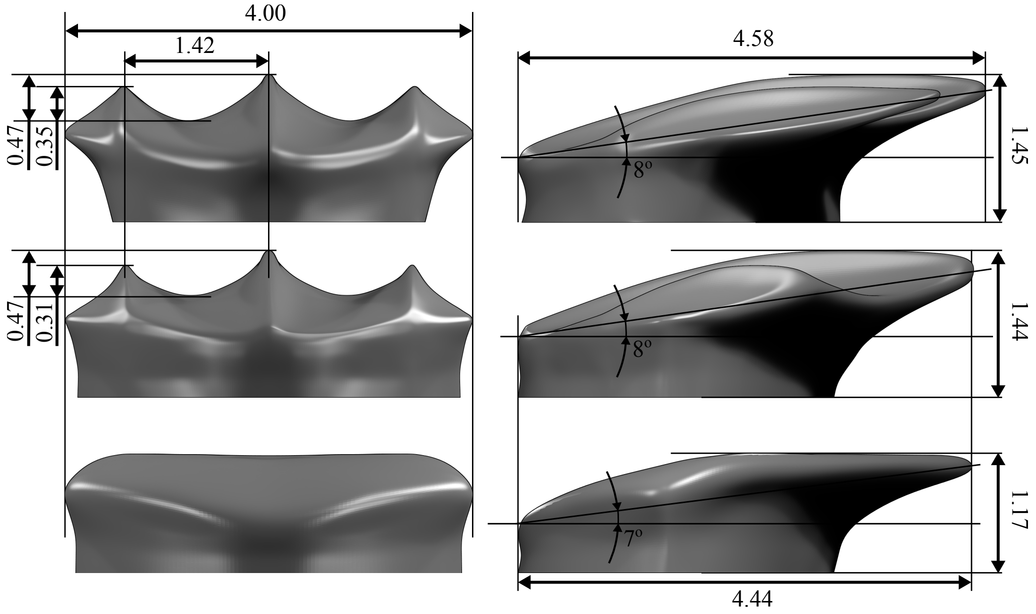

FIGURE A.2: Dimensions of the three denticle CAD models (mm).

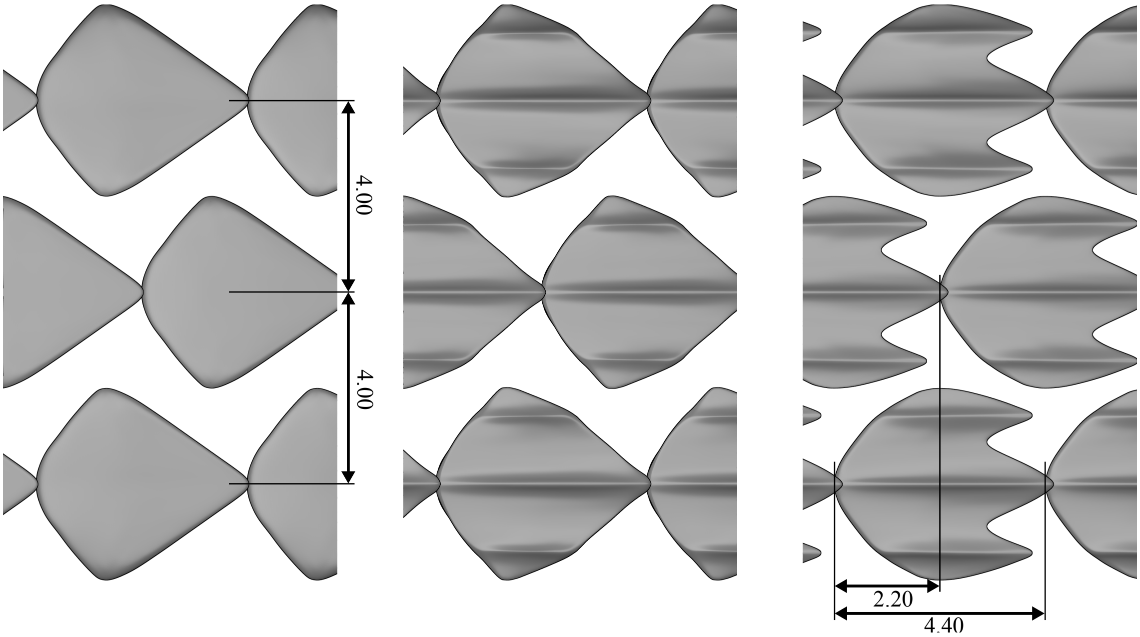

FIGURE A.3: Array dimensions (mm).

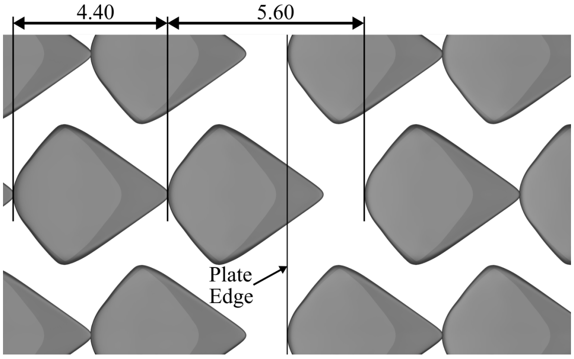

FIGURE A.4: Array dimensions at the joint between two plates (mm).

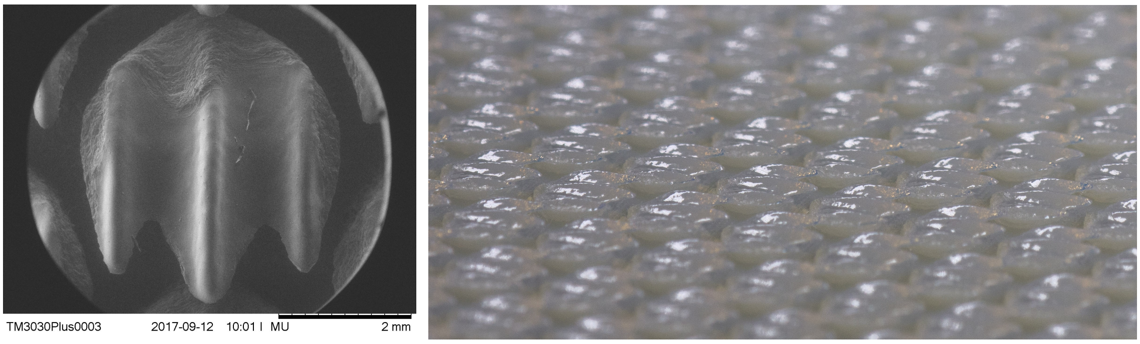

FIGURE A.5: 3D printed array of ribletted shark skin denticles.

Appendix B

The Whittaker smoother

As per Mehdi and White (2011) a Whittaker smoother is adopted, originally developed by Whittaker (1922), and later implemented by Eilers (2003). The Whittaker smoother is a discrete penalised least squares method which balances smoothness of the fit with conformity to the actual data. This particular smoother is extremely valuable since it is fast to compute, and it can handle large regions of missing data (or in this case unevenly distributed data). The principle behind the smoother is the minimisation of the function

$$Q = \left|\underline{\mathbf{y}} - \underline{\mathbf{z}}\right|^2 + \lambda \left|\underline{\underline{\mathbf{D}}}\,\underline{\mathbf{z}}\right|^2 \tag{B.1}$$

where $\underline{\mathbf{y}}$ is the data set to be smoothed, $\underline{\mathbf{z}}$ is the smoothed approximation of $\underline{\mathbf{y}}$, λ is a smoothing parameter, and $\underline{\underline{\mathbf{D}}}$ is a differencing matrix such that $\underline{\underline{\mathbf{D}}}\ \underline{\mathbf{z}} = \Delta\underline{\mathbf{z}}$ (second order differencing is adopted here). λ essentially controls the weighting between smoothness and conformity to the data, its value is dependent on the data set being smoothed. Through some vector calculus one finds that the smoothed data can be found by solving the linear algebra (Eilers, 2003)

$$\left(\underline{\mathbf{I}} + \lambda \underline{\underline{\mathbf{D}}}'\underline{\underline{\mathbf{D}}}\right)\underline{\mathbf{z}} = \underline{\mathbf{y}} \tag{B.2}$$

which can be solved using a sparse linear matrix solver. In its current form there are two disadvantages. Firstly, the equation assumes that the data set $\underline{\mathbf{y}}$ is uniformly distributed, and secondly it is sensitive to the value of λ.

In order to account for the unevenly distributed data the method detailed by Eilers (2003) is adopted. A fine grid of spacings 12.5 µm is defined. The corresponding fine data set, $\underline{\tilde{\mathbf{y}}}$ takes the value of $\underline{\mathbf{y}}$ at the nearest corresponding grid points, and the value of zero in the gaps between the true data points. This introduces rounding errors to the original grid, but does not require re-sampling of the data; with this selected grid spacing these errors are negligible, verified by successive refinement of the grid. A corresponding weighting vector $\underline{\mathbf{w}}$ is created with values of 1 when the $\underline{\tilde{\mathbf{y}}}$ has a data point, and 0 otherwise. A weighted matrix $\underline{\underline{\mathbf{W}}}$ is then constructed, the diagonal of which is equal to

$\underline{\mathbf{w}}$. The linear algebra problem becomes

$$\left(\underline{\underline{\mathbf{W}}} + \lambda \underline{\underline{\mathbf{D}}}' \underline{\underline{\mathbf{D}}}\right) \underline{\tilde{\mathbf{z}}} = \underline{\underline{\mathbf{W}}}\, \underline{\tilde{\mathbf{y}}}, \tag{B.3}$$

leading to

$$\underline{\tilde{\mathbf{z}}} = \underline{\underline{\mathbf{W}}} \left(\underline{\underline{\mathbf{W}}} + \lambda \underline{\underline{\mathbf{D}}}' \underline{\underline{\mathbf{D}}}\right)^{-1} \underline{\tilde{\mathbf{y}}} = \underline{\underline{\mathbf{H}}}\, \underline{\tilde{\mathbf{y}}}, \tag{B.4}$$

where $\underline{\tilde{\mathbf{z}}}$ now has the length of $\underline{\tilde{\mathbf{y}}}$. Given the smoothness of $\underline{\tilde{\mathbf{z}}}$ it is trivial to resample back to the original grid spacing if required.

In order to account for the sensitivity on λ an optimisation process is adopted detailed by Zuliana and Perperoglou (2017) and Lee, Nelder, and Pawitan (2006). The error between the smoothed and real data sets is defined as $e = \underline{\tilde{\mathbf{y}}} - \underline{\underline{\mathbf{W}}}\, \underline{\tilde{\mathbf{z}}}$, and two variances

$$\hat{\sigma}^2 = \frac{\underline{\mathbf{e}}' \underline{\mathbf{e}}}{n - \mathbf{Tr}\left(\underline{\underline{\mathbf{H}}}\, \underline{\underline{\mathbf{W}}}\right)}, \quad \hat{\sigma}_z^2 = \frac{\underline{\mathbf{z}}' \underline{\underline{\mathbf{D}}}' \underline{\underline{\mathbf{D}}}\, \underline{\mathbf{z}}}{\mathbf{Tr}\left(\underline{\underline{\mathbf{H}}}\, \underline{\underline{\mathbf{W}}}\right) - 2}, \tag{B.5}$$

where n is the number of original data points. This provides the prediction $\lambda = \hat{\sigma}^2 / \hat{\sigma}_z^2$. By recalculating the coefficient matrix $\underline{\underline{\mathbf{H}}}$ for the new λ and updating $\underline{\mathbf{z}}$, one can iterate until a constant value of λ has been found. This typically occurs after just a few iterations, given reasonable initialisation of λ.

Appendix C

Turbulence models

C.1 $k - \varepsilon$ (Lam and Bremhorst, 1981)

This model is based on the standard $k - \varepsilon$ model (Launder and Spalding, 1974) but includes additional damping functions in order to integrate more efficiently through the boundary layer. The model of Launder and Spalding (1974) is obtained when the damping functions $f_\mu = f_1 = f_2 = 1$. The turbulent viscosity is calculated by

$$\nu_t = \mu_t/\rho = C_\mu f_\mu \frac{k^2}{\varepsilon}, \tag{C.1}$$

where f_μ is a damping function:

$$f_\mu = \left(1 - \exp\left[-0.0165 \frac{\sqrt{k} y_w}{\nu}\right]\right)\left(1 + \frac{20.5}{Re_T}\right), \tag{C.2}$$

where

$$Re_T = \frac{k^2}{\varepsilon \nu}, \tag{C.3}$$

and y_w is the normal distance to the wall. The transport of k is identical to the standard $k - \varepsilon$ model:

$$\frac{Dk}{Dt} = \mathcal{P} - \varepsilon + \frac{\partial}{\partial x_j}\left[\left(\nu + \frac{\nu_t}{\sigma_k}\right)\frac{\partial k}{\partial x_j}\right], \tag{C.4}$$

where $\mathcal{P} = -\overline{u_i' u_j'} \frac{\partial \overline{U}_i}{\partial x_j}$. The transport of ε is

$$\frac{D\varepsilon}{Dt} = C_{\varepsilon 1} f_1 \mathcal{P} \frac{\varepsilon}{k} - C_{\varepsilon 2} f_2 \frac{\varepsilon^2}{k} + \frac{\partial}{\partial x_j}\left[\left(\nu + \frac{\nu_t}{\sigma_\varepsilon}\right)\frac{\partial \varepsilon}{\partial x_j}\right], \tag{C.5}$$

where f_1 and f_2 are calculated by

$$f_1 = 1 + \left(\frac{0.05}{f_\mu}\right)^3, \qquad f_2 = 1 - \exp(-Re_T^2). \tag{C.6}$$

Suggested values of the empirical constants are

$$C_\mu = 0.09, \qquad \sigma_k = 1, \qquad C_{\varepsilon 1} = 1.44, \qquad C_{\varepsilon 2} = 1.92, \qquad \sigma_\varepsilon = 1.3.$$

The boundary conditions suggested by Patel, Rodi, and Scheuerer (1985) are such that $k = 0$, and

$$n_i \frac{\partial \varepsilon}{\partial x_i} = 0, \tag{C.7}$$

at the wall, with $y_1^+ \lesssim 1$.

C.2 $k - \omega$ (Wilcox, 1998)

The $k - \omega$ model, developed by Wilcox (1998), solves for k and ω, the specific dissipation rate. These quantities are related to the turbulent viscosity by

$$\mu_t = \rho \frac{k}{\omega}. \tag{C.8}$$

The transport of k is:

$$\frac{Dk}{Dt} = \mathcal{P} - \beta^* k\omega + \frac{\partial}{\partial x_j}\left[\left(\nu + \frac{\nu_t}{\sigma^*}\right)\frac{\partial k}{\partial x_j}\right], \tag{C.9}$$

The transport of ω is:

$$\frac{D\omega}{Dt} = \gamma \frac{\omega}{k}\mathcal{P} - \beta\omega^2 + \frac{\partial}{\partial x_j}\left[\left(\nu + \frac{\nu_t}{\sigma}\right)\frac{\partial \omega}{\partial x_j}\right]. \tag{C.10}$$

The empirical constants for this model are

$$\gamma = 0.52, \qquad \sigma = 2, \qquad \sigma^* = 2, \qquad \beta = 0.072, \qquad \beta^* = 0.09.$$

Note that the original model includes a 'Pope correction' to the coefficient β. This has no impact on 2D or 1D flows (Wilcox, 1998) and has subsequently been neglected in the present work. The appropriate boundary conditions are such that $k = 0$ at the wall and ω is specified using

$$\omega_1 = \frac{6\nu}{\beta d^2}. \tag{C.11}$$

where d is the normal distance to the wall, or if using 'slightly-rough' wall boundary conditions,

$$\omega_0 = \frac{40000\nu}{k_s^2}, \tag{C.12}$$

where k_s is the roughness height. The Low Reynolds number corrections of Wilcox (2006) can also be implemented in this model which can improve predictions of transitional flows and the prediction of k in the near wall region. The coefficients are damped based on the local turbulent Reynolds number: $Re_T = k/\nu\omega$. The damping takes the form:

$$\nu_t = \alpha^* k/\omega, \tag{C.13}$$

$$\alpha^* = \left(\frac{\beta/3 + Re_T/R_k}{1 + Re_T/R_k}\right), \tag{C.14}$$

$$\beta^* = \beta^*_\infty \left(\frac{100\beta/27 + (Re_T/R_\beta)^4}{1 + (Re_T/R_\beta)^4}\right), \tag{C.15}$$

$$\gamma = \frac{\gamma_\infty}{\alpha^*}\left(\frac{\alpha_0 + (Re_T/R_\omega)}{1 + (Re_T/R_\omega)}\right), \tag{C.16}$$

where the additional coefficients take the values

$$\beta^*_\infty = 0.09, \qquad \alpha_0 = 1/9, \qquad R_k = 6, \qquad R_\beta = 8, \qquad R_\omega = 2.61.$$

C.3 $k-\omega'$ (Tomboulides et al., 2018)

This model decomposes ω into $\omega = \omega' + \omega_w$, where ω_w is calculated from an analytical expression:

$$\omega_w = \frac{6\nu}{\beta y_w^2}. \tag{C.17}$$

where y_w is the wall-normal distance. The turbulent viscosity is calculated by

$$\mu_t = \rho \frac{k}{\omega' + \omega_w}. \tag{C.18}$$

The transport of k is:

$$\frac{Dk}{Dt} = \mathcal{P} - \beta^* k(\omega' + \omega_w) + \frac{\partial}{\partial x_j}\left[\left(\nu + \frac{\nu_t}{\sigma^*}\right)\frac{\partial k}{\partial x_j}\right], \tag{C.19}$$

The transport of ω' is:

$$\begin{aligned}\frac{D\omega'}{Dt} = \gamma\frac{\omega' + \omega_w}{k}\mathcal{P} - \beta(\omega' + \omega_w)^2 + \frac{\partial}{\partial x_j}\left[\left(\nu + \frac{\nu_t}{\sigma}\right)\frac{\partial \omega'}{\partial x_j}\right] - \overline{U}_j\frac{\partial \omega_w}{\partial x_j} \\ + \frac{\partial}{\partial x_j}\left[\left(\nu + \frac{\nu_t}{\sigma}\right)\frac{\partial \omega_w}{\partial x_j}\right].\end{aligned} \tag{C.20}$$

The two last terms of the transport of ω' are further manipulated by using (C.17):

$$\overline{U}_j\frac{\partial \omega_w}{\partial x_j} = -2\frac{\omega_w}{y_w}\overline{U}_j\frac{\partial y_w}{\partial x_j} \tag{C.21}$$

$$\frac{\partial}{\partial x_j}\left[\left(\nu+\frac{\nu_t}{\sigma}\right)\frac{\partial \omega_w}{\partial x_j}\right]=\nu\nabla^2\omega_w+\frac{\nu_t}{\sigma}\nabla^2\omega_w+\frac{1}{\sigma}\frac{\partial \omega_w}{\partial x_j}\frac{\partial \nu_t}{\partial x_j} \tag{C.22}$$

$$\nu\nabla^2\omega_w=\nu\omega_w\left[6\frac{\nabla y_w\cdot\nabla y_w}{y_w^2}-2\frac{\nabla^2 y_w}{y_w}\right] \tag{C.23}$$

$$\frac{\nu_t}{\sigma}\nabla^2\omega_w=\frac{k\omega_w}{\sigma(\omega'+\omega_w)}\left[6\frac{\nabla y_w\cdot\nabla y_w}{y_w^2}-2\frac{\nabla^2 y_w}{y_w}\right] \tag{C.24}$$

$$\frac{1}{\sigma}\frac{\partial \omega_w}{\partial x_j}\frac{\partial \nu_t}{\partial x_j}=-\frac{2\omega_w}{\sigma(\omega'+\omega_w)}\left[\frac{1}{y_w}\nabla k\cdot\nabla y_w+2k\frac{\omega_w}{(\omega'+\omega_w)y_w^2}\nabla y_w\cdot\nabla y_w\right.$$
$$\left.-\frac{k}{(\omega'+\omega_w)y_w}\nabla\omega'\cdot\nabla y_w\right]. \tag{C.25}$$

This closes the equations, given that the wall-normal coordinate, y_w, and its derivatives, can be accurately calculated. Coefficients are as in Appendix C.2. Boundary conditions are such that at $y=0$ $k=0$ and $\omega'=0$. ω_w is closed analytically using (C.17).

The cases presented in this work adopt the algebraic solution $|\nabla y_w|=1$ and $\nabla^2 y_w=0$ for stability.

C.4 $k-\tau$ (Kalitzin, Gould, and Benton, 1996)

This model is derived from $k-\omega$ by substituting $\omega=1/\tau$ into the transport equations. β^* has been neglected from this definition, deviating slightly from its original formulation by Kalitzin, Gould, and Benton (1996). In addition to this, Kalitzin, Gould, and Benton (1996) also include a viscosity limiter in order to reduce sensitivity to freestream boundary conditions. This has also been neglected due to its lack of importance near the wall. The kinematic turbulent viscosity is calculated from

$$\nu_t=k\tau, \tag{C.26}$$

the transport of k is

$$\frac{Dk}{Dt}=\mathcal{P}-\beta^*\frac{k}{\tau}+\frac{\partial}{\partial x_j}\left[\left(\nu+\frac{\nu_t}{\sigma^*}\right)\frac{\partial k}{\partial x_j}\right], \tag{C.27}$$

and the transport of τ is

$$\frac{D\tau}{Dt}=-\frac{\gamma\tau}{k}\mathcal{P}+\beta-8\left(\nu+\frac{\nu_t}{\sigma}\right)\frac{\partial\sqrt{\tau}}{\partial x_j}\frac{\partial\sqrt{\tau}}{\partial x_j}+\frac{\partial}{\partial x_j}\left[\left(\nu+\frac{\nu_t}{\sigma}\right)\frac{\partial \tau}{\partial x_j}\right]. \tag{C.28}$$

The diffusion term of (C.28) has been reformulated according to the suggestion of Kok and Spekreijse (2000) to improve numerical accuracy. Boundary conditions are such that at $y=0$, $k=0$ and $\tau=0$. Coefficients are identical to those of the $k-\omega$ model, Appendix C.2.

C.5 Updated $k - \tau$

This model extends the original formulation of Kalitzin, Gould, and Benton (1996) to include a cross diffusion term and updated coefficients, as per Wilcox (2006).

The cross-diffusion term is limited to positive values, which ensures that the standard $k - \omega$ model is retained close to the wall. These corrections were first introduced by Wilcox (2006) to improve predictions of strongly separated and free shear flows.

Equations for ν_t and k are as in Appendix C.4. The transport of τ is modified to

$$\frac{D\tau}{Dt} = -\frac{\gamma\tau}{k}\mathcal{P} + \beta - 8\left(\nu + \frac{\nu_t}{\sigma}\right)\frac{\partial\sqrt{\tau}}{\partial x_j}\frac{\partial\sqrt{\tau}}{\partial x_j} + \frac{\partial}{\partial x_j}\left[\left(\nu + \frac{\nu_t}{\sigma}\right)\frac{\partial\tau}{\partial x_j}\right] + \sigma_d\tau\frac{\partial\tau}{\partial x_j}\frac{\partial k}{\partial x_j}, \quad \text{(C.29)}$$

where

$$\sigma_d = \begin{cases} 0, & \text{for } \frac{1}{\tau^2}\frac{\partial\tau}{\partial x_j}\frac{\partial k}{\partial x_j} \geq 0, \\ \sigma_{d0}, & \text{for } \frac{1}{\tau^2}\frac{\partial\tau}{\partial x_j}\frac{\partial k}{\partial x_j} < 0. \end{cases} \quad \text{(C.30)}$$

The empirical constants for this model are

$$\gamma = 0.52, \qquad \sigma = 2, \qquad \sigma^* = 5/3, \qquad \sigma_{d0} = 0.125, \qquad \beta = 0.0708, \qquad \beta^* = 0.09.$$

Boundary conditions are identical to those specified in Appendix C.4. The low Reynolds number corrections of Wilcox (2006) (Appendix C.2) can also be applied to this model.

C.6 $k - g$ (Kalitzin, Gould, and Benton, 1996)

This model is derived by substituting $\omega = 1/g^2$ into the transport of ω. The turbulent viscosity is calculated by

$$\nu_t = kg^2, \quad \text{(C.31)}$$

the transport of k is

$$\frac{Dk}{Dg} = \mathcal{P} - \beta^*\frac{k}{g^2} + \frac{\partial}{\partial x_j}\left[\left(\nu + \frac{\nu_t}{\sigma^*}\right)\frac{\partial k}{\partial x_j}\right], \quad \text{(C.32)}$$

and the transport of τ is

$$\frac{Dg}{Dt} = -\frac{\gamma g}{2k}\mathcal{P} + \frac{\beta}{2g} - \frac{3}{g}\left(\nu + \frac{\nu_t}{\sigma}\right)\frac{\partial g}{\partial x_j}\frac{\partial g}{\partial x_j} + \frac{\partial}{\partial x_j}\left[\left(\nu + \frac{\nu_t}{\sigma}\right)\frac{\partial g}{\partial x_j}\right]. \quad \text{(C.33)}$$

Boundary conditions are such that at $y = 0$, $k = 0$ and $g = 0$. Coefficients are identical to those of the $k - \omega$ model, Appendix C.2.

C.7 $\overline{v^2} - f$ (Durbin, 1991)

This model also includes the modifications of Lien and Kalitzin (2001) and Davidson, Nielsen, and Sveningsson (2003). Equations are solved for k, ε, $\overline{v^2} = \overline{u_2'u_2'}$, and f. The turbulent viscosity is calculated by

$$\nu_t = \min\left(C_{\mu 1}\frac{k^2}{\varepsilon}; C_{\mu 2}\overline{v^2}T\right), \tag{C.34}$$

where T is a timescale limiter which limits the minimum value of k/ε with the Kolmogorov timescale:

$$T = \max\left[\frac{k}{\varepsilon}; C_T\sqrt{\frac{\nu}{\varepsilon}}\right]. \tag{C.35}$$

A transport equation is solved for k:

$$\frac{Dk}{Dt} = \mathcal{P} - \varepsilon + \frac{\partial}{\partial x_j}\left[\left(\nu + \frac{\nu_t}{\sigma_k}\right)\frac{\partial k}{\partial x_j}\right], \tag{C.36}$$

And ε is calculated from

$$\frac{D\varepsilon}{Dt} = C'_{\varepsilon 1}\frac{\mathcal{P}}{T} - C_{\varepsilon 2}\frac{\varepsilon}{T} + \frac{\partial}{\partial x_j}\left[\left(\nu + \frac{\nu_t}{\sigma_\varepsilon}\right)\frac{\partial \varepsilon}{\partial x_j}\right]. \tag{C.37}$$

$C'_{\varepsilon 1}$ is calculated by

$$C'_{\varepsilon 1} = C_{\varepsilon 1}(1 + 0.05\sqrt{k/\overline{v^2}}). \tag{C.38}$$

$\overline{v^2}$ is calculated from an additional transport equation:

$$\frac{D\overline{v^2}}{Dt} = \frac{\partial}{\partial x_j}\left[\left(\nu + \frac{\nu_t}{\sigma_k}\right)\frac{\partial \overline{v^2}}{\partial x_j}\right] - \frac{N\overline{v^2}\varepsilon}{k} + S_v, \tag{C.39}$$

where S_v is a source term calculated by

$$S_v = \min\left[kf; -\frac{1}{T}\left((C_1 - N)\overline{v^2} - \frac{2}{3}k(C_1 - 1)\right) + C_2\frac{\mathcal{P}}{\rho}\right]. \tag{C.40}$$

f is a source term related to the energy distribution in the equation of $\overline{v^2}$. It is calculated via an elliptic relaxation equation:

$$-L^2\frac{\partial^2 f}{\partial x_j \partial x_j} = -f - \frac{1}{T}\left[(C_1 - N)\frac{\overline{v^2}}{k} - \frac{2}{3}(C_1 - 1)\right] - C_2\frac{\mathcal{P}}{k}, \tag{C.41}$$

where L is a timescale limiter of the same principle as T:

$$L = C_L\max\left[\frac{k^{3/2}}{\varepsilon}; C_\eta\left(\frac{\nu^3}{\varepsilon}\right)^{1/4}\right]. \tag{C.42}$$

Model coefficients are

$$
\begin{array}{llllll}
C_{\mu 1} = 0.09, & C_{\mu 2} = 0.22, & \sigma_k = 1.0, & \sigma_\varepsilon = 1.3, & C_1 = 1.4, & C_2 = 0.3 \\
C_T = 6.0, & C_L = 0.23, & C_\eta = 70, & C_{\varepsilon 1} = 1.4, & C_{\varepsilon 2} = 1.9, & N = 6.0.
\end{array}
$$

Boundary conditions are such that at $y = 0$, $k = f = \overline{v^2} = 0$. An algebraic closure is used to evaluate ε at the cell centre closest to the wall: $\varepsilon_1 = 2\nu k/d^2$.

C.8 Stress-τ

This model is based on Wilcox (2006) Stress-ω model, but with τ as the scale-determining variable for better near-wall behaviour. The transport of the Reynolds stresses is given by

$$\frac{D\overline{u_i'u_j'}}{Dt} = \mathcal{P}_{ij} + \Pi_{ij} + \mathcal{D}_{ij} - \varepsilon_{ij}, \tag{C.43}$$

where the production of the Reynolds stresses is given by

$$\mathcal{P}_{ij} = -\overline{u_i'u_k'}\frac{\partial \overline{U}_j}{\partial x_k} - \overline{u_j'u_k'}\frac{\partial \overline{U}_i}{\partial x_k}, \tag{C.44}$$

and $\mathcal{D}_{ij}$ represents viscous and turbulent diffusion, ε_{ij} is destruction, and Π_{ij} is the pressure-strain or redistribution tensor. A scalar eddy-diffusion model is adopted for $\mathcal{D}_{ij}$ such that

$$\mathcal{D}_{ij} = \frac{\partial}{\partial x_k}\left[\left(\nu + \frac{\nu_t}{\sigma^*}\right)\frac{\partial \overline{u_i'u_j'}}{\partial x_k}\right], \tag{C.45}$$

where $\nu_t = k\tau$ and $\varepsilon = k/\tau$. The pressure-strain correlation is modelled using the LRR (Launder, Reece, and Rodi, 1975) model:

$$\begin{aligned}\Pi_{ij} = {}& -2C_1\varepsilon b_{ij} + 2(\hat{\alpha} + \hat{\beta})k\left(b_{ik}S_{jk} + b_{jk}S_{ik} - \frac{2}{3}b_{kl}S_{kl}\delta_{ij}\right) \\ & + 2(\hat{\alpha} - \hat{\beta})k(b_{ik}\Omega_{jk} + b_{jk}\Omega_{ik}) + \left(\frac{4}{3}(\hat{\alpha} + \hat{\beta}) - \hat{\gamma}\right)kS_{ij},\end{aligned} \tag{C.46}$$

where b_{ij} is the anisotropy tensor given by

$$b_{ij} = \frac{\overline{u_i'u_j'}}{2k} - \frac{1}{3}\delta_{ij}, \tag{C.47}$$

and the mean rate of strain tensor S_{ij} and the mean vorticity tensor Ω_{ij} are given by

$$S_{ij} = \frac{1}{2}\left(\frac{\partial \overline{U}_i}{\partial x_j} + \frac{\partial \overline{U}_j}{\partial x_i}\right), \quad \Omega_{ij} = \frac{1}{2}\left(\frac{\partial \overline{U}_i}{\partial x_j} - \frac{\partial \overline{U}_j}{\partial x_i}\right). \tag{C.48}$$

The remaining parameters $\hat{\alpha}$, $\hat{\beta}$, and $\hat{\gamma}$ are empirical constants. The dissipation tensor is calculated by

$$\varepsilon_{ij} = \frac{2}{3}\beta^* \frac{k}{\tau}\delta_{ij}. \tag{C.49}$$

The transport of τ is

$$\frac{D\tau}{Dt} = -\frac{\gamma\tau}{k}\mathcal{P} + \beta - 8\left(\nu + \frac{\nu_t}{\sigma}\right)\frac{\partial\sqrt{\tau}}{\partial x_j}\frac{\partial\sqrt{\tau}}{\partial x_j} + \frac{\partial}{\partial x_j}\left[\left(\nu + \frac{\nu_t}{\sigma}\right)\frac{\partial\tau}{\partial x_j}\right] + \sigma_d\tau\frac{\partial\tau}{\partial x_j}\frac{\partial k}{\partial x_j}, \tag{C.50}$$

$$\sigma_d = \begin{cases} 0, & \text{for } \frac{1}{\tau^2}\frac{\partial\tau}{\partial x_j}\frac{\partial k}{\partial x_j} \geq 0, \\ \sigma_{d0}, & \text{for } \frac{1}{\tau^2}\frac{\partial\tau}{\partial x_j}\frac{\partial k}{\partial x_j} < 0. \end{cases} \tag{C.51}$$

The transport of τ and related model coefficients are identical to those specified in Appendix C.5. Model coefficients are

$$\hat{\alpha} = (8 + C_2)/11, \qquad \hat{\beta} = (8C_2 - 2)/11, \qquad \hat{\gamma} = (60C_2 - 4)/55,$$

$$\gamma = 0.52, \qquad \sigma = 2, \qquad \sigma^* = 5/3, \qquad \sigma_{d0} = 0.125, \qquad \beta = 0.0708,$$

$$\beta^* = 0.09. \qquad C_1 = 1.8, \qquad C_2 = 10/19.$$

Low Reynolds number corrections can be applied in a similar fashion to C.2:

$$\nu_t = \alpha^* k\tau, \qquad Re_T = \frac{k\tau}{\nu}, \tag{C.52}$$

and adjust the model coefficients by

$$\alpha^* = \frac{\beta/3 + Re_T/R_k}{1 + Re_T/R_k}, \tag{C.53}$$

$$\beta^* = \beta^*_\infty \frac{100\beta/27 + (Re_T/R_k)^4}{1 + (Re_T/R_k)^4}, \tag{C.54}$$

$$\gamma = \gamma_\infty \frac{1/9 + Re_T/R_\omega}{1 + Re_T/R_\omega} \cdot \frac{3 + Re_T/Re_\omega}{\beta + Re_T/R_\omega}, \tag{C.55}$$

$$C_1 = \frac{9}{5}\frac{5/3 + (Re_T/R_\beta)^4}{1 + (Re_T/R_\beta)^4}, \tag{C.56}$$

$$\hat{\alpha} = \frac{1 + \hat{\alpha}_\infty (Re_T/R_\beta)^4}{1 + (Re_T/R_\beta)^4}, \tag{C.57}$$

$$\hat{\beta} = \hat{\beta}_\infty \frac{(Re_T/R_\beta)^4}{1 + (Re_T/R_\beta)^4}, \tag{C.58}$$

$$\hat{\gamma} = \hat{\gamma}_\infty \frac{\hat{\gamma}_0 + (Re_T/R_\beta)^4}{1 + (Re_T/R_\beta)^4}, \tag{C.59}$$

with

$$\hat{\alpha}_\infty = (8 + C_2)/11, \qquad \hat{\beta}_\infty = (8C_2 - 2)/11, \qquad \hat{\gamma}_\infty = (60C_2 - 4)/55,$$

$$\hat{\gamma}_0 = 21/2000, \qquad \beta^*_\infty = 0.09, \qquad R_\beta = 8, \qquad R_k = 6, \qquad R_\omega = 22/9.$$

Boundary conditions are $\overline{u_i'u_j'} = 0$ and $\tau = 0$ at the wall.

C.9 Elliptic Blending SSG (Manceau, 2015)

The EB-SSG model of Manceau (2015) solves an additional elliptic equation for a blending parameter α. The transport of the Reynolds stresses is

$$\frac{D\overline{u_i'u_j'}}{Dt} = \mathcal{P}_{ij} + \Pi_{ij} + \mathcal{D}_{ij} - \varepsilon_{ij}. \tag{C.60}$$

Diffusion is modelled using an anisotropic gradient diffusion of the form

$$\mathcal{D}_{ij} = \frac{\partial}{\partial x_l}\left[\left(\frac{C_\mu}{\sigma_k}\overline{u_l'u_m'}T + \nu\delta_{lm}\right)\frac{\partial\overline{u_i'u_j'}}{\partial x_m}\right], \tag{C.61}$$

where C_μ and σ_k are empirical constants, and T is a turbulent time scale. The remaining open terms of (C.60) are closed using a near-wall model, blended into a isotropic model. The pressure-strain correlation is calculated by

$$\Pi_{ij} = (1-\alpha^2)\Pi^w_{ij} + \alpha^2\Pi^h_{ij}, \tag{C.62}$$

which blends the SSG model Speziale, Sarkar, and Gatski (1991),

$$\begin{aligned}\Pi^h_{ij} &= -(C_1\varepsilon + C_1^*\mathcal{P})b_{ij} + (C_3 - C_3^*\sqrt{b_{lm}b_{lm}})kS_{ij} \\ &+ C_4k(b_{ik}S_{jk} + b_{jk}S_{ik} - \frac{2}{3}b_{lm}S_{lm}\delta_{ij}) + C_5k(b_{ik}\Omega_{jk} + b_{jk}\Omega_{ik}),\end{aligned} \tag{C.63}$$

into a near-wall model,

$$\Pi^w_{ij} = -5\frac{\varepsilon}{k}\left[\overline{u_i'u_k'}n_jn_k + \overline{u_j'u_k'}n_in_k - \frac{1}{2}\overline{u_k'u_l'}n_kn_l(n_in_j + \delta_{ij})\right], \tag{C.64}$$

based on the value of α. Here n_i is the unit wall-normal vector. The blending parameter α is calculated from an elliptic equation:

$$\alpha - L^2\nabla^2\alpha = 1, \tag{C.65}$$

where L is a turbulent length scale. n is calculated by

$$n_i = \frac{\nabla \alpha}{||\nabla \alpha||}. \tag{C.66}$$

The time and length scales are calculated by

$$T = \max\left(\frac{k}{\varepsilon}; C_T \left(\frac{\nu}{\varepsilon}\right)^{1/2}\right), \tag{C.67}$$

and

$$L = C_L \max\left(\frac{k^{3/2}}{\varepsilon}; C_\eta \frac{\nu^{3/4}}{\varepsilon^{1/4}}\right). \tag{C.68}$$

ε_{ij} is also blended based on α, which varies from an isotropic freestream form and an anisotropic near-wall form:

$$\varepsilon_{ij} = (1-\alpha^2)\frac{\overline{u_i' u_j'}}{k}\varepsilon + \frac{2}{3}\alpha^2 \varepsilon \delta_{ij}, \tag{C.69}$$

where ε is the specific dissipation of turbulent kinetic energy. It is modelled using the transport equation

$$\frac{D\varepsilon}{Dt} = \frac{C'_{\varepsilon 1}\mathcal{P} - C_{\varepsilon 2}\varepsilon}{T} + \frac{\partial}{\partial x_l}\left[\left(\frac{C_\mu}{\sigma_\varepsilon}\overline{u_l' u_m'}T + \nu \delta_{lm}\right)\frac{\partial \varepsilon}{\partial x_m}\right]. \tag{C.70}$$

The constant $C'_{\varepsilon 1}$ is adjusted to enhance dissipation in the buffer region:

$$C'_{\varepsilon 1} = C_{\varepsilon 1}\left[1 + A_1(1-\alpha^2)\frac{\mathcal{P}}{\varepsilon}\right]. \tag{C.71}$$

Model coefficients are

$$C_1 = 3.4, \quad C_1^* = 1.8, \quad C_3 = 0.8, \quad C_3^* = 1.4, \quad C_4 = 1.25, \quad C_5 = 0.4,$$

$$C_\mu = 0.21, \quad \sigma_k = 1.0, \quad \sigma_\varepsilon = 1.15, \quad C_T = 6, \quad C_L = 0.161, \quad C_\eta = 80,$$

$$C_{\varepsilon 1} = 1.44, \quad C_{\varepsilon 2} = 1.83, \quad A_1 = 0.095.$$

Note that model coefficients are as per the low Reynolds number calibrations of Manceau (2015); the high Reynolds number formulation modifies coefficients C_L and A_1, and adopts blending functions based on α^3 rather than α^2. Wall boundary conditions are $\overline{u_i' u_j'} = 0$ and $\alpha = 0$. An algebraic closure is used to evaluate ε at the cell centre closest to the wall: $\varepsilon_1 = 2\nu k/d^2$.